

## DESIGN OF A 2.45 GHZ COMPACT WEARABLE ANTENNA FOR WIRELESS BODY AREA NETWORKS AND INDUSTRIAL WIRELESS APPLICATIONS

D. Ramesh Varma

M. Murali

M. Vamshi Krishna

M. Venkata Subbarao<sup>1</sup>

### Keywords:

Wireless Body Area Network; Wearable Antenna; Flexible substrate material; Compact; Surface Currents.



### A B S T R A C T

This paper presents designing and optimizing a compact wearable antenna in Wireless Body Area Networks (WBANs) and Industrial Wireless Applications. The antenna is specifically developed to operate at a frequency of 2.45GHz, which is commonly used in wireless communication systems. By leveraging a flexible substrate material with a dielectric constant of 2.2, the antenna achieves compactness while maintaining efficient performance. The design process involves meticulous optimization to maximize the antenna's bandwidth, enabling fast and reliable wireless data transmission within the WBAN network. The antenna's characteristics, such as radiation pattern, gain, and impedance matching, are thoroughly evaluated through extensive simulations using specialized software. The results demonstrate the effectiveness of the proposed design, highlighting its capability to facilitate high-bandwidth communication in WBANs. The optimized wearable antenna offers improved real-time data transmission, enabling the enhanced performance of wearable devices in healthcare, sports, and other relevant applications.

© 202x Published by Faculty of Engineering

### 1. INTRODUCTION

Wireless body area networks (WBAN) have become a promising technology for several uses, including measuring well-being, analyzing sports performance, and monitoring illness. WBANs are made up of tiny, low-power wireless devices that are worn on the body to gather and communicate crucial information including movement, temperature, and heart rate. Athletes, people looking to better their health and well-being, and medical professionals can all benefit from the seamless

and real-time monitoring made possible by these networks.

The effectiveness of the wireless communication antennas is crucial to the success of WBANs. To provide reliable and effective data transmission throughout the network, antennas play a critical role in signal transmission and reception. For smooth and real-time communication in WBANs to be possible, tiny wearable antennas that can function at high bandwidths must be designed and optimized. In this study, the

<sup>1</sup>Corresponding author: M. Venkata Subbarao  
Mail ID: mvsbbarao@svecw.edu.in

design and optimization of a small wearable antenna for high-bandwidth WBAN applications are presented. The antenna is made to function at 2.45 GHz, a frequency that is frequently employed in wireless communication systems. The selection of this frequency makes it possible to work with current wireless devices and infrastructure.

Using a flexible substrate material with a dielectric constant of 2.2 can obtain a small form factor appropriate for wearable devices. The performance of the antenna can be reduced without sacrificing size by using a flexible substrate. To enable quick and dependable wireless data transfer inside the WBAN network, careful optimization is used during the design phase to maximize the antenna's bandwidth. By employing a flexible substrate material with a dielectric constant of 2.2, this antenna can create wearable device-friendly, compact form factors. By adopting a flexible substrate, the performance of the antenna can be decreased without sacrificing size. This is crucial in healthcare applications since rapid transmission of patient data and vital signs is essential. Extensive simulations are performed using specialized software to assess the performance of the proposed design. This can assess the antenna's many properties, including radiation pattern, gain, and impedance matching. These assessments help us improve the design for optimum performance by revealing important information about the antenna's functionality.

The radiation pattern, gain, and impedance-matching features of the microstrip patch antenna can be investigated by simulating its activity using CST software. The software offers a thorough platform for enhancing and perfecting the antenna design, enabling us to adjust variables for optimum performance. The validation of the proposed architecture and assurance of its performance in high-bandwidth applications within WBANs depend heavily on the insights obtained from CST simulations. The outcomes of the simulations show how effective the suggested little wearable antenna is. The examination of the radiation pattern shows that the antenna reliably transmits and receives signals within the intended frequency range. This results in efficient signal transmission and reception. The antenna also has great impedance matching, which reduces signal loss and improves power transfer efficiency.

The better performance of wearable devices in healthcare, sports, and other related applications is made possible by wearable antenna, which provides improved real-time data transmission. The improved wearable antenna advances wearable technology for use in sports, healthcare, and other relevant fields. While its high-performance features enable accurate data collecting and an enhanced user experience, its compactness improves user comfort. The proposed antenna design opens up new opportunities for personalized healthcare, sports performance analysis, and wellness tracking by

providing dependable and effective wireless communication. This advances WBAN technology. The antennas can be designed for the Ka band applications.

Based on the insights from the earlier works, this article proposes a compact wearable antenna for wireless body area networks. The article is arranged as follows. Section II conducts literature survey on flexible antennas Section III describes the antenna modeling and the mathematical foundation. Section IV describes the results and discussions. Section V describes the bending effects. Section VI concludes the work.

## 2. LITERATURE REVIEW

Wearable antennas have gained importance in the field of communications and biomedical. The researchers have been thoroughly continuing their research on the wearable antennas. A proposed ultra-wideband coplanar waveguide feed antenna with an exceptionally high bandwidth is presented, targeting applications in the medical field, smart homes, and futuristic industrial settings (Shastri et al., 2023). The study on wideband wearable antennas designed for applications in 5G, IoT, and medical fields is presented. The antennas are presented in conjunction with metamaterial to enhance their performance and characteristics (Sabban et al., 2020). An emphasis of the architecture of Wireless Body Area Network (WBAN) and the technology's prerequisites are outlined (Arefin et al., 2017). They also explored its evolution and adoption across various domains such as biomedicine, communication, and defense. S-shaped antenna for the applications of the Ka band applications is proposed (Rama Krishna et al., 2019).

A Wireless Body Area Networks (WBANs) and their potential in various medical applications is explained (Darwish et al., 2023). They conducted an extensive survey of systems and applications in healthcare, focusing on wearable and implantable sensors. The paper addresses the significant challenges and ongoing research issues within WBANs. Furthermore, they provided examples of how individuals can benefit from wireless sensor technologies in home environments, enhancing overall quality of life, while emphasizing key considerations during the development process. A flexible antenna incorporating polyimide (PI) material and featuring a defected ground structure is suggested for applications in telemedicine and wireless communication (Kumar et al., 2022). Numerous energy harvesting and power management techniques were thoroughly examined by researchers (Preethichandra et al., 2023). They subsequently provided an overview of recent advancements in wearable sensors and novel materials used for their development. A compact wearable antenna for biomedical applications is proposed (Ramesh Varma et al., 2023). The antenna performance is investigated by different textile substrates. In this study, the proposed antenna is used to detect the malicious tissues in the human body.

A wearable antenna with two configurations is proposed (Ramesh Varma et al., 2023). One is, without slots and other with slots. From the results, the antenna works better in the case of antenna with the slots. This antenna is placed on the human phantom model to detect the malicious tissues in the human body and it is observed that there is a frequency shift for the phantom with the tumor inside. A wearable antenna for the wireless body area networks which can be applicable for the different fields of communication is proposed (Jhunjhunwala et al., 2022). The review on wearable antennas outlines various challenges and issues associated with the design, including aspects such as material selection and fabrication techniques (Paracha et al., 2019). A meandered shaped antenna applicable for the Ku band applications with the concept of slots in it is proposed (Nanda Kumar et al., 2019). Flexible substrates in the wearable antennas are proposed (Dang et al., 2020). This study explains about parameters of antennas for different substrates. A flexible substrate for a patch antenna utilizing nickel aluminate synthesized via the sol-gel method is introduced (Rahman et al., 2019). They examined the microwave dielectric properties of nickel aluminate to assess its suitability as an antenna substrate for microwave wave applications.

An adapted nonagonal monopole antenna with four ports is introduced for compact Multiple Input Multiple Output (MIMO) applications, designed specifically for use in Ultra-Wideband (UWB) scenarios (Addepalli et al., 2023). The flexible composite was synthesized using the sol-gel method. A flexible antenna for the ultra-wide band wireless body area network applications is proposed (Reshma et al., 2016). A study involving the design and simulation of a U-shaped slot rectangular microstrip patch antenna (RMSA) utilizing the High-Frequency Structure Simulator (HFSS) is conducted (Subhadra Panda et al., 2021). They examined the antenna's performance across various flexible substrates. The RMSA was crafted using diverse flexible substrate materials, including Epoxy, Teflon, Polyethylene, Polyamide, RT Duroid, and PDMS, with the aim of achieving an operational frequency range of 2.4–2.6 GHz. A novel Coral Reefs Optimization with Substrate Layer (CRO-SL) algorithm aimed at adjusting the resonant frequency and bandwidth of a wearable antenna intended for off-body communications within Wireless Body Area Network (WBAN) services at 2.42 GHz is proposed (Sanchez-Montero et al., 1982). A review on ultra-wide band antennas for the wireless body area networks is conducted (Mahmood et al., 2020). The paper examines the latest developments in wearable, textile, and flexible antennas that are integrated with metamaterial structures. The emphasis is on utilizing wearable and flexible substrate materials, with a particular focus on the design aspects of single and dual-band antennas (Ali et al., 2023). A MIMO antenna for the 5G communication is proposed (Venkat Rao et al., 2023). It is designed with the concept of bending curves.

### 3. ANTENNA MODELLING AND MATHEMATICAL FOUNDATION

The mathematical and computational modeling of an antenna's behavior and properties is known as antenna modeling. Without the requirement for a physical prototype, it makes it possible to examine and analyze the antenna's performance, radiation pattern, impedance, gain, and other crucial factors. Analytical methods, empirical models, and numerical methods are some of the methodologies utilized for antenna modeling. Analytical modeling describes the behavior of the antenna using mathematical equations and formulas based on electromagnetic principles. It offers closed-form answers for straightforward antenna designs and geometries. Engineers may investigate various antenna designs, enhance their performance, and forecast how they will behave under various operating conditions. It enables a better knowledge and optimization of antenna performance prior to manufacturing and cuts down on the time and expense associated with physical prototyping. These parameters play a significant role in determining the antenna's behavior and characteristics.

The width of the patch refers to the lateral dimension of the radiating element in the antenna design. It is an important parameter that influences the antenna's impedance matching, bandwidth, and radiation pattern. The overall dimensions of the antenna are 48 X 43 X 0.938mm. The slots are made in the radiating patch with the polygon shape. The geometry of the polygon can influence the radiation pattern of the antenna. This control is vital for directing the signal in a specific direction, increasing the antenna's gain and efficiency.

$$W_p = \left( \frac{c}{2f_0\sqrt{\frac{\epsilon_r+1}{2}}} \right) \quad (1)$$

Where,

$W_p$  is the Width of the patch (lateral dimension of the radiating element)

c: Speed of light in free space (approximately  $3 \times 10^8$  meters per second)

$f_0$ : Resonant frequency of the antenna (desired operating frequency)

$\epsilon_r$ : Effective relative dielectric constant of the substrate material used in the antenna design.

The effective relative dielectric constant  $\epsilon_{eff}$  is a critical factor in determining the propagation characteristics of the antenna. It accounts for the influence of the substrate material used in the antenna design and affects the antenna's impedance and resonant frequency.

$$\epsilon_{eff} = \frac{\epsilon_r+1}{2} + \frac{\epsilon_r-1}{2} \left[ \frac{1}{\sqrt{1+12\left(\frac{h}{W_p}\right)}} \right] \quad (2)$$

The extension of length  $\Delta L$  refers to the additional length added to the antenna structure to achieve the desired resonant frequency. By adjusting the length, the antenna's resonant frequency can be fine-tuned to the desired operating frequency, such as 2.45 GHz in this case.

$$\Delta L = 0.824h \left( \frac{(\epsilon_{eff}+0.3)(\frac{W_p}{h}+0.264)}{(\epsilon_{eff}-0.258)(\frac{W_p}{h}+0.8)} \right) \quad (3)$$

The antenna's effective length  $L_{eff}$  is a parameter that considers the extension of length and the antenna's physical length.

$$L_{eff} = c/f_r = \frac{c_0}{2f_r\sqrt{\epsilon_{eff}}} \quad (4)$$

The length of the antenna  $L$  refers to the physical length of the radiating element, excluding any extensions. It is an important parameter that affects the antenna's resonant frequency and radiation pattern.

$$L = L_{eff} - 2\Delta L \quad (5)$$

The ground dimensions of the antenna refer to the size and shape of the ground plane or substrate upon which the antenna is placed. The ground dimensions impact the antenna's impedance matching, radiation efficiency, and radiation pattern.

$$W_G = W + 6h \quad (6)$$

$$L_G = L + 6h \quad (7)$$

## 4. RESULTS & DISCUSSIONS

### 4.1 Iteration 1

#### A) Return Loss

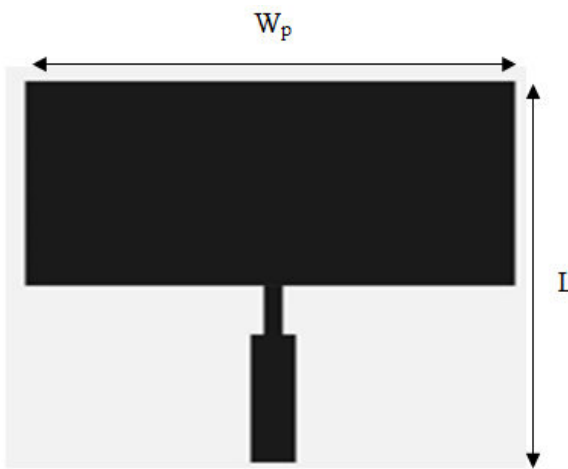


**Figure 1.** Proposed Antenna Design

Foundational components were meticulously put together in the antenna design's initial iteration to create a starting point. The substrate, made of lossy FR4 material, was put on top of a copper (annealed) ground layer, which gave a reliable grounding. A simulation port was added to the patch, a crucial radiating

component, to make it easier to link to an external system. It was positioned onto the substrate at a height of 0.938mm as shown in Figure 1. Modifying the length of the transmission line allows for precise adjustment of the electrical length of the feed line, enabling effective matching of the complex impedance of the antenna with that of the transmission line and the connected circuitry.

In this initial iteration, the design's 3.22 GHz resonance frequency and  $S_{11}$  return loss of about -22 dB were highlighted as promising features as shown in Figure 2. A notable finding, meanwhile, was that the resonance frequency significantly departed from the 2.45 GHz range anticipated for seamless integration with the human body. An intentional movement was made towards establishing resonance alignment with the required human-interaction frequency spectrum as a result of this divergence, which indicated possible difficulties in optimizing the antenna for on-body applications. Health monitoring sensors, sports performance tracking, gesture-controlled devices, environmental monitoring, etc. is a few uses for antennas with a frequency of 3.22GHz. The antenna surprisingly demonstrated resonance at additional frequencies in addition to our intended frequency. These frequencies demonstrate the versatility of the antenna and are distinguished by their distinctive  $S_{11}$  values. Even though it wasn't our main aim, the device showed effective resonance at 6.3 GHz with an  $S_{11}$  value of -14.8. As a result, it is possible that our antenna will be useful in situations requiring the use of various frequency bands. More shocks emerged with further investigation.

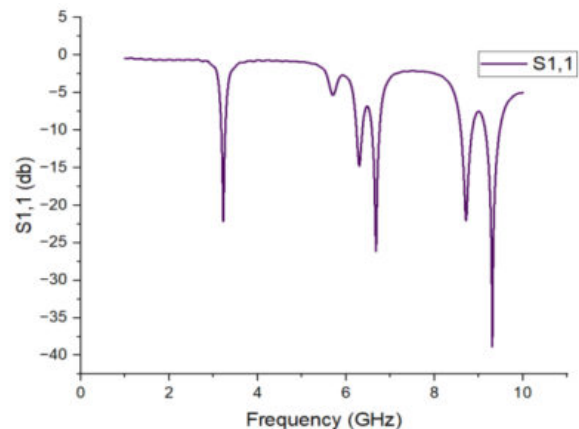


**Figure 2.** Return Loss ( $S_{11}$ ) vs Frequency at various Frequencies

The antenna displayed strong resonance characteristics at 6.6 GHz ( $S_{11} = -26.6$  dB) and 8.7 GHz ( $S_{11} = -22$  dB), suggesting the possibility of high-frequency communication scenarios. At 9.3 GHz, where our antenna resonated very well ( $S_{11} = -38.9$  dB), the most unexpected result was found. While not our primary goal, this demonstrates how the antenna may be adjusted to even higher.

### B) Voltage Standing Wave Ratio

Voltage Standing Wave Ratio (VSWR) evaluates how well power is transferred from the transmission line to the antenna and discovers that the VSWR was 1.17. A positive indication is a VSWR value of 1.17 as depicted in Figure 3.

It implies that our antenna efficiently and with little loss transmits power at 3.22 GHz. The fact that hardly much energy is reflected back into the transmission line by our antenna suggests that it is properly tuned. For an antenna to perform well, such efficiency is essential. Although resonance at 3.22 GHz was our main objective, this VSWR measurement at 3.22 GHz shows that our antenna is adaptable and can function well at other frequencies. In a variety of wireless communication applications, antennas need to be adaptable.

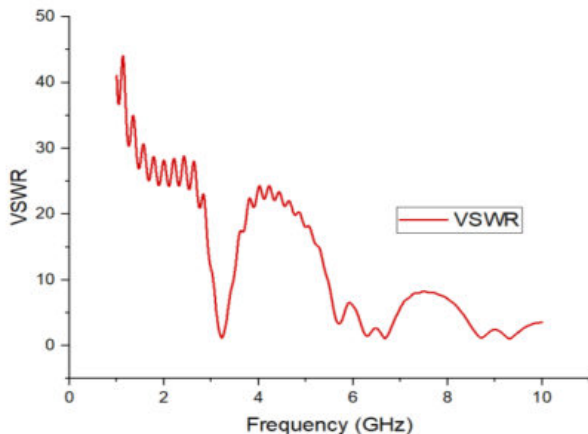


Figure 3. VSWR vs Frequency at various Frequencies

### C) Surface Current Distribution

Understanding the behaviour of microstrip patch antennas depends on surface currents. The electromagnetic fields' interactions with the antenna's conducting surfaces directly result in these currents. Surface currents are essential in determining the radiation parameters. Surface currents in the antenna construction during our initial iteration at a frequency of 2 GHz ranged from -41.9 to 41.9 A/m as depicted in Figure 4. An important component of antenna operation, these surface currents can be seen as lines and highlight areas where electromagnetic energy flows. The transmission line and patch elements had the highest surface current values, suggesting the importance of these components in efficiently radiating electromagnetic energy. Surface current visualisation aids in understanding the behaviour of the antenna and influences design choices.

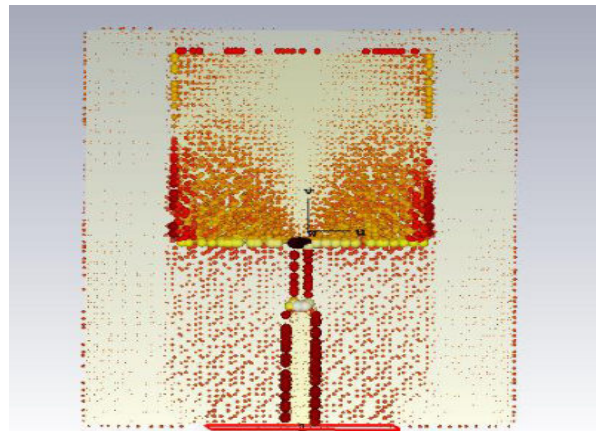


Figure 4. Surface Current distribution of the Proposed Antenna

### D) Directivity

The ability of an antenna to focus its radiated energy in a particular direction is measured using the fundamental notion of directivity in antenna design. The effectiveness of the antenna's capacity to broadcast and receive signals is directly impacted by this essential parameter. At a frequency of 3 GHz, the antenna attained a main lobe magnitude of 6.27 dBi, suggesting a power concentration in the principal direction of 7.0 degrees. The main radiation beam's width, which is commonly measured in terms of the 3 dB beam width, was 90.4 degrees as shown in Figure 5. The far field directivity at a 90-degree azimuthal angle also demonstrated the antenna's capability to focus energy in the desired direction. This data, visualized as a polar graph, highlights the antenna's directivity properties and emphasizes its capability to concentrate energy for dependable wireless communication in your high-bandwidth Wireless Body Area Network (WBAN) applications.

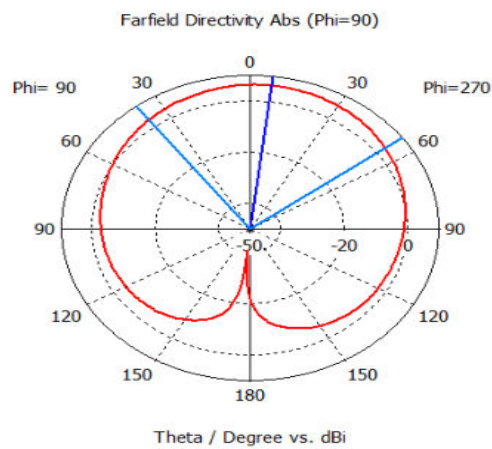


Figure 5. Directivity of the Proposed Antenna

## 4.2 Iteration 2

### A) Return Loss

Enhancements were included in the antenna design in the second iteration to address the frequency deviation

seen in the first iteration. These adjustments were made to better match the antenna's operating frequency with the targeted 3.03 GHz range and  $S_{11}$  return loss of about -12.22 dB were highlighted as promising features and improve its ability to interact with the human body. To accomplish this, five strategically placed diamond-shaped cuts were made to the patch structure as shown in Figure 6. These cuts, which served as slots, were strategically placed to change the resonance properties of the antenna and increase its operational bandwidth. The goal of this adjustment was to raise the likelihood of reaching resonance close to the 2.45 GHz target frequency. The resonance frequency, which is presently measured at 3.03 GHz, has significantly decreased, according to the modeling findings for this iteration. This change in the direction of the desired frequency demonstrated the effectiveness of the rhombus shaped slots in modifying the antenna's resonant behavior.

Our antenna, however, offered more pleasant surprises. It displayed substantial resonance characteristics at 5.5 GHz ( $S_{11} = -11.4$  dB) and 6.28 GHz ( $S_{11} = -13.8$  dB) as shown in Figure 7. Although not our primary objective, these frequencies demonstrate the antenna's versatility in terms of its ability to function well in several frequency bands. The most fascinating finding was made at 9.15 GHz when our antenna showed extraordinary resonance with an  $S_{11}$  value of -13.3 dB. This result indicates that our antenna has the potential for high-frequency transmission, much beyond the bounds of our initial design. In essence, Iteration 2's frequencies highlight the antenna's adaptability, demonstrating its performance at a range of frequencies.

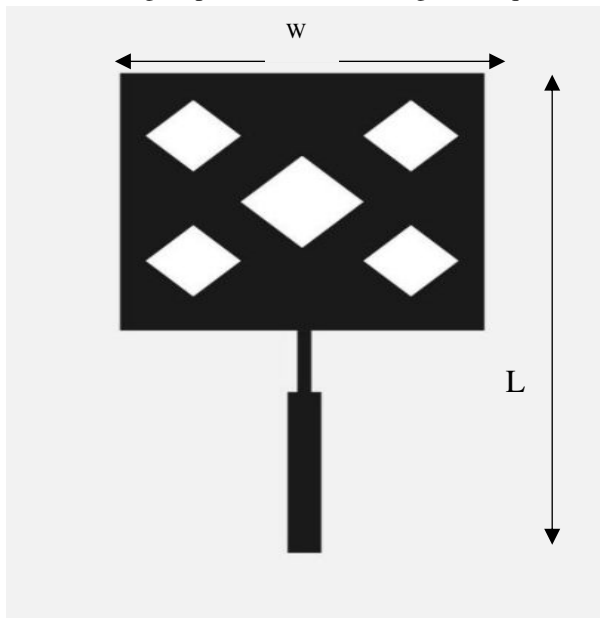


**Figure 6.** Second Iteration of the Proposed Antenna Design

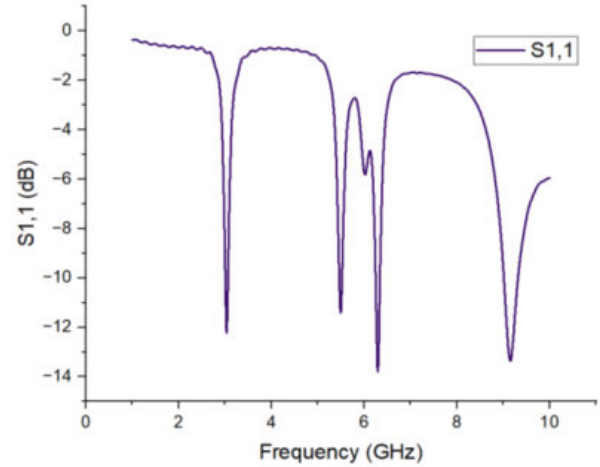


**Figure 7.** Return Loss ( $S_{11}$ ) vs Frequency at various Frequencies

#### B) Voltage Standing Wave Ratio

At 3.03 GHz, the observed VSWR value was 1.7. Despite being slightly greater than the ideal value of 1, which indicates no reflection, a VSWR value of 1.7 indicates a reasonably acceptable impedance match as depicted in Figure 8. This measurement shows that our antenna transfers power well at 3.03 GHz, although with a little higher amount of reflected energy than a perfect match.

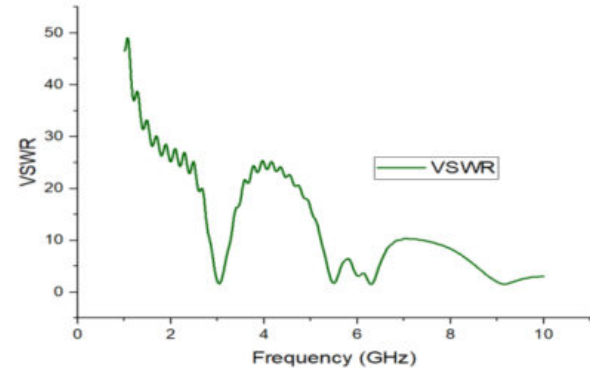


**Figure 8.** VSWR vs Frequency at various Frequencies

Although obtaining resonance at 3.03 GHz was our main goal, this VSWR test sheds light on the antenna's impedance behavior at this frequency. It means that, in general, our antenna design is well-tuned and capable of functioning well at this particular frequency, which can be important for some wireless communication applications.

#### C) Surface Current Distribution

The second iteration of the proposed antenna, which works at a frequency of 2 GHz, continues the investigation into how surface currents affect the functionality of the designed antenna. The paths electromagnetic energy takes as it moves along the

antenna's conducting surfaces are represented by surface currents. Observed that these currents had a minimum magnitude of -12.4 A/m and a maximum magnitude of 12.4 A/m in this iteration as depicted in Figure 9. Antenna's ability to broadcast signals depends heavily on these surface currents. These currents are important for the operation of the antenna even if they are not as powerful as those seen in the first iteration.

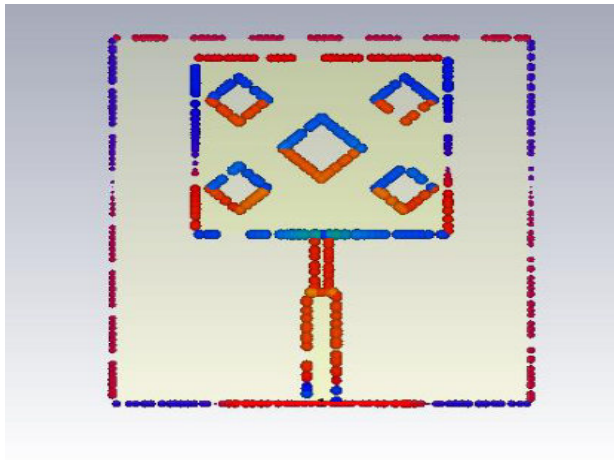


**Figure 9.** Surface Current distribution of the Second Iteration of the Proposed Antenna

#### D) Directivity

At a frequency of 3 GHz, the antenna achieved a main lobe magnitude of 6.32 dBi in the second iteration of the antenna design, working at a frequency of 3 GHz, indicating the power concentration in the principal direction at 4.0 degrees as shown in Figure 10. The principal radiation beam's width was represented by the angular width, which was 91.4 degrees and is sometimes expressed as the 3 dB beamwidth. Furthermore, the antenna's ability to efficiently direct energy in the appropriate direction is shown by the farfield directivity at a 90-degree azimuthal angle.

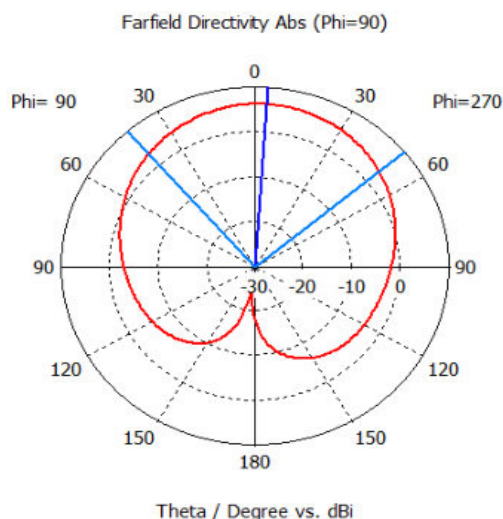


**Figure 10.** Directivity of the Second Iteration of the Proposed Antenna

### 4.3 Iteration 3

#### A) Return Loss

Inset feed is intentionally added to the patch structure in the third iteration as shown in Figure 11. With these strategically positioned slots, the antenna's resonant frequency with the targeted 3.06 GHz range and S<sub>11</sub> return loss of about -20.6 dB behavior will be subtly altered, improving impedance matching and radiation patterns when they come into contact with the human body.

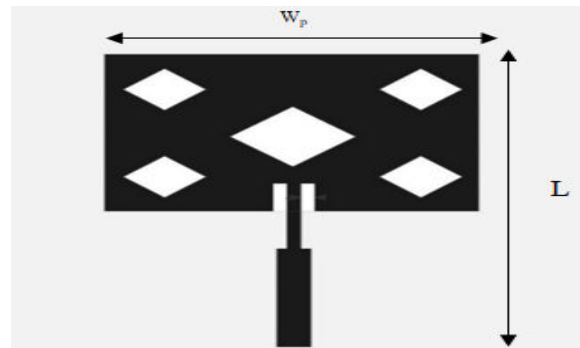


**Figure 11.** Third Iteration of the Proposed Antenna Design

According to the simulation findings, these changes brought the resonance frequency closer to the intended 2.45 GHz range. The antenna's potential for efficient on-body communication is highlighted by this measured improvement, which is in line with the objectives of wearable applications within the Wireless Body Area Network (WBAN) domain.

At other frequencies, observed fascinating resonance occurrences. The S<sub>11</sub> value was around -10 dB at 5.5 GHz, indicating effective power transfer. Similar to this, have found a significant resonance with an S<sub>11</sub> value of -35.2 dB at 6.3 GHz. It is depicted in Figure 12. It is while not the main interest, these frequencies demonstrate the antenna's adaptability to work well in a variety of frequency bands. These results indicate that the antenna design exhibits flexibility to several frequencies within the studied range and is not restricted to a particular frequency.

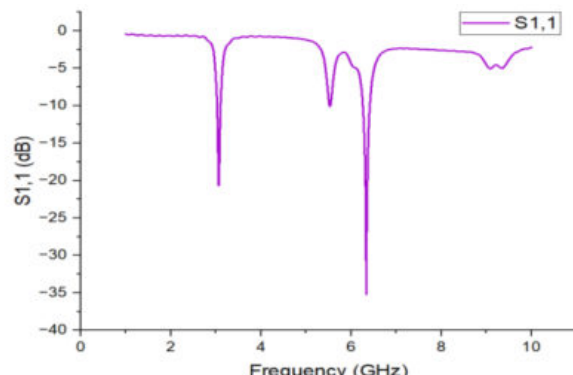


**Figure 12.** Return Loss (S<sub>11</sub>) vs Frequency at various Frequencies

### B) Voltage Standing Wave Ratio

As depicted in Figure 13, the measured VSWR value was an impressive 1.2. A VSWR value of 1.2 indicates an excellent impedance match.

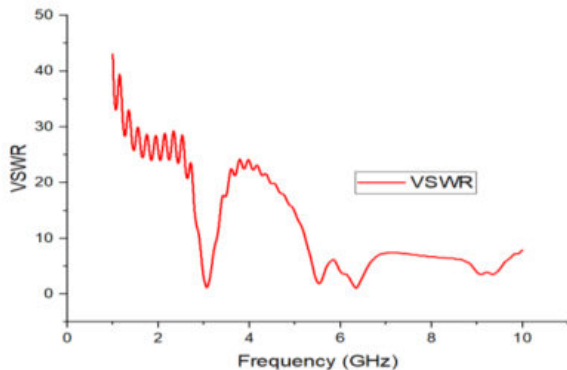


**Figure 13.** VSWR vs Frequency at various Frequencies

It suggests that at 3.06 GHz, the antenna efficiently transfers power with minimal reflection. This is a highly favorable outcome as it ensures that nearly all the energy is effectively delivered to the antenna for radiation. While, the primary goal was to achieve resonance at 3.05 GHz, this VSWR measurement at 3.06 GHz demonstrates the antenna's versatility and capability to provide efficient power transfer at closely related frequencies.

### C) Surface Current Distribution

As shown in Figure 14, the behaviour of surface currents within the confines of the antenna design in the third iteration is intended to operate at a frequency of 2.45 GHz. The movement of electromagnetic energy along the conducting surfaces of the antenna structure is represented by surface currents. The surface currents show a minimum magnitude of -10.5 A/m and a maximum magnitude of 10.5 A/m in this iteration. The operation of the designed antenna is fundamentally dependent on these surface currents. They establish where and how the antenna structure will most effectively radiate electromagnetic energy. Despite having a smaller magnitude than in earlier versions, these currents are crucial for enhancing the antenna's radiating properties.

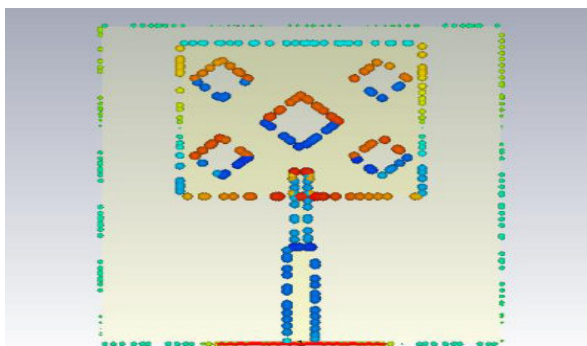


**Figure 14.** Surface Current distribution of the Third Iteration of the Proposed Antenna

### D) Directivity

The antenna achieved a main lobe magnitude of 6.04 dBi in the third iteration of the antenna design, working at a frequency of 2.45 GHz as depicted in Figure 15. This suggests that the principal direction, which was at 3.0 degrees, had a concentration of radiated power. The principal radiation beam's width, which is commonly measured in terms of the 3 dB beamwidth, was 95.4 degrees. Furthermore, the antenna's ability to focus energy in the appropriate direction was demonstrated by its farfield directivity at a 90-degree azimuthal angle. This information, which is graphically depicted in a polar graph, efficiently highlights the antenna's directivity properties and highlights its capacity to focus energy.

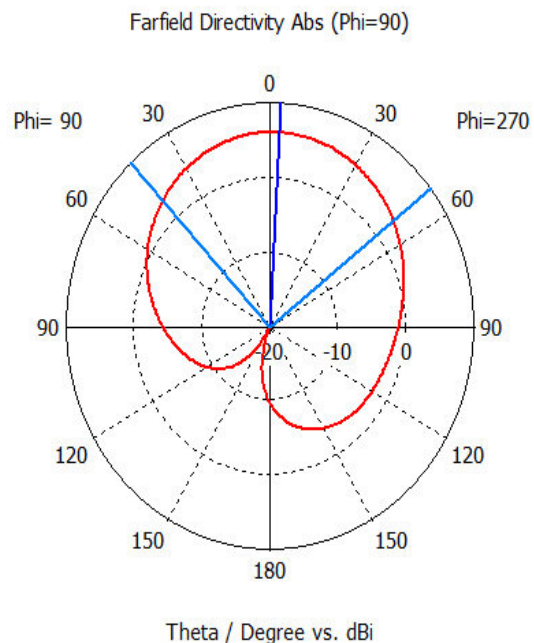


**Figure 15** Directivity of the Third Iteration of the Proposed Antenna

## 4.4 Iteration 4

### A) Return Loss

The fourth version of the antenna design marked a significant advance. As shown in Figure 16, this stage required a strategic adjustment in the shape of three-square incisions along the patch's sides, building on the accumulated advancements from earlier iterations. Better possibility for getting the desired resonance frequency for the best on-body performance turned out to be these carefully placed incisions. The resonant frequency was impressively aligned with the target frequency of 2.54 GHz and the  $S_{11}$  value of -15.5dB, according to simulation results. This -15.5 dB accomplishment demonstrated how well the square slots were able to modify the behaviour of the antenna. The antenna design now complied with the operational requirements necessary for flawless interaction with the human body as a result of this alignment.

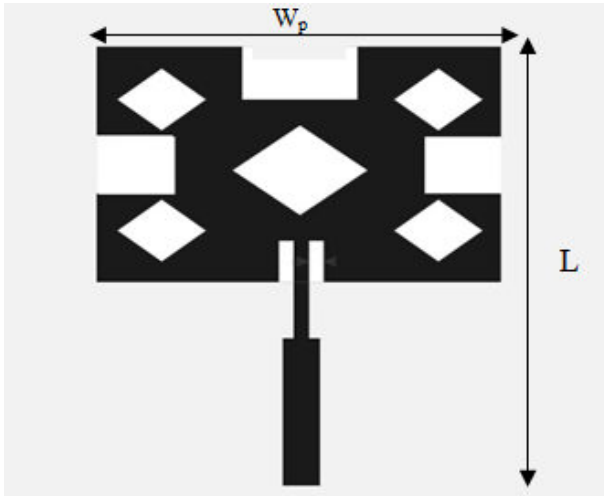


**Figure 16.** Fourth Iteration of the Proposed Antenna Design

This important result is the result of a methodical design process that produced an antenna configuration that satisfies the criteria for Wireless Body Area Network (WBAN) applications. Square slots are used to illustrate how the iterative process works and to demonstrate how even small changes may have a big impact. The antenna's readiness for practical application has been confirmed by the fourth iteration's success, creating opportunities for its incorporation into wearables that advance interactive wearable systems, sports monitoring, and healthcare. In design, also noticed intriguing resonance features at 5.5 GHz ( $S_{11} = -8.5$  dB) and 5.95 GHz ( $S_{11} = -15.2$  dB). Although not the main interest, these frequencies demonstrate the antenna's adaptation to other frequency bands and confirm its versatility. Figure 17, presents resonance at 2.45 GHz in Iteration 4 demonstrated a considerable accomplishment and confirmed the antenna's appropriateness for basic wireless communication applications. The investigation of different frequencies also raises the possibility of using it in various communication contexts.

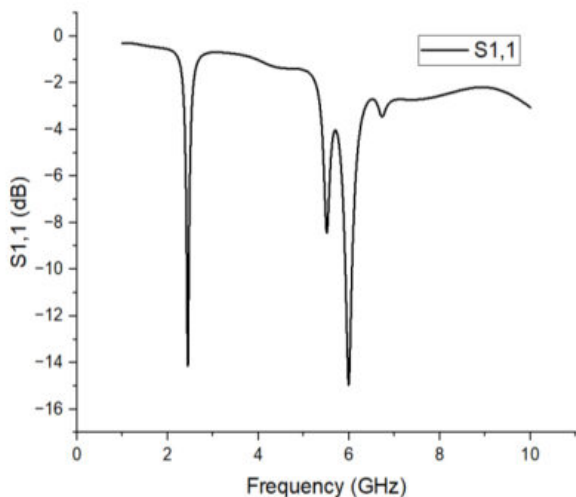


**Figure 17.** Return Loss ( $S_{11}$ ) vs Frequency at various Frequencies

### B) Voltage Standing Wave Ratio

The VSWR measurement came in at 1.4. A very good impedance match is indicated by a VSWR value of 1.4. It shows that the designed antenna efficiently transmits power at 2.45 GHz with little reflection, ensuring that most of the energy is focused towards radiation.

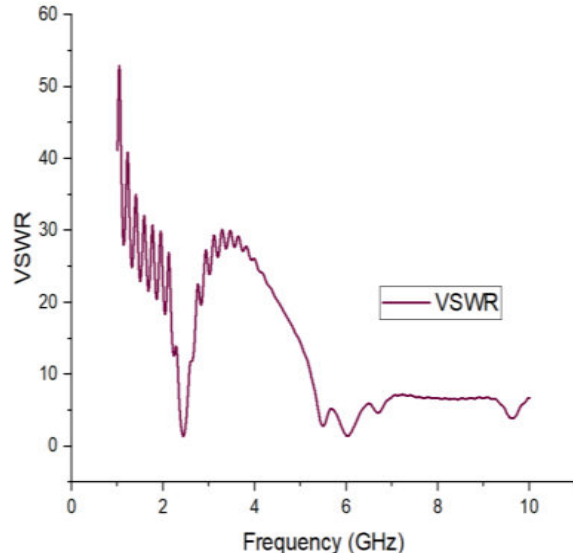


**Figure 18.** VSWR vs Frequency at various Frequencies

It is depicted in Figure 18 while achieving resonance at 2.45 GHz was main goal, this VSWR measurement at that frequency highlights the antenna's consistent impedance characteristics. It illustrates that, at this crucial frequency, which is commonly applied in wireless communication applications, the designed antenna design constantly maintains an effective impedance match. The antenna is better suited for crucial wireless communication jobs as a result of its durability.

### C) Surface Current Distribution

The radiation pattern of the antenna is shaped by how surface currents are distributed. Surface currents in the fourth iteration of antenna design running at a frequency of 2.45 GHz. The movement of electromagnetic energy along the conducting surfaces of the antenna structure is represented by surface currents as shown in Figure 19. The surface currents show a minimum magnitude of -9 A/m and a maximum magnitude of 9 A/m in this iteration. These surface currents play a crucial role in determining the way antenna structure radiates electromagnetic energy. These currents continue to be an essential part of enhancing the antenna's radiated properties despite variations in magnitude. These currents continue to be an essential part of enhancing the antenna's radiated properties despite variations in magnitude. A steady reduction in surface current magnitudes during iteration is observed. This pattern denotes improved antenna performance and better-controlled EM radiation.

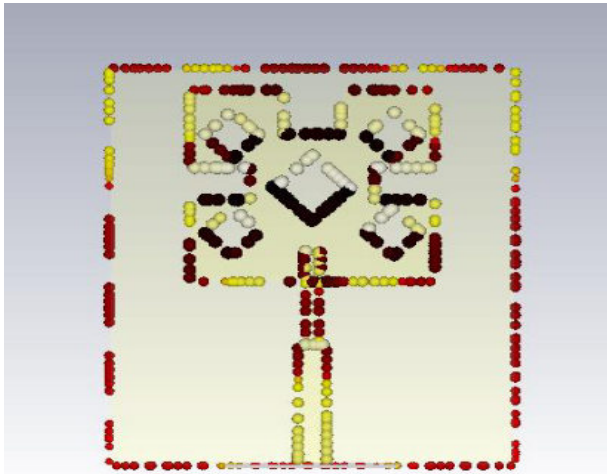


**Figure 19.** Surface Current distribution of the Fourth Iteration of the Proposed Antenna

#### D) Directivity

The antenna was able to attain a main lobe magnitude of 5.96 dBi with the antenna design while operating at a frequency of 2.45 GHz. This shows the concentration of radiated power at 6.0 degrees in the main direction. The principal radiation beam's width, which is commonly measured in terms of the 3 dB beam width, was 97.4 degrees as shown in Figure 20. Additionally, you reduced side lobes to a level of -8.5 dB, improving the antenna's capacity to concentrate radiation. Furthermore, the far field directivity at a 90-degree azimuthal angle shows how effectively the antenna directs energy in the desired direction. The polar graph used to display this data clearly illustrates the antenna's directivity properties. It highlights how well the antenna concentrates energy, which is important for trustworthy wireless communication in high-bandwidth Wireless Body Area Network (WBAN) applications, providing real-time monitoring and analysis of data from worn sensors.

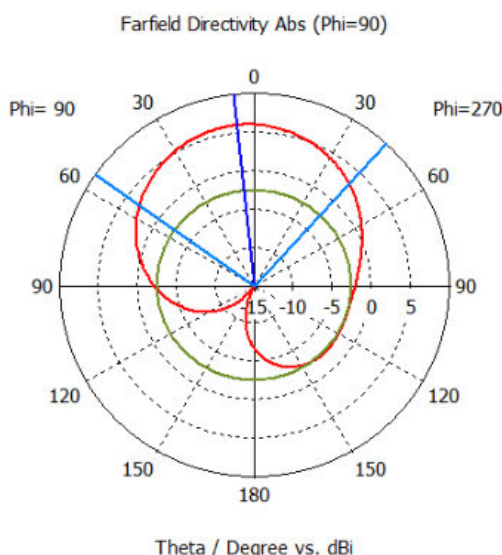


**Figure 20.** Directivity of the Fourth Iteration of the Proposed Antenna

## 5. ANTENNA PERFORMANCE UNDER BENDING CONDITIONS

The suggested Wearable microstrip patch antenna's design was simulated, and measurements were taken when the antenna was bent due to its wearability. When the antenna bends, return loss is simulated and measured. Under flat conditions, the bandwidth is the same as the antenna in size. The gain is 4.2 dBi on bending applications, and the efficiency of the suggested antenna is 50% under some bending which is still acceptable for wearable applications. Additionally, there are some similarities between the simulation and measured outcomes. We investigated how bending conditions affected its performance. By looking into three distinct bending angles  $-10^\circ$ ,  $-15^\circ$ , and  $-20^\circ$  for the bending criteria, results are simulated. An antenna's structural changes when bent have a big impact on its radiation properties and resonant frequency as shown in Figure 21. As expected, the antenna's resonance frequency significantly decreased as the bending angle increased.

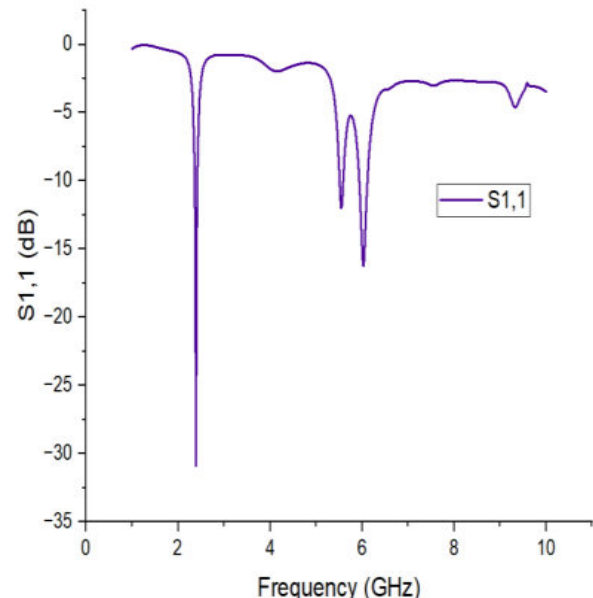


**Figure 21.** Return Loss vs Frequency for bending angle  $-10^\circ$  degrees

This discovery is explained by the fact that the antenna's physical shape changes as it bends, changing its electrical characteristics. These bending circumstances have a wide range of effects. First off, the antenna's adaptability for wearable applications were adhering to the contours of the body is crucial is enhanced by its ability to adjust to various bending angles. The frequency shift seen under bending conditions, on the other hand, emphasizes how crucial it is to fine-tune antenna designs in order to keep resonance within the required frequency band as shown in Figure 22 and Figure 23.

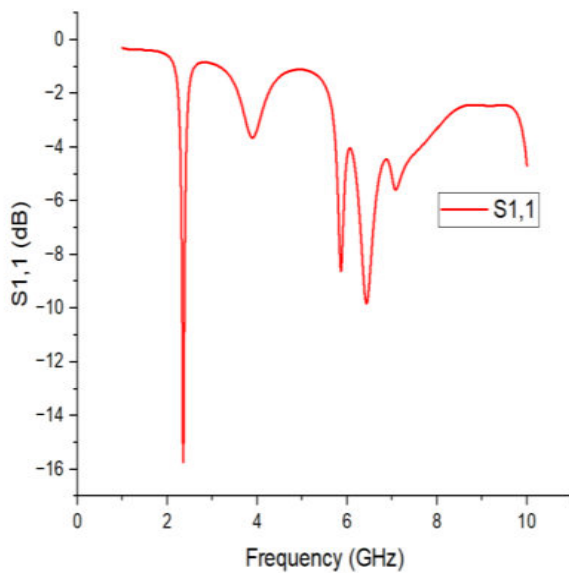


**Figure 22.** Return Loss vs Frequency for bending angle -15 degrees

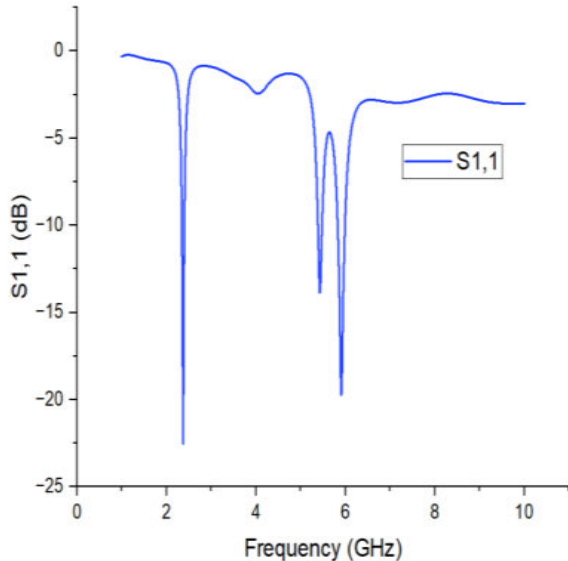


**Figure 23.** Return Loss vs Frequency for bending angle -20 degrees

Table 1 summarizes the parameters of proposed antenna for multiple iterations. These findings highlight the requirement for adaptable and flexible antennas in wearable technology, offering enhanced performance and dependability in changing on-body environments. Applications of antenna bending conditions include environmental sensing, emergency response, tracking athletic performance and military and defense. The

specific absorption rate is measured for all the iterations as; it is important parameter for the wearable antenna.

**Table 1.** Parameters of Proposed Antenna for Multiple Iterations

Parameter	Iteration			
	1	2	3	4
Resonant Frequency (GHz)	3.22	3.02	3.06	2.45
S <sub>11</sub> (dB)	-22	-12.22	-20.6	-15.5
VSWR	1.17	1.7	1.2	1.4
Surface Current (A/m)	-41.9 to 41.9	-12.4 to 12.4	-10.5 to 10.5	-9 to 9
SAR(W/kg)	0.000785	0.000698	0.000642	0.000545

## 6. CONCLUSION

In this paper, a compact wearable microstrip patch antenna designed for high-bandwidth applications within Wireless Body Area Networks (WBANs) is presented. The antenna is optimized to operate at a frequency of 2.45 GHz, aligning with the requirements of modern wireless communication systems. The use of a flexible substrate material with a dielectric constant of 2.2 enables a compact design without compromising efficiency. The antenna's bandwidth is gradually increased throughout four cycles, ensuring quick and dependable data transmission inside the WBAN network. A decline in surface current magnitude, a sign of progressive optimization, shows advancements in the antenna's performance with iteration. The efficiency of the suggested design is supported by the simulation results, which also cover radiation pattern analysis, gain, impedance matching, and surface current behavior. The wearable microstrip patch antenna improves real-time data transmission capabilities by enabling high-bandwidth connectivity in WBANs. This innovation promises to have a profound impact on a variety of industries, including sports and healthcare. The wearable microstrip patch antenna described in this research marks a significant development in WBAN technology. Because of its small size, effective operation, and high bandwidth capabilities, it stands out as a valuable asset in the expanding field of wearable technology and promises to have a revolutionary impact on a variety of industries.

## References:

- Addepalli, T., K. V. Babu, T. Vidyavathi, et al. (2023). Design and analysis of nonagonal patch unite with rectangular shaped 4-element UWB-MIMO antenna for portable wireless device applications. *Analog Integr Circ Sig Process* 114, 459–473 (2023). doi:10.1007/s10470-023-02138-y

- Ali, U., Ullah, S., Kamal, B., Matekovits, L., & Altaf, A. (2023). Design, Analysis and Applications of Wearable Antennas: A review. *IEEE Access*, 11, 14458–14486. doi: 10.1109/access.2023.3243292.
- Arefin, M., Ali, M. and Haque, A. (2017). Wireless Body Area Network: An Overview and Various Applications. *Journal of Computer and Communications*, 5, 53-64. doi: 10.4236/jcc.2017.57006.
- Dang, Q. H., Chen, S. J., Zhang, D. D., Kimtai, D. D., & Fumeaux, C. (2020). Flexible Substrate Materials for Wearable Antennas. *2020 4th Australian Microwave Symposium (AMS)*, Sydney, NSW, Australia. doi: 10.1109/ams48904.2020.9059490.
- Darwish A, Hassanien AE. (2023). Wearable and implantable wireless sensor network solutions for healthcare monitoring. *Sensors (Basel)*. 11(6):5561-95. doi: 10.3390/s110605561.
- Jhunjhunwala VK, Ali T, Kumar P, Kumar P, Kumar P, Shrivastava S, Bhagwat AA (2022). Flexible UWB and MIMO Antennas for Wireless Body Area Network: A Review. *Sensors (Basel)*. 6:22(23):9549. doi: 10.3390/s22239549.
- Kumar P. R, B.Y.V.N.R. Swamy, B. Prasad, K. Krishna, A. Narendra Babu & P. S. Brahmanandam (2022). Polyimide-based Flexible Antenna for Telemedicine and Wireless Applications. Recent Advances in Electrical & Electronic Engineering, *Recent Patents on Electrical & Electronic Engineering*. 16. doi:10.2174/2352096516666221201095009.
- Mahmood, S. N., Aris, I., Ismail, A., Soh, A. C., Zakaria, Z., & Alani, S. (2020). ON-OFF Body Ultra-Wideband (UWB) antenna for Wireless Body Area Networks (WBAN): A review. *IEEE Access*, 8, 150844–150863. doi:10.1109/access.2020.3015423.
- Nanda Kumar M, K Yogaprasad, V.R Anitha (2029). Meandered Shaped Microstrip feed Antenna for Ku-band Applications. *International Journal of advanced Science and Technology*, 28 (19), 16-20.
- Paracha, K. N., Rahim, S. K. A., Soh, P. J., & Khalily, M. (2019). Wearable Antennas: A review of materials, structures, and innovative features for autonomous communication and sensing. *IEEE Access*, 7, 56694–56712. doi: 10.1109/access.2019.2909146.
- Preethichandra, D. M. G., L. Piyathilaka, U. Izhar, R. Samarasinghe and L. C. De Silva (2023). Wireless Body Area Networks and Their Applications—A Review. *IEEE Access*, vol. 11, pp. 9202-9220, 2023, doi: 10.1109/ACCESS.2023.3239008.
- Rahman, M.A., M.R.I. Faruque & M. T. Islam (2019). Preparation of Flexible Substrate for Patch Antenna Based on Nickel Aluminate (NiAl<sub>2</sub>O<sub>4</sub>) Synthesized by Sol-Gel Method. *J. Electron. Mater.* 48, 2932–2939. doi: 10.1007/s11664-019-07041-9
- Rama Krishna, Ch Prabhu Anand, D Durga Prasad (2019). Design of S-Shaped Micro-strip Patch Antenna for Ka Band Applications. *International Conference on Intelligent Computing and Communication Technologies*, Pages 260-268.
- Ramesh Varma, D., B. Durga Saranya, G. Pavani, M. Venkata Subbarao, G. Challa Ram, D. Girish Kumar (2023), Design of fabric antennas for body protective garment applications and analysis on their performance, *Materials Today: Proceedings*, 80, Part 2, 1538-1547, doi:10.1016/j.matpr.2023.01.384.
- Ramesh Varma, D., M. Murali, M.Vamshi Krishna (2023). Compact, robust and low-profile textile antennas for biomedical applications with upgraded bandwidth for integration of easy garment. *Materials Today: Proceedings*, 80 (2), 1548-1555, doi:10.1016/j.matpr.2023.01.388.
- Reshma Lakshmanan and K. S. Shinoj (2016). Ultra-Wide Band Antenna for WBAN Applications, *Procedia Technology*, 24, 880-887. doi:10.1016/j.protcy.2016.05.149
- Sabban, A (2020). *Wideband Wearable Antennas for 5G, IoT, and Medical Applications, Advanced Radio Frequency Antennas for Modern Communication and Medical Systems*. IntechOpen, Sep. 23, 2020. doi: 10.5772/intechopen.93492.
- Sanchez-Montero, Rocío, Carlos Camacho-Gómez, Pablo-Luís López-Espí, and Sancho Salcedo-Sanz (1982). Optimal Design of a Planar Textile Antenna for Industrial Scientific Medical (ISM) 2.4 GHz Wireless Body Area Networks (WBAN) with the CRO-SL Algorithm. *Sensors*, 18 (7). doi:10.3390/s18071982
- Shastri, A. and M. G. Siddiqui (2023). Miniature Ultra- Wideband Antenna for Smart Homes and Wearable Advanced Industrial and Medical Applications. *IEEE-APS Topical Conference on Antennas and Propagation in Wireless Communications (APWC)*, Venice, Italy, 2023, pp. 128-133, doi: 10.1109/APWC57320.2023.10297506.
- Subhadra Panda, Anshul Gupta, Bibhudendra Acharya (2021). Wearable microstrip patch antennas with different flexible substrates for health monitoring system, *Materials Today: Proceedings*, 45, 4002-4007. doi:10.1016/j.matpr.2020.09.127
- Varma D. R., M. Murali, M. V. Krishna and G. S. N. Raju (2023). Miniaturized Novel Textile Antenna for Biomedical Applications, 2nd International Conference on Paradigm Shifts in Communications Embedded Systems, Machine Learning and Signal Processing (PCEMS), Nagpur, India, 1-6, doi: 10.1109/PCEMS58491.2023.10136066.
- Venkat Rao, K., Sriramam, Y.S.S., Suguna, N., Tirumani, N.P., Rama Krishna, C., Murali Krishna, C. (2023). Modern Four-Port MIMO Antenna Design Using Bended Curves for 5G Communications. In: Gupta, D., Khanna, A., Hassanien, A.E., Anand, S., Jaiswal, A. (eds) *International Conference on Innovative Computing and Communications. Lecture Notes in Networks and Systems*, 492. Springer, Singapore. doi:10.1007/978-981-19-3679-1\_59.

**Author Affiliations**

---

**D Ramesh Varma**

Assistant Professor  
Department of ECE  
Shri Vishnu Engineering College for Women(A),  
Bhimavaram, India  
varmaramesh422@svecw.edu.in  
Research Scholar  
Centurion University of Technology and  
Management, Vizianagaram, AP, India  
ORCID 0000-0002-9517-4964

**M. Murali**

Professor  
Department of ECE  
Centurion University of Technology and  
Management, Vizianagaram, AP, India  
muralitejas@cutmap.ac.in  
ORCID 0000-0002-8559-0091

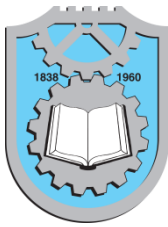
**M. Vamshi Krishna**

Professor  
Department of ECE  
Dhanekula Institute of Engineering and Technology  
profvamshi@gmail.com  
ORCID 0000-0002-7312-7526

**M. Venkata Subbarao**

Associate Professor  
Department of ECE  
Shri Vishnu Engineering College for Women(A),  
Bhimavaram, India  
mvsubbarao@svecw.edu.in  
ORCID 0000-0001-5840-2190

---



Vol. xx, No. x (202x) x-x, doi:

# Proceedings on Engineering Sciences



www.pesjournal.net

## NOVEL MICROWAVE SENSOR FOR ENHANCED BIOCHEMICAL DETECTION AND PREDICTION THROUGH MACHINE LEARNING FOR INDUSTRIAL APPLICATIONS

G. Challa Ram<sup>1</sup>

M. Venkata Subbarao

K. Padma Satya Sri

Naveen Kumar Maurya

D. Ramesh Varma

M. Prema Kumar

Received XXX

Accepted XXX

UDC – XXX

Keywords:

### ABSTRACT

This paper presents a novel sensor design that incorporates a microstrip patch antenna accompanied by a ground plane integrating a complementary split-ring resonator (CSRR). Integration of a circular CSRR into the microchip antenna has the potential to significantly improve radiation characteristics. The designed sensor operates at a frequency of 2.45 GHz, achieving an attenuation level of -27 dB. This design proposes the sensor's potential to function as a highly sensitive sensor by utilizing changes in the dielectric constant of biological samples. The changing dielectric constant of the analyte induces a frequency shift, allowing for the identification of different materials. Additionally, various regression algorithms based on machine learning have been employed to accurately assess the analyte's dielectric constant by studying the sensor's frequency response. Performance analysis indicates that exponential regression outperforms other approaches, showcasing a minimal root mean squared error of 0.0013. Machine learning techniques bring about substantial enhancements in sensor performance, thereby creating pathways for sophisticated applications in biochemical sensing.

© 2023 Published by Faculty of Engineering



### 1. INTRODUCTION

In recent times, there have been notable advancements in the field of biochemical sensing, driven by the increasing demand for precise, rapid, and non-intrusive

detection methods across various domains, including healthcare, environmental monitoring, and food safety. Among the array of available sensor technologies, microwave sensors have emerged as a promising solution for biochemical sensing due to their distinctive

<sup>1</sup> Corresponding author: G. Challa Ram  
Email: [challaram.grandhi@svecw.edu.in](mailto:challaram.grandhi@svecw.edu.in)

capacity to investigate the molecular interactions and attributes of biological substances (Song et al. 2023), (Zhang et al. 2022). Microwave sensors function within the electromagnetic spectrum, typically operating at frequencies ranging from hundreds of megahertz (MHz) to tens of gigahertz (GHz). When interacting with biochemical samples, which can encompass liquids like ethanol, benzene and ethylene glycol, these sensors provide valuable insights into the dielectric properties, composition, and structural changes of these substances (Rydosz et al. 2018), (Wu et al. 2022), (Gao et al. 2022). This interaction is the foundation for creating susceptible and specific microwave sensors capable of identifying and quantifying a broad spectrum of biological samples.

The core principle underpinning microwave biochemical sensing involves the measurement of alterations in the propagation characteristics of microwave signals, including aspects such as reflection, transmission, and resonance, when they encounter the target sample. These modifications arise from variances in the sample's dielectric constant, conductivity, and other electromagnetic properties. By analyzing these changes, researchers and scientists can extract valuable information about essential parameters such as concentration, molecular weight, and structural conformation of the target analyte (Zhou et al. 2018), (Farsinezhad et al. 2015), (Mirzavand et al. 2017).

Microchip patch antennas play a crucial role in wireless communication due to their compact dimensions, ease of integration, and versatile capabilities (Shastry et al. 2020), (Mok et al. 2013). These microchip patch antennas are known for their compactness, lightweight construction, and high efficiency. They are widely utilized in various wireless communication applications, including mobile devices, satellite communication, RFID (Radio Frequency Identification), and more (Behdad et al. 2004), (Zhao et al. 2011). Their design and performance continuously evolve, driven by advancements in materials, fabrication techniques, and design algorithms, solidifying their pivotal role in modern wireless technology. The fundamental structure of a microchip patch antenna comprises three key elements: a radiating patch, a dielectric substrate, and a ground plane. The radiating patch typically takes the form of a metallic component, often square or rectangular, and is connected to the electronic circuit's feed line. The dielectric substrate is a supportive medium for the patch, isolating it from the ground plane. The ground plane acts as a point of reference for the antenna's radiation and aids in achieving proper impedance matching. The design of compact, low-profile antennas, including conductive patch antennas situated over substrates, has become indispensable to meet the requirements of smaller devices while ensuring dependable wireless communication.

A microchip patch antenna incorporating a complementary split ring resonator (CSRR) represents

an inventive and compact device that amalgamates two pivotal components in contemporary wireless communication and microwave engineering (Caloz et al. 2006), (Ramesh Varma et al. 2023). The inclusion of a CSRR on the ground plane of the patch antenna is designed to amplify the antenna's capabilities by harnessing the unique electromagnetic characteristics offered by CSRR. Patch antennas hold widespread utility across various wireless communication systems due to their attributes of being low-profile, lightweight, and facile to integrate. These antennas are composed of a metal patch situated on a dielectric substrate, proficiently emitting electromagnetic waves in a specific direction. Nonetheless, their performance can be susceptible to factors such as frequency, bandwidth, and radiation pattern.

Complementary split ring resonators (CSRRs) represent a unique category of metamaterial distinguished by their captivating electromagnetic properties. These structures are comprised of resonant components featuring split ring geometry, allowing them to manipulate the propagation of electromagnetic waves in unconventional manners. CSRRs are renowned for their capacity to demonstrate negative permeability or permittivity characteristics. When a CSRR is strategically incorporated with a patch antenna, it can be positioned on the substrate or ground plane of the antenna to effectively modify its electromagnetic attributes. The fusion of a microchip patch antenna and a CSRR marks a fascinating intersection of conventional antenna principles and cutting-edge metamaterial advancements. This blended configuration promises to surmount the limitations typically associated with standard patch antennas, thereby ushering in novel opportunities for sophisticated wireless communication systems within our ever-expanding interconnected global landscape (Ram et al. 2022). Microwave and THz circuitry, featuring filters, antennas, and absorbers, is essential for precise, non-invasive material sensing applications (Ram et al. 2022), (Maurya et al. 2023).

This paper introduces a patch antenna design that incorporates a circular CSRR in the ground plane and analyzes its characteristics. The intended application of this design is to serve as a highly sensitive sensor for sensing various liquid samples, including water, ethanol, ethylene glycol, and benzene. Additionally, the design is enhanced by applying ML regression methods like linear, exponential, and polynomial regression to predict the dielectric value of samples using their resonant frequencies (Farooq et al. 2016), (Su et al. 2010), (Islam et al. 2014), (Ngoune et al. 2022). These sensors find extensive applications in industries, environmental analysis, and safety measures. These sensors excel in liquid-level sensing, offering real-time data for substances like ethanol, water, and benzene in tanks or containers. Industries benefit from precise control and optimization of production processes, while

environmental monitoring aids in pollution control and regulatory compliance. In sectors like oil and gas, microwave sensors detect hydrocarbons like benzene, ensuring safety and compliance. Moreover, they support chemical analysis, biomedical applications, food and beverage quality control, and agricultural operations by providing accurate measurements and enhancing safety protocols. Microwave sensors stand as versatile tools in diverse domains, enhancing efficiency and safety. In (Song et al. 2023) a metamaterial-based microwave sensor is designed to sense and detect ethanol. A microwave sensor of exceptional sensitivity with a commendable quality factor is presented in (Zhang et al. 2022) for the detection of ethanol concentration. In (Rydosz et al. 2018) a microwave sensor to detect acetone and ethanol is discussed. The novelty of this research lies in how ML-based techniques are adopted with the sensor measurements to achieve high accuracy in predicting the sample dielectric values.

The paper's organization is as follows: Section II discusses the analysis of the proposed sensor, Section III explores its sensing abilities, Section IV outlines the ML-based regression approach employed for predicting sample dielectric values, and Section V draws conclusions.

## 2. DESIGN OF SENSOR

In this paper, we have employed a circular CSRR. A microstrip antenna featuring a circular CSRR represents an innovative way to design antennas. It combines the unique electromagnetic characteristics of CSRRs with the patch antenna. The design configuration comprises three distinct layers. The top layer consists of a copper metal sheet serving as the metallic radiating patch with dimensions  $L_1 = 47$  mm and  $W_1 = 38.5$  mm and a thickness of 0.035 mm. In the middle layer, a substrate crafted from Rogers material RT5880 with dielectric constant value 2.2 provides support to the patch and exerts an influence on its properties. Finally, the bottom layer functions as a reflective ground plane, constructed from copper metal, and play a role in shaping the antenna's radiation pattern. An inset feed, as shown in Figure 1 is used to feed the design, and the dimensions of the feed line are  $L_2 = 30$  mm and  $W_2 = 3.4$  mm.

In our design concept, we've placed a circular CSRR on the ground plane. These complementary rings are etched on the ground plane with an outer ring radius ( $R_1$ ) of 8 mm and an inner ring radius ( $R_2$ ) of 4 mm. Each ring has a width of 2 mm. This particular CSRR is designed to create a strong electric field at a specific spot. Fluctuations in the tested sample's dielectric constant cause alterations in the electric field, consequently leading to a shift in the frequency response of the sensor. This unique property makes it suitable for use as a highly effective sensor. The top view and a ground plane featuring the CSRR are shown in Figure 1 and Figure 2, respectively.

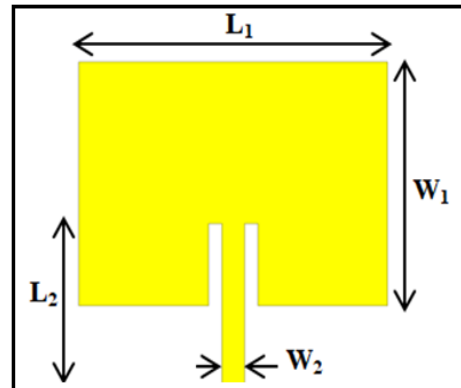


**Figure 1.** Top view of the proposed design

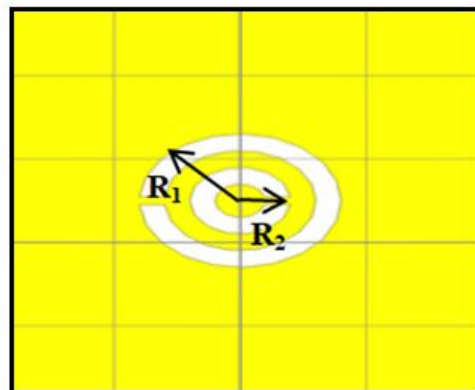


**Figure 2.** A Defective ground plane with CSRR

The proposed design is simulated using HFSS software. The reflection coefficient of the designed sensor is given in Figure 3. The designed sensor is simulating at a resonant frequency of 2.45 GHz with an attenuation of about -27 dB.

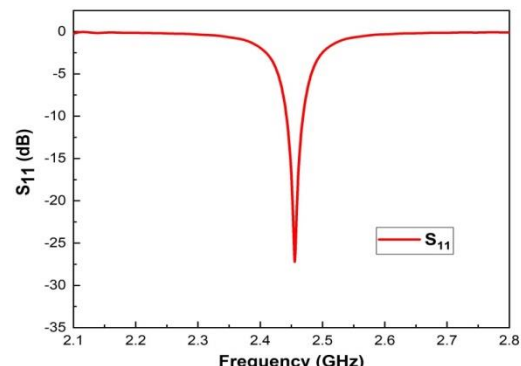


**Figure 3.**  $S_{11}$  response of the proposed design

Figure 4 illustrates the fabricated prototype of the designed sensor. The design is tested for S-parameters with Anritsu MS2037C VNA. Figure 5 depicts the simulated and measured results of the proposed design. From these results, it is evident that the measured and the simulated results have a close resemblance. These slight deviations are due to the losses incurred in the measurement.

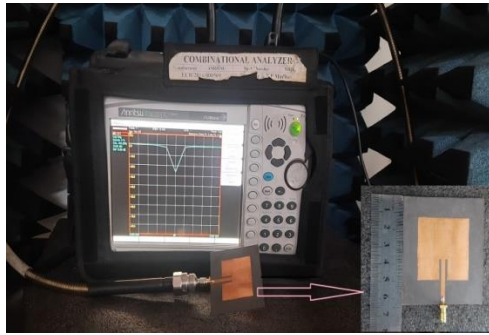


**Figure 4.** Measuring setup with fabricated design.

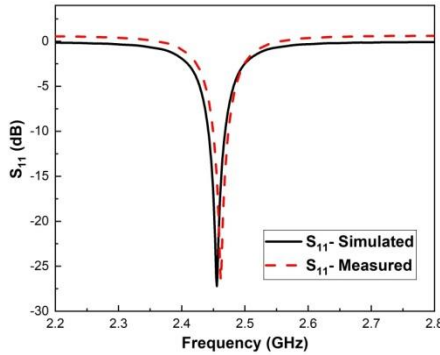


**Figure 5.** Measured Vs simulated response of the proposed design.

### 3. PERFORMANCE ANALYSIS OF SENSOR

The proposed design functions as a sensor by positioning an analyte at a specific location over the CSRR on the ground plane, as shown in Figure 6. This region is susceptible to changes in analyte due to its high electric field concentration over the concentric split ring resonator. When the Analyte's dielectric constant is changed, it disrupts the electric field, leading to shifts in the frequency response.

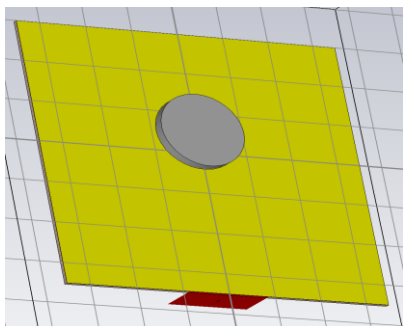


**Figure 6.** Sensor with sample under test.

In the figure above, the circular grey disc represents the analyte under test. The proposed design resonates at a frequency of 2.45 GHz and can function as a sensor with high sensitivity to changes in analyte. A change in the analyte's dielectric value causes changes in the electric field, resulting in variations in the frequency response. In this specific design, when the analyte's dielectric value varies from 2 to 20, there is a noticeable frequency shift of approximately 0.14 GHz. This shift

occurs from 2.46 GHz to 2.32 GHz, as shown in Figure 7. This frequency change serves as a reliable indicator of different materials based on their dielectric constants. The sensor sensitivity is given by the following equation.

$$S = \frac{\Delta f_r}{\Delta \epsilon} \quad (1)$$

The proposed sensor has achieved a maximal sensitivity of 70 MHz/DU (Dielectric unit change).

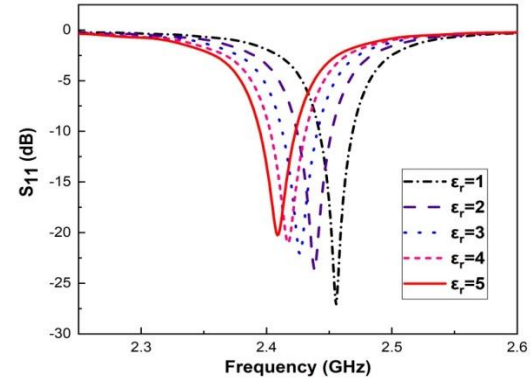


**Figure 7.** Frequency response of sensor for varying analyte

Further, the proposed sensor can detect various bio samples like ethanol, ethylene glycol, benzene and water. Figure 8 depicts the frequency response of the sensor for different bio-samples. As all the bio samples have different dielectric constant values, the proposed sensor could able to sense these bio samples with high precision. Table.1 illustrates the sensor's reaction to different biological samples. From these results it is evident that these liquid samples can be easily identified by the resonant frequency response of the proposed sensor.

**Table 1.** Sensor's response to biological samples.

S. No	Analyte	Dielectric constant ( $\epsilon$ )	Frequency (GHz)
1	Water	1.77	2.4418
2	Ethanol	1.84	2.4401
3	Ethylene Glycol	1.98	2.4387
4	Glycerine	2.16	2.4355
5	Benzene	2.25	2.4351

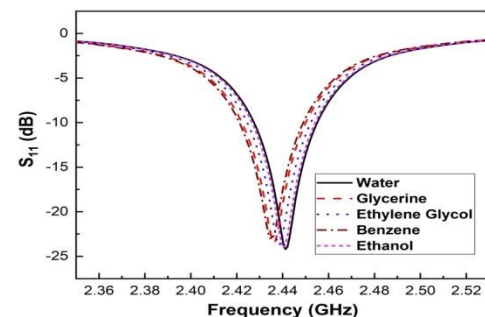


**Figure 8.** Sensor response for various bio samples.

#### 4. DIELECTRIC CONSTANT PREDICTION WTH ML BASED REGRESSION

Predicting the frequency response from the dielectric constant using regression models can be valuable in sensor design for several reasons. It can help in the design and optimization of sensors for specific applications. By predicting the frequency response, it can tailor sensor designs to maximize sensitivity and accuracy. Further it is also useful for the identification of the right material for designing the sensor. Predictive models can aid in material selection by predicting the relation between the dielectric constant of the material and the sensor's behavior. In applications where power consumption is critical (e.g., IoT devices or battery-powered sensors), optimizing the sensor's frequency response can help reduce energy consumption by ensuring that the sensor operates efficiently.

Machine learning based Regression techniques are employed in order to estimate the dielectric value of the sample (Ngoune et al. 2022). In these regression models, the response of the sensor is utilized to obtain the corresponding dielectric value of the sample. In this paper, several regression models are investigated in order to estimate the dielectric value of the sample with minimal error. This paper explores several regression models, including the linear regression model, polynomial regression model, and exponential regression model. The performance evaluation of the regression models are given by

$$MSE = \frac{1}{n} \sum_{j=1}^n (y_j - x_j)^2 \quad (2)$$

$$RMSE = \sqrt{MSE} \sum_{j=1}^n (y_j - x_j)^2 \quad (3)$$

$$R^2 Error = 1 - \frac{MSE}{MSE(\text{base line model})} \quad (4)$$

##### 4.1 Linear regression model

A core statistical technique, the linear regression model, serves to analyze the connection between variables (Farooq and Sazonov 2016). Its goal is to create a linear equation that optimally fits the data, enabling comprehension and prediction of how one variable changes in correspondence to alterations in other variables (referred to as the independent variables). Figure 9 depicts the resonant frequency versus dielectric constant and curve fitting plot. The empirical formulae to estimate the dielectric value of unknown sample using linear regression is given by

$$f = -0.006099x + 2.443 \quad (5)$$

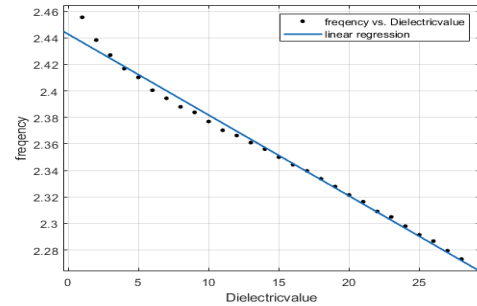


Figure 9. Relation between dielectric value and frequency using linear regression.

##### 4.2 Polynomial regression model

The polynomial regression model, as described by (Su et al. 2010), extends beyond linear regression by handling non-linear associations among variables. Unlike fitting only a straight line, it uses polynomial functions to capture curve-shaped patterns in datasets. This method's flexibility in modeling complex relationships renders it a versatile tool for prediction and data analysis. The following Figure 10 depicts the resonant frequency versus dielectric constant and curve fitting plot. The empirical formulae to estimate the dielectric constant of an unknown sample using polynomial regression is given by

$$f = (4.922 \times 10^{-5}) \times x^2 + (-0.007526) \times x^3 + 2.45 \quad (6)$$

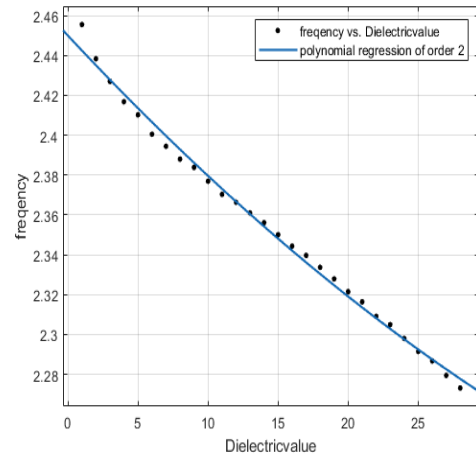


Figure 10. Relation between dielectric value and frequency using polynomial regression model

##### 4.3 Exponential regression model

Exponential regression models are used to analyze data with exponential growth or decay patterns, making them valuable for understanding and predicting phenomena where values change rapidly at a consistent percentage rate over time or with changing inputs (Islam et al. 2014). Figure 11 depicts the resonant frequency versus dielectric constant and curve fitting diagram. The empirical formulae to estimate the dielectric value of an

unknown sample using exponential regression is given by

$$f = 0.04655 \times e^{-0.6143x} + 2.436 \times e^{-0.002435x} \quad (7)$$

**Table. 2.** Performance comparison of regression algorithms.

Regression method	RMSE	R-Square Error
Linear	0.0049757	0.9906
Polynomial	0.0040670	0.9940
Exponential	0.0013720	0.9993

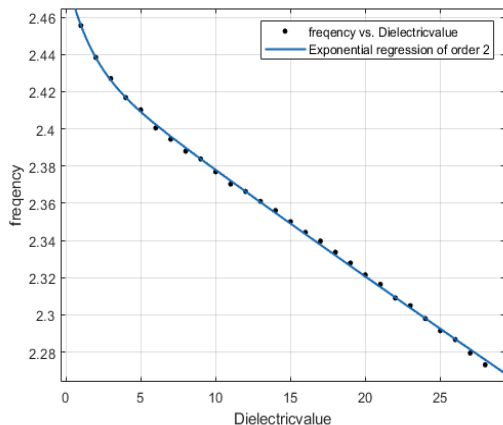


**Figure 11.** Relation between dielectric value and frequency using the exponential regression model.

The Root Mean Square error (RMSE) and R-Square Error ( $R^2$ ) for various regressions like linear, polynomial and exponential are tabulated in Table. 2. From the results, it is observed that the exponential

regression outperforms linear and polynomial regression techniques. By employing the exponential regression the proposed sensor can predict the dielectric constant of the sample with RMSE value of 0.00137.

## 5. CONCLUSION

A Novel sensor is designed that amalgamates a microstrip patch with etched CSRR on the ground plane operating at 2.45 GHz with an attenuation level of -27 dB. This design underscores the sensor's potential to operate as a highly sensitive detector by leveraging the variations in the dielectric constant of biological samples. The ability of the analyte's changing dielectric constant to induce a frequency shift opens up avenues for identifying diverse materials based on their dielectric constants. Moreover, the utilization of various regression algorithms based on Machine Learning allows for an effective prediction of the analyte's dielectric constant using the frequency response of the designed sensor. Performance analysis underscores the superiority of exponential regression, demonstrating a minimal root mean squared error of 0.0013. These machine learning-driven approaches substantially augment the sensor's performance, paving the way for advanced applications in biochemical sensing. The findings of this study provide valuable insights into the potential of integrating machine learning techniques in sensor design for enhanced functionality and applicability in the field of biochemical sensing.

## References

- Behdad N., and K. Sarabandi (2004). Bandwidth Enhancement and FurtherSize Reduction of a Class of Miniaturized Slot Antennas. *IEEE Transaction on Antennas and Propagation*, 52 (8), 1928-1935. doi: 10.1109/TAP.2004.832330.
- Caloz C. and T. Itoh, Electromagnetic metamaterials: transmission Line Theory and Microwave Application, Wiley Interscience, 2006.
- Farooq M., and E. Sazonov (2016). Linear regression models for chew count estimation from piezoelectric sensor signals. 10<sup>th</sup> International Conference on Sensing Technology (ICST), Nanjing, China, 1-5, doi: 10.1109/ICST.2016.7796222.
- Farsinezhad S., K. Shankar, M. Daneshmand and S. Member (2015). Liquid Sensing Using Active Feedback Assisted Planar Microwave Resonator. *IEEE Microw. Wirel. Components Lett.*, 25 (9), 621-623, 2015. doi: 10.1109/LMWC.2015.2451354
- Gao K., J. K. Wu, X. Wang, N. Y. Kim, X. F. Gu and J. G. Liang (2022). Specific Detection of Organic and Inorganic Solution Based on Microwave Resonator Array. *IEEE Sens. J.*, 22 (11), 10532-10540, 2022. doi: 10.1109/JSEN.2022.3169768.
- Islam S. K. M., and A. Banerjee (2014). Variational Inference on Infinite Mixtures of Inverse Gaussian, Multinomial Probit and Exponential Regression. 2014 13th International Conference on Machine Learning and Applications, Detroit, MI, USA. 276-281, doi: 10.1109/ICMLA.2014.50.
- Maurya, N.K., J. Ghosh, S. P. (2023). Design of graphene-based tunable ultra-thin UWB metasurface for terahertz regime, *Optik*, 279, 170753, doi: 10.1016/j.ijleo.2023.170753.
- Maurya, N.K., S. Kumari, P. Pareek, L. Singh (2023). Graphene-based frequency agile isolation enhancement mechanism for MIMO antenna in terahertz regime, *Nano Communication Networks*. 35, 100436, doi:10.1016/j.nancom.2023.100436.
- Mirzavand R., M. M. Honari and P. Mousavi (2017). High-Resolution Balanced Microwave Material Sensor with Extended Dielectric Range. *IEEE Trans. Ind. Electron.*, 64 (2), 1552-1560, 2017. doi: 10.1109/TIE.2016.2612621

- Mok W. C., S. H. Wong, K. M. Luk and K. F. Lee (2013). Single-Layer Single-Patch Dual-Band and Triple-Band Patch Antennas. *IEEE Transactions on Antennas and Propagation*, 61 (8), 4341-4344. doi: 10.1109/TAP.2013.2260516.
- Ngoune B. B., et al., (2022). Humidity Monitoring Using a Flexible Polymer- based Microwave Sensor and Machine Learning, *IEEE Sensors*, Dallas, TX, USA, 2022, pp. 1-4, doi: 10.1109/SENSORS52175.2022.9967126.
- Ram, G. C., P. Sambaiah, S. Yuvaraj, M. Kartikeyan (2022). Graphene based tunable bandpass filter for terahertz spectroscopy of polymers. *Optik*, 268, 169792, doi:10.1016/j.ijleo.2022.169792.
- Ram, G. C., P. Sambaiah, S. Yuvaraj, M. Kartikeyan (2022). Tunable bandstop filter using graphene in terahertz frequency band. *AEU Int. J. Electron. Commun.* 144 (2022), 154047, doi:10.1016/j.aeue.2021.154047.
- Ramesh Varma, D., B. Durga Saranya, G. Pavani, M. Venkata Subbarao, G. Challa Ram, D. Girish Kumar (2023). Design of fabric antennas for body protective garment applications and analysis on their performance. *Materials Today: Proceedings*, 80, 1538-1547. doi:10.1016/j.matpr.2023.01.384.
- Rydosz, A. E. Maciak, K. Wincza and S. Gruszcynski (2018). Microwave-based sensors for exhaled acetone and ethanol detection, International Conference on Electromagnetics in Advanced Applications (ICEAA), Cartagena, Colombia, 2018, pp. 32-34, doi: 10.1109/ICEAA.2018.8520366.
- Shastry P. N., and A. Sankarasubramaniam (2020). Design Optimization of a Tunable Coplanar Patch Antenna. IEEE International Symposium on Antennas and Propagation and North American Radio Science Meeting, Montreal, QC, Canada. 119-120, doi: 10.1109/IEEECONF35879.2020.9329868.
- Song Y. et al., "Metamaterial-Inspired Microwave Sensor for Ethanol Detection," 2022 10th International Symposium on Next-Generation Electronics (ISNE), Wuxi, China, 2023, pp. 1-3, doi: 10.1109/ISNE56211.2023.10221672.
- Su, W., H. Yang and Z. Liu (2010). System identification based on orthogonal polynomial regression analysis method, *Proceedings of the 29th Chinese Control Conference*, Beijing, China. 1441-1446.
- Wu J., et al. (2022). A way to determine the optimum detection frequency for microwave sensing. *Measurement*, 202, 111736. doi:10.1016/j.measurement.2022.111736
- Zhang, F., Y. Chen, S. Lin, E. Wu, J. Liang and X. -L. Huang (2023). High quality factor microwave sensor for ethanol solution concentration detection. 10th International Symposium on Next-Generation Electronics (ISNE), Wuxi, China, 1-3, doi:10.1109/ISNE56211.2023.10221655.
- Zhao, X., Y. Lee and J. Choi (2011). Design of compact patch antenna using split-ring resonator embedded substrate. *Microwave and Optical Technology Letters*, 53 (12), 2789-2790. doi: <https://doi.org/10.1002/mop.26411>
- Zhou et al., (2018). Multi-Band Sensing for Dielectric Property of Chemicals Using Metamaterial Integrated Microfluidic Sensor. *Sci. Rep.*, 8 (1), 2018. doi: 10.1038/s41598-018-32827-y

---

G. Challa Ram

Department of ECE

Shri Vishnu Engineering College for  
Women, Bhimavaram, India.  
challaram.grandhi@svecw.edu.in  
ORCID 0000-0002-3790-1318

Naveen Kumar Maurya  
Department of ECE,

Vishnu Institute of Technology  
Bhimavaram, India  
Naveen.maurya222@gmail.com  
ORCID 0000-0001-8006-3316

M. Venkata Subbarao

Department of ECE,

Shri Vishnu Engineering College for  
Women, Bhimavaram, India.  
mvsbarao@svecw.edu.in  
ORCID 0000-0001-5840-2190

D. Ramesh Varma  
Department of ECE,

Shri Vishnu Engineering College for  
Women, Bhimavaram, India  
varmaramesh422@gmail.com  
ORCID 0000-0002-9517-4964

K. Padma Satya Sri

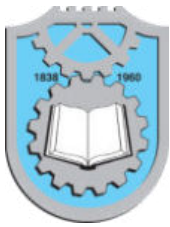
Department of ECE

Shri Vishnu Engineering College for  
Women, Bhimavaram, India.  
satyasrikomatlappalli11@gmail.com  
ORCID 0009-0006-0329-0746

M. Prema Kumar  
Department of ECE,

Shri Vishnu Engineering College for  
Women, Bhimavaram, India  
medapatipremkumar@gmail.com  
ORCID 0000-0002-8702-8828

---



Vol. xx, No. x (202x) x-x, doi:

# Proceedings on Engineering Sciences



www.pesjournal.net

## EXPLORING THE POTENTIAL OF FEDERATED LEARNING TO EMPOWER CREDIT CARD FRAUDULENT TRANSACTION DETECTION WITH DEEP LEARNING TECHNIQUES

Chandra Sekhar Kolli <sup>1</sup>

Venkata Naga Raju D

Pavan Kumar V

Srinivasa Rao D

Vinay P

GAKS Rajeev Kumar

Keywords:

### A B S T R A C T

*Federated Learning, Credit Card fraud detection, Optimization.*

The rapid expansion of communication systems and computing technology has led to a significant increase in both traditional and online credit card transactions. Unfortunately, this surge has also resulted in a corresponding rise in fraudulent activities, posing a serious challenge for organizations such as banking and financial institutions. To address this issue, the implementation of precise and secure transaction techniques, as well as effective fraud detection methods, becomes imperative. In this article, a novel approach utilizing a hybrid algorithmic optimization-based deep learning technique is proposed. Specifically, the Jellyfish Namib Beetle Optimization Algorithm-SpinalNet (JNBO-SpinalNet) is developed for the purpose of detecting fraudulent credit card transactions. The input data undergoes pre-processing using quantile normalization, followed by the selection of pertinent features employing diverse distance measures. To enhance the selected features, the Bootstrapping method is employed. Subsequently, the SpinalNet model is employed to identify instances of credit card fraud. The JNBO-SpinalNet model surpasses traditional detection models. The obtained results clearly demonstrate the outstanding effectiveness and efficiency of the proposed approach in identifying instances of credit card fraud.



© 202x Published by Faculty of Engineering

### 1. INTRODUCTION

Federated learning, a learning paradigm that addresses privacy concerns and governance issues without the need for data exchange, has gained significant attention McMahan et al. (2017) Kairouz et al. (2021). By

<sup>1</sup> Corresponding author: Dr. Chandra Sekhar Kolli  
Email: kcsit@svecw.edu.in

enabling collaborative insights without transferring data beyond institutional firewalls, federated learning offers a promising approach. Recent research has demonstrated that federated learning models achieve superior performance compared to centrally hosted databases and isolated single-institutional data Li et al. (2019) and Rieke et al. (2020). This new branch of Artificial Intelligence (AI) revolutionizes machine learning by training Deep Neural Networks (DNN) without sharing individual samples from local nodes that hold local data. Instead, a global model is generally introduced, leveraging decentralized computing power and data to enhance personalized user experiences without relying on homomorphic encryption. Various applications of federated learning include credit card fraud detection, improving safety in self-driving connected cars, and enhancing the privacy of healthcare data. The benefits of adopting federated learning include the creation of low-latency intelligent models, improved privacy, and reduced power consumption. Ultimately, federated learning enables the separation of intelligent models from massive data storage in the cloud Suvarna et al. (2020).

In recent years, the rapid growth of global communication and advancements in computing technology has led to a significant increase in the importance of credit card transactions. Unfortunately, this surge in usage has also given rise to a corresponding escalation in credit card fraud. According to data from the European Central Bank, Europe experiences billions of Euros in losses each year due to credit card fraud Bahnsen et al. (2016). Typically, credit card fraud is committed with the intention of acquiring large sums of money quickly and with minimal risk Zarepoor et al. (2015).

There are several common forms of credit card transaction fraud, including online transaction fraud, offline transaction fraud, card counterfeiting, and fraud within banking applications. Among these, application fraud poses the greatest threat and is widely prevalent. It involves the use of fake personal details on a credit card or the unauthorized use of someone else's information by fraudsters Bolton and Hand (2022). Counterfeit fraud occurs when credit card details are remotely used in places that require credit card information. Offline transaction fraud usually occurs when fraudsters steal physical plastic cards and use them in stores as if they were the legitimate owners Laleh and Abdollahi (2009, Yang et al. (2019)).

The increased utilization of credit cards has resulted in a corresponding surge in fraudulent activities within the credit card industry. Credit card transaction fraud typically occurs when fraudsters engage in malicious activities to obtain authentication information, enabling them to access services or withdraw money without the owner's permission Jovanovic et al. (2022).

Effectively designing a system to detect and address fraudulent activities in credit card transactions is crucial. Such a system not only monitors transaction activities but also safeguards users and institutions affected by

fraudsters Jovanovic et al. (2022). Fraud can be categorized into two main types: behaviour fraud and application fraud Phua et al. (2009). Application fraud typically occurs when fraudulent applications are submitted, often using counterfeit identity information, leading to the approval of new credit cards by issuers. On the other hand, behaviour fraud involves the misuse of issued and approved credit cards, manifesting as fraudulent behaviour in credit card transactions. The detection and prevention of fraud have become significant research areas and a major concern for card issuers, as even detecting and preventing a small portion of fraudulent activities can save millions of dollars Zhang et al. (2021).

In the detection of credit card fraud, feature engineering techniques commonly revolve around aggregating features Cheng et al. (2021) and Zhang et al. (2021). Researchers have conducted various studies utilizing data mining and machine learning methods to uncover credit card fraud Alharbi et al. (2022). However, the application of machine learning techniques in the fraud detection process often faces challenges related to grouping and requires large training models. To overcome these limitations, deep learning models are employed for fraud detection tasks, leveraging the transformation capabilities of multiple nonlinear layers. This article presents the development of a deep learning model based on algorithmic optimization for detecting fraudulent credit card transactions. The input credit card data is first pre-processed using the quantile normalization technique to ensure a well-structured format. Various measures, such as Fisher score, Bray Curtis Distance, and Jeffrey Divergence, are employed to select the optimal features from the pre-processed data. To enhance the selected features, a bootstrapping data augmentation process is applied. Subsequently, the SpinalNet model is utilized to identify credit card frauds. The detection process of the classifier is further improved by tuning SpinalNet with the designed JNBO model.

The JNBO-SpinalNet model is utilized for identifying fraudulent credit card transactions. It combines the Jellyfish Search Optimization (JSO) algorithm and the Namib Beetle Optimization (NBO) to fine-tune the SpinalNet, which serves as the detection mechanism for credit card fraud activities.

The paper organized as follows: In Section 2 presents an assessment of different classical research approaches for detecting fraudulent credit card transactions. In Section 3, we describe the designed model utilized for detecting such transactions, along with the evaluation results obtained from the models. The subsequent discussion is presented in Section 4. Finally, Section 5 concludes the article.

## 2. LITERATURE REVIEW

The rapid expansion of globalization has led to a significant surge in credit card usage. Unfortunately,

this has also given rise to a corresponding increase in fraudulent activities associated with credit card transactions. Detecting and preventing such fraudulent transactions remains a challenge, as it requires a comprehensive understanding of diverse patterns and addressing the issue of imbalanced data. Therefore, there is a pressing need to develop a hybrid technique that combines different approaches, such as federated learning, to enhance the detection of fraudulent credit card transactions.

Yang et al. (2019) introduced the Federated Fraud Detection (FFD) framework, aiming to mitigate the losses incurred by both cardholders and banks. This technique combines behavioural features with federated learning to train the fraud detection system. Although the framework demonstrated faster convergence due to its small batch size, it incurred high communication costs to ensure privacy protection of credit card user data.

Suvarna and Kowshalya (2020) devised the Auto Encoder (AE) and Restricted Boltzmann Machine (RBM) techniques for predicting and identifying fraudulent credit card users. These models effectively computed the available card limit based on fraudsters' usage limits. However, their decentralized nature hindered accurate results.

Alharbi et al. and Alharbi et al. (2019) developed a Text to Image (text2IMG) conversion approach to address text-related issues in fraud detection databases during credit card transaction fraud detection. By utilizing computer vision models, this approach introduced a novel dimension for credit card fraud detection. Nevertheless, the data balancing technique using the inverse frequency approach did not consider other class-imbalance methods.

Jovanovic et al. (2022) introduced the Group Search Firefly Algorithm (GSFA) for real-world fraud detection in credit cards, utilizing transaction details of European credit card users. This method achieved a remarkably low misclassification error rate. However, it did not undergo testing with supplementary real-life credit card databases.

Malik et al. (2022) proposed two hybrid machine learning techniques, Adaboost and Light Gradient Boosting Machine (LGBM), for detecting fraudulent activities during credit card transactions. These models exhibited high training speed, improved performance, and low memory utilization. However, the techniques used for detection were not extended to other databases concerning fraudulent credit card transaction detection.

Zhang et al. (2021) designed the Homogeneity-Oriented Behaviour Analysis (HOBA) approach to detect credit card fraud by evaluating homogeneous transactions. This technique effectively utilized an acceptable false positive rate to determine fraudulent transactions. However, it did not consider the computational cost associated with the feature engineering framework.

Ghosh et al. (2022) introduced the Neural Aggregate Generator (NAG) technique, which learns aggregate features for end-to-end fraud classification. This method

outperformed contextual models and static learners that rely on manual feature aggregates. However, it did not extend its learning capabilities to other functions within the given set of constraints.

Esenogho et al. (2022) developed the Synthetic Minority Oversampling Technique and Edited Nearest Neighbor (SMOTE-ENN) technique to analyse credit card client behaviour during dynamic shopping. It effectively addressed imbalanced data issues encountered in fraudulent credit card transaction detection. However, it did not enhance the feature selection process or utilize sampling approaches to improve classification performance.

## 2.1 Challenges

Outlined below are the primary challenges faced by different classical approaches when utilizing federated learning for the detection of fraudulent credit card transactions:

The FFD model described in Yang et al. (2019) successfully constructed a fraud detection framework with reduced computation costs. However, it overlooked the inclusion of more reliable measures for protecting data privacy.

The RBM approach utilized in Suvarna and Kowshalya (2020) enhanced database privacy and improved training and testing accuracy. Nevertheless, it did not demonstrate real-time predictive capabilities for credit card fraud.

The Adaboost+LGBM technique Malik et al. (2022) was able to detect fraudulent activities within real-world databases. However, it did not explore alternative feature selection methods or consider an appropriate hybridized model for effective detection of fraudulent credit card transactions.

The NAG approach employed in Ghosh et al. (2022) effectively computed transaction similarities among various categorical features. However, it did not account for the skewness of the target variable distribution.

Although numerous authorization approaches have been employed for preventing and detecting fraudulent credit card transactions, they often fell short in gathering comprehensive information about credit card fraud and proved to be inconvenient for customers.

## 3. METHODOLOGY

It utilizes a decentralized model for detecting fraudulent credit card transactions using federated learning. It involves training on local nodes, where the raw information is stored on local devices. By personalizing the training model with local data, it enables accurate detection of fraudulent credit card transactions. The performance of the local model is improved by leveraging the knowledge obtained from locally learned data. The primary objective of federated learning is to perform diverse local training tasks using local data, and then exchange the generated gradients or weights with local nodes to create a global model.

### 3.1 Node-Level Training

Figure 1 illustrates the training levels in abstract way. During the local training phase, nodes strive to achieve the best local parameters by minimizing the loss function. These optimized parameters are then sent to the server, which collects and combines the node weights to generate a global model. This iterative process continues until the desired number of epochs is reached. At each time stamp, the local nodes undergo training to detect fraudulent credit card transactions using the available data. It involves incorporating the local nodes' contributions into the acquired data for improved detection accuracy.

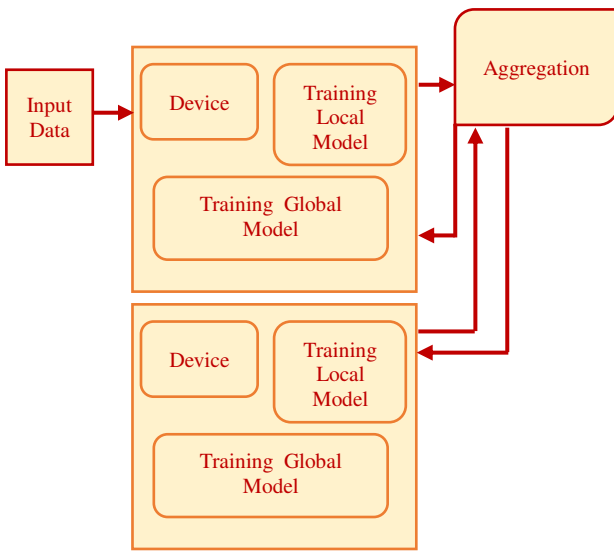


**Figure 1.1** Proposed Model

### 3.2 Training the Model

Our main objective is to develop a novel algorithm, called the JNBO model, specifically designed for detecting fraudulent credit card transactions. Initially, the input data is obtained from the credit card fraud detection dataset Zhao et al. (2020) and undergoes a preprocessing phase. During this preprocessing phase, quantile normalization is applied to convert the unstructured data into a structured format. Next, optimal features are selected from the pre-processed data using the Fisher score, Bray Curtis Distance, and Jeffrey Divergence. These selected features are then utilized in the Bootstrapping method for data augmentation. Fraud detection is performed using the SpinalNet network Kabir et al. (2022). The SpinalNet network is trained using our designed JNBO model, which combines the JSO Chou . and Truong (2021) and NBO Chahardoli (2022) approaches, Figure 2 illustrates the same.

### 3.3 Data Procurement: Fetching Valuable Information

The below provided expression provides the input data for detecting fraudulent credit card transactions, which is obtained from the database through data acquisition.

$$C = \{C_1, C_2, \dots, C_M, \dots, C_Y\}$$

The credit card database, referred to as C, which contains information regarding credit card transactions. The acquired data, denoted as CM, is utilized for detecting fraudulent credit card transactions, CY represents the total number of transactions in the data set C. This acquired credit card fraud detection database is subsequently subjected to a pre-processing phase.

### 3.4 Pre-Processing phase

During the pre-processing phase Quantile Normalization Zhao et al. (2020)is used. The data ranking is processed with the help of magnitude and computer average value for the rank. In the next phase optimal parameters will be identified.

### 3.5 Feature Selection phase

The pre-processed data, after normalization, will be utilized as input for the feature selection phase. The goal is to select the optimal attributes that will enable accurate classification of fraudulent transactions within the credit card dataset. Since the input data (pre-processed data) is of substantial size, it is crucial to choose the features in the most effective manner to minimize computational time. The selection of optimal attributes is facilitated by employing similarity measures.

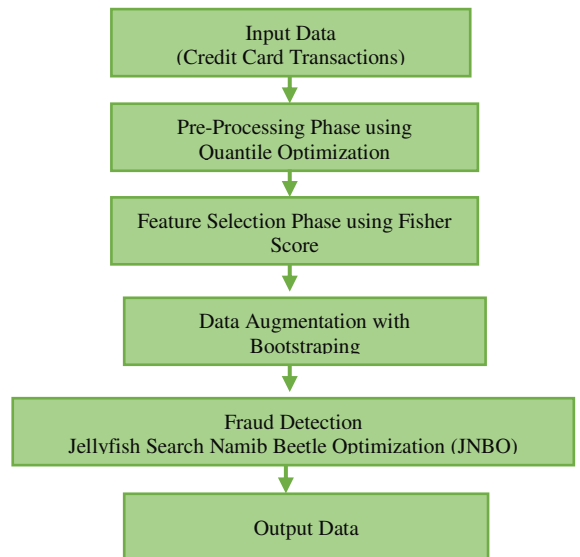


**Figure 2.** Detecting Fraudulent Credit Card Transactions: Training Model

### 3.6 Fisher Score

The Fisher score, also referred to as Fisher's discriminant ratio or Fisher's linear discriminant analysis, is a statistical measure used for feature selection and dimensionality reduction. It maximizes class separability in a dataset by assessing the discriminatory power of each feature. It calculates the ratio of between-class variance to within-class variance for each feature. Features with higher Fisher scores are more effective at distinguishing between different classes in the dataset. Selecting features with high Fisher scores helps identify the most relevant features that significantly contribute to the classification task. Fisher score is commonly employed in machine learning algorithms for tasks like pattern recognition, classification, and feature extraction.

### 3.7 SpinalNet for fraud detection

Detecting credit card transaction fraud is essential for timely identification and prevention of fraudulent activities. In this study, the detection of specific fraudulent activities is accomplished using the SpinalNet model, as presented in Kabir et al. (2022). SpinalNet demonstrates a considerable reduction in detection errors while maintaining low computational costs. To further enhance the detection rate, the JNBO model, which combines JSO (Chou . and Truong (2021) and NBO Chahardoliet et al. (2022), is employed to fine-tune SpinalNet. The subsequent section provides a brief overview of the SpinalNet model utilized for the detection purposes.

### 3.8 Architecture of SpinalNet

SpinalNet is an architecture specifically crafted to improve the detection of fraudulent activities in credit card transactions. It employs a neural network framework that integrates specialized spinal units, enabling the network to effectively learn and represent intricate patterns and relationships in the data. The architecture comprises multiple levels, each featuring a combination of stacked spinal units that extract features at various levels of abstraction. This hierarchical structure enables the network to capture both detailed information and broader context, resulting in precise identification of fraudulent transactions. Notably, SpinalNet is designed to be computationally efficient, facilitating swift and real-time processing of large credit card transaction datasets. By achieving a balance between computational cost and detection accuracy, SpinalNet presents a practical solution for effective fraud detection in credit card transactions.

The development of SpinalNet incorporates principles inspired by the functioning of the human spinal cord, resulting in several notable similarities. SpinalNet's

design draws from the workings of the human spinal cord, manifesting in features such as gradual input, local output with potential global influence, and weight reconfiguration during training.

**Gradual Input:** SpinalNet operates on a gradual input mechanism, similar to how the human spinal cord processes information.

**Local Output and Potential Global Influence:** Similar to the human spinal cord, SpinalNet exhibits local output capabilities while also potentially influencing the broader network.

**Weight Reconfiguration during Training:** During the training phase, the weights in SpinalNet are reconfigured, akin to the adaptive nature of the human spinal cord's responses. In line with the brain's operation, SpinalNet receives inputs in a gradual manner. Each layer in the proposed model contributes to the local output, analogous to reflexes, while a modulated portion of the input is transmitted to the global output, resembling the brain's functioning. The architecture of SpinalNet is depicted in Figure 3, showcasing the categorization of each layer into three distinct types: intermediate, output, and input layers.

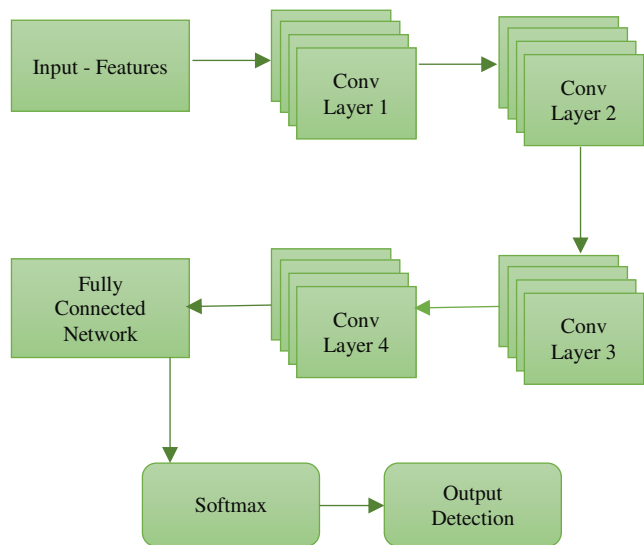


**Figure 3.** Architecture of SpinalNet

### 3.9 Enhancing SpinalNet Training: Introducing JNBO Algorithm

The performance of credit card fraud detection in SpinalNet Kabir et al. (2022) is improved by exploiting the JNBO algorithmic model, which combines the JSO Chou (2021) and NBO Chahardoliet et al. (2022) techniques. The JSO approach takes into account various characteristics of jellyfish swarms. During the exploration phase, jellyfish actively and passively change their positions, moving with the ocean current in search of food. The JSO model is formulated based on three key principles: time mechanism control, jellyfish movement towards food, and determination of

food. By incorporating different time control mechanisms, the JSO algorithm effectively addresses optimization problems, achieving a balance between exploration and exploitation phases. Similarly, the NBO technique is inspired by the Namib black desert beetles, which optimize their water collection process by climbing to dune heights in the early morning. To obtain moisture from the air, the beetles raise their bodies to reach the moist air currents, causing water droplets to condense and roll towards their mouths. This algorithmic model effectively selects optimal features and leverages the movement of Namib beetles to solve various optimization problems. By combining the JSO model with NBO enhances its ability to reduce the dimensionality of optimization issues and provides greater stability in determining the optimal minimal error, resulting in the creation of the JNBO technique. The mathematical representation of the designed JNBO algorithmic model is as follows:

### Population Initialization:

To prevent premature convergence with low probability, the population of jellyfish is initialized using logistic chaotic maps, ensuring population diversity. This ensures that the chaotic value, which corresponds to the location.

### Fitness Computation:

The estimation of fitness is accomplished by employing the Mean Square Error (MSE) metric.

$$\text{MSE} = \frac{1}{N} \sum_{i=1}^N (y_i - \hat{y}_i)^2$$

Where N denotes the total number of samples,  $y_i$  represents targeted and and  $\hat{y}_i$  represents actual outputs.

### Ocean current:

The high concentration of nutrients present in the ocean currents serves as a strong attraction, causing jellyfish to migrate in alignment with the prevailing water flow. Precisely determining the direction of these ocean currents becomes essential in identifying the optimal and advantageous locations. This involves calculating the ocean current and trend direction, a task achievable through the following expression:

$$\vec{CL} = H^* - \eta$$

wherein the ocean current direction is indicated as  $\vec{CL}$ ,  $H^*$  symbolizes the current location of best jellyfish, and  $\eta$  is the difference among jellyfish's present mean and optimal location, which is expressed by,

$$\eta = ga_c \gamma$$

here, the factor governing attraction is denoted as  $ga_c$  and the jellyfish mean location is indicated as  $\lambda$ .

Considering the jellyfish is spatial distributed along the mean location distance  $\pm \varpi \alpha$  in all dimensions, and the expression of  $\alpha$  standard deviation distribution is expressed by,

$$\eta = \varpi \times \alpha \times \text{Rand}^r(0,1)$$

Where,  $\alpha = \text{Rand}^s(0,1) \times \gamma$

$$\eta = \varpi \times \text{Rand}^s(0,1) \times \gamma \times \text{Rand}^r(0,1)$$

In general form, the equation is expressed by,

$$\eta = \varpi \times$$

$$\text{Rand}(0,1) \times \gamma$$

It denotes a random number between 0 and 1

Substituting equation becomes,

$$\vec{U} = H^* - \varpi \times \text{Rand}(0,1) \times \gamma$$

The  $i^{th}$ jellyfish updated location is given by the expression,

$$H_i(e+1) = H_i(e) + \text{Rand}(0,1) \times \vec{U}$$

### Solution feasibility check:

To ascertain the optimal outcome, the solution's feasibility is evaluated using a fitness function denoted by equation (6). Should an alternative solution outperform the current optimal one, it will replace the previously recorded best solution.

### Termination phase:

The proposed model's algorithmic steps are carried out iteratively until the best optimal solution is reached and same are illustrated below:

PSEUDO CODE OF	: Proposed JNBO Model
INPUT	: Maximum iterations
OUTPUT	: Optimum solution
START	

Initialize the jellyfish population
Look for the current location
Repeat until Max Iterations
calculate the time taken during the iterations if (jellyfish is continued in the current ocean)
estimate the current ocean
update the location
else update as jellyfish swarm
if (rand(0,1) > 1- Ke)
print A by jellyfish
else print type B by jellyfish
estimate the direction of jellyfish
END IF
END FOR
Compute boundary condition
Compute the updated location
END FOR STOP

The chosen features are fed as input into SpinalNet and trained using the designed JNBO model to produce the output. This is attributed to the technique's high stability and dimensionality reduction capabilities.

### Applying the globally trained model on every Local Model

After training individual models on local devices, the global model is created by aggregating weights on a central server. The averaged weights from the server are then sent back to the local devices, enhancing detection efficiency. This iterative process is repeated until the optimal output is achieved.

#### Result Discussion

The different results collected from the experimentation of the designed JNBO-SpinalNet model, along with the accompanying discussion, are outlined below:

#### Experimental set-up

The MATLAB tool was used to implement the JNBO-SpinalNet model for credit card fraud detection.

#### Dataset description

The credit card fraud detection database [23] has been created to assist diverse credit card companies in identifying fraudulent credit card transactions. This database contains transaction information spanning two days, involving European cardholders. Characterized by a significant class imbalance, the database encompasses numerical input variables and encompasses a total of 284,807 transactions, among which 492 are classified as fraudulent.

#### Evaluation measures

The distinct assessment metrics employed to ascertain the superiority of the JNBO-SpinalNet model are presented as follows:

**Accuracy:** The accuracy of the devised model in precisely detecting fraudulent credit card transactions is referred to as its efficacy and is defined as follows:

$$\text{Accuracy}, \lambda = \frac{\psi_1 + \psi_2}{\psi_1 + \psi_2 + \psi_3 + \psi_4}$$

**Loss Function:** The enhancement of the designed model's effectiveness during the training process is achieved through the utilization of a loss function, which is assessed using the following expression:

$$\text{Loss Function} = 1 - \lambda$$

**MSE:** The actual and expected output between the mean of squared deviation is termed MSE, which is evaluated by the expression,

$$\text{MSE}, \kappa = \frac{1}{N} \sum_{C=1}^N (D_C^* - D_C)^2$$

here, the total training samples are denoted by  $N$ , and the targeted and actual output is represented as  $D_C^*$  and  $D_C$ .

**FPR:** The FPR is used to determine the total number of incorrect negative labels to the determined total negative labels, which is formulated by,

$$FPR = \frac{\psi_3}{\psi_3 + \psi_2} \quad (34)$$

**MAP:** The MAP determines the average precision mean of all classes, which is estimated using the expression,

$$MAP = \frac{1}{R} \sum_{t=1}^R A_t \quad (35)$$

here, the identified number of classes is denoted as  $R$ , and the average precision is indicated as  $A$ .

**RMSE:** The square root of MSE is computed using RMSE, and is given by the expression,

$$RMSE = \sqrt{\kappa} \quad (36)$$

here, the term  $\kappa$  represents MSE.

#### Aggregation at the server:

When a fraudulent transaction is identified, the weights fetched from various local training data and aggregated at the central server. In the local model, the previously collected weights are averaged to determine the global model weights, Fig 4 illustrates the data aggregation at the central server.

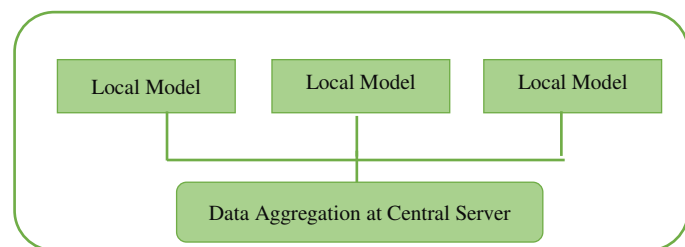


Figure 4. Data Aggregation at Central server

#### Performance Measurement

The performance evolution is done by various performance metrics. These evaluations are illustrated in Figure. 5. Specifically, Fig. 5(a) provides the proposed model (JNBO-SpinalNet) accuracy. For a time-stamp of 450 seconds, the achieved accuracy values are as follows: 0.849 for 20 epochs, 0.850 for 40 epochs, 0.875 for 60 epochs, 0.883 for 80 epochs, and 0.883 for 100 epochs.

**Figure 5 (a).** Accuracy

The loss function results of the JNBO-SpinalNet method are presented in Figure. 5(b). This graph showcases the application of 20, 40, 60, 80, and 100 epochs to the

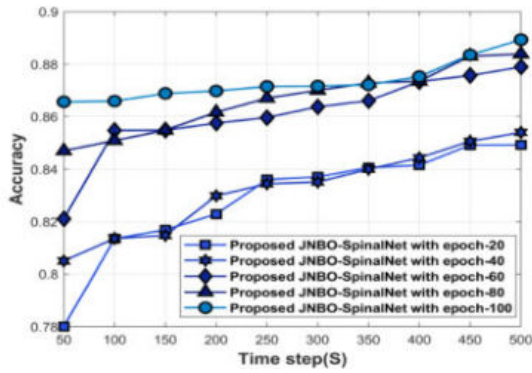


**Figure 5(a).** Accuracy

proposed JNBO-SpinalNet model. The computed values for the loss function are 0.18, 0.18, 0.14, 0.144, and 0.129, all corresponding to a time stamp of 450 seconds.

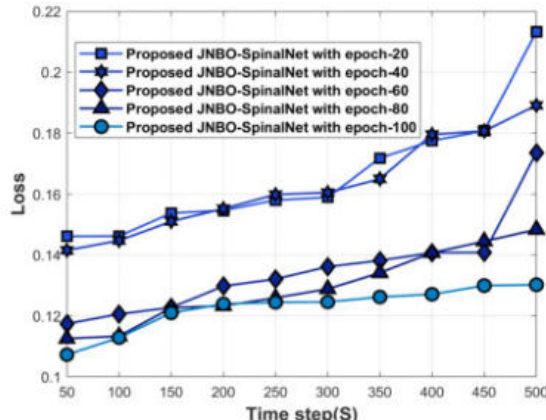


**Figure 5 (b).** Loss function

In Figure 5(c), there is an illustration of an alternative measure, namely the MSE rate, which pertains to the JNBO-SpinalNet model. Specifically, at the time stamp of 450 seconds, the MSE rates exhibit the subsequent values: 0.436 for 20 epochs, 0.389 for 40 epochs, 0.347 for 60 epochs, 0.305 for 80 epochs, and 0.286 for 100 epochs. The representation of the JNBO-SpinalNet approach's FPR can be found in Figure 5(d). Corresponding to the time stamp of 450 seconds, the computed FPR values stand at 0.201 for 20 epochs, 0.183 for 40 epochs, 0.161 for 60 epochs, 0.147 for 80 epochs, and 0.116 for 100 epochs.

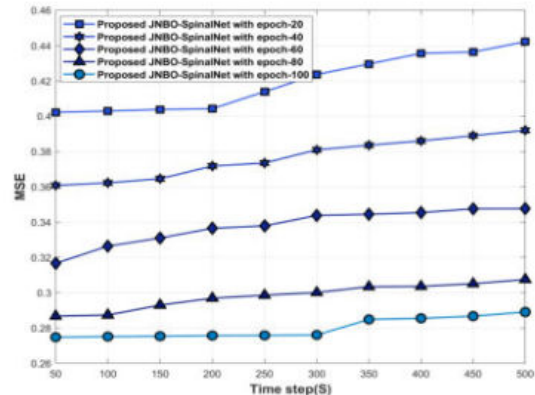


**Figure 5 (c).** MSE

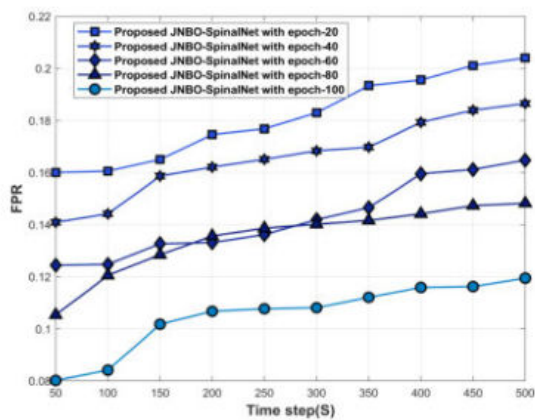


**Figure 5 (d)** MSE

In figure 5(e), the graph illustrates the measured MAP values. Specifically, at the 450-second time stamp, the JNBO-SpinalNet model achieved MAP values of 0.856, 0.858, 0.893, 0.895, and 0.909 for the epochs 20, 40, 60, 80, and 100, respectively. The corresponding RMSE results for the JNBO-SpinalNet technique are presented in figure 5(f). For the same 450-second time stamp, the JNBO-SpinalNet method demonstrated RMSE values of 0.660, 0.623, 0.589, 0.552, and 0.535 for 20, 40, 60, 80, and 100 epochs, respectively.

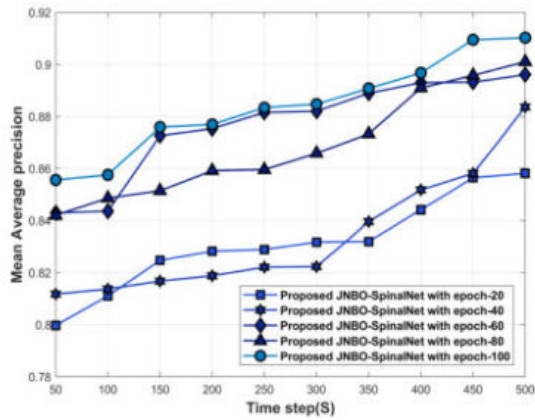


**Figure 5 (e).** Mean Average Precision

The MAP value for the JNBO-SpinalNet at various epochs (20, 40, 60, 80, and 100) for the time stamp of 450 seconds is shown in fig 5(e), with corresponding values of 0.856, 0.858, 0.893, 0.895, and 0.909. The RMSE results achieved by the JNBO-SpinalNet method are presented in fig 5(f), indicating RMSE values of 0.660, 0.623, 0.589, 0.552, and 0.535 for 20, 40, 60, 80, and 100 epochs respectively, all at the time stamp of 450 seconds.

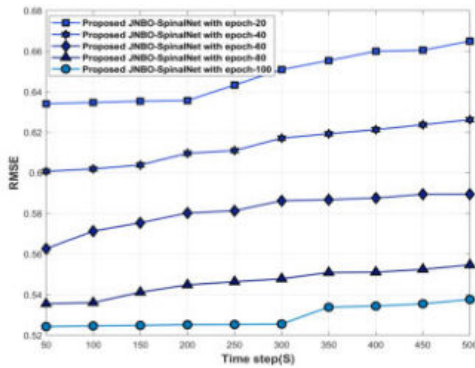


Figure 5 (e). RMSE

### 3.10 Comparative Analysis

The proposed model JNBO-SpinalNet for credit card fraudulent transactions detections compared with various existing traditional methods such as FFD Yang et al. (2019), RBM Suvarna and Kowshalya (2020), Adaboost + LGBM Malik et al. (2022), and NAG Ghosh et al.(2022).

The comparative assessment of JNBO-SpinalNet model is performed for determination of performance using different evaluation parameters is portrayed in figure 6. The MSE measured by the different models based on the fraudulent credit card transaction detection is depicted in the figure 6(a). For the time stamp of 450S, the JNBO-SpinalNet measured MSE of 0.890, where other models recorded MSE of FFD is 0.823, RBM is 0.845, Adaboost + LGBM is 0.860, and NAG is 0.870. Figure 6 illustrates the comparative evaluation of the JNBO-SpinalNet model's performance across various assessment parameters. Specifically, Figure 6(a) presents the Mean Squared Error (MSE) measurements for fraudulent credit card transaction detection conducted by different models. At a timestamp of 450S, the JNBO-SpinalNet model exhibited an MSE of 0.890. In comparison, alternative models registered MSE values, with FFD at 0.823, RBM at 0.845, Adaboost + LGBM at 0.860, and NAG at 0.870.

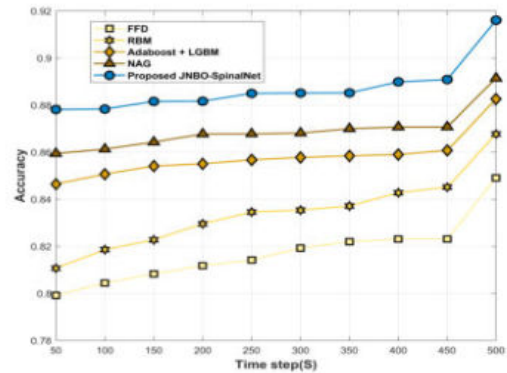


Figure 6 (a). Accuracy

The JNBO-SpinalNet outperformed the RBM approach with a superior performance margin of 5.14%. In Figure 6(b), the loss function of the models is depicted, with the JNBO-SpinalNet model showing a measured loss function of 0.131. In comparison, other techniques such as FFD, RBM, Adaboost + LGBM, and NAG recorded loss functions of 0.209, 0.186, 0.149, and 0.137, respectively, at the 450S time stamp.

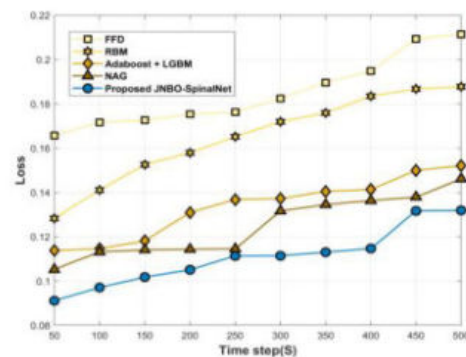


Figure 6(b). Loss

Figure 6(c) illustrates the Mean Squared Error (MSE) observed through various detection techniques. At the 450S timestamp, the MSE values for different detection approaches—FFD, RBM, Adaboost + LGBM, NAG, and JNBO-SpinalNet—are 0.438, 0.391, 0.352, 0.304, and 0.286, respectively.

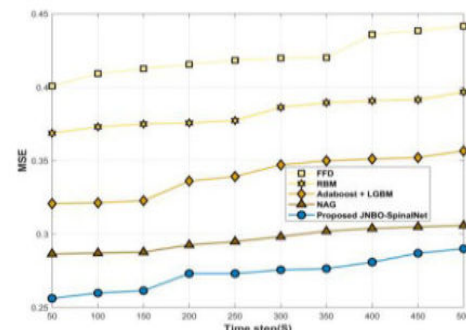


Figure 6(c). MSE

In Figure 6(d), the False Positive Rates (FPR) of these approaches are detailed. The JNBO-SpinalNet model achieves an FPR of 0.102, while FFD, RBM, Adaboost + LGBM, and NAG record FPR values of 0.186, 0.183, 0.163, and 0.143, respectively, at the 450S time stamp.

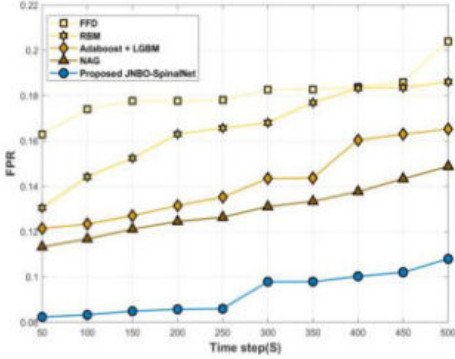


Figure 6(d). FPR

The MAP recorded by various traditional approaches based on the fraudulent credit card transaction detection is described in the figure 6(e).

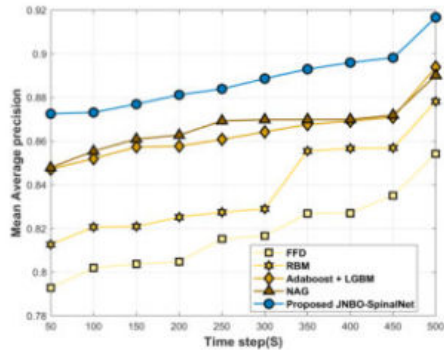


Figure 6(e). Mean Average Precision

The JNBO-SpinalNet achieved MAP of 0.898 for the time stamp of 450S, where other approaches measured MAP of FFD is 0.835, RBM is 0.856, Adaboost+LGBM is 0.870, and NAG is 0.871. The JNBO-SpinalNet achieved greater performance of 7.03% than FFD technique. The RMSE measured by the detection schemes are given in figure 6(f). The credit card fraud detection techniques, namely FFD, RBM, Adaboost + LGBM, NAG, and JNBO-SpinalNet recorded RMSE of

0.662, 0.625, 0.593, 0.552, and 0.535 for the time stamp of 450S

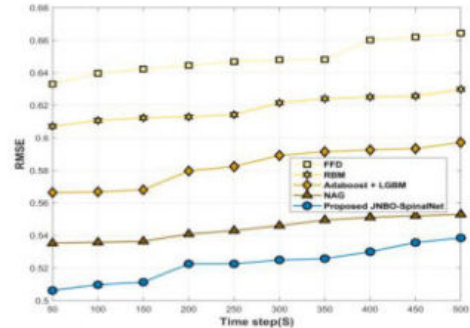


Figure 6(f). RMSE

#### 4. COMPARATIVE DISCUSSION

Table 1 demonstrates the JNBO-SpinalNet model's robust performance in identifying fraudulent credit card transactions across a range of evaluation metrics. In comparison to traditional methods, the JNBO-SpinalNet model delivers notable results: an accuracy of 89.10%, a loss function value of 13.16%, an MSE of 28.68%, a low FPR of 10.20%, an impressive MAP of 89.82%, and an RMSE of 53.56%. In contrast, classical approaches such as FFD, RBM, Adaboost + LGBM, and NAG achieved accuracy rates of 82.31%, 84.52%, 86.08%, and 87.08%, with corresponding loss function values of 20.94%, 18.68%, 14.99%, and 13.79%. The different methods exhibited MSE values of 43.85% (FFD), 39.15% (RBM), 35.20% (Adaboost + LGBM), and 30.49% (NAG). Regarding FPR, FFD, RBM, Adaboost + LGBM, and NAG recorded rates of 18.60%, 18.37%, 16.31%, and 14.34%, respectively. For MAP, the traditional techniques yielded values of 83.50%, 85.69%, 87.09%, and 87.18%, along with RMSE values of 66.22%, 62.57%, 59.33%, and 55.22%. The JNBO model, employing a well-tuned time control mechanism, significantly enhances the effectiveness of fraudulent credit card transaction detection within the SpinalNet classifier. This improvement also contributes to an increased computational capacity of the system.

Table 1. Comparative analysis with the proposed JNBO-SpinalNet model

Evaluation parameter	FFD	RBM	Adaboost + LGBM	NAG	Designed JNBO-SpinalNet model
Accuracy (%)	82.31%	84.52%	86.08%	87.08%	89.10%
Loss function (%)	20.94%	18.68%	14.99%	13.79%	13.16%
MSE (%)	43.85%	39.15%	35.20%	30.49%	28.68%
FPR (%)	18.60%	18.37%	16.31%	14.34%	10.20%
MAP (%)	83.50%	85.69%	87.09%	87.18%	89.82%
RMSE (%)	66.22%	62.57%	59.33%	55.22%	53.56%

This exploratory study introduces a novel approach, JNBO-SpinalNet, which leverages a hybrid optimization algorithm and deep learning techniques for detecting

credit card transaction frauds. The initial step involves preprocessing the input data through quantile normalization, transforming it into a more organized

format. Through a series of measures, an optimal feature subset is extracted from this pre-processed data. The feature set is then augmented using the bootstrapping method, enhancing the dataset for fraud detection purposes. For the actual fraudulent transaction detection, the SpinalNet classifier is employed. This classifier is further refined and optimized by the JNBO model, contributing to the improved identification of fraudulent activities. The efficacy of this devised model is assessed using diverse evaluation parameters, encompassing accuracy, loss function, MSE, FPR, MAP, and RMSE. Notably, the JNBO-SpinalNet model outperforms other models, demonstrating a remarkable 89.10% accuracy, a minimal 13.16% loss function, a well-contained 28.68% MSE, a low 10.20% FPR, a high 89.82% MAP, and a reasonable 53.56% RMSE. In the future, the research will extend its scope by considering various normalization techniques to effectively restructure imbalanced data into a more organized form. Furthermore, the inclusion of additional distance measures for selecting pertinent features holds the potential to enhance the accuracy of fraudulent activity detection.

## 5. CONCLUSION

This preliminary investigation introduces an innovative method named JNBO-SpinalNet, which utilizes a hybrid optimization algorithm and deep learning techniques to

identify credit card transaction fraud. The initial phase involves preprocessing the input data through quantile normalization, transforming it into a more structured format. Subsequently, an optimal subset of features is extracted from this pre-processed data through a series of measures. To enhance the dataset for fraud detection, the feature set is expanded using the bootstrapping method. The SpinalNet classifier is employed for actual fraudulent transaction detection, and this classifier is further refined and optimized by the JNBO model, contributing to improved identification of fraudulent activities. The effectiveness of the proposed model is evaluated using various metrics, including accuracy, loss function, MSE, FPR, MAP, and RMSE. Notably, the JNBO-SpinalNet model surpasses other models, achieving an impressive 89.10% accuracy, a minimal 13.16% loss function, a well-contained 28.68% MSE, a low 10.20% FPR, a high 89.82% MAP, and a reasonable 53.56% RMSE. In future research, the scope will be expanded by exploring various normalization techniques to effectively restructure imbalanced data into a more organized form. Additionally, the incorporation of additional distance measures for selecting relevant features has the potential to further enhance the accuracy of fraudulent activity detection.

## References:

- Alharbi, A., Alshammari, M., Okon, O. D., Alabrah, A., Rauf, H. T., Alyami, H., & Meraj, T. (2022). A novel text2IMG mechanism of credit card fraud detection: A deep learning approach. *Electronics*, 11(5), 756. doi:10.3390/electronics11050756.
- Correa Bahnsen, A. C., Aouada, D., Stojanovic, A., & Ottersten, B. (2016). Feature engineering strategies for credit card fraud detection. *Expert Systems with Applications*, 51, 134–142. doi:10.1016/j.eswa.2015.12.030
- Bolton, R. J., & Hand, D. J. (2022). Statistical fraud detection: A review. *Statistical Science*, 17(3), 235–255. doi:10.1214/ss/1042727940
- Chahardoli, M., Eraghi, N. O., & Nazari, S. (2022). Namib beetle optimization algorithm: A new meta-heuristic method for feature selection and dimension reduction. *Concurrency and Computation: Practice and Experience*, 34(1), e6524. doi:10.1002/cpe.6524
- Cheng, D., Xiang, S., Shang, C., Zhang, Y., Yang, F., & Zhang, L. (April 2020). Spatio-temporal attention-based neural network for credit card fraud detection. In. *Proceedings of the AAAI Conference on Artificial Intelligence*, 34(1), 362–369. doi:10.1609/aaai.v34i01.5371
- Chou, J. S., & Truong, D. N. (2021). A novel metaheuristic optimizer inspired by behavior of jellyfish in ocean. *Applied Mathematics and Computation*, 389, 125535. doi:10.1016/j.amc.2020.125535
- Esenogho, E., Mienye, I. D., Swart, T. G., Aruleba, K., & Obaido, G. (2022). A neural network ensemble with feature engineering for improved credit card fraud detection. *IEEE Access*, 10, 16400–16407. doi:10.1109/ACCESS.2022.3148298
- Ghosh Dastidar, K., Jurgovsky, J., Siblini, W., & Granitzer, M. (2022). NAG: Neural feature aggregation framework for credit card fraud detection. *Knowledge and Information Systems*, 64(3), 831–858. doi:10.1007/s10115-022-01653-0
- Jovanovic, D., Antonijevic, M., Stankovic, M., Zivkovic, M., Tanaskovic, M., & Bacanin, N. (2022). Tuning machine learning models using a group search firefly algorithm for credit card fraud detection. *Mathematics*, 10(13), 2272. doi:10.3390/math10132272
- Kabir, H. M. D., Abdar, M., Khosravi, A., Jalali, S. M. J., Atiya, A. F., Nahavandi, S., & Srinivasan, D. (2022). Spinalnet: Deep neural network with gradual input. *IEEE Transactions on Artificial Intelligence*, 4(5), 1165–1177. doi:10.1109/TAI.2022.3185179

- Kairouz, P., McMahan, H. B., Avent, B., Bellet, A., Bennis, M., Nitin Bhagoji, A. N. (2021). Advances and open problems in federated learning. Foundations and Trends® in Machine Learning, 14(1–2), 1–210. doi:10.1561/2200000083
- Laleh, N., & AbdollahiAzgomi, M. (2009). A taxonomy of frauds and fraud detection techniques. In Proceedings of the Information Systems, Technology and Management. Proceedings of the vol: Third International Conference, ICISTM 2009, Ghaziabad, India, March 12–13, 3 (pp. 256–267). Berlin, Heidelberg: Springer.
- Li, W., Milletari, F., Xu, D., Rieke, N., Hancox, J., Zhu, W., ... Feng, A. (2019). Privacy-preserving federated brain tumour segmentation. In Proceedings of the Machine Learning in Medical Imaging [10th international workshop]. Proceedings of the vol, MLMI 2019, Held in Conjunction with MICCAI, 10 (pp. 133–141). Shenzhen, China: October 13. Springer International Publishing.
- Malik, E. F., Khaw, K. W., Belaton, B., Wong, W. P., & Chew, X. (2022). Credit card fraud detection using a new hybrid machine learning architecture. Mathematics, 10(9), 1480. doi:10.3390/math10091480
- McMahan, B., Moore, E., & Ramage, D. Hampson, S. and y Arcas, B.A. Communication-Efficient Learning of Deep Networks from Decentralized Data, In Proceedings of the Artificial Intelligence and Statistics. (April 2017). PMLR. In (pp. 1273–1282).
- Phua, C., Gayler, R., Lee, V., & Smith-Miles, K. (2009). On the communal analysis suspicion scoring for identity crime in streaming credit applications. European Journal of Operational Research, 195(2), 595–612. doi:10.1016/j.ejor.2008.02.015
- Rieke, N., Hancox, J., Li, W., Milletarì, F., Roth, H. R., Albarqouni, S. (2020). The future of digital health with federated learning. npj Digital Medicine, 3(1), 119. doi:10.1038/s41746-020-00323-1
- Suvarna, R., & Kowshalya, A. M. (2020). Credit card fraud detection using federated learning techniques.
- Yang, W., Zhang, Y., Ye, K., Li, L., & Xu, C. Z. (2019). Ffd: A federated learning-based method for credit card fraud detection. In Proceedings of the Big Data–Bigdata. Proceedings: 8th International Congress, Held as Part of the Services Conference Federation, SCF 2019, San Diego, CA, USA, June 25–30, 8 (pp. 18–32). Springer International Publishing.
- Zareapoor, M., & Shamsolmoali, P. (2015). Application of credit card fraud detection: Based on bagging ensemble classifier. Procedia Computer Science, 48, 679–685. doi:10.1016/j.procs.2015.04.201
- Zhang, C., Bengio, S., Hardt, M., Recht, B., & Vinyals, O. (2021). Understanding deep learning (still) requires rethinking generalization. Communications of the ACM, 64(3), 107–115. doi:10.1145/3446776
- Zhang, X., Han, Y., Xu, W., & Wang, Q. (2021). HOBA: A novel feature engineering methodology for credit card fraud detection with a deep learning architecture. Information Sciences, 557, 302–316. doi:10.1016/j.ins.2019.05.023
- Zhao, Y., Wong, L., & Goh, W. W. B. (2020). How to do quantile normalization correctly for gene expression data analyses. Scientific Reports, 10(1), 15534. doi:10.1038/s41598-020-72664-6

---

**Chanda Sekhar Kolli**

Shri Vishnu Engineering College for Women,  
Bhimavaram,  
India  
[kcsit@svecw.edu.in](mailto:kcsit@svecw.edu.in)  
ORCID 0000-0002-7553-1901

**Venkata Naga Raju D**

Shri Vishnu Engineering College for Women,  
Bhimavaram,  
India  
[dvnraju@svecw.edu.in](mailto:dvnraju@svecw.edu.in)  
ORCID 0000-0002-0480-663X

**Pavan Kumar V**

Shri Vishnu Engineering College for Women,  
Bhimavaram,  
India  
[vadrevu.pavan@svecw.edu.in](mailto:vadrevu.pavan@svecw.edu.in)  
ORCID 0000-0002-7459-9437

**Srinivasa Rao D**

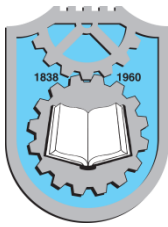
Shri Vishnu Engineering College for Women,  
Bhimavaram,  
India  
[dsrinivasaraoit@svecw.edu.in](mailto:dsrinivasaraoit@svecw.edu.in)  
ORCID 0000-0002-6417-3686

**Vinay**

Shri Vishnu Engineering College for Women,  
Bhimavaram,  
India  
[pvinayit@svecw.edu.in](mailto:pvinayit@svecw.edu.in)  
ORCID 0009-0007-4902-247X

**GAKS Rajeev kumarraju**

Shri Vishnu Engineering College for Women,  
Bhimavaram,  
India  
[gaksit@svecw.edu.in](mailto:gaksit@svecw.edu.in)  
ORCID 0009-0007-0221-6269



## AREA AND POWER EFFICIENT LEAST MEAN SQUARE ADAPTIVE FILTER USING APPROXIMATE ARITHMETIC

G. R. L. V. N. Srinivasa Raju<sup>1</sup>

Doondi Kumar Janapala

J. Naga Vishnu Vardhan

Chinnaiah M C

Praveen Kumar Nalli

Jannu Teja Sri

Keywords:

### A B S T R A C T

*Finite Impulse Response (FIR); Rounding Based Approximate Multiplier (ROBA); Least Mean Square (LMS); Adaptive Filter (AF); Weight Update Block (WUB); Digital Signal Processing (DSP); Multiply and Accumulate (MAC).*

The efficiency of a digital signal processing system heavily relies on the performance of multipliers, which are crucial arithmetic functional units. Approximate arithmetic techniques have emerged as a promising approach to significantly reduce circuit complexity, latency, and energy consumption. This paper presents a rounding-based approximate multiplier, grounded in approximate arithmetic principles, to execute a Least Mean Square (LMS) adaptive filter. Within the LMS adaptive filter, conventional multipliers are replaced with approximate arithmetic-based multipliers. These approximations simplify the multiplication operations, resulting in reduced area and power consumption. The LMS adaptive filter adjusts filter coefficients based on the LMS algorithm. This proposed system is realized using the Verilog hardware description language, and its performance is validated through simulation and synthesis using Xilinx ISE 14.7 simulator and Vivado design suite. Simulation results showed that implementing the LMS adaptive filter algorithm with rounding-based approximate multipliers yields a substantial reduction in area, latency, and power consumption.



© 202x Published by Faculty of Engineering

### 1. INTRODUCTION

Digital filters play a pivotal role in modern digital signal processing (DSP) applications. These filters are essential devices employed to shape and manipulate the spectral characteristics of a signal while rejecting unwanted or undesirable components. In DSP, one innovative category of filters is Adaptive Filters (AF),

which holds a crucial position due to their ability to automatically adjust their coefficients based on adaptive algorithms, thereby enhancing their performance. Adaptive filters, in contrast to conventional linear filters, are nonlinear in nature, allowing them to adapt dynamically to changing input signals. One widely used algorithm for adapting filter coefficients is the Least Mean Squares (LMS) algorithm. LMS adaptive filters

<sup>1</sup> Corresponding author: Dr. G.R.L.V.N. Srinivasa Raju  
Email: grlvnsr@svecw.edu.in

iteratively adjust their coefficients to minimize the error between the desired and actual filter outputs. This adaptation enables them to approximate and track time-varying signals accurately, making them indispensable in applications like noise cancellation, echo cancellation, and adaptive beamforming. Multipliers constitute a primary source of power consumption in digital signal processing circuits. To meet stringent power budgets in VLSI circuits, strategies are employed to reduce power consumption. One effective approach is to optimize the use of multipliers and adders within digital filters. By minimizing unnecessary data transitions and employing efficient arithmetic operations, power consumption can be significantly lowered.

In this context, approximate arithmetic designs have gained prominence. These designs offer a trade-off between accuracy and power efficiency. They employ techniques such as reduced-precision arithmetic and approximate algorithms to achieve computational savings while still delivering acceptable signal processing performance. This approach is particularly valuable in battery-powered and energy-efficient devices, where minimizing power consumption is paramount. Previous studies show that approximate computing has appeared as a good prototype to upgrade the circuit performance i.e., speed and power dissipation (Han and Orshansky, 2013). The reduction in the hardware complication of LMS AF supposed error free arithmetic (Allred et al., 2005).

The conditions which involved in replacing of MAC unit with LUT are presented by Khan et al., (2017). It is also proved that approximate multipliers are used to reduce the logic compression of the design (Qiqieh et al., 2017). In other work, a well-organized architecture for the execution of a delay LMS AF propose a plan of action for maximize remaining pipelining over time taking connectional blocks of the shape is presented (Meher and Park 2014). A new strategy AF using Offset Binary Coding (OBC) technique and removes two oldest sample permit attainable decomposition of LUT (Khan and Ahamed, 2017). Approximate multiplier offer rounding the quantity to nearby supporter of two and it is relevant for both signed and unsigned multiplications (Zendegani et al., 2017). A FIR filter designed using ROBA multipliers and rounding quantities to the nearest power of two is aimed at optimizing the multiplication process to reduce area and enhance processing speed. This approach involves explaining the multiplication operation in a way that minimizes computational complexity and maximizes efficiency (Shabhana Begum and Vijaya Kumar, 2017). Recently, the implementation of approximate multipliers, judges' effect on execution of LMS algorithm and presents approximate multiplier, whose precision adjusted results in low hardware complexity (Esposito et al., 2019).

The research gap of the study pertains to the underexplored area of leveraging approximate arithmetic methods to enhance area and power efficiency in adaptive filters. A more thorough investigation is needed to develop innovative techniques that can improve performance while minimizing computational complexity and resource utilization. With these motivations, this paper presents a LMS adaptive filter design using ROBA multiplier to lower the power requirement, and to reduce area, delay with the improved performance of design.

The paper is structured as detailed below. Section II outlines the LMS adaptive filter algorithm. The design methodology is presented in section III. Section IV presents the results and discussions. Section V discusses the implications of the proposed design.

## 2. LMS ADAPTIVE FILTER

Machine learning algorithms can be used to analyze clinical LMS AF balances Filter co-efficient to adapt input signal and act as negative feedback to lower the error between FIR Filter output and desired signal (Riaz et al., 2018). When differentiated with additional algorithms used for applying AF the LMS algorithm is seen to present very well in terms of simplicity (Mohanty and Meher, 2013; Krishnamurthy et al. 2017; Sadeghi et al. 2019). FIR filter is linear whose output is linear to the input signal and operates only on current and past input values. FIR filters are used to filter the unwanted signals from the discrete input signals (Haykin, Simon S. 2003; Prakash and Ahamed 2013; Venkatachalam and Ko, 2017).

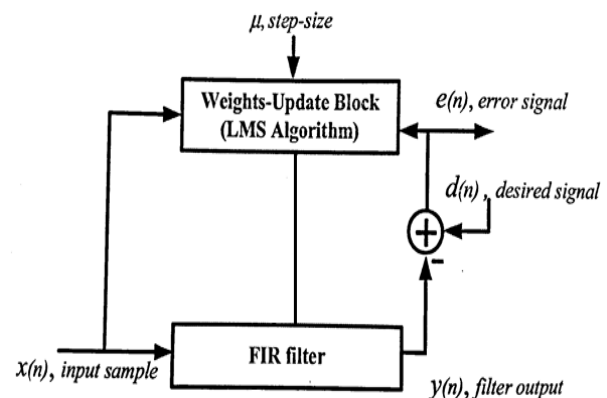


**Figure 1.** LMS Adaptive Filter

The Figure 1 conveys the input signal  $x(n)$ , output signal  $y(n)$ , error signal  $e(n)$ , desired signal  $d(n)$ , filter output  $y(n)$ . The above structure shows in which way the output signal of the Filter is determined from input signal. LMS AF varies the filter transfer function in accordance with the adaptive algorithm to enhance the performance and it requires the number of iterations equals to the input signal (Farshchi, et al., 2013). The LMS adaptive Algorithm reports how the parameters

are modified from one time instant to another. There is an input, a desired response and the error between them to adjust the filter parameters (Simon Haykin 1996; Bhardwaj et al., 2014). The WUB regulate the FIR filter coefficients using the LMS algorithm. The FIR Filter utilizes the perpetually substituting the co-efficient planned by the WUB to calculate an output signal.

Filter output:

$$y(n) = \sum_{n=0}^{N-1} x[n] w(n) \quad (1)$$

Estimation error:

$$e(n) = d(n) - y(n) \quad (2)$$

This measures the difference between the output of the adaptive filter and the output of the unknown system. On the basis of this measure, the adaptive filter will change its coefficients in an attempt to reduce the error. Tap weight adaptation:

$$W(n+1) = w(n) + \mu e(n) x(n) \quad (3)$$

### 3. DESIGN METHODOLOGY

This section introduces the structure of ROBA Multiplier design. It is an efficient multiplier to bring down the power dissipation in circuits (Vasudeva Reddy et al., 2023) The sign detector structure detects the sign of the input variables if they are negative, they are converted into two's complement form and for each absolute value is generated.

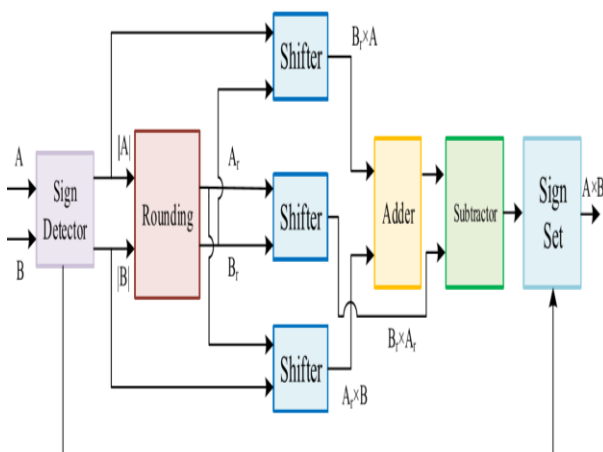


**Figure 2.** Block diagram of ROBA multiplier

The block diagram of ROBA multiplier is shown in Figure 2, and is applicable for both unsigned multiplication and signed multiplication. For unsigned multiplication, sign detector and sign set is disabled that can speed up the multiplication process. The inputs given to sign detector block which discover MSB of input and transferred to sign set indicated signed

multiplication or unsigned multiplication. Rounded block is used for round off purposes and it extracts the nearest value in the form of  $2^n$ . The inputs A, B are rounded by  $A_r, B_r$ . Then A and B written as

$$AB = (A_r - A)(B_r - B) + A_r B + B_r A - A_r B \quad (4)$$

The shifter blocks are used to implement the product terms. The operations of  $A_r B_r$ ,  $A_r B$ ,  $B_r A$  applied to functioning of shifting i.e., shown equation (4). Application of  $(A_r - A)(B_r - B)$  is difficult. So, that part is omitted and simplifies the multiplication operation shown in the equation (5).

$$AB = A_r B + B_r A - A_r B_r \quad (5)$$

The adder block adds the product to get the final result if the input variables are negative subtraction block is preferred. Finally, the relevant sign is set according to the sign of the input variables (Maddela et al., 2021; Parvathi and Chinnaiah2023). In the proposed design ROBA multiplier is used for the execution of LMS AF. The structure continuously changed the filter input and output. Figure. 3 present the structure of LMS AF that uses multiplier.

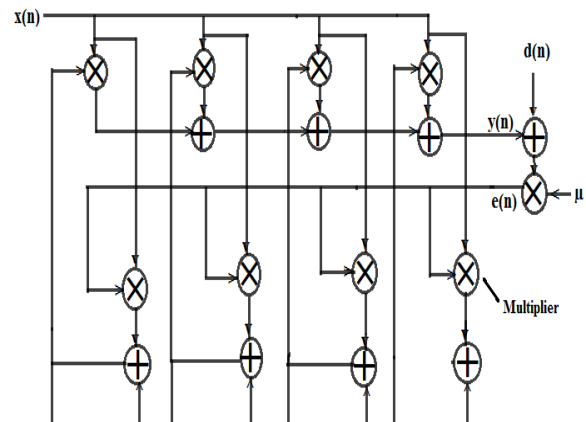


**Figure 3.** Structure of LMS AF using ROBA multiplier

In the proposed design that multiplier can be replaced with ROBA Multiplier which gives less area and less delay and less power consumption when compared with other approximate multipliers. The output equal to the desired, then error between the two is zero and weights of LMS AF match to the weights of the FIR filter results a good convergence. The delay input is multiplied with the corresponding coefficient by the multiplier and remaining is added to configure the filter output. Proposed LMS AF designed based on proposed multiplier permit decrease in power consumption and gives less area and delay.

### 4. RESULTS & DISCUSSIONS

The LMS Adaptive Filter, employing a ROBA multiplier, is accurately designed using the Verilog hardware description language. This specialized approach was subjected to thorough simulation and synthesis processes using both the Xilinx ISE 14.7 simulator and the Vivado design suite. The integration of the ROBA multiplier into the LMS Adaptive Filter yielded several notable advantages. Firstly, it demonstrated superior resource efficiency, consuming less FPGA resources. Specifically, the LMS AF using the ROBA multiplier occupied 540 slice Look-Up Tables (LUTs) and 576 slice registers. In contrast, traditional LMS AF implementations typically utilize more FPGA resources. Moreover, this innovative design exhibited reduced power consumption, making it an attractive choice for power-sensitive applications. Lower power requirements contribute to enhanced energy efficiency and longer battery life in portable devices.

#### 4.1 RTL Schematic of Approximate Multiplier

Figure 4 depicts the RTL schematic of a proposed approximate multiplier used in LMS AF algorithm. This specific configuration of the multiplier provides a way to perform multiplication. To evaluate its functionality and performance testing is conducted. During the simulation process it is examined how it behaves, under different input conditions and compared its accuracy to traditional multipliers. The investigations ensured that the approximate multiplier could be efficiently implemented and used in real world applications while striking a balance, between accuracy and resource utilization.

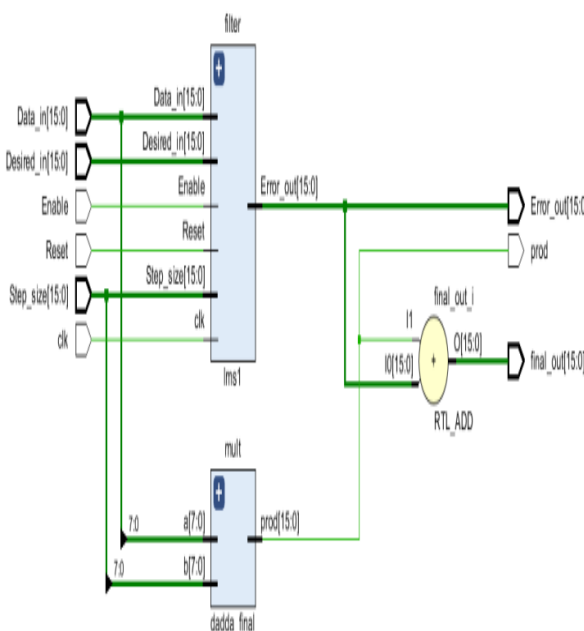


**Figure 4.** RTL Schematic of Approximate Multiplier

#### 4.2 RTL Schematic of LMS AF using ROBA Multiplier

Figure 5 presents the RTL schematic of the LMS AF incorporating the ROBA multiplier. This specialized design harnesses the power of adaptive filtering while optimizing resource utilization and performance. To evaluate and implement this innovative design, a two-step process involving simulation and synthesis was carried out using the Vivado design suite. In the simulation phase, the behaviour of the LMS AF with the ROBA multiplier was rigorously tested under various input conditions, allowing for an assessment of its accuracy and efficiency compared to traditional implementations. Following successful simulation, the synthesis step within Vivado converted the RTL description into a hardware configuration that can be deployed on FPGA devices. This process ensured that the LMS AF with the ROBA multiplier could be efficiently realized, offering a compelling balance between computational performance and resource utilization. Ultimately, this design holds promise for applications requiring adaptive filtering with enhanced area efficiency and reduced power consumption.

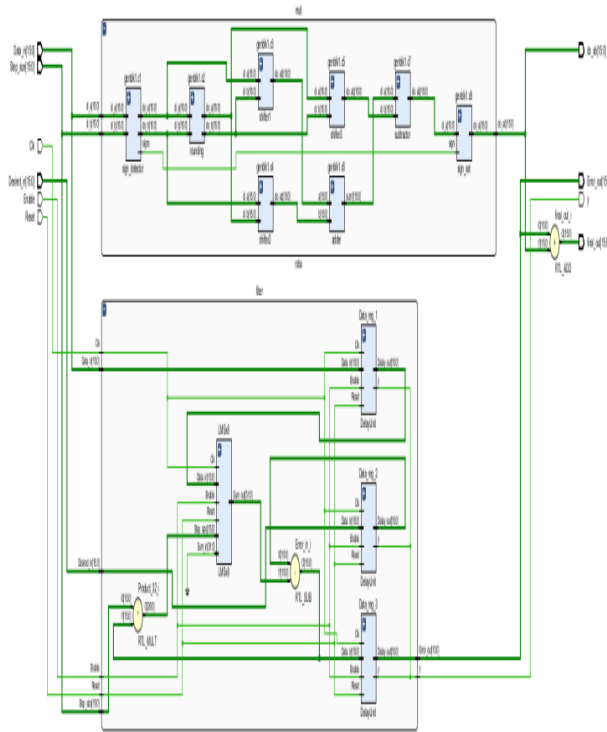


**Figure 5.** RTL Schematic of LMS filter using ROBA Multiplier

#### 4.3 Simulation Waveform of LMS AF using ROBA multiplier

Figure 6 shows the simulation waveform for the LMS AF utilizing the ROBA multiplier, implemented and analyzed within the Vivado design suite. This waveform offers a visual representation of the filter's performance

and behavior, enabling engineers to assess its effectiveness in adapting coefficients and achieving desired signal processing outcomes.

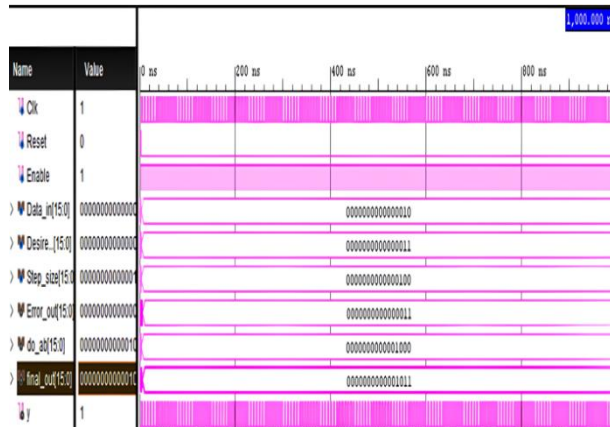


**Figure 6.** Simulation waveform of LMS Adaptive filters using ROBA multiplier

#### 4.4 Performance Comparison

The comparison presented in Table 1 provides compelling evidence of the superiority of the ROBA multiplier in the execution of the LMS AF. It demonstrates remarkable power efficiency, with a substantial 99.86% reduction in power consumption compared to existing approximate multipliers. Additionally, the ROBA multiplier occupies significantly less FPGA area, utilizing 6% fewer resources. This efficient use of resources is critical for optimizing chip real estate. Moreover, the ROBA multiplier contributes to a 10.04% reduction in signal propagation delay, making it invaluable for applications demanding low-latency signal processing. These results underscore the ROBA multiplier's prowess in enhancing the performance and efficiency of LMS AF implementations

**Table 1.** Performance Comparison of Approximate and ROBA Multipliers

Parameter	(11)	(12)	Approximate Multiplier (10)	ROBA Multiplier (proposed)
Delay (ns)	595	517.5	11.228	10.1
Power (mw)	16.004	125.76	57877	81
Area (slice LUTS & slice registers)	23265	21105	1195	1116

From the investigations it is observed that the ROBA multiplier within the LMS AF design showcased

reduced signal propagation delays. This reduction in delay can be crucial in real-time signal processing applications, where minimizing latency is essential. Overall, the integration of the ROBA multiplier into the LMS Adaptive Filter represents a significant advancement in hardware design. It optimizes FPGA resource utilization, lowers power consumption, and reduces signal propagation delays, making it a compelling choice for various applications, such as communications, image processing, and embedded systems, where efficient and low-latency signal processing is paramount. This demonstrates the ongoing drive in the field of digital hardware design to strike a balance between performance and resource efficiency, offering solutions that meet the demands of modern technology

#### 5. CONCLUSION

Adaptive filtering stands as a cornerstone in the realm of digital signal processing, enabling the refinement of signal characteristics. This paper presents a novel approach, realized through Verilog language, aimed at enhancing both area efficiency and power conservation in the operation of the LMS AF by leveraging the ROBA multiplier. The design underwent comprehensive validation through simulation utilizing Xilinx ISE 14.7 and Vivado, two prominent FPGA development tools. The results are indeed noteworthy, with the adoption of the ROBA multiplier leading to power and delay improvements. Specifically, this design achieved 99.86% reduction in power consumption, significantly contributing to energy-efficient signal processing. Furthermore, it occupied 6% less FPGA area (LUTs), demonstrating an efficient use of hardware resources. Additionally, a notable 10.04% reduction in signal propagation delay was observed, crucial for applications demanding minimal latency. As for future directions, the proposed architecture holds great promise. Further exploration can focus on refining the ROBA multiplier's design and exploring its applicability in other adaptive filtering techniques. Research can also extend to optimizing the trade-off between power savings and signal processing accuracy, ensuring that the system remains adaptable to varying requirements. Moreover, investigating the scalability of this approach for more complex and demanding applications could pave the way for broader adoption. In summary, the proposed design not only presents significant immediate benefits in power efficiency, area utilization, and signal latency but also offers a compelling foundation for future research and applications in the field of adaptive filtering.

## References:

- Allred, D., Yoo, H., Krishnan, V., Huang, W., & Anderson, D. V. (2005b). LMS adaptive filters using distributed arithmetic for high throughput. *IEEE Transactions on Circuits and Systems I-regular Papers*, 52(7), 1327–1337. doi: 10.1109/tcsi.2005.851731.
- Bhardwaj, K., Mane, P., & Henkel, J. (2014). Power- and area-efficient Approximate Wallace Tree Multiplier for error-resilient systems. *Fifteenth International Symposium on Quality Electronic Design*, Santa Clara, CA, USA, 263-269. doi: 10.1109/isqed.2014.678335.
- Esposito, D., De, D., Di Meo, G., Napoli, E., & Strollo, A. (2019b). Low-Power hardware implementation of Least-Mean-Square adaptive filters using approximate arithmetic. *Circuits, Systems, and Signal Processing*, 38(12), 5606–5622. doi: 10.1007/s00034-019-01132-y.
- Farshchi, F., Abrishami, M. S., and Fakhraie, S. M. (2013). New approximate multiplier for low power digital signal processing. *Proc. 17th Int. Symp. Comput. Archit. Digit. Syst.*, 25–30.
- Han J., and Orshansky, M. (2013). Approximate computing: An emerging paradigm for energy-efficient design. *18<sup>th</sup> IEEE European Test Symposium (ETS)*, Avignon, France, 1-6. doi: 10.1109/ETS.2013.6569370.
- Haykin, Simon S. (2003). Least-Mean-Square Adaptive Filters. Wiley: *Bernard Widrow*, ISBN 0-471-21570-8.
- Khan, M. T., Ahamed, S. R., & Brewer, F. (2017). Low Complexity and Critical Path Based VLSI Architecture for LMS Adaptive Filter Using Distributed Arithmetic. *2017 30<sup>th</sup> International Conference on VLSI Design and 2017 16<sup>th</sup> International Conference on Embedded Systems (VLSID)*, Hyderabad, India, 127–132. doi: 10.1109/vlsid.2017.16.
- Khan, M.T., Ahamed, S.R. (2017). VLSI Implementation of Throughput Efficient Distributed Arithmetic Based LMS Adaptive Filter. In: *Kaushik, B., Dasgupta, S., Singh, V. (eds) VLSI Design and Test. VDAT 2017. Communications in Computer and Information Science*, vol 711. Springer, Singapore. doi: 10.1007/978-981-10-7470-7\_3.
- Krishnamurthy, S., Kannan, R., Yahya, E. A., & Bingi, K. (2017). Design of FIR filter using novel pipelined bypass multiplier. *2017 IEEE 3<sup>rd</sup> International Symposium in Robotics and Manufacturing Automation (ROMA)*, Kuala Lumpur, Malaysia, 1-6. doi: 10.1109/roma.2017.8231838.
- Maddela, V., Sinha, S. K., & Parvathi, M. (2021b). Extraction of undetectable faults in 6T- SRAM cell. *2021 International Conference on Communication, Control and Information Sciences (ICCISe)*. doi: 10.1109/iccisc52257.2021.9484987.
- Meher, P. K., & Park, S. (2014). Area-Delay-Power Efficient Fixed-Point LMS Adaptive Filter with Low Adaptation-Delay. *IEEE Transactions on Very Large Scale Integration Systems*, 22(2), 362–371. doi: 10.1109/tvlsi.2013.2239321.
- Mohanty B. K. and P. K. Meher. (2013). A High-Performance Energy-Efficient Architecture for FIR Adaptive Filter Based on New Distributed Arithmetic Formulation of Block LMS Algorithm. *IEEE Transactions on Signal Processing*, 61 (4), 921-932. doi: 10.1109/TSP.2012.2226453.
- Parvathi, M., & Chinnaiah, M. C. (2022). Implementation and performance evaluation of hybrid SRAM architectures using 6T and 7T for Low-Power applications. *In Lecture notes in networks and systems*, 235–245. doi: 10.1007/978-981-19-4990-6\_22.
- Prakash, M. S., & Ahamed, S. R. (2013). Low-Area and High-Throughput architecture for an adaptive filter using distributed arithmetic. *IEEE Transactions on Circuits and Systems II-express Briefs*, 60(11), 781–785. doi: 10.1109/tcsii.2013.2281747.
- Qiqieh, I., Shafik, R., Tarawneh, G., Sokolov, D., & Yakovlev, A. (2017). Energy-efficient approximate multiplier design using bit significance-driven logic compression. *Design, Automation & Test in Europe Conference & Exhibition (DATE)*, 7–12. doi: 10.23919/date.2017.7926950.
- Riaz, M., Ahmed, S. A., Javaid, Q., & Kamal, T. (2018). Low power 4×4 bit multiplier design using dadda algorithm and optimized full adder. *2018 15<sup>th</sup> International Bhurban Conference on Applied Sciences and Technology (IBCAST)*, 392-396. doi: 10.1109/ibcast.2018.8312254.
- Sadeghi, M., Zahedi, M., & Ali, M. (2019). The Cascade Carry Array Multiplier – a novel structure of digital unsigned multipliers for Low-Power consumption and Ultra-Fast applications. *Annals of Emerging Technologies in Computing*. doi: 10.33166/aetic.2019.03.003.
- Shabhana Begum, Vijaya Kumar, M. (2017). Design of FIR Filter using Rounding Based Approximate (ROBA) Multiplier. *International Journal of Scientific Engineering and Technology Research*. 06 (22), 4483-4489.
- Simon Haykin. (1996). Adaptive Filter Theory. *Third Edition, Prentice-Hall, Inc.*
- Vasudeva Reddy, T., Madhava Rao, K., Santhosh Kumar, V., Hindumathi, V. (2023). Energy Efficient Memory Architecture for High Performance and Low Power Applications Under Sub-threshold Regime. *Communication, Software and Networks. Lecture Notes in Networks and Systems*, vol 493. Springer, Singapore. doi: 10.1007/978-981-19-4990-6\_21.

Venkatachalam, S., & Ko, S. (2017). Design of power and area efficient approximate multipliers. *IEEE Transactions on Very Large Scale Integration Systems*, 25(5), 1782–1786. doi: 10.1109/tvlsi.2016.2643639.

Zendegani, R., Kamal, M., Bahadori, M., Afzali-Kusha, A., & Pedram, M. (2017). ROBA Multiplier: a Rounding-Based approximate multiplier for High-Speed yet Energy-Efficient digital signal processing. *IEEE Transactions on Very Large Scale Integration Systems*, 25(2), 393–401. doi: 10.1109/tvlsi.2016.2587696.

---

**Dr. G. R. L. V. N. S. Raju**

Department of ECE,  
Shri Vishnu Engineering College for  
Women, Bhimavaram, India  
[grlvnsr@svecw.edu.in](mailto:grlvnsr@svecw.edu.in)  
ORCID 0000-0003-1157-1856

**Doondi Kumar Janapala**

Department of ECE,  
Vishnu Institute of Technology,  
Bhimavaram, India  
[jdoondikumarece@gmail.com](mailto:jdoondikumarece@gmail.com)  
ORCID 0000-0001-5346-0877

**J Naga Vishnu Vardhan**

Department of ECE,  
BVRIT Hyderabad College of Engineering  
for Women, India  
[vishnu.j@bvrithyderabad.edu.in](mailto:vishnu.j@bvrithyderabad.edu.in)  
ORCID 0000-0002-6257-7644

**Chinnaiah M C**

Department of ECE,  
B V Raju Institute of Technology, Medak  
502313, India  
[chinnaiah.mc@bvit.ac.in](mailto:chinnaiah.mc@bvit.ac.in)  
ORCID 0000-0002-1489-7686

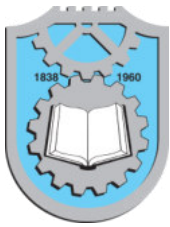
**Praveen Kumar Nalli**

Department of ECE,  
B V Raju Institute of Technology, Medak  
502313, India  
[chinnaiah.mc@bvit.ac.in](mailto:chinnaiah.mc@bvit.ac.in)

**Jannu Teja Sri**

Department of ECE,  
Shri Vishnu Engineering College for  
Women, Bhimavaram, India  
[jannutejasri@gmail.com](mailto:jannutejasri@gmail.com)  
ORCID 0009-0005-5522-2043

---



Vol. xx, No. x (202x) x-x, doi:

# Proceedings on Engineering Sciences



www.pesjournal.net

## SOME ASPECTS OF FRICTION AND ANISOTROPIC RATIOS ON THE WORK HARDENING BEHAVIOR IN THE UPSETTING TESTS

Harikrishna Chirala<sup>1</sup>

Varun Chandra C

Murahari Kolli

Srinivasaraju pericherla

N Malleswararao Battina

Srinivasarao Gajula

Keywords:

### A B S T R A C T

AA2014; upsetting; anisotropy; friction; strain hardening; Finite element simulation;

*Metal upsetting is a primary mechanical working operation to reduce the cross-section of the billets, and there are few challenges that are to be solved. When the billets undergo severe plastic deformation, the friction prevailing at the die/billet interface causes differential strain hardening and anisotropy in the metallic billets. The current work focuses on the effect of friction and anisotropy on the strain hardening behavior and hardness. AA2014 cast alloy were machined to an outer diameter of 24 mm, and an inner diameter of 12 mm with a thickness of 8 mm. Friction calibration curves were plotted from the ring compression test. Another set of solid cylindrical billets of the same composition with a height and diameter of 24 mm were compressed between the rigid dies. A distortion in the shape solid cylinders caused by friction, anisotropy, and their effect on strain hardening was studied after deformation. An equation was developed to predict the strain hardening behavior to investigate the effect anisotropy ratios on the strain hardening behavior. A novel approach to identify the effect of anisotropy ratios on the strain hardening behavior and hardness was proposed.*

© 202x Published by Faculty of Engineering



### 1. INTRODUCTION

AA2014 is a high-strength heat-treatable aluminum alloy primarily composed of aluminum (Al), copper (Cu), and small amounts of other elements. The alloy is known for its excellent strength-to-weight ratio, good machinability and for this reason, this alloy is widely used in automotive and aerospace industries. Bulk metal forming process, such as upsetting, aids in improving the strength and hardness of the material. Upsetting

being the primary operation to reduce the cross-section of the billets draws the attention of researchers to work on the strain hardening behavior and friction. It is always challenging to improve the hardness of the material to a large extent with homogeneity. Because friction is one of the major process parameters that influence the upsetting process, a quantification technique by name Male and Cockcroft calibration curves has been used over the decades to determine the magnitude of the friction at the die/billet interface. The

Corresponding author: Dr. Harikrishna Ch  
Email: [harinitw@gmail.com](mailto:harinitw@gmail.com)

studies of Male (1964) reported that the friction factor ( $m$ ) could be determined based on the dimensional changes of the ring compressed between two sets of dies. Further studies on friction were carried out by Avitzur (1968), assuming that the billet will not barrel to plot friction calibration curves from a wide range of  $m = 0$  to  $m = 1$ . The results reported by Avitzur were disproved by Sofuoğlu et al. (2001) and suggested that as the deformation progresses, the magnitude of the friction factor will not be constant. The above studies reported so far could not differentiate good lubrication and poor lubrication based on dimensional changes of the ring. Robinson et al. (2004) concluded in their studies that expansion of the hole is an indication of good lubrication, and contraction of the hole is an indication of poor lubrication.

Strain hardening makes the metal stronger and harder, and the study of the strain hardening coefficient ( $k$ ) is necessary to analyze the hardness of the billet after plastic deformation. Baskaran and Narayanasamy (2008) studied the work-hardening behavior of elliptical billets and concluded that the level of strain along the major and minor axes would influence the work-hardening behavior. The state of stress considered in the investigation also influences strain-hardening and the height to the diameter ratios of the billet. Al powder preforms with iron and aluminum oxide as reinforcements are made from a powder metallurgy route, and the powder preforms are compressed between the set of dies (Krishna et al., 2015, Inigraj et al., 1998). The authors concluded that axial stress increases strain levels and reduces porosity. Recent studies reported that the combined effect of sintering temperature and lubrication greatly influences the work-hardening behavior (Ananthanarayanan et al., 2019).

Developing an equation by correlating the strain hardening coefficient ( $k$ ) and strain hardening exponent ( $n$ ) will be useful in conducting simulation studies and strain in homogeneity can be minimized (Sommez and Demir, 2007). Similar kinds of studies were done by Narayanan et al. (2008) on annealed aluminum using finite element simulations. The equivalent strain obtained from the simulation was used to develop an equation for hardness measurement. The equation holds good when the material flows in the radial directions. Hari Krishna et al. (2017) and Seetharam et al. (2017) worked on the upsetting process of different alloys of aluminum. The authors conducted upsetting tests on Al-4%B4C preforms and observed a significant improvement in hardness when the billets were upset at a temperature of 400°C and under hot forming and examined that there is an increase in the hardness of billets when operated at a strain rate of 0.1 S-1. Aging treatment can be best utilized for obtaining desired properties. AA2014 alloys were aged and upset to different strain levels, and a set of equations were

developed constituting the equivalent strain and hardness.

To optimize the heterogeneous distribution of the hardness inside the billet, HariKrishna et al. (2015) optimized the process parameters and suggested that billets with lower height to the diameter ratio and low friction will reduce the heterogeneity of hardness distribution. Experimental studies related to the solid cylindrical upsetting tests and ring compression tests were carried out, and the authors analyzed the hardness distribution inside the billets by employing different lubricants. Hardness variations near the dead zone areas, bulge head, and at various places were well explained (HariKrishna et al., 2016a, HariKrishna et al., 2016b). Pöhlandt et al. (1998) and Pöhlandt et al. (2006) derived the anisotropy ratios and analyzed the formability of the formed billets produced from drawing and extrusion operation. Chirala et al. (2017) and HariKrishna et al. (2018) studied the above reports, and the effect of anisotropy on the formability of the billets and hardness in upsetting was investigated. After thoroughly investigating the literature, the authors attempted the effect of anisotropy on the strain hardening behavior, which is not available in the literature. Since friction also plays a role in the bulging of the cylinders, a correlation is required between friction and anisotropy.

Pöhlandt et al. (2006) categorized the anisotropy into tangential-axial anisotropy and axial-radial anisotropy, but the effect of these anisotropy ratios was not clearly distinguished anywhere in the bibliography. Fewer studies were report related to the effect of anisotropy assuming  $R_{rz}=R_{tz}$ , but no clear indication of the effect of  $R_{rz}$  and  $R_{tz}$  on hardness. The issues reported here motivated the authors to work on the effect of  $R_{rz}$  and  $R_{tz}$  on strain hardening and hardness distribution inside the billets.

## 2. MATERIALS AND METHODS

### 2.1 Ring compression test

AA2014 melt at a pouring temperature of 750°C and flash of 3% and 6% was added to the matrix to make 3 sets of cast alloys. The fly ash mix was stirred at 700 rpm for better homogenization, and AA2014, AA2014+3% fly ash, and AA2014+6% fly ash solid rods of diameter 1 inch were obtained. The solid rods were turned to an outer diameter of 24 mm with a hole inside it of 12 mm and height of 8mm on the lathe machine. Thus, the samples are maintained at a size of 6:3:2 (Outer diameter: Inner diameter: height). To compare the friction variations, a ring compression test was carried out by employing soap, boric acid powder, and no lubricant in between H13 dies as illustrated in Figure. 1. Over the years green lubricants such as Boric acid and Soap have been used extensively as lubricant in the literature (Hari 2016c). These lubricants, such as boric acid, have excellent lubrication properties without requiring expensive disposal techniques (Erdemir 1991; Erdemir et al., 1991b).

The effectiveness of boric acid can be attributed to its low friction and shear strength values. Male (1964) developed a methodology to evaluate the friction prevailing at the die/billet interface. The friction factor is evaluated based on the dimensional changes of the ring compressed to different height reductions. The change in the hole diameter to the corresponding height reduction of the ring specimen is taken as a measurement.



**Figure 1.** Ring compression test performed under different friction conditions

A curve is plotted by joining all the points of the diametral change at each and every instant of height reduction, as illustrated in Figure. 2. To evaluate friction between the workpiece and the dies, the ring compression was carried out at incremental level of 10% reduction in height. At each and every stage of the deformation, the reduction in the height and change in the inner diameter of the ring was noted down. The ratio of the strain due to the height reduction and change in the diameter gives the friction factor at any level of deformation. The average value of all the ratios gives the friction factor for the lubricant applied at the die/billet interface. The normal pressure applied at the each and every height reduction is listed in Table.1

**Table 1.** Normal pressure applied at each and every level of deformation

% reduction in height	Force applied (KN)		
	m=0.2	m=0.5	m=0.55
10	102	108	109
20	135	150	151
30	182	193	197
40	220	247	252
50	307	359	362
60	417	556	563

An indication of good lubrication and poor lubrication is was also explained by Robinson et al. (2004) based on the contraction and expansion of hole diameter which are examples of good and poor lubrication. When there is no lubrication, the slope of the curve corresponding to the lubricant applied is positive, and this tendency can be observed in Figure. 2. When a good lubricant such as soap is applied, the slope of the curve is negative.

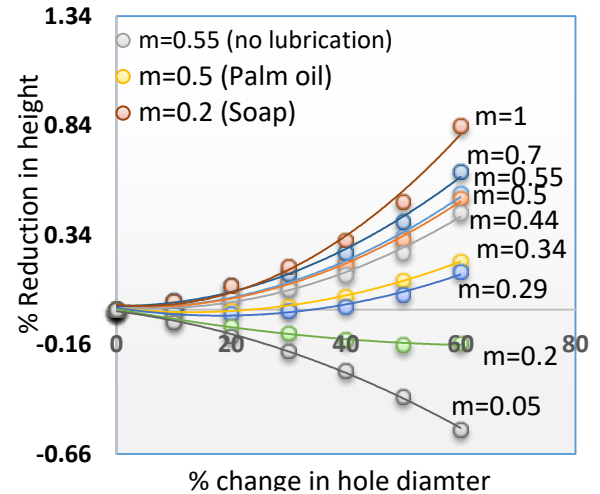


**Figure. 2** Male and Cockcroft calibration curves for different friction conditions.

Three sets of billets, namely AA2014, AA2014+3% fly ash, and AA2014+6% fly ash was made out of the stir casting technique (HariKrishna and Davidson, 2019). As illustrated in Figure. 3a, the cylinders undergo some distortion on the shape, and this causes anisotropy. For a deformed cylinder, the strains after deformations are given by

$$\text{Axial strain } \varepsilon_z = \ln\left(\frac{h}{h_0}\right) \quad (1)$$

$$\text{Circumferential strain } \varepsilon_t = \ln\left(\frac{w}{w_0}\right) \quad (2)$$

$$\text{Radial strain } \varepsilon_r = \ln\left(\frac{r}{r_0}\right) \quad (3)$$

$$\text{Tangential-axial anisotropy } R_{tz} = \frac{\varepsilon_z}{\varepsilon_t} \quad (4)$$

$$\text{Radial-axial anisotropy } R_{rz} = \frac{\varepsilon_z}{\varepsilon_r} \quad (5)$$

a)

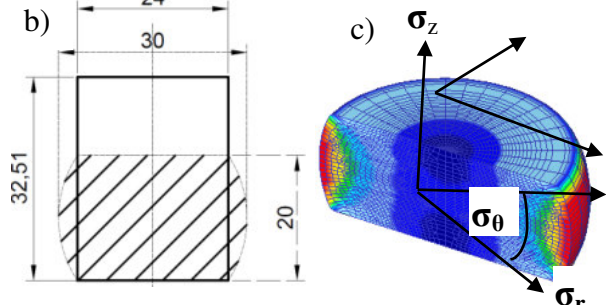
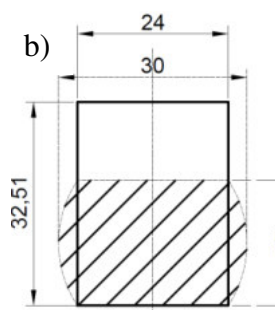


Figure 3a. Upset billets (a) i. AA2014 ii. AA2014+3% fly ash iii. AA2014+6% fly ash. b) Geometry of the

billet before and after deformation, and c) Upset billet representing anisotropy factor and stress planes.

In the cylindrical upsetting test, the maximum principal stress ( $\sigma_1$ ) is the circumferential stress, which is tensile in nature ( $\sigma_\theta$ ), and the minimum principal stress is ( $\sigma_2$ ) the axial stress ( $\sigma_z$ ). The parameters of anisotropy ( $R_0$ ,  $R_{90}$ ) are defined in 2 directions normal to each other. The anisotropy along the minor axis ( $R_0$ ) is equal to tangential-axial anisotropy ( $R_{rz}$ ), and the anisotropy along the major axis is the radial-axial anisotropy ( $R_{tz}$ ). To analyze the effect of anisotropy on strain hardening, Hills quadratic yield equation known as the Hosford-Backofen equation was considered. This equation holds good for analyzing the anisotropy factors, and it is equivalent to flow stress ( $\sigma_o$ ) (Hill, 1948).

$$\sigma_1^2 + \left(\frac{R_0(1+R_{90})}{R_0(1+R_{90})}\right) \sigma_2^2 - \left(\frac{2R_0}{(1+R_{90})}\right) \sigma_1 \sigma_2 \approx \sigma_o^2 \quad (6)$$

Rewriting the equation (11) in terms of axial stress, hoop stress and antitropy ratios as equation (12).

$$\sigma_1^2 + \left(\frac{R_{rz}(1+R_{tz})}{R_{tz}(1+R_{rz})}\right) \sigma_2^2 - \left(\frac{2R_{rz}}{(1+R_{tz})}\right) \sigma_1 \sigma_2 \approx \sigma_o^2 \quad (7)$$

$$\sigma_z^2 + \left(\frac{R_{rz}(1+R_{tz})}{R_{tz}(1+R_{rz})}\right) \sigma_\theta^2 - \left(\frac{2R_{rz}}{(1+R_{tz})}\right) \sigma_z \sigma_\theta \approx (K\epsilon)^{2n} \quad (8)$$

$$K = \left( \frac{1}{\epsilon} \sqrt{\sigma_z^2 + \left(\frac{R_{rz}(1+R_{tz})}{R_{tz}(1+R_{rz})}\right) \sigma_\theta^2 - \left(\frac{2R_{rz}}{(1+R_{tz})}\right) \sigma_z \sigma_\theta} \right)^n \quad (9)$$

## 2.2 Simulation studies for Upsetting

To predict the effective strain in the radial direction, it is necessary to conduct finite element simulations. Axisymmetric configuration of the cylindrical upsetting tests and ring compressions test were carried out for predicting the strain contours. The whole configuration was modeled axisymmetric, as illustrated in Figure. 4. Billet material was assumed plastic, and the die was modeled as rigid. The levels of deformation were similar to the experimental investigations. Ludwik-Hollomon equation derived from the solid cylindrical upsetting was given as input to the finite element software (HariKrishna and Davidson, 2019).

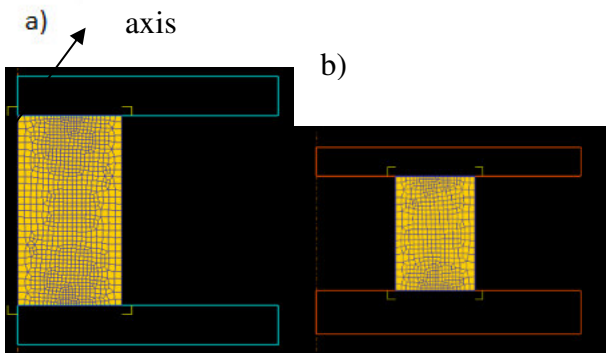


**Figure 4.** Axisymmetric modelling of (a) cylindrical upsetting and (b) ring compression test.

$$\sigma_o = K \epsilon^n \quad (10)$$

$$= 154 \epsilon^{0.25} \quad \text{for AA2014 cast alloy} \quad (11)$$

$$= 248 \epsilon^{0.21} \quad \text{for AA2014+3% fly ash} \quad (12)$$

$$= 379 \epsilon^{0.18} \quad \text{for AA2014+6% fly ash} \quad (12)$$

The hollomon equation is given as input to the finite element software and the strain distribution inside the billet is measured as illustrated in Figure. 5. Strain is measured in the radial direction (points: P1, P2, P3.....) from the center of the specimen towards bulge head of the barreled cylinder. The intensity of strain is more at the center and decreases gradually on moving towards the bulge head because of differential strain hardening (Narayanan 2008). On the top of the billet and at the center, the strain will be zero because of the existence of dead zone region.

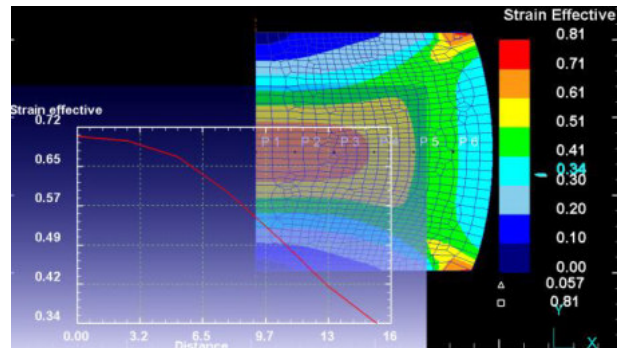


**Figure 5.** Strain Distribution at several zones inside the metallic axis symmetric cylinder.

It can be observed that the  $R_{rz}$  was low initially and starts raising as the level of strain increases. In the case of  $R_{tz}$ , the anisotropy is high initially and decreases slowly as the strain level decreases. Both the anisotropy ratios are increasing after reaching a strain level of more than 0.4. At first, the radial strain increases because of the increase in the magnitude of the radial stress, which is very much smaller in magnitude compared to hoop stress. This radial stress promotes axial-radial anisotropy. Hoops stress promotes tensile strain in the circumferential direction, and this required a much higher load for deformation compared to radial strain. Due to this reason, the hoop strain is initially smaller compared to radial strain, and the magnitude of the  $R_{tz}$  is decreasing in magnitude compared to  $R_{rz}$ . After reaching a threshold value of more than 0.4, the tensile nature of both the stresses ( $\sigma_r$ ,  $\sigma_\theta$ ) promotes higher tensile strains along the major axis and minor axis, resulting in the increase of anisotropy ratios.

To predict the effect of anisotropy on strain hardening coefficient ( $K$ ) with the increasing axial strain, a plot between  $K$  and  $\epsilon_z$  was plotted (Figure 6 & Figure 7). The increasing axial strain increased both the radial-axial anisotropy and tangential-axial anisotropy. The increase in the  $R_{rz}$  coefficient decreased the magnitude of the

strain hardening coefficient, and it is vice versa in the case of  $R_{tz}$ . This implies that an increase in the  $R_{tz}$  makes it hard to generate the required axial stress for deformation. The deformation becomes easier in the r-z plane compared to the t-z plane, and this is the reason for the variation in the strain hardening behaviour with the anisotropy ratios.

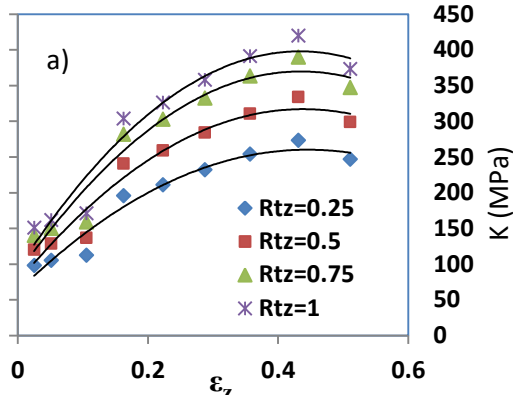


Figure. 6 Effect of anisotropy on the strain hardening coefficient.

## 5. CONCLUSIONS

The concept of the correlation between friction and anisotropy was well addressed. New lubricants that are environment friendly were used, and the friction factor corresponding to each lubricant was evaluated. The axial-tangential anisotropy has more effect on the strain hardening behavior compared to axial-radial anisotropy, and there is a threshold value of strain beyond which the  $R_{tz}$  is more predominant. The effect of anisotropy on the strain hardening coefficient was analyzed. Anisotropy in

the stress required for deformation easy. The increase in the tangential-anisotropy caused by the hoop stress

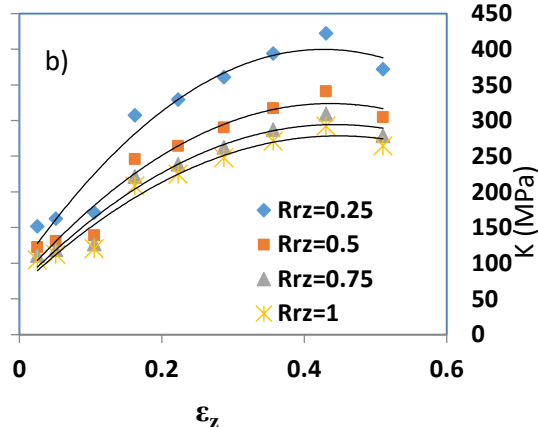


Figure. 7 Effect of anisotropy on the strain hardening coefficient.

conjunction with the friction and level of deformation will have negative effect on the anisotropy.

## References:

- Ananthanarayanan, R., Ahmed, Z., Prasad, A. & S. Narayan (2019). Strain hardening analysis and modelling of its parameters for sintered Al and Al-1% C preforms during cold upsetting. *Journal of Materials Research and Technology*, 8(5), 1789-1797. doi.org/10.1016/j.jmrt.2020.08.065
- Avitzur, B. 1968. Metal forming: processes and analysis, McGraw-Hill New York.
- Baskaran, K. & R. Narayanasamy (2008). An experimental investigation on work hardening behaviour of elliptical shaped billets of aluminium during cold upsetting. *Materials & Design*, 29(6), 1240-1265. doi.org/10.1016/j.matdes.2006.06.016.
- Chirala, H., Davidson, M., Srinivasarao, G. & P. Srinivasaraju (2017). Modeling of anisotropic behavior of aluminum alloys to investigate ductile fracture for the improved formability in the upsetting process. *Journal of Testing and Evaluation*, 46(3), 1054-1063. doi: 10.1520/JTE20160591
- Erdemir, A. (1991). Tribological properties of boric acid and boric-acid-forming surfaces. Part II: mechanisms of formation and self-lubrication films on boron- and boric oxide-containing surfaces. *Lubrication Engineering* 47, 179–184. doi.org/10.1016/j.triboint.2022.107541
- Erdemir, A., Fenske, G. R., Erck, R. A., Nicholas, F. A. & D. E. Busch (1991b). Tribological properties of boric acid

and boric-acid-forming surfaces. Part 1: crystal chemistry and mechanism of self-lubrication of boric acid. Argonne National Laboratory, Tribology section, Materials and components Technology Division, 1-21.

Hari Krishna, C., Davidson, M. & Nagaraju, C. (2017). Effect of aging on hardness in the upsetting tests using experimental and finite element investigations. *Proceedings of the Institution of Mechanical Engineers Part C: Journal of Mechanical Engineering Science*, 231(24), 4512-4520. doi:10.1177/0954406216671347

Harikrishna, C. & Davidson, M. (2019). Damage modeling and critical damage evaluation of AA2014 cast alloy embedded with fly ash composite under upsetting. *Proceedings of the Institution of Mechanical Engineers, Part C: Journal of Mechanical Engineering Science*, 233(15), 5227-5236. doi: 10.1177/0954406219844285

Harikrishna, C., Davidson, M. & Nagaraju, C. (2015). Optimum Process Parameters for Enhanced Uniform Hardness Distribution and Barreling Behavior in Upsetting. *Transactions of the Indian Institute of Metals*, 68(2), 219-228. doi: 10.1007/s12666-014-0447-y.

Harikrishna, C., Davidson, M., Nagaraju, C. & Anil Kumar, B. (2016a). Effect of lubrication on hardness in the ring compression test. *Proceedings of the Institution of Mechanical Engineers, Part C: Journal of Mechanical Engineering Science*, 230(12), 1939-1950. doi:10.1177/0954406215586590.

Harikrishna, C., Davidson, M., Nagaraju, C. & A. Ratnaprasad (2016b). Effect of lubrication and anisotropy on hardness in the upsetting test. *Transactions of the Indian Institute of Metals*, 69(7), 1449-1457. doi:10.1177/0954406215586590

Harikrishna, C., Davidson, M., Nagaraju, C., Srinivasa Rao, G. & Srinivasarao, P. (2016c). Effect of adhesion and cohesion on the ductile fracture in upsetting. *Journal of Testing and Evaluation*. 44(2), 983-994. doi: 10.1520/JTE20150320

Harikrishna, C., Davidson, M., Nagaraju, C., Srinivasa Rao, G. & Srinivasa Raju, P. (2018). Modeling of anisotropic behavior to investigate the effect of hardness on AA2014 aluminum alloys under upsetting. *Proceedings of the Institution of Mechanical Engineers, Part C: Journal of Mechanical Engineering Science*, 232(21), 3797-3806. doi.org/10.1177/095440621774293

Harikrishna, C., Davidson, M., Nagaraju, C., Srinivasa Rao, G. & Srinivasa Raju, P. (2020). Analysis of anisotropy in the upsetting process of AA2014 cast alloy embedded with fly ash. *Proceedings of the Institution of Mechanical Engineers, Part C: Journal of Mechanical Engineering Science*, 234(14), 2833-2841. doi: 10.1177/0954406220911389

Harikrishna, C. & C. Nagaraju (2021). Modeling of cylindrical upsetting process for enhanced ductile fracture. *Materials Today: Proceedings*, 24(4), 1629-1634. doi:10.1016/j.matpr.2020.05.767

Harikrishna, C., Davidson, M., Malleswararao BN, K. Obulareddy (2023). Hardness prediction in the upsetting process of Al%ZrO<sub>2</sub>—an approach to machine learning using regression and classification models. *Transactions of the Canadian Society for Mechanical Engineering*, doi: 10.1139/tcsme-2023-0063.

Hill, R. 1948. A theory of the yielding and plastic flow of anisotropic metals. *Proceedings of the Royal Society of London. Series A. Mathematical and Physical Sciences*, 193, 281-297. doi.org/10.1098/rspa.1948.0045

Inigoraj, A., Narayanasamy, R. & K. Pandey (1998). Strain-hardening behaviour in sintered aluminium–3.5% alumina composite preforms during axial compression with and without annealing. *Journal of Materials Processing Technology*, 84(1-3), 143-148. doi: 10.1016/S0924-0136(98)00089-2.

Krishna, C. H., Davidson, M. & C. Nagaraju (2015). Investigation of work hardening behavior and failure analysis of billets due to biaxial stresses in simple upsetting process. *The International Journal of Advanced Manufacturing Technology*, 79, 2017-2030. doi: 10.1007/s00170-015-6948-y

Male, A. (1964). A method for the determination of the coefficient of friction of metals under conditions of bulk plastic deformation. *Journal of Institute of Metals*. 93, 38. doi:10.1016/0043-1648(66)90161-x

Narayanan, R. G., Gopal, M. & A. Rajadurai (2008). Influence of friction in simple upsetting and prediction of

hardness distribution in a cold forged product. *Journal of Testing and Evaluation*, 36(4), 371-383. doi: 10.1520/JTE101443

Pöhlandt, K., Lange, K. & M. Zucko (1998). Concepts and experiments for characterizing plastic anisotropy of round bars, wires and tubes. *Steel research*, 69(4-5), 170-174. doi: 10.1002/srin.199801468.

Pöhlandt, K., Lange, K. & M. Zucko (2006). Effects of anisotropy in drawing and extrusion processes of bulk metal forming. *Steel research international*, 77(1), 49-53. doi:10.1002/srin.200606130.

Robinson, T., Ou, H. & Armstrong, C. G. (2004). Study on ring compression test using physical modelling and FE simulation. *Journal of Materials Processing Technology*, 153, 54-59. doi: 10.1016/j.jmatprotec.2004.04.045.

Sofuooglu, H., Gedikli, H. & J. Rasty (2001). Determination of friction coefficient by employing the ring compression test. *Journal of Engineering Materials and Technology*, 123(3), 338-348. doi:10.1115/1.1369601

Sonmez, F. O. & Demir, A. (2007). Analytical relations between hardness and strain for cold formed parts. *Journal of materials processing technology*, 186(1-3), 163-173. doi:10.1016/j.jmatprotec.2006.12.031

---

**Harikrishna Ch**

Department of Mechanical Engineering,  
Shri Vishnu Engineering College for  
Women, Vishnupur, Bhimavaram,  
India, 534202  
[harinitw@gmail.com](mailto:harinitw@gmail.com)

[ORCID: 0000-0002-3055-3314](#)

**Srinivasaraju Perecherla**

Department of Mechanical Engineering,  
Shri Vishnu Engineering College for  
Women, Vishnupur, Bhimavaram,  
India, 534202

[viceprincipal@svecw.edu.in](mailto:viceprincipal@svecw.edu.in)

[ORCID: 0000-0002-1309-5796](#)

**VarunChandra Samudrala**

Chaitanya Bharati Institute of  
Technology, Hyderabad,  
India  
[varuncnitw@gmail.com](mailto:varuncnitw@gmail.com)

**N Malleswararao Battina**

Department of Mechanical Engineering,  
Shri Vishnu Engineering College for  
Women, Vishnupur, Bhimavaram,  
India, 534202

[malleswararaobn@svecw.edu.in](mailto:malleswararaobn@svecw.edu.in)

[ORCID: 0000-0002-1378-2350](#)

**Murahari kolli**

Department of Mechanical Engineering,  
Lakkireddy Balireddy College of  
Engineering, Mylavaram, India, 521230  
[kmhari.nitw@gmail.com](mailto:kmhari.nitw@gmail.com)

ORCID: 0000-0002-2005-6234

**Srinivasarao Gajula**

Department of Mechanical Engineering,  
Shri Vishnu Engineering College for  
Women, Vishnupur, Bhimavaram,  
India, 534202

[principal@svecw.edu.in](mailto:principal@svecw.edu.in)

[ORCID: 0000-0001-9523-9986](#)

---



## Non-linearity parameter B/A and available volume Va of binary liquid mixtures: thermo-acoustical approach

Srinivasu J.V.<sup>1</sup>

Narendra K.

Kavitha Ch.

Srinivasa Krishna T.

Keywords:

Available volume; thermoacoustical parameter; 1,4-butanediol; cresol; non-linearity parameter..

### A B S T R A C T

When high amplitude sound waves propagate through liquid mixtures, various non-linear phenomena can occur, and ultrasonic research in these systems can reveal important details about their structure and interaction. Thermoacoustical parameters have been calculated for a binary system containing 1,4-butanediol(1,4-BD) + o-cresol(OC) or m-cresol (MC) or p-cresol(PC) at varying concentrations and temperatures ranging from 303.15 to 318.15 K. These parameters have been used to calculate available volume by using two different approaches. The results of both methods are used to examine the existence and intensity of interactions between the molecules in the systems under study. Additionally, several methods have also been used to derive the non-linearity parameter, or B/A. The excess values of B/A have also been calculated. In order to determine whether molecular interactions exist, a comparison analysis was conducted.

© 202x Published by Faculty of Engineeringg



### 1. INTRODUCTION

When researching various thermodynamic properties and intermolecular interactions, the quantity known as accessible volume, or  $V_a$ , is highly helpful. It is simply estimable using the characteristics of thermos-acoustics. The B/A parameter can reveal information about the medium's structural characteristics and calculates the nonlinear adjustment to velocity resulting from nonlinear effects brought on by the propagation of a finite amplitude wave (Hartman 1979; Beyer 1960; Sehgal 1995; Thakur 1978; Bjorno 2002; Duck 2002). A review of the literature indicates that there have been fewer attempts to use thermos-acoustical characteristics in pure liquids and liquid mixtures to determine  $V_a$ , the non-linearity parameter, and B/A. There are two principal methods for determining the nonlinearity

parameter B/A: The measurement of the amplitude of the second harmonic produced by the propagating sinusoidal wave's distortion is the basis of the finite amplitude approach. (Krishna et al., 2021; Aditi Prabhune et al., 2022; Nain 2022). Density, sound velocity, absolute temperature, specific heat capacity at constant pressure, and volume coefficient of thermal expansion are the foundations of the thermodynamic approach. Many scholars have estimated the non-linearity parameter of binary and multicomponent liquid mixtures (Bhatia et al., 2011; Pandey et al., 2000; Anjali et al., 2017). This encourages us to continue our study in order to use thermos-acoustical characteristics to compute  $V_a$  and B/A in pure liquids and liquid mixtures at different temperatures and link the results with those derived from thermodynamic relations. The

<sup>1</sup> Corresponding author: Srinivasu J.V.  
Email: [srinivas.jaddu@gmail.com](mailto:srinivas.jaddu@gmail.com)

computation's required data were extracted from our earlier work (Srinivasu 2017).

## 2. PROCEDURE

**Materials:** The Cresols and 1,4-butanediol were of the Chemlab (purity 0.99) variety. Standard techniques were employed to further purify these (Vogel 1989; Riddick 1986). To lower the water content, all of the compounds were carefully dried over 0.4 nm molecular sieves for 72 hours while being securely sealed off from ambient pressure. A vacuum pump was used to partially degas each liquid before any experimental observations were made. With an accuracy of  $\pm 0.1$  mg, the weights were measured using an electronic balance.

### 2.1 Apparatus and methods

A Borosil glass single-capillary pycnometer was used to measure liquid densities. The capillary included graded markings, a consistent diameter, and a glass cap that fit snugly to seal it shut. Triple-distilled water was used to calibrate the capillary markings. The densities of pure water were obtained from the literature at the necessary temperature (Stokes 1965). The density measurements were repeatable to within an error of  $\pm 2 \times 10^{-5}$  g.cm<sup>-3</sup>. The temperature of a thermostatically controlled, well-stirred water bath was maintained at  $\pm 0.02$ K during the experimental procedures. Using a single-crystal ultrasonic interferometer (Mittal Enterprises, India) running at a frequency of 2 MHz, the sound speeds at various temperatures were measured. Using a high frequency generator, the quartz crystal, which was fixed at the bottom of the measuring cell, was excited at its resonance frequency to create sound waves in the test liquid inside the cell that had a frequency of 2 MHz. There was a micrometer located at the cell's top. The wavelength of the sound waves was measured by measuring the distance that a metallic reflector plate covered between consecutive resonance peaks. The metallic reflector plate may be elevated or lowered through a known distance in the test liquid. Water from a thermostatically controlled water bath was circulated through the water jacketed cell to keep the solution's temperature constant. The accuracy of the speed readings was within  $\pm 0.2$  m s<sup>-1</sup>.

### 2.2 Theory

The following relations can be used to get the reduced volume ( $V$ ), Molalwyn-Hughes parameter ( $C_1$ ), and Sharma parameter ( $S^*$ ) from the thermal expansivity ( $\alpha$ ) and absolute temperature ( $T$ ):

$$\hat{V} = \left[ 1 + \frac{\alpha T}{3(1+\alpha T)} \right]^3 \quad - \quad (1)$$

$$C_1 = \frac{13}{3} + \frac{1}{\alpha T} + \frac{4}{3} \alpha T \quad - \quad (2)$$

$$S^* = 1 + \frac{4\alpha T}{3} \quad - \quad (3)$$

The coefficient of internal pressure ( $X$ ) at isochoric temperature has been calculated using the following relation:

$$X = \frac{-2(1+2\alpha T)}{\bar{v} C_1} \quad - \quad (4)$$

The isobaric acoustical parameter ( $K$ ), isothermal acoustical parameter ( $K'$ ), and isochoric acoustical parameter ( $K''$ ) can be computed using the values of  $S^*$ , and  $X$ .

$$K = \frac{1}{2} \left[ 1 + \frac{S^*(1+\alpha T)}{\alpha T} \right] \quad - \quad (5)$$

$$K' = \frac{1}{2} \left[ 3 + \frac{S^*(1+\alpha T)+X}{\alpha T} \right] \quad - \quad (6)$$

$$K'' = 1 + \frac{X}{2\alpha T} \quad - \quad (7)$$

The thermo-acoustical parameter  $K'$  can be used to calculate the accessible volume as follows:

$$V_a = \frac{V_m}{K'+1} \quad - \quad (8)$$

The relation can be used to compute accessible volume using the thermodynamic relation and the critical temperature:

$$V_a = V - \left[ V \left( 1 - \frac{T}{T_c} \right)^{0.3} \right] \quad - \quad (9)$$

It is necessary to employ the coefficient of thermal expansion,  $\gamma$ , and isothermal compressibility,  $T$ , in order to calculate the non-linearity parameter,  $B/A$ .

The following equation is used to calculate  $\beta_T$ ,

$$\beta_T = \frac{1.71 \times 10^{-3}}{T^{4/9} u^2 \rho^{4/3}} \quad - \quad (10)$$

where  $u$ ,  $\rho$  and  $T$  are the ultrasonic velocity, density and temperature of the liquid system respectively.

Using the expression for the sound velocity  $u$ , the non-linearity parameter is further generalized in terms of the acoustical characteristics of liquids by adding the contributions from the isobaric and isochoric acoustic parameters,  $K$  and  $K''$ .

The expression for  $B/A$  can be expressed as,

$$B/A = 2K + 2\gamma K''$$

$$(B/A)_{\text{thermoacoustical(I)}} = 2K + 2\gamma(i)K'' \quad - \quad (11)$$

where  $\gamma(i) = \beta_{T(0)} / \beta_s$

$$B/A = 2K + 2\gamma K''$$

$$(B/A)_{\text{thermoacoustical(II)}} = 2K + 2\gamma(ii)K'' \quad - \quad (12)$$

where

$$\gamma(ii) = \alpha \Gamma T + 1$$

where  $\Gamma$ , the pseudo Gruneisen parameter, has been computed using,

$$\Gamma = \frac{2}{3} \alpha T + \frac{3+4\alpha T}{2\alpha T}$$

Hartmann and Balizer obtained the following relation for  $B/A$ :

$$\frac{B}{A} = 2 + \frac{0.98 \times 10^4}{u} \quad - \quad (13)$$

where  $u$  is in m/s.

An empirical relation proposed by Ballou is given by,

$$\frac{B}{A} = -0.5 + \frac{1.2 \times 10^4}{u} \quad - \quad (14)$$

The excess values of nonlinearity parameter  $(B/A)^E$  are calculated by the relation:

$$(B/A)^E = (B/A)_{\text{mix}} - (B/A)_{\text{ideal}} \quad - \quad (15)$$

$$(B/A)_{\text{ideal}} = \sum_{i=1}^n X_i \left( \frac{B}{A} \right)_i \quad - \quad (16)$$

where,  $X_i$  is the mole fraction of pure components.

### 3. RESULTS AND DISCUSSION

Table 1 displays the computed values of the following: isobaric acoustical parameter, K; isothermal acoustical parameter, K'; reduced volume, V'; Moelwyn-Hughes parameter, C1; Sharma parameter, S\*; isochoric temperature coefficient of internal pressure, X; isobaric acoustical parameter, K; and isochoric acoustical parameter, K''. Table 2 displays the accessible volume (Va) values that were determined using the two approaches. Table 3 displays the non-linearity parameter, B/A, which was determined using equations (11) through (14). Table 4 lists the values of the following parameters: isochoric thermo-acoustical parameter,  $\Delta$ , isothermal Gruneisen parameter,  $\Gamma_{ith}$ , isochoric Gruneisen parameter,  $\Gamma_{ich}$ , isobaric Gruneisen parameter,  $\Gamma_{iba}$ , isothermal Anderson-Gruneisen parameter,  $\delta$ , and reduced bulk modulus, B.

A detailed examination of Table 1 shows that in all three systems, the values of V' are nearly increasing with temperature and decreasing with mole fraction of 1,4-BD.

As a stringent test for equation of state for liquids and solids, Moelwyn-Hughes established the dimensionless thermodynamic parameter C1, which is defined as the pressure coefficient of bulk modulus. In certain materials, this value provides the most straightforward scale for determining molecular ordering, structure, inter-chain, and anharmonicity. The C1 behaves in a completely different way from  $\alpha$ .

For each of the three systems, it is found that the values of the Sharma parameter, S\*, decrease as the mole fraction increases and increase as the temperature rises. The isochoric temperature coefficient of internal pressure has negative computed values for quantity X. X's absolute values vary from roughly 0.199 to 0.331. It is shown that the negative values rise with rising temperatures and fall with rising mole fractions. For all three of the systems, the same pattern is seen.

It is found that as the mole fraction of 1,4-BD increases, the isobaric and isothermal acoustical characteristics increase and decrease with temperature. On the other hand, it is noticed that the values of the isochoric acoustical parameter increase with temperature and decrease with mole fraction. Table 2 shows that the accessible volume increases as the temperature rises. It results from a decrease in intermolecular attraction and an increase in molecular mobility. Va results obtained using the two methods appear to be quite consistent. There is the greatest agreement at T=303.15K. These findings demonstrate how the thermoacoustical parameter can be used to calculate accessible volume in both pure liquids and liquid mixtures.

**Table 1.** The following parameters were measured as a functions of mole fraction 1,4-BD at four different temperatures: Thermal expansivity,  $\alpha$ , Molar volume,  $V_m$ , Reduced volume,  $\hat{V}$ , Moelwyn-Hughes parameter,  $C_1$ , Sharma

A consistent drop in accessible volume is shown with a rise in the mole percentage of 1,4-butanediol, as shown in Figures 1, 2, and 3. The reason for this is that 1,4-butanediol's accessible volume is smaller than that of o-, m-, or p-cresol. This study sheds insight on two strategies for determining available volume: one involves measuring thermo-acoustical characteristics in binary mixes. It is observed that the current method for calculating available volume is straightforward and accurate, offering a new avenue for the purposeful investigation of available volume in liquid mixtures (Narendra 2022). Data from aqueous solutions of both organic and inorganic substances indicate that B/A depends on the solute's molecular structure and the chemical makeup of the solution (Apfel 1989; Sehgal et al. 1986; Coppens et al., 1965). The amount that represents the degree of liquid hardness has been determined by interpreting the B/A values for the liquids. When the concentration of 1,4-BD increases, the values of B/A computed using Hartmann and Ballou relations exhibit a declining trend, as can be seen by closely examining the data in Table 3.

Table 3, when closely examined, indicates that the following pattern can be seen in the variations of the computed values of B/A from thermo-acoustical methods, Hartmann relation, and Ballou relation: 1,4-BD+o-cresol < 1,4-BD+p-cresol < 1,4-BD+m-cresol. The same table also shows that the B/A values for thermo-acoustical methods increase with an increase in the mole fraction of 1,4-BD. The interaction between the components of the binary mixes is stronger at lower concentrations of 1,4-BD and decreased at higher values.

Figs. 4 to 6 display the excess values of B/A for various models at 303.15K for each of the three systems. It can be shown from Figs. 4 to 6 that, in comparison to the other two models, the thermoacoustical models have larger negative excess B/A values. For 1,4-BD+p-cresol combinations, the excess B/A values are observed to be positive and negative for models H & B and Ballou, but they are observed to be negative for the other two systems. As a measure of the anharmonicity of molecular vibrations, the Gruneisen parameter is a significant quantity of current interest that has proven to be highly helpful in the investigation of the internal structure, molecular order, and other thermo-acoustic features. Table 4 shows that as the mole fraction of 1,4-BD increases, the values of the reduced bulk modulus and Gruneisen parameters increase while the isochoric thermo-acoustic parameter decreases. For each of the three systems, the same pattern is seen. The same table also shows that, for a given mole percentage, values for the Gruneisen and decreased bulk modulus fall with increasing temperature, while values for the isochoric thermo-acoustic parameter increase.

Parameter, S\*, isochoric temperature coefficient of internal pressure, X, isobaric acoustical parameter, K, isothermal acoustical parameter, K' and isochoric acoustical parameter, K''

$x_1$	$\alpha (10^3)$	$V_m (10^6)$	$\hat{V} (10^6)$	$C_1$	$S^*$	$X$	$K$	$K'$	$K''$
1,4-butanediol + o-cresol									
T= 303.15K									
0.0000	1.032	104.32	1.258	7.954	1.417	-0.325	3.473	3.954	0.480
0.1001	0.976	102.67	1.246	8.113	1.395	-0.315	3.553	4.021	0.468
0.2001	0.921	101.08	1.234	8.295	1.372	-0.304	3.644	4.099	0.455
0.3002	0.865	99.52	1.222	8.503	1.350	-0.293	3.748	4.189	0.441
0.4002	0.809	97.99	1.210	8.742	1.327	-0.282	3.868	4.294	0.426
0.5002	0.754	96.48	1.198	9.020	1.305	-0.270	4.007	4.417	0.410
0.6002	0.698	94.98	1.185	9.346	1.282	-0.257	4.170	4.563	0.393
0.7002	0.643	93.50	1.172	9.732	1.260	-0.244	4.363	4.738	0.375
0.8001	0.587	92.05	1.159	10.196	1.237	-0.230	4.595	4.950	0.355
0.9001	0.532	90.63	1.145	10.761	1.215	-0.215	4.877	5.211	0.334
1.0000	0.476	89.28	1.131	11.462	1.192	-0.199	5.228	5.539	0.311
T= 308.15K									
0.0000	1.027	104.90	1.260	7.922	1.422	-0.327	3.458	3.941	0.483
0.1001	0.980	103.24	1.250	8.054	1.403	-0.319	3.524	3.996	0.472
0.2001	0.933	101.62	1.240	8.202	1.383	-0.310	3.598	4.059	0.461
0.3002	0.886	100.03	1.230	8.368	1.364	-0.300	3.681	4.130	0.450
0.4002	0.839	98.46	1.220	8.555	1.345	-0.291	3.774	4.211	0.437
0.5002	0.791	96.91	1.209	8.766	1.325	-0.281	3.880	4.304	0.424
0.6002	0.744	95.38	1.198	9.006	1.306	-0.270	4.000	4.410	0.411
0.7002	0.697	93.87	1.187	9.281	1.286	-0.259	4.137	4.533	0.396
0.8001	0.650	92.39	1.176	9.599	1.267	-0.248	4.296	4.677	0.381
0.9001	0.603	90.93	1.165	9.969	1.248	-0.236	4.481	4.846	0.364
1.0000	0.556	89.51	1.154	10.405	1.228	-0.224	4.699	5.046	0.347
T= 313.15K									
0.0000	1.021	105.37	1.262	7.894	1.426	-0.329	3.444	3.929	0.485
0.1001	0.983	103.72	1.254	8.000	1.410	-0.322	3.497	3.973	0.477
0.2001	0.944	102.09	1.246	8.116	1.394	-0.315	3.555	4.022	0.468
0.3002	0.906	100.48	1.238	8.243	1.378	-0.307	3.618	4.077	0.458
0.4002	0.868	98.88	1.229	8.382	1.362	-0.300	3.688	4.137	0.449
0.5002	0.829	97.31	1.221	8.536	1.346	-0.292	3.765	4.203	0.439
0.6002	0.791	95.76	1.212	8.707	1.330	-0.283	3.850	4.278	0.428
0.7002	0.753	94.23	1.203	8.896	1.314	-0.275	3.945	4.362	0.417
0.8001	0.715	92.72	1.194	9.107	1.298	-0.266	4.050	4.456	0.405
0.9001	0.676	91.24	1.185	9.344	1.282	-0.257	4.169	4.562	0.393
1.0000	0.638	89.78	1.176	9.612	1.266	-0.248	4.302	4.683	0.380
T= 318.15K									
0.0000	1.015	105.88	1.264	7.867	1.431	-0.331	3.430	3.918	0.488
0.1001	0.985	104.22	1.258	7.948	1.418	-0.325	3.470	3.951	0.481
0.2001	0.956	102.58	1.252	8.033	1.406	-0.320	3.513	3.988	0.474
0.3002	0.926	100.95	1.245	8.126	1.393	-0.314	3.560	4.027	0.467
0.4002	0.897	99.33	1.239	8.225	1.380	-0.308	3.609	4.069	0.460
0.5002	0.867	97.74	1.232	8.331	1.368	-0.302	3.662	4.115	0.452
0.6002	0.838	96.17	1.226	8.447	1.355	-0.296	3.720	4.164	0.444
0.7002	0.808	94.62	1.219	8.571	1.343	-0.290	3.782	4.218	0.436
0.8001	0.779	93.10	1.212	8.706	1.330	-0.283	3.849	4.277	0.428
0.9001	0.749	91.58	1.205	8.852	1.318	-0.277	3.923	4.342	0.419
1.0000	0.720	90.08	1.198	9.011	1.305	-0.270	4.002	4.413	0.410
1,4-butanediol + m-cresol									
T= 303.15K									
0.0000	0.796	105.43	1.198	9.009	1.306	-0.270	4.001	4.412	0.411
0.0992	0.764	103.70	1.190	9.202	1.292	-0.262	4.098	4.498	0.400
0.1986	0.732	102.02	1.183	9.405	1.279	-0.255	4.199	4.589	0.390
0.2982	0.700	100.35	1.176	9.619	1.266	-0.247	4.306	4.686	0.380
0.3979	0.668	98.71	1.169	9.843	1.254	-0.240	4.418	4.788	0.370

0.4979	0.636	97.09	1.162	10.079	1.243	-0.233	4.536	4.896	0.360
0.5979	0.604	95.48	1.155	10.327	1.232	-0.226	4.660	5.010	0.350
0.6982	0.572	93.89	1.149	10.589	1.221	-0.219	4.791	5.131	0.340
0.7986	0.540	92.32	1.143	10.864	1.211	-0.212	4.929	5.259	0.331
0.8992	0.508	90.78	1.137	11.155	1.202	-0.205	5.074	5.395	0.321
1.0000	0.476	89.28	1.131	11.462	1.192	-0.199	5.228	5.539	0.311
<b>T= 308.15K</b>									
0.0000	0.798	105.82	1.212	8.716	1.330	-0.283	3.855	4.282	0.427
0.0992	0.774	104.11	1.205	8.861	1.317	-0.276	3.927	4.346	0.419
0.1986	0.750	102.42	1.198	9.012	1.305	-0.270	4.002	4.413	0.410
0.2982	0.726	100.75	1.192	9.167	1.294	-0.264	4.080	4.482	0.402
0.3979	0.702	99.09	1.186	9.327	1.283	-0.258	4.160	4.554	0.394
0.4979	0.678	97.45	1.180	9.493	1.273	-0.252	4.243	4.629	0.386
0.5979	0.653	95.83	1.174	9.664	1.264	-0.246	4.328	4.706	0.378
0.6982	0.629	94.22	1.169	9.840	1.254	-0.240	4.417	4.787	0.370
0.7986	0.605	92.63	1.164	10.022	1.245	-0.235	4.508	4.870	0.362
0.8992	0.580	91.06	1.158	10.211	1.237	-0.229	4.602	4.957	0.355
1.0000	0.556	89.51	1.154	10.405	1.228	-0.224	4.699	5.046	0.347
<b>T= 313.15K</b>									
0.0000	0.802	106.29	1.225	8.456	1.354	-0.296	3.725	4.168	0.444
0.0992	0.786	104.58	1.219	8.563	1.344	-0.290	3.778	4.215	0.437
0.1986	0.769	102.88	1.214	8.672	1.333	-0.285	3.833	4.263	0.430
0.2982	0.753	101.21	1.208	8.783	1.324	-0.280	3.888	4.312	0.423
0.3979	0.737	99.54	1.203	8.896	1.314	-0.275	3.945	4.361	0.417
0.4979	0.720	97.88	1.198	9.011	1.305	-0.270	4.002	4.412	0.410
0.5979	0.704	96.24	1.193	9.127	1.297	-0.265	4.060	4.464	0.404
0.6982	0.688	94.60	1.189	9.245	1.289	-0.261	4.119	4.517	0.398
0.7986	0.671	92.98	1.184	9.366	1.281	-0.256	4.179	4.571	0.392
0.8992	0.655	91.37	1.180	9.488	1.274	-0.252	4.241	4.627	0.386
1.0000	0.638	89.78	1.176	9.612	1.266	-0.248	4.302	4.683	0.380
<b>T= 318.15K</b>									
0.0000	0.805	106.69	1.238	8.232	1.380	-0.308	3.612	4.072	0.459
0.0992	0.797	104.98	1.234	8.309	1.371	-0.304	3.651	4.105	0.454
0.1986	0.788	103.30	1.229	8.386	1.362	-0.299	3.690	4.138	0.449
0.2982	0.780	101.62	1.225	8.463	1.354	-0.295	3.728	4.172	0.443
0.3979	0.771	99.95	1.220	8.541	1.346	-0.291	3.767	4.206	0.438
0.4979	0.763	98.29	1.216	8.619	1.338	-0.288	3.806	4.240	0.433
0.5979	0.754	96.63	1.212	8.697	1.331	-0.284	3.845	4.274	0.429
0.6982	0.746	94.98	1.209	8.776	1.324	-0.280	3.884	4.308	0.424
0.7986	0.737	93.34	1.205	8.854	1.318	-0.277	3.924	4.343	0.419
0.8992	0.729	91.70	1.202	8.932	1.311	-0.273	3.963	4.378	0.415
1.0000	0.720	90.08	1.198	9.011	1.305	-0.270	4.002	4.413	0.410
<b>1,4-butanediol + p-cresol</b>									
<b>T= 303.15K</b>									
0.0000	1.032	105.33	1.258	7.954	1.417	-0.325	3.473	3.954	0.481
0.0961	0.979	103.68	1.247	8.107	1.396	-0.315	3.550	4.018	0.469
0.1931	0.925	102.04	1.235	8.281	1.374	-0.305	3.637	4.093	0.456
0.2909	0.870	100.42	1.224	8.482	1.352	-0.294	3.738	4.180	0.442
0.3895	0.815	98.80	1.212	8.715	1.330	-0.283	3.854	4.282	0.427
0.4890	0.760	97.19	1.199	8.987	1.307	-0.271	3.990	4.402	0.412
0.5894	0.704	95.59	1.186	9.308	1.285	-0.258	4.151	4.546	0.395
0.6907	0.648	93.99	1.173	9.693	1.262	-0.245	4.343	4.720	0.377
0.7929	0.591	92.40	1.160	10.159	1.239	-0.231	4.576	4.933	0.357
0.8960	0.534	90.83	1.146	10.735	1.216	-0.215	4.864	5.199	0.335
1.0000	0.476	89.28	1.131	11.462	1.192	-0.199	5.228	5.539	0.311
<b>T= 308.15K</b>									
0.0000	1.027	105.77	1.260	7.922	1.422	-0.327	3.458	3.941	0.483
0.0961	0.982	104.12	1.251	8.049	1.403	-0.319	3.521	3.994	0.473
0.1931	0.936	102.48	1.241	8.191	1.385	-0.310	3.592	4.055	0.462

0.2909	0.890	100.84	1.231	8.352	1.366	-0.301	3.673	4.123	0.451
0.3895	0.844	99.21	1.221	8.534	1.347	-0.292	3.764	4.202	0.439
0.4890	0.797	97.58	1.210	8.741	1.327	-0.282	3.867	4.293	0.426
0.5894	0.749	95.95	1.200	8.978	1.308	-0.271	3.986	4.398	0.412
0.6907	0.702	94.33	1.189	9.253	1.288	-0.260	4.123	4.521	0.398
0.7929	0.654	92.72	1.177	9.574	1.269	-0.249	4.284	4.666	0.382
0.8960	0.605	91.11	1.166	9.953	1.249	-0.237	4.473	4.838	0.365
1.0000	0.556	89.51	1.154	10.405	1.228	-0.224	4.699	5.046	0.347
<b>T= 313.15K</b>									
0.0000	1.021	106.13	1.262	7.894	1.426	-0.329	3.444	3.929	0.485
0.0961	0.984	104.49	1.255	7.996	1.411	-0.322	3.494	3.972	0.477
0.1931	0.947	102.86	1.247	8.107	1.395	-0.315	3.550	4.019	0.468
0.2909	0.910	101.22	1.238	8.231	1.380	-0.308	3.612	4.071	0.459
0.3895	0.872	99.59	1.230	8.367	1.364	-0.300	3.680	4.130	0.450
0.4890	0.834	97.95	1.222	8.518	1.348	-0.293	3.756	4.196	0.440
0.5894	0.795	96.32	1.213	8.688	1.332	-0.284	3.840	4.270	0.429
0.6907	0.756	94.68	1.204	8.877	1.316	-0.276	3.935	4.353	0.418
0.7929	0.717	93.05	1.195	9.091	1.300	-0.267	4.042	4.448	0.406
0.8960	0.678	91.41	1.186	9.334	1.283	-0.257	4.164	4.557	0.394
1.0000	0.638	89.78	1.176	9.612	1.266	-0.248	4.302	4.683	0.380
<b>T= 318.15K</b>									
0.0000	1.015	106.62	1.264	7.867	1.431	-0.331	3.430	3.918	0.488
0.0961	0.987	104.99	1.258	7.944	1.419	-0.326	3.469	3.950	0.481
0.1931	0.958	103.35	1.252	8.027	1.406	-0.320	3.510	3.985	0.475
0.2909	0.929	101.71	1.246	8.117	1.394	-0.315	3.555	4.023	0.468
0.3895	0.900	100.06	1.240	8.214	1.382	-0.309	3.604	4.064	0.461
0.4890	0.871	98.41	1.233	8.319	1.369	-0.303	3.656	4.109	0.453
0.5894	0.841	96.75	1.226	8.434	1.357	-0.297	3.714	4.159	0.445
0.6907	0.811	95.09	1.219	8.559	1.344	-0.291	3.776	4.213	0.437
0.7929	0.781	93.43	1.213	8.695	1.331	-0.284	3.844	4.273	0.429
0.8960	0.751	91.76	1.205	8.846	1.318	-0.277	3.919	4.339	0.420
1.0000	0.720	90.08	1.198	9.011	1.305	-0.270	4.002	4.413	0.410

**Table 2.** Available volume, **Va**, in binary liquid mixtures as a function of mole fraction 1,4-BD at four different temperatures.

$x_1$	$V_a (10^{-6}) \text{ m}^3 \text{ mol}^{-1}$							
	Eqn. (8)	Eqn. (9)						
<b>1,4-butanediol + o-cresol</b>								
T = 303.15 K								
0.0000	21.057	16.401	21.231	16.829	21.377	17.248	21.529	17.678
0.1001	20.447	16.080	20.663	16.496	20.854	16.903	21.048	17.322
0.2001	19.823	15.763	20.086	16.166	20.327	16.562	20.566	16.970
0.3002	19.180	15.449	19.497	15.839	19.792	16.225	20.083	16.622
0.4002	18.511	15.139	18.893	15.517	19.250	15.892	19.597	16.278
0.5002	17.811	14.832	18.272	15.197	18.701	15.562	19.110	15.937
0.6002	17.075	14.528	17.630	14.881	18.143	15.235	18.622	15.600
0.7002	16.297	14.227	16.965	14.568	17.575	14.912	18.132	15.266
0.8001	15.471	13.929	16.274	14.258	16.996	14.592	17.640	14.936
0.9001	14.591	13.634	15.555	13.951	16.405	14.276	17.144	14.610
1.0000	13.653	13.342	14.805	13.648	15.799	13.962	16.643	14.286
<b>1,4-butanediol + m-cresol</b>								
T = 303.15 K								
0.0000	18.164	17.047	18.702	17.492	19.209	17.945	19.649	18.384
0.0992	17.649	16.530	18.233	16.955	18.777	17.388	19.252	17.810
0.1986	17.153	16.056	17.787	16.463	18.372	16.878	18.885	17.286
0.2982	16.675	15.621	17.361	16.011	17.991	16.410	18.542	16.804
0.3979	16.211	15.220	16.955	15.595	17.631	15.978	18.221	16.360
0.4979	15.760	14.848	16.564	15.209	17.289	15.579	17.919	15.949

0.5979	15.322	14.504	16.189	14.852	16.964	15.209	17.636	15.568
0.6982	14.893	14.183	15.828	14.520	16.654	14.865	17.368	15.214
0.7986	14.473	13.884	15.477	14.209	16.358	14.544	17.116	14.884
0.8992	14.060	13.605	15.136	13.919	16.073	14.243	16.874	14.575
1.0000	13.653	13.342	14.805	13.648	15.799	13.962	16.643	14.286
<b>1,4-butanediol + p-cresol</b>								
	T = 303.15 K		T = 308.15 K		T = 313.15 K		T = 318.15 K	
0.0000	21.262	16.357	21.408	16.760	21.531	17.156	21.680	17.580
0.0961	20.660	16.057	20.849	16.450	21.018	16.838	21.209	17.252
0.1931	20.036	15.757	20.275	16.140	20.495	16.520	20.733	16.924
0.2909	19.386	15.456	19.682	15.830	19.960	16.201	20.250	16.595
0.3895	18.707	15.155	19.070	15.519	19.413	15.882	19.759	16.266
0.4890	17.992	14.854	18.436	15.208	18.853	15.563	19.261	15.937
0.5894	17.236	14.552	17.775	14.897	18.278	15.244	18.755	15.607
0.6907	16.433	14.250	17.087	14.585	17.687	14.924	18.241	15.278
0.7929	15.574	13.948	16.365	14.273	17.078	14.604	17.718	14.947
0.8960	14.651	13.645	15.606	13.960	16.449	14.283	17.186	14.617
1.0000	13.653	13.342	14.805	13.648	15.799	13.962	16.643	14.286

**Table 3.** Non-linearity parameter **B/A**, values computed by four different approaches as a function of mole fraction 1,4-BD at four different temperatures.

x <sub>1</sub>	303.15K	308.15K	313.15K	318.15K	303.15K	308.15K	313.15K	318.15K
<b>1,4-butanediol + o-cresol</b>								
(B/A) – Hartmann and Balizer								
(B/A) – Ballou								
0.0000	8.598	8.681	8.748	8.819	7.579	7.680	7.763	7.850
0.1001	8.524	8.601	8.666	8.734	7.489	7.583	7.663	7.745
0.2001	8.465	8.537	8.598	8.664	7.417	7.504	7.579	7.660
0.3002	8.416	8.483	8.541	8.606	7.356	7.438	7.510	7.589
0.4002	8.371	8.434	8.490	8.553	7.302	7.378	7.447	7.525
0.5002	8.328	8.386	8.440	8.502	7.249	7.320	7.386	7.462
0.6002	8.282	8.336	8.388	8.448	7.193	7.258	7.322	7.396
0.7002	8.238	8.287	8.337	8.396	7.138	7.199	7.260	7.332
0.8001	8.197	8.242	8.290	8.347	7.088	7.143	7.202	7.272
0.9001	8.167	8.209	8.254	8.311	7.051	7.102	7.158	7.228
1.0000	8.162	8.201	8.245	8.301	7.045	7.093	7.147	7.216
(B/A) – Thermoacoustical (i)								
(B/A) – Thermoacoustical (ii)								
0.0000	6.952	6.920	6.892	6.866	8.171	8.152	8.137	8.122
0.1001	7.111	7.053	6.998	6.946	8.269	8.232	8.198	8.167
0.2001	7.293	7.200	7.114	7.032	8.391	8.328	8.271	8.219
0.3002	7.500	7.366	7.241	7.124	8.541	8.443	8.355	8.277
0.4002	7.740	7.552	7.380	7.223	8.724	8.580	8.453	8.343
0.5002	8.018	7.763	7.534	7.329	8.946	8.742	8.566	8.417
0.6002	8.343	8.003	7.704	7.444	9.217	8.934	8.696	8.499
0.7002	8.729	8.278	7.894	7.569	9.548	9.162	8.845	8.592
0.8001	9.192	8.596	8.105	7.703	9.956	9.432	9.017	8.695
0.9001	9.757	8.966	8.341	7.849	10.465	9.755	9.215	8.810
1.0000	10.459	9.402	8.609	8.008	11.111	10.144	9.443	8.938
<b>1,4-butanediol + m-cresol</b>								
(B/A) – Hartmann and Balizer								
(B/A) – Ballou								
0.0000	8.979	9.076	9.179	9.285	8.046	8.164	8.290	8.420
0.0992	8.876	8.956	9.043	9.134	7.919	8.018	8.124	8.236
0.1986	8.772	8.844	8.923	9.007	7.792	7.880	7.977	8.080
0.2982	8.676	8.741	8.813	8.891	7.674	7.755	7.843	7.938
0.3979	8.587	8.647	8.712	8.784	7.565	7.639	7.719	7.807
0.4979	8.504	8.559	8.618	8.685	7.464	7.532	7.604	7.685
0.5979	8.428	8.477	8.532	8.593	7.371	7.431	7.498	7.573
0.6982	8.357	8.401	8.451	8.509	7.284	7.338	7.399	7.471
0.7986	8.291	8.330	8.377	8.432	7.203	7.251	7.308	7.375

0.8992	8.229	8.264	8.307	8.360	7.127	7.170	7.223	7.288
1.0000	8.162	8.201	8.245	8.301	7.045	7.093	7.147	7.216
(B/A) – Thermoacoustical (i)					(B/A) – Thermoacoustical (ii)			
0.0000	8.006	7.714	7.454	7.230	8.937	8.703	8.506	8.347
0.0992	8.199	7.859	7.561	7.307	9.096	8.818	8.586	8.400
0.1986	8.403	8.009	7.670	7.384	9.267	8.939	8.669	8.455
0.2982	8.616	8.164	7.781	7.461	9.449	9.066	8.756	8.512
0.3979	8.840	8.324	7.893	7.539	9.644	9.200	8.845	8.569
0.4979	9.076	8.490	8.008	7.617	9.852	9.341	8.938	8.628
0.5979	9.324	8.661	8.124	7.695	10.074	9.488	9.033	8.688
0.6982	9.585	8.837	8.243	7.773	10.309	9.642	9.132	8.750
0.7986	9.861	9.019	8.363	7.851	10.560	9.802	9.233	8.812
0.8992	10.152	9.207	8.485	7.930	10.827	9.969	9.337	8.874
1.0000	10.459	9.402	8.609	8.008	11.111	10.144	9.443	8.938
1,4-butanediol + p-cresol								
(B/A) – Hartmann and Balizer					(B/A) – Ballou			
0.0000	8.669	8.733	8.803	8.838	7.666	7.744	7.830	7.874
0.0961	8.628	8.690	8.756	8.790	7.616	7.692	7.772	7.815
0.1931	8.579	8.641	8.703	8.737	7.556	7.631	7.708	7.749
0.2909	8.527	8.584	8.641	8.677	7.492	7.562	7.632	7.676
0.3895	8.475	8.524	8.574	8.611	7.429	7.489	7.550	7.596
0.4890	8.422	8.464	8.511	8.546	7.364	7.415	7.472	7.516
0.5894	8.372	8.412	8.457	8.496	7.302	7.351	7.407	7.455
0.6907	8.322	8.366	8.412	8.455	7.242	7.295	7.352	7.404
0.7929	8.274	8.318	8.364	8.410	7.183	7.237	7.293	7.349
0.8960	8.222	8.265	8.310	8.360	7.118	7.171	7.226	7.287
1.0000	8.162	8.201	8.245	8.301	7.045	7.093	7.147	7.216
(B/A) – Thermoacoustical (i)					(B/A) – Thermoacoustical (ii)			
0.0000	6.952	6.920	6.892	6.866	8.171	8.152	8.137	8.122
0.0961	7.105	7.047	6.994	6.943	8.265	8.228	8.196	8.165
0.1931	7.279	7.189	7.105	7.026	8.381	8.320	8.265	8.215
0.2909	7.480	7.350	7.229	7.115	8.526	8.431	8.347	8.271
0.3895	7.713	7.531	7.365	7.212	8.702	8.564	8.442	8.335
0.4890	7.984	7.738	7.516	7.317	8.919	8.722	8.552	8.408
0.5894	8.306	7.976	7.685	7.432	9.185	8.912	8.681	8.490
0.6907	8.690	8.250	7.875	7.556	9.513	9.138	8.830	8.583
0.7929	9.156	8.571	8.089	7.693	9.924	9.411	9.004	8.687
0.8960	9.732	8.949	8.331	7.843	10.442	9.741	9.206	8.805
1.0000	10.459	9.402	8.609	8.008	11.111	10.144	9.443	8.938

**Table 4.** Reduced bulk modulus, B, isochoric thermo-acoustical parameter,  $\Delta$ , isothermal Gruneisen parameter,  $\Gamma_{ith}$ , isochoric Gruneisen parameter,  $\Gamma_{ich}$ , isobaric Gruneisen parameter,  $\Gamma_{iba}$ , isothermal Anderson-Gruneisen parameter,  $\delta$ , as a function of mole fraction 1,4-BD at four different temperatures.

$x_1$	B	$\Delta$	$\Gamma_{ith}$	$\Gamma_{ich}$	$\Gamma_{iba}$	$\delta$	B	$\Delta$	$\Gamma_{ith}$	$\Gamma_{ich}$	$\Gamma_{iba}$	$\delta$
1,4-butanediol + o-cresol												
<b>303.15 K</b>												
0.0000	0.161	0.118	3.477	0.247	3.229	6.459	0.160	0.122	3.461	0.248	3.212	6.425
0.1001	0.168	0.108	3.557	0.261	3.295	6.591	0.165	0.113	3.527	0.260	3.267	6.534
0.2001	0.174	0.098	3.647	0.277	3.371	6.741	0.171	0.104	3.601	0.273	3.328	6.656
0.3002	0.181	0.088	3.751	0.294	3.457	6.914	0.177	0.096	3.684	0.288	3.397	6.793
0.4002	0.189	0.079	3.871	0.314	3.557	7.114	0.183	0.088	3.777	0.304	3.474	6.948
0.5002	0.196	0.071	4.010	0.337	3.673	7.346	0.189	0.080	3.883	0.321	3.561	7.123
0.6002	0.205	0.063	4.173	0.364	3.809	7.618	0.196	0.073	4.003	0.342	3.661	7.323
0.7002	0.213	0.056	4.366	0.395	3.971	7.942	0.203	0.066	4.140	0.364	3.776	7.552
0.8001	0.222	0.049	4.598	0.432	4.166	8.331	0.210	0.059	4.299	0.391	3.909	7.818
0.9001	0.232	0.042	4.880	0.477	4.403	8.806	0.218	0.053	4.484	0.421	4.064	8.127
1.0000	0.243	0.036	5.231	0.532	4.699	9.398	0.226	0.047	4.703	0.456	4.246	8.493
<b>313.15 K</b>												
0.0000	0.159	0.127	3.447	0.250	3.197	6.394	0.158	0.131	3.434	0.251	3.182	6.365
<b>308.15 K</b>												

0.1001	0.163	0.119	3.500	0.259	3.241	6.481	0.161	0.124	3.474	0.259	3.215	6.430
0.2001	0.168	0.111	3.558	0.270	3.288	6.576	0.165	0.118	3.517	0.267	3.250	6.500
0.3002	0.172	0.104	3.621	0.281	3.340	6.681	0.168	0.112	3.563	0.275	3.288	6.576
0.4002	0.177	0.097	3.691	0.293	3.398	6.796	0.172	0.106	3.612	0.284	3.328	6.657
0.5002	0.182	0.090	3.768	0.307	3.461	6.923	0.176	0.101	3.666	0.293	3.372	6.745
0.6002	0.188	0.083	3.853	0.321	3.532	7.064	0.179	0.095	3.723	0.304	3.420	6.839
0.7002	0.193	0.077	3.948	0.338	3.610	7.221	0.183	0.090	3.785	0.315	3.471	6.942
0.8001	0.199	0.071	4.054	0.356	3.698	7.396	0.187	0.085	3.853	0.326	3.526	7.053
0.9001	0.204	0.065	4.172	0.376	3.797	7.593	0.192	0.080	3.926	0.339	3.587	7.173
1.0000	0.211	0.060	4.306	0.398	3.908	7.816	0.196	0.075	4.005	0.353	3.653	7.305
1,4-butanediol + m-cresol												
<b>303.15 K</b>												
0.0000	0.196	0.071	4.004	0.336	3.668	7.336	0.188	0.082	3.858	0.317	3.541	7.081
0.0992	0.201	0.066	4.101	0.352	3.749	7.498	0.192	0.077	3.931	0.329	3.601	7.202
0.1986	0.206	0.062	4.203	0.369	3.834	7.668	0.196	0.072	4.006	0.342	3.664	7.328
0.2982	0.211	0.058	4.309	0.386	3.923	7.847	0.200	0.068	4.083	0.355	3.728	7.457
0.3979	0.216	0.054	4.422	0.404	4.018	8.035	0.204	0.065	4.164	0.368	3.795	7.591
0.4979	0.220	0.051	4.539	0.423	4.117	8.233	0.208	0.061	4.246	0.382	3.864	7.729
0.5979	0.225	0.047	4.664	0.443	4.221	8.442	0.212	0.058	4.332	0.396	3.936	7.872
0.6982	0.229	0.044	4.794	0.463	4.331	8.662	0.215	0.055	4.420	0.410	4.010	8.019
0.7986	0.234	0.041	4.932	0.485	4.447	8.894	0.219	0.052	4.511	0.425	4.086	8.172
0.8992	0.238	0.039	5.078	0.508	4.569	9.139	0.223	0.050	4.605	0.440	4.165	8.330
1.0000	0.243	0.036	5.231	0.532	4.699	9.398	0.226	0.047	4.703	0.456	4.246	8.493
<b>313.15 K</b>												
0.0000	0.180	0.093	3.728	0.300	3.428	6.856	0.172	0.106	3.616	0.285	3.331	6.663
0.0992	0.183	0.089	3.782	0.309	3.472	6.945	0.175	0.102	3.654	0.291	3.363	6.726
0.1986	0.186	0.085	3.836	0.319	3.518	7.035	0.177	0.098	3.693	0.298	3.395	6.789
0.2982	0.190	0.081	3.892	0.328	3.564	7.127	0.180	0.094	3.732	0.305	3.427	6.853
0.3979	0.193	0.077	3.948	0.338	3.610	7.221	0.182	0.091	3.771	0.312	3.459	6.917
0.4979	0.196	0.074	4.005	0.347	3.658	7.316	0.185	0.088	3.810	0.319	3.491	6.981
0.5979	0.199	0.071	4.064	0.357	3.706	7.413	0.187	0.085	3.849	0.326	3.523	7.046
0.6982	0.202	0.068	4.123	0.367	3.755	7.511	0.190	0.082	3.888	0.333	3.555	7.110
0.7986	0.205	0.065	4.183	0.377	3.806	7.611	0.192	0.080	3.927	0.339	3.588	7.175
0.8992	0.208	0.062	4.244	0.388	3.856	7.713	0.194	0.077	3.966	0.346	3.620	7.240
1.0000	0.211	0.060	4.306	0.398	3.908	7.816	0.196	0.075	4.005	0.353	3.653	7.305
1,4-butanediol + p-cresol												
<b>303.15 K</b>												
0.0000	0.161	0.118	3.477	0.247	3.229	6.459	0.160	0.122	3.461	0.248	3.212	6.425
0.0961	0.167	0.108	3.553	0.261	3.293	6.585	0.165	0.113	3.524	0.260	3.265	6.529
0.1931	0.174	0.098	3.641	0.276	3.365	6.730	0.171	0.105	3.596	0.272	3.323	6.647
0.2909	0.181	0.089	3.741	0.293	3.448	6.897	0.176	0.096	3.676	0.286	3.390	6.780
0.3895	0.188	0.080	3.857	0.312	3.545	7.091	0.182	0.088	3.767	0.302	3.465	6.930
0.4890	0.195	0.072	3.994	0.335	3.659	7.318	0.189	0.081	3.870	0.319	3.551	7.102
0.5894	0.204	0.064	4.154	0.361	3.793	7.587	0.195	0.073	3.989	0.339	3.650	7.300
0.6907	0.212	0.057	4.346	0.392	3.954	7.909	0.202	0.066	4.127	0.362	3.764	7.529
0.7929	0.222	0.049	4.580	0.429	4.150	8.300	0.210	0.060	4.287	0.389	3.898	7.797
0.8960	0.232	0.043	4.868	0.475	4.392	8.785	0.218	0.053	4.476	0.419	4.057	8.114
1.0000	0.243	0.036	5.231	0.532	4.699	9.398	0.226	0.047	4.703	0.456	4.246	8.493
<b>313.15 K</b>												
0.0000	0.159	0.127	3.447	0.250	3.197	6.394	0.158	0.131	3.434	0.251	3.182	6.365
0.0961	0.163	0.119	3.498	0.259	3.239	6.477	0.161	0.125	3.472	0.258	3.214	6.427
0.1931	0.167	0.112	3.554	0.269	3.285	6.569	0.164	0.119	3.514	0.266	3.248	6.495
0.2909	0.172	0.104	3.615	0.280	3.335	6.670	0.168	0.113	3.558	0.274	3.284	6.568
0.3895	0.177	0.097	3.683	0.292	3.391	6.783	0.171	0.107	3.607	0.283	3.324	6.648
0.4890	0.182	0.091	3.759	0.305	3.454	6.908	0.175	0.101	3.660	0.292	3.367	6.734
0.5894	0.187	0.084	3.844	0.320	3.524	7.048	0.179	0.096	3.717	0.303	3.414	6.829
0.6907	0.192	0.078	3.939	0.336	3.603	7.205	0.183	0.090	3.779	0.314	3.466	6.932
0.7929	0.198	0.071	4.046	0.354	3.691	7.383	0.187	0.085	3.848	0.326	3.522	7.044
0.8960	0.204	0.066	4.167	0.375	3.792	7.585	0.192	0.080	3.923	0.339	3.584	7.168
1.0000	0.211	0.060	4.306	0.398	3.908	7.816	0.196	0.075	4.005	0.353	3.653	7.305

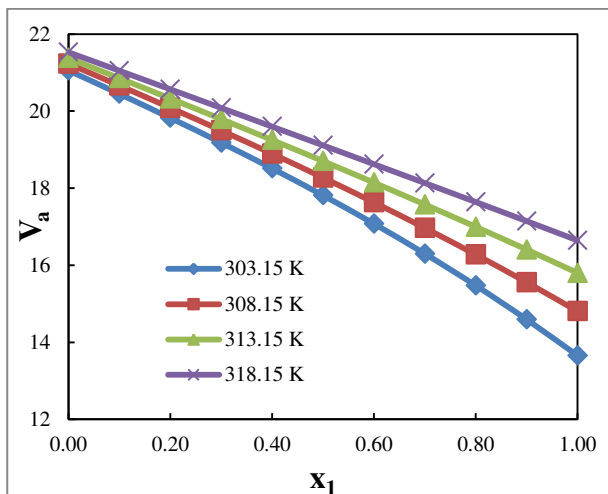


**Fig. 1** Available volume in binary liquid mixtures of 1,4-butanediol + o-cresol at different temperatures.

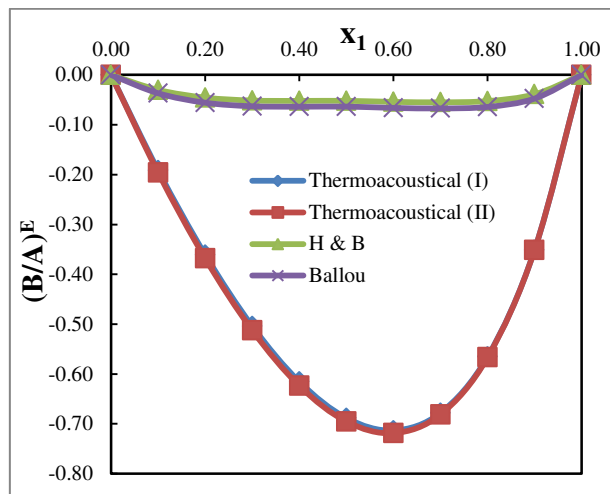


**Fig. 4** Variation of excess B/A with mole fraction of 1,4-BD of 1,4-butanediol + o-cresol at  $T=303.15\text{K}$ .

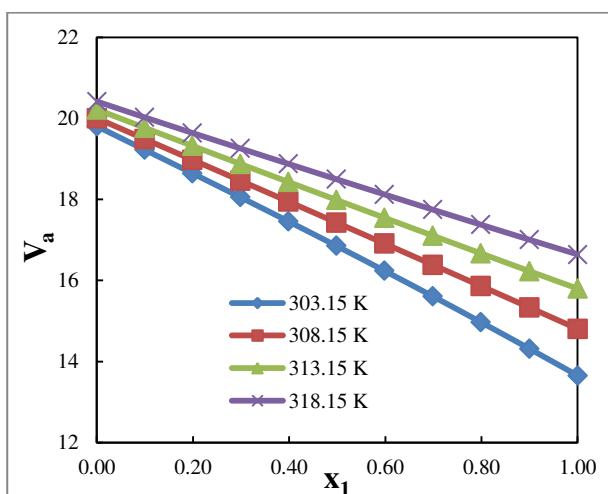


**Fig. 2** Available volume in binary liquid mixtures of 1,4-butanediol + m-cresol at different temperatures.

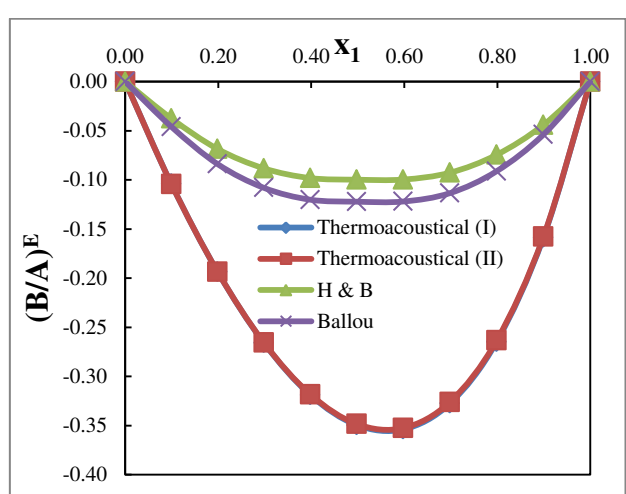


**Fig. 5** Variation of excess B/A with mole fraction of 1,4-BD of 1,4-butanediol + m-cresol at  $T=303.15\text{K}$ .

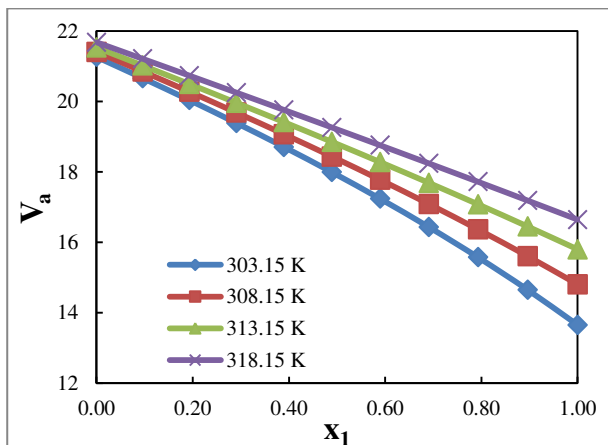


**Fig. 3** Available volume in binary liquid mixtures of 1,4-butanediol + p-cresol at different temperatures.

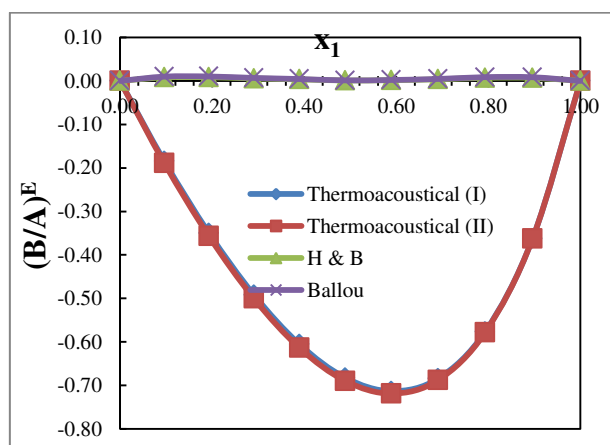


**Fig. 6** Variation of excess B/A with mole fraction of 1,4-BD of 1,4-butanediol + p-cresol at  $T=303.15\text{K}$ .

#### 4. CONCLUSIONS

A few acoustic parameters, reduced volume, the Moelwyn-Hughes parameter, and the Sharma parameter are computed. These parameters are used to compute available volume using two alternative ways. Four approaches are used to calculate the non-linearity parameter, B/A, and the results are compared. The interpretation of the magnitude of the liquid's hardness

in terms of the non-linearity parameter is aided by the conclusion that the fluctuation of the computed values of B/A will rely on the ultrasonic sound wave in a particular medium. Additionally, Gruneisen parameters are computed. The present observations give more insight into the molecular interactions between the taken binary liquid components.

#### References

- Anjali, A., & Aashees, A. (2017). Study of parameter of nonlinearity in 2-chloroethanol with 2-dimethyl ethanolamine/ 2-diethylethanalamine at different temperatures. *Physica, B* 515, 1-7. doi:10.1016/j.physb.2017.03.045
- Apfel, R. E., & Everbach, E. C. (1989). Using the acoustic nonlinearity parameter for tissue composition prediction. *Proceedings of the 13th International Congress on Acoustics*, Belgrade, 167-170.
- Beyer, R.T. (1960). Parameter of nonlinearity in fluids. *Journal of the Acoustical Society of America*, 32, 719-721.
- Bhatia, S.C., Rani, R., Bhatia, R., & Anand, H. (2011). Volumetric and ultrasonic behavior of binary mixtures of 1-nonanol with o-cresol, m-cresol, p-cresol and anisole at T=(293.15 and 313.15) K. *The Journal of Chemical Thermodynamics*, 43, 479-486. doi:10.1016/j.jct.2010.10.025
- Bjorno, L. (2002). Forty years of nonlinear ultrasound. *Ultrasonics*, 40, 11-17. doi:10.1016/S0041- 624X(02)00084-7
- Coppens, A. E., Beyer, R. T., Seiden, M. B., Donohue, J., Guepin, F., Hodson, R. H., & Townsend, C. (1965). Parameter of nonlinearity in fluids-II. *Journal of the Acoustical Society of America*, 38, 797-804.
- Duck, F.A. (2002). Nonlinear acoustics in diagnostic ultrasound. *Ultrasound in Medicine & Biology*, 28, 1-18. doi:10.1016/S0301-5629(01)00463-X
- Hartman, B. (1979). Potential energy effects on the sound speed in liquids. *Journal of the Acoustical Society of America*, 65, 1392-1397.
- Krishna, T.S., Rama Rao, P.V.V.S. Narendra, K., Bala Karuna Kumar, D., & Ramachandran, D. (2021) Studies of solute - solvent interaction of ethyl acetate with 1-Butyl-3-methylimidazolium tetrafluoroborate at T=(298.15–323.15)K, *Journal of Molecular Liquids*, 339, 117-187, doi:10.1016/j.molliq.2021.117187.
- Moelwyn-Hughes, E.A. (1951). *Journal of Physical Chemistry*, 55, 246.
- Narendra, K., Kavitha, Ch., & Krishna, T. S. (2022). Computation of available volume and non-linearity parameter in liquid mixtures using thermoacoustic and thermodynamic parameters, *International Journal of Ambient Energy*, 43:1, 1113-1119. doi:10.1080/01430750.2019.1691652
- Nain A.K.(2022). Study of intermolecular interactions in binary mixtures of methyl acrylate with benzene and methyl substituted benzenes at different temperatures: An experimental and theoretical approach. *Chinese Journal of Chemical Engineering*, 4, 212-238. doi:10.1016/j.cjche.2021.05.024
- Pandey, J.D., Chhabra, J., Dey, R., Sanguri, V., & Verma, R. (2000). Non-linearity parameter B/A of binary liquid mixtures at elevated pressures. *Pramana Journal of Physics*, 55, 433-439. doi:10.1007/S12043-000-0073-6

Prabhune, A., Natekar, A., & Ranjan Dey. (2022). Thermophysical Properties of Alkanone + Aromatic Amine Mixtures at Varying Temperatures. *Sec. Chemical Physics and Physical Chemistry*, 10,1-12.  
doi:10.3389/fchem.2022.868836

Riddick, J.A., Bunger, W.B., & Sakano, T. (1986). Organic solvents: Physical Properties and Methods of Purification. *Wiley-Interscience*, New York.

Sehgal, C.M. (1995) . Nonlinear ultrasonics to determine molecular properties of pure liquids. *Ultrasonics*, 33, 155 161.

Sehgal, B. C. M., Porter, B. R., & Greenleaf, J. F. (1986). Ultrasonic nonlinearity parameters and sound speed of alcohol-water mixtures. *Journal of the Acoustical Society of America*, 79, 566-570.

Srinivasu, J.V., Krishna, T.S., Narendra, K., Srinivasa Rao, G., & Subba Rao, B. (2017) . Elucidation of H-bond and molecular interactions of 1,4-butanediol with cresols: Acoustic and volumetric data. *Journal of Molecular Liquids*, 236, 27-37. doi:10.1016/j.molliq.2017.04.004

Stokes, R.H., & Mills, R. (1965). Viscosity of Electrolytes and Related Properties. *Pergamon Press*, New York.

Thakur K.P. (1978). Non-linearity acoustic parameter in higher alkanes. *Acustica*, 39, 270-272.

Vogel, A.I. (1989). Text Book of Practical Organic Chemistry, 5<sup>th</sup> ed. Longman Green, London.

---

**Srinivasu J.V.**

Shri Vishnu Engineering College for Women ,  
Bhimavaram,  
India  
srinivas.jaddu@gmail.com

[ORCID ID: 0000-0002-7208-2450](#)

**Narendra K.**

V. R. Siddhartha Engineering College,  
Vijayawada,  
India  
narenk75@gmail.com

[ORCID ID: 0000-0002-0347-3845](#)

**Kavitha Ch.**

V. R. Siddhartha Engineering College,  
Vijayawada,  
India  
chkavitha.chem@gmail.com

[ORCID ID: 0000-0002-4091-0821](#)

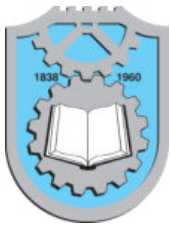
---

**Srinivasa Krishna T.**

P.B. Siddhartha College of Arts and Science,  
Vijayawada,  
India  
sritadikonda@gmail.com

[ORCID ID: 0000-0002-4395-7326](#)

---



## NAMED ENTITY RECOGNITION FOR MEDICAL DATA EXTRACTION USING BIOBERT

Kayal Padmanandam\*

Nikitha Pitla

Yeshasvi Mogula

P.S. Brahmanandam

### Keywords:

*Natural Language Processing; Named Entity Recognition; SciSpacy; BioBERT; Science; Medicine Data*

### A B S T R A C T

*Technological advancements have caused widespread shifts in the medical industry. A vast quantity of information may be found in the medical literature publications released by researchers. Natural language processing innovations have made it simple to extract information on drugs, illnesses, symptoms, routes doses, species, and routes of administration from a documented source. This proposed research is used to identify the named entities from the medical literature. The BioBERT model is used to train the corpus that has been annotated. The proposed framework can outperform many state-of-the-art baselines and provide state-of-the-art results for BioNER. When compared to the existing model, the accuracy provided by the proposed system is satisfactory. The BioBERT is used for the extraction of medical entities like drugs, chemicals, genes, etc and to train the corpus that has been annotated. The BioBERT has in-built data of the medical entities, that will identify all the medical-related data or entities from the given statement. More entities can be found by this method than by the current standard model. When compared to the existing model, the accuracy provided by the trained version is satisfactory. The proposed system comes with a GUI for users to type the clinical words or components for analysis.*



© 202x Published by Faculty of Engineering

### 1. INTRODUCTION

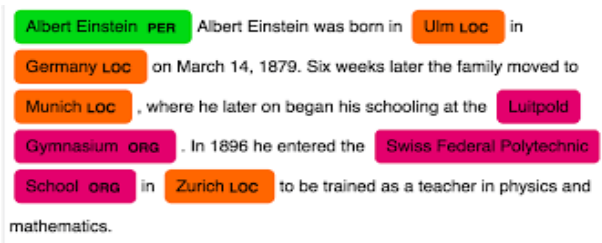
Subsequent words in a sentence can be predicted and generated with the help of Natural Language Processing by analyzing and learning from the previous words in the sentence. Like many NLP processes, Named Entity Recognition (NER) extracts important entities like people, places, organizations, and medical terminology from the given text or document. Python libraries like Spacy, SciSpacy, and *BioBERT* are used for NER practices. Medical Information on drugs, illnesses, and

symptoms can be extracted from the textual source using the SciSpacy or the *BioBERT* model. However, there is a limitation that users cannot create user-defined entities. To overcome this, the BlankSpacy model can be used to train the user-defined annotated entities (Alam, Tanvir et al, 2021). Many clinical Natural Language Processing (NLP) tools and systems have been published (Amogh Kamat Tarcar et al, 2019; Xiaodong Liu et al, 2019). The growing quantity of textual biomedical information allows for the pre-training of language (Noha S Tawfik et al, 2020), which may then be used for a wide range of

\*Corresponding author: Kayal Padmanandam  
Email: kayalpaddu@gmail.com

tasks in the biomedical domain. The practice of automatically recognizing and categorizing names of entities like the persons, locations, organizations, nations, day date, time of the day or year, numbers, ordinal numbers, and cardinal numbers in the text which have given is known as Named-Entity Recognition (NER) (Devopedia 2020). In the biomedical discipline, a large variety of entities such as diseases, drugs, genes, and proteins are available and can be recognized using the BioBERT Model. BIONER is used in several text mining applications in the healthcare industry, such as drug-drug interaction extraction and disease-treatment relationship discovery (BioNER). Models used in biomedical text mining have recently been improved and there is development using deep learning (R Ramachandran et al., 2021) techniques in NLP. In recent years, several different methods have been applied to improve BioNER (Vikas Yadav et al. 2019).

A few of the methods are LSTM (Long Short-Term Memory) and Conditional Random Field (CRF). Although there are several implementations, limitations to biomedical text mining when using state-of-the-art natural language processing techniques and graph-based algorithms (Matthew E. Peters et al., 2018) exist. Word2Vec (Jacob Devlin et al., 2019), ELMo (Zhenzhong Lan et al., 2019), BERT (Iz Beltagy et al., 2019), and ALBERT (Tomas Mikolov et al., 2013) are a few word representation approaches that provide their own set of difficulties when evaluating their efficacy on biological text datasets.



Albert Einstein PER Albert Einstein was born in Ulm LOC in Germany LOC on March 14, 1879. Six weeks later the family moved to Munich LOC, where he later on began his schooling at the Luitpold Gymnasium ORG. In 1896 he entered the Swiss Federal Polytechnic School ORG in Zurich LOC to be trained as a teacher in physics and mathematics.

**Figure 1.** Sample output of NER

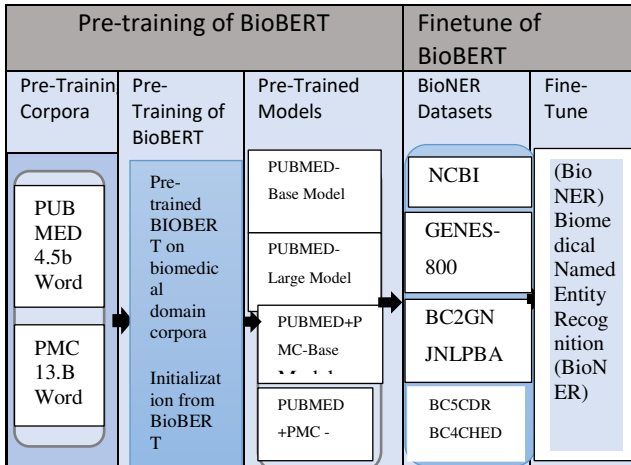


**Figure 2.** Overview of the pre-training and fine-tuning of BioBERT on NER

#### NLP Libraries:

Figure 1 shows the named entity recognized, where the person's name is identified as PER, the Location is identified as Loc, and the organization is identified as ORG. Figure 2 depicts the overview of the pre-training and fine-tuning of BioBERT on NER.

#### Spacy:

Python's Spacy is a powerful Natural Language Processing (NLP) module that is available and open-source. Spacy is optimized for production use and may be used to create programs that understand and analyze enormous amounts of text. It may be utilized as a pre-processing step for deep learning and the development of information extraction and natural language comprehension systems.

#### Scispacy:

An open-source and free library for sophisticated Natural Language Processing, Scispacy was developed in Python and CPython. Statistical neural network models for processing biomedical, scientific, or clinical literature are now available in the library, which is licensed under the MIT license.

#### BioBERT:

Bidirectional Encoder Representations from Transformers (BERT) is one of the deep learning models that takes its cues from Transformers, in which each output is linked to each input and the weights between them are created on the fly depending on their relationship. Figure 3 shows how the BioBERT Architecture works.

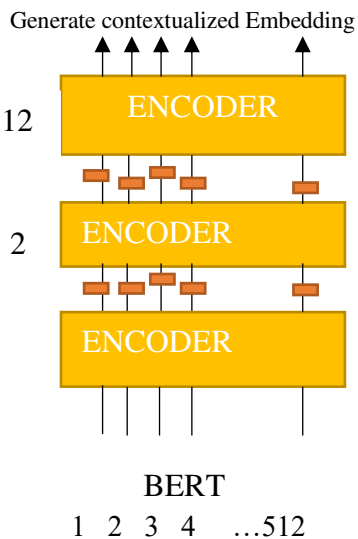


**Figure 3.** BioBERT Architecture

## 2. RELATED WORKS

An effective method for learning high-level distributed vector representation for the semantic word relations is captured by a large number of words. The regular word representation is used to speed up and learn the frequent words by subsampling (Tomas Mikolov et al., 2013). BioSentVec represents the initial launch of an open set of sentence embeddings, developed using a vast corpus exceeding 30 million scientific documents from the PubMed database, in conjunction with clinical data derived from the MIMIC II Clinical Database. In this study, BioSentVecs embeddings are evaluated using two separate phrase pair similarity tasks in a variety of biomedical text genres (Qingyu Chen et al, 2019). Rather than viewing BioNER tasks through the lens of sequence labelling, the study by (Sampo Pyysalo et al., 2013) reframes them as problems of machine reading comprehension (MRC). This conceptual reorientation allows for the integration of additional prior knowledge through the utilization of carefully crafted queries, thereby eliminating the necessity for decoding procedures such as conditional random fields (CRF). The technique of bacterial-named entity recognition is also discussed, which incorporates domain-specific features into a sophisticated deep learning framework. This framework merges the capabilities of a convolutional neural network with a bidirectional long short-term memory network. (Henghui Zhu et al, 2018) can attain superior performance in bacterial NER (Devopedia, 2020). Yuqi Si et al. (2019) obtained superior performance in bacterial NER by utilizing the domain properties (Yuqi Si et al, 2019). In the study referenced by (Jinhyuk Lee et al, 2016), the authors found that contextual embeddings, which were pre-trained on an extensive clinical dataset, set new benchmarks in all concept extraction tasks. The top-performing model outperformed all existing leading methods, which had F1 scores ranging between 80.74 and 81.65, with 80.74 being the highest score previously recorded.

In the study (Yifan Peng et al, 2019), it is posited that BioBERT, pre-trained on biomedical datasets, outstrips not only BERT but also other previous leading models. This can be credited to BioBERT's architecture which remains consistent across tasks. Though BERT matches the performance of other top-notch models, BioBERT markedly surpasses them in three standard biomedical text-mining tasks. Further research conducted by (Jeremy Howard and Sebastian Ruder, 2018) evaluated multiple baselines based on BERT and ELMo, concluding that the BERT model, pre-trained using PubMed abstracts and MIMIC-III clinical notes, delivered the optimal outcome. Meanwhile, (Dani Yogatama et al, 2019) broach the subject of Universal Language Model Fine-tuning (ULMFiT), a transfer learning methodology efficacious for an array of tasks in natural language processing, and describe the pertinent strategies. The study identified (Xipeng Qiu et al, 2020) executing a comprehensive empirical examination to ascertain performance against a

crucial benchmark. The capacity to quickly adjust to new tasks by leveraging prior knowledge about a language's vocabulary, grammar, meaning, and practical rules is considered the essence of broad linguistic intelligence. Finally, Pengfei Liu et al. (2016) present a succinct overview of language representation learning and its accompanying research trajectories. (Ling, Y et al, 2023) research develops natural language processing (NLP) to analyze drug reviews of patient with their level of satisfaction. (Dara S, et al, 2022) discuss the importance of machine and intelligent learning in drug discovery. (Padmanandam K, et al, 2023) described how NER is used for information extraction from massive data using BERT algorithm.

## 3. DATASET FOR MEDICAL NAMED ENTITY RECOGNITION

The proposed system employs the Scispacy and Biobert models to identify medical phrases in text documents. It will categorize entities like Disease, drug/Chemical, Gene, etc., as shown in Figure 6, and highlight the entities with the help of displacy in the statements.

### Dataset

The model has built on the following different datasets and the entities identified are the drug/chemical, the disease, and the Gene.

**BC5CDR:** This corpus, available through the Bio-Creative workshop (Jiao Li et al, 2016), is a challenge set by the Bio-Creative community for the extraction of chemical-disease relations. It aids in identifying chemical and disease entities from Medline abstracts.

**BC4CHEMD:** This dataset comprises chemical compounds and drugs extracted from PubMed abstracts. It's provided by the Bio-Creative challenge for the development and evaluation of tools for Chemical NER (Martin Krallinger et al, 2015). The BioNER datasets include Annotations of the NCBI Disease, which contains 6,881 values.

**NCBI Disease:** This dataset provides information on disease-related data from the National Center for Biotechnology Information (NCBI). It is used to access biomedical and genomic data, as mentioned in the release by Leaman et al (Rezarta Islamaj Dounedan et al, 2014).

**JNLPBA:** This dataset, provided by (Jin-Dong Kim et al, 2004), is employed to identify DNA, cell type, RNA, protein, and cell line.

**BC2GM:** Bio Creative II Gene Mention Recognition (BC2GM) is a semi-supervised learning task that uses alternating structure optimization. This dataset, provided by ANDO (Rie Kubota Ando, 2007), holds the state-of-the-art in the BC2GM task.

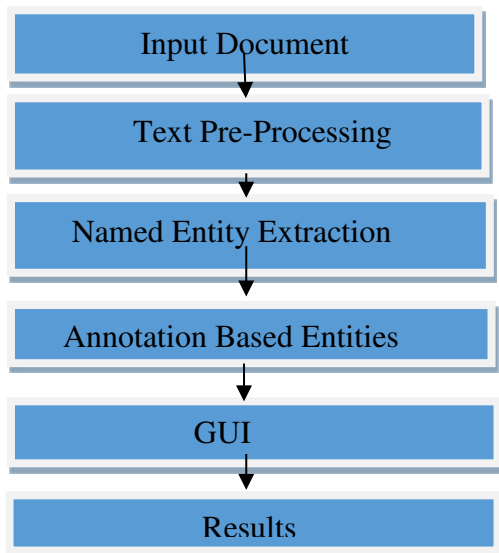


**Figure 4.** Proposed NER Flow Diagram

**Table 1.** Dataset Table

Name	Entity Types	Train Sentence	Train entity	Test Sentence	Test Entity
BC2GM	Gene/ Protein	14093	18257	5038	6325
BC4CHEM D	Drug/ Chem	10321	58964	26364	25346
BC5CDR- chem	Drug/ Chem	7041	10550	4797	5385
BC5CDR- disease	Disease	7031	8427	4797	4424
NCBI- Disease	Disease	5217	5921	.0822	940
JNLPBA	Gene/ Protein	12326	40753	3856	6241

	description	medical_specialty	sample_name	transcription
0	A 23-year-old white female presents with comp...	Allergy / Immunology	Allergic Rhinitis	SUBJECTIVE: This 23-year-old white female pr...
1	Consult for laparoscopic gastric bypass.	Bariatrics	Laparoscopic Gastric Bypass Consult - 2	PAST MEDICAL HISTORY: He has difficulty climb...
2	Consult for laparoscopic gastric bypass.	Bariatrics	Laparoscopic Gastric Bypass Consult - 1	HISTORY OF PRESENT ILLNESS: , I have seen ABC ...
3	2-D M-Mode, Doppler.	Cardiovascular / Pulmonary	2-D Echocardiogram - 1	2-D M-MODE ,1. Left atrial enlargement wit...
4	2-D Echocardiogram	Cardiovascular / Pulmonary	2-D Echocardiogram - 2	1. The left ventricular cavity size and wall ...

**Figure 5.** Dataset accessed from  
<https://www.kaggle.com/datasets/tboyle10/medicaltranscriptions>

The above Figure 5 shows the dataset which is used with Scispacy. It has the statement description, transcripts, and keywords. According to the keywords, the entities will be identified and they will be annotated.

TEXT	START	END	ENTITY	TYPE
iron-deficiency anemia	79	101	DISEASE	
chronic blood loss	109	127	DISEASE	
colitis	133	140	DISEASE	
iron	203	207	CHEMICAL	
colitis	286	293	DISEASE	
hematoma	391	399	DISEASE	
venous thrombosis	473	490	DISEASE	
DVT	492	495	DISEASE	
pelvic hematoma	742	757	DISEASE	
vancomycin	781	791	CHEMICAL	
infectious disease	873	891	DISEASE	
improved.,PT	1348	1360	CHEMICAL	
vitamin K	1503	1512	CHEMICAL	
uric acid	1830	1839	CHEMICAL	
bilirubin	1853	1862	CHEMICAL	
Creatinine	1911	1921	CHEMICAL	
creatinine	1951	1961	CHEMICAL	
Folic acid	2079	2089	CHEMICAL	
Iron	2103	2107	CHEMICAL	

**Figure 6.** Biomedical entities identified

## 4. METHODOLOGY

### 4.1 NLP Pipeline

1. Sentence Segmentation: It is the foremost step in the Natural Language Processing (NLP) pipeline. It involves breaking down a large body of text into its individual sentence constituents for easier processing. Take, for instance, the sentence, "Hyderabad is the capital and most populous city of Telangana and also for AP before the Telangana formation. It is also referred to as the pearl city. It was once under the rule of the Nizams, who constructed the renowned Charminar." In this case, sentence segmentation would separate this text into distinct sentence units for further analysis.

2. Word Tokenization: Word tokenization divides the large statements to the small phrases or the tokens breaks the sentence into separate phrases or tokens. This helps apprehend the context of the textual content. While tokenizing the above sentence " Hyderabad is the capital and most populous city of Telangana and the city ", the sentence will be separated into single words, i.e., "Hyderabad", "is", "the", "capital", "and", "most", "populous", "city", "of", "Telangana", "and", "the", "pearl", "City".

3. Stemming: It simplifies words to their root or base form, a process known as normalization thereby enabling more precise prediction of the parts of speech for each token.

4. Lemmatization: It refines words by removing inflectional endings and returning the base or dictionary

form of a word, also known as the lemma. Unlike stemming, which may result in non-standard words, lemmatization ensures the output is a valid term or phrase found in the language.

5. Stop word analysis: Stop word analysis involves evaluating the relevance of each word in a sentence. Some words, like "is," "a," "the," and "and," are more common in English and often carry less meaningful information. These are designated as "stop words" in natural language processing (NLP). As they occur frequently but don't contribute much to the overall meaning, they can be filtered out to highlight more critical, information-rich words.

6. Dependency parsing: It is primarily utilized to decipher the interrelationships among words in a sentence. It works by creating a tree to visualize these relationships, with each word represented as a node. The central verb of the sentence serves as the root of this tree, signifying its foundational role in the overall sentence structure.

7. Part-of-speech tagging: It involves assigning grammatical categories, such as verbs, adverbs, nouns, and adjectives, to each word in a sentence. This process aids in comprehending the linguistic and semantic significance of words, thereby ensuring grammatical correctness and enhancing sentence understanding.

The CRF, employed by both the NLP Speech Tagger and NLTK, represents a statistical model suitable for handling sequential data, like words. It is capable of capturing a comprehensive understanding of a sentence's context. In this model, the input is  $X = \{\vec{x}_1, \vec{x}_2, \vec{x}_3, \dots / \vec{x}_T\}$ .

$$P(y - x) = \frac{1}{z(\vec{x})} \prod_{t=1}^T \exp\{\sum_{k=1}^K \omega_k f_k(y_t, y_{t-1}, \vec{x}_t)\} \quad (1)$$

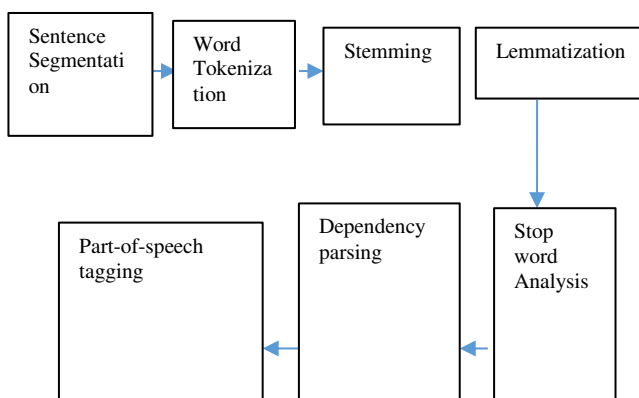


**Figure 7.** NLP Pipeline

## 4.2 Pre-trained models and hyper parameter tuning:

Deep learning technique, the hyperparameters of the BERT model must be initialized. On the other hand,

finding the sweet spot at the beginning might be a challenge. Modifications may be made after comparing the model's results with data. The improved model may be referenced from the NER database of the transformers. Like training any other deep learning network, the approach is easy. A loop that takes into consideration the intended training length, or epochs, and the availability of graphics processing units (GPUs), will be created.

## 4.3 NER Model Accuracy Prediction

A NER model's effectiveness may be estimated in a variety of ways. This is commonly done by the use of measurements like the Precision, Recall, F1 score, or relaxed match. The below Figure 8 show the relation between the drug and the dosage of the drug.

DRUG_DOSE	137	140	Xylocaine	20 ml
DRUG_DOSE	141	144	Marcaine	0.25%
DRUG_DOSE	208	211	Aspirin	81 mg
DRUG_DOSE	216	219	Spiriva	10 mcg
DRUG_DOSE	399	402	nifedipine	10 mg
DRUG_DOSE	226	229	aspirin	one tablet
DRUG_DOSE	245	248	Warfarin	2.5 mg
DRUG_DOSE	67	70	Topamax	100 mg
DRUG_DOSE	73	76	Zoloft	100 mg
DRUG_DOSE	79	82	Abilify	5 mg
DRUG_DOSE	84	87	Motrin	800 mg
DRUG_DOSE	110	113	Xanax	1 mg
DRUG_DOSE	125	128	Colace	100 mg
DRUG_DOSE	168	171	Paxil	10 mg
DRUG_DOSE	175	178	Prednisone	20 mg
DRUG_DOSE	193	196	Metamucil	one pack
DRUG_DOSE	207	210	Nexium	40 mg
DRUG_DOSE	1133	1136	Naprosyn	one p.o.
DRUG_DOSE	298	293	Lidocaine	1%
DRUG_DOSE	37	40	Altrua	60

**Figure 8.** Relation between the drug and the dosage

## 5. EXPERIMENTAL RESULTS

BioBERT is a space-explicit language portrayal model optimized for large-scale biomedical corpora, which we call a "transformer for biomedical message mining." BioBERT, which uses almost identical engineering for different tasks, outperforms the BERT and other state-of-the-art models when trained on a large number of biomedical corpora, the biomedical text mining tasks. When compared to prior-generation models, BERT's performance is on par, but BioBERT outperforms them in three key areas, delegate biomedical message named entity recognition, connection extraction, and question-response rate. The study has shown that BERT can better understand difficult biomedical texts if it is first trained on relevant biomedical corpora. The system is evaluated using the performance measures such as precision, recall, and F1-score as given in the equation 1,2,3. The two different algorithms Scispacy and the BioBERT are compared. The model has been loaded with 3 different datasets. A comparison study between the built-in model Scispacy and the customized model using BioBERT is made and the results are shown in Table 2 and 3.

**Table:2** BioBERT Training and Testing Result

Bio Bert						
	Training			Testing		
Datasets	Precision	Recall	F1Score	Precision	Recall	F1Score
Disease	87.67	89.02	88.79	87.54	88.98	86.67
Drug/Chemical	88.65	88.23	87.97	88.86	89.66	85.97
Gene	89.87	87.32	88.68	83.45	84.98	84.23

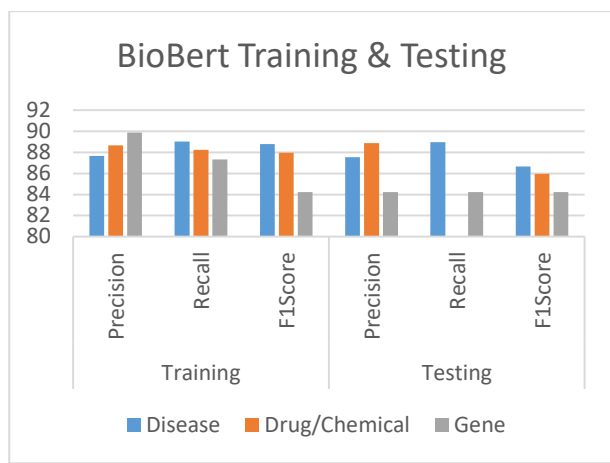


**Figure 9.** BioBERT training and testing

$$F1\ Score = \frac{2 * precision * recall}{Precision + Recall} \quad (2)$$

$$Precision = \frac{TP}{TP+FP} \quad (3)$$

$$Recall = \frac{TP}{TP+FN} \quad (4)$$

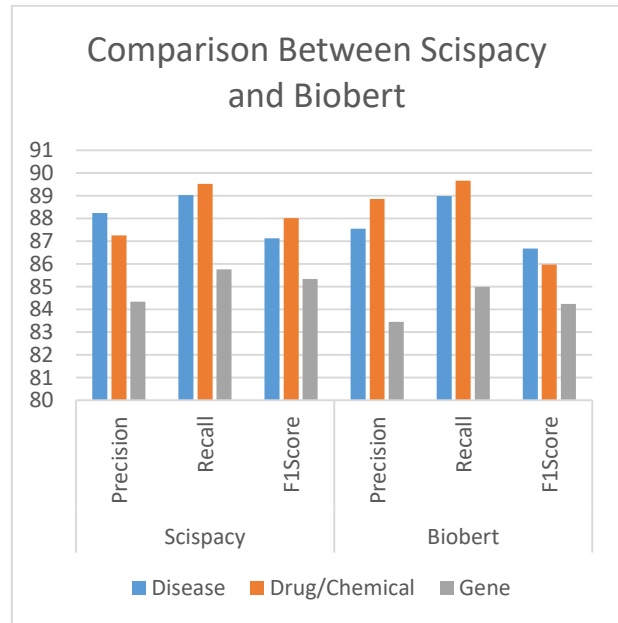
Table 2 shows the model training & testing results of the data using BioBERT model to extract the entities that are related to the medical or clinical texts. The dataset is collected from PubMed and the PMC. Figure 9 depicts the comparison of training and testing accuracy.

Table 3 shows the comparison between the Scispacy and the BioBERT. For every dataset, the precision, recall,

and F1-score of both models are displayed. The customized BioBERT model built and trained to extract the named entity of medical terms works equally good to the existing built in model Scispacy. Figure 10 depicts the comparison of precision, recall and F1Score results of the same.

**Table 3.** Comparison table

Comparison Between Scispacy and BioBERT						
	Scispacy			BioBERT		
Datasets	Precision	Recall	F1Score	Precision	Recall	F1Score
Disease	88.23	89.02	87.12	87.54	88.98	86.67
Drug/Chemical	87.25	89.52	88.01	88.86	89.66	85.97
Gene	84.34	85.76	85.34	83.45	84.98	84.23



**Figure 10.** Comparison between Scispacy and BioBERT

#### GUI:

In GUI the TensorFlow, PyTorch, and carafe, model encourage a site page where clients can get the nuances of the clinical words or components. Exactly when the client types or paste the substance in the text area and clicks analyse, the model identifies the trained named entity biomedical terms – Disease, Chemical, drug, and gene as shown in Figure.11.

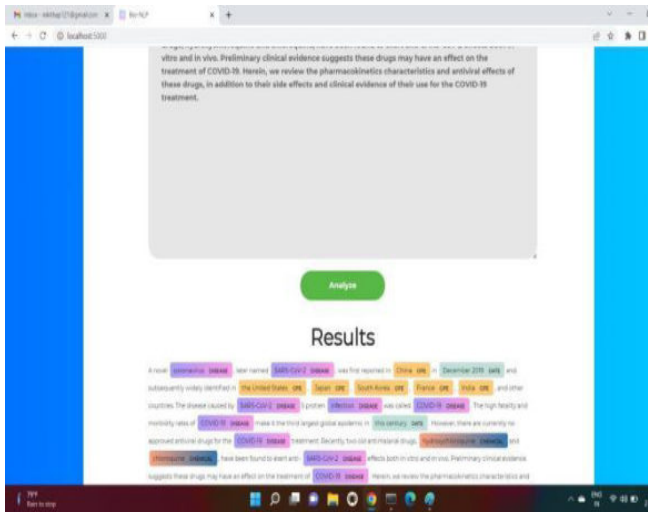


**Figure 11.** Screenshot of GUI Application

## 6. CONCLUSION

In NER, it accomplice the named components to their legitimate sorts and the entities are eliminated for the data. For a particular space model for clinical data, it will eliminate clinical terms like disease, drug, treatment, and so on. In this work the entities are isolated from the sentence for clinical data. Here we proposed a comprehensive plan for the BioNER. suggested with a novel portrayal layer, which is processed by a BiLSTM-CRF layer, based on cognitive processes. Using a combination of BioBERT and substantial level word description, the proposed system created a layer that may be employed in a variety of contexts. This representation layer is trained on the biomedical corpora and is unique in its ability to deal with phonetic issues such as polysemy, meaning, accentuation, OOV, and disruption within the biomedical composition. The proposed framework can outperform many state-of-the-art baselines and provide state-of-the-art results for BioNER. In the future, we want to extend our model to other geographies and investigate new methods for bolstering more data qualities, languages, and complexity.

## References:

- Alam, Tanvir & Schmeier, Sebastian, R. Ramachandra, K.Arutchelvan (2021). Deep Learning in Biomedical Text Mining: Contributions and Challenges. *Multiple Perspectives on Artificial Intelligence in Healthcare*. doi.org/10.1007/978-3-030-67303-1\_14, doi:10.5772/intechopen.75924

Amogh Kamat Tarcar, Aashis Tiwari, Vineet Naique Dhaimodker, Penjo Rebelo, Rahul Desai, Dattaraj Rao, (2019). Healthcare NER Models Using Language Model Pretraining. doi.org/10.48550/arXiv.1910.11241

Dani Yogatama, Cyprien de Masson d'Autume, Jerome Connor, Tomas Kociský, Mike Chrzanowski, Lingpeng Kong, Angeliki Lazaridou, Wang Ling, Lei Yu, Chris Dyer, et al, (2019). Learning and evaluating general linguistic intelligence. *arXiv preprint arXiv:1901.11373*. doi: 10.48550/arXiv.1901.11373.

Dara S, Dhamercherla S, Jadav SS, Babu CM, and Ahsan MJ,(2022). Machine Learning in Drug Discovery: A Review. *Artif Intell Rev*, 55(3), 1947-1999. doi.org/10.1007/s10462-021-10058-4

Devopedia. (2020). Named Entity Recognition. Version 5, February 4. Accessed 2022-10-09. <https://devopedia.org/named-entity-recognition>

Henghui Zhu, Ioannis C. Paschalidis, and Amir M. Tahmasebi, (2018). Clinical concept extraction with contextual word embedding. *NIPS Machine Learning for Health Workshop*. doi.org/10.48550/arXiv.1810.10566

Iz Beltagy, Kyle Lo, and Arman Cohan, (2019). Scibert: A pretrained language model for scientific text. *Proceedings of the 2019 Conference on Empirical Methods in Natural Language Processing and the 9th International Joint Conference on Natural Language Processing (EMNLP-IJCNLP)*. doi.org/10.48550/arXiv.1903.10676

Jacob Devlin, Ming-Wei Chang, Kenton Lee, and Kristina Toutanova, (2019). “BERT: Pre-training of deep bidirectional transformers for language understanding”, *In Proceedings of the 2019 Conference of the North American Chapter of the Association for Computational Linguistics: Human Language Technologies*, 4171–4186. doi.org/10.18653/v1/N19-1423

Jeremy Howard and Sebastian Ruder, (2018). Universal language model finetuning for text classification. *In Proceedings of the 56th Annual Meeting of the Association for Computational Linguistics*, 328–339. doi.org/10.18653/v1/P18-1031.

Jiao Li, Yueping Sun, Robin J. Johnson, Daniela Sciaky, ChihHsuan Wei, Robert Leaman, Allan Peter Davis, Carolyn J. Mattingly, Thomas C. Wiegers, and Zhiyong Lu, (2016). Biocreative v cdr task corpus: a resource for chemical disease relation extraction. *The Journal of Biological databases and curation*. doi.org/10.1093%2Fdatabase%2Fbaw068.

Jin-Dong Kim, Tomoko Ohta, Yoshimasa Tsuruoka, Yuka Tateisi and Nigel Collie, (2004). Introduction to the bio-entity recognition task at jnlpba. *Proceedings of the International Joint Workshop on Natural Language Processing in Biomedicine and Its Applications*, 70-75. doi.org/10.3115/1567594.1567610.

Jinhyuk Lee, Wonjin Yoon, Sungdong Kim, Donghyeon Kim, Sunkyu Kim, Chan Ho So, and Jaewoo Kang, (2019). Biobert: a pre-trained biomedical language representation model for biomedical text mining. doi.org/10.1093/bioinformatics/btz682.

Ling, Y. (2023). Bio+Clinical BERT, BERT Base, and CNN Performance Comparison for Predicting Drug Review Satisfaction. ArXiv. /abs/2308.03782. doi.org/10.48550/arXiv.2308.03782

Matthew E. Peters, Mark Neumann, Mohit Iyyer, Matt Gardner, Christopher Clark, Kenton Lee, and Luke Zettlemoyer, (2018). Deep contextualized word representations. *CoRR*, abs/1802.05365. doi.org/10.48550/arXiv.1802.05365.

Martin Krallinger, Obdulia Rabal, Florian Leitner, Miguel Vazquez, David Salgado, Zhiyong lu, Robert Leaman, Yanan Lu, Donghong Ji, Daniel Lowe, Roger Sayle, Riza Batista-Navarro, Rafal Rak, Torsten Huber, Tim Rocktschel, Srgio Matos, David Campos, Buzhou Tang, Hua Xu, and Alfonso Valencia, (2015). The chemdner corpus of chemicals and drugs and its annotation principles. *Journal of Cheminformatics*, 7(S2), 03. doi.org/10.1186/1758-2946-7-S1-S2.

Noha S Tawfik 1, Marco R Spruit 2, (2020). Evaluating sentence representations for biomedical text: Methods and experimental result. *Journal of biomedical informatics*, 104. doi.org/10.1016/j.jbi.2020.103396.

Qingyu Chen, Yifan Peng, and Zhiyong Lu, (2019). Biosentvec: creating sentence embeddings for biomedical texts. *2019 IEEE International Conference on Healthcare Informatics (ICHI)*, pages 1–5. doi.org/10.1109/ICHI.2019.8904728.

Padmanandam K, Sunitha K, Jafari B M, Jafari A, Zhao, M, and Pitla N,(2023). Customized Named Entity Recognition Using Bert for the Social Learning Management System Platform CourseNetworking. *Journal of Computer Science*, 20(1), 88-95. doi.org/10.3844/jcssp.2024.88.95

Pengfei Liu, Xipeng Qiu, and Xuanjing Human, (2016). Recurrent neural network for text classification with multi-task learning. *arXiv preprint arXiv:1605.05101*. doi.org/10.48550/arXiv.1605.05101

R Ramachandran 1, K Arutchelvan, (2021). Named entity recognition on bio-medical literature documents using hybrid-based approach. *Journal of Ambient Intelligence and Humanized Computing*. doi.org/10.1007/s12652-021-03078-z

Rezarta Islamaj Dounduffedan, Robert Leaman, and Zhiyong LU, (2014). NCBI disease corpus: a resource for disease name recognition and concept normalization. doi: 10.1016/j.jbi.2013.12.006.

Rie Kubota Ando, (2007). Biocreative II Gene Mention Tagging System At IBM Watson. [https://riejohnson.com/rie/Ando\\_biocreative\\_cr.pdf](https://riejohnson.com/rie/Ando_biocreative_cr.pdf)

Sampo Pyysalo, Filip Ginter, Hans Moen, Tapio Salakoski, and Sophia Ananiadou, (2013). Distributional semantics resources for biomedical text processing. <http://lmb2013.biopathway.org/lmb2013proceedings.pdf>

Tomas Mikolov, Ilya Sutskever, Kai Chen, Greg S Corrado, and Jeff Dean, (2013). Distributed representations of words and phrases and their compositionality. In Advances in neural information processing systems. pages 3111–9. doi.org/10.48550/arXiv.1310.4546

Vikas Yadav and Steven Bethard, (2019). A survey on recent advances in named entity recognition from deep learning models. doi.org/10.48550/arXiv.1910.11470

Xipeng Qiu, Tianxiang Sun, Yige Xu, Yunfan Shao, Ning Dai, and Xuanjing Huang, (2020). Pre-trained models for natural language processing: A survey. *arXiv preprint arXiv:2003.0827*. doi:10.48550/arXiv.2003.08271

Xiaodong Liu, Pengcheng He, Weizhu Chen, and Jianfeng Gao, (2019). Multitask deep neural networks for natural language understanding. *arXiv preprint arXiv:1901.11504*. doi.org/10.48550/arXiv.1901.11504

Yuqi Si, Jingqi Wang, Hua Xu, and Kirk Roberts, (2019). Enhancing clinical concept extraction with contextual embeddings. *Journal of the American Medical Informatics Association*, 26(11),1297–1304. doi.org/10.1093/jamia/ocz096

Yifan Peng, Shankai Yan, and Zhiyong Lu, (2019). Transfer learning in biomedical natural language processing: An evaluation of bert and elmo on ten benchmarking datasets. doi.org/10.48550/arXiv.1906.05474

Zhenzhong Lan, Mingda Chen, Sebastian Goodman, Kevin Gimpel, Piyush Sharma, and Radu Soricut, (2019). Albert: A lite bert for self-supervised learning of language representations. doi.org/10.48550/arXiv.1909.11942

---

**Kayal Padmanandam**

BVRIT HYDERABAD College of  
Engineering for Women,  
Hyderabad,  
India  
[kayalpaddu@gmail.com](mailto:kayalpaddu@gmail.com)  
0000-0002-3872-8422

**Nikitha Pitla**

BVRIT HYDERABAD College of  
Engineering for Women,  
Hyderabad,  
India  
[nikithap121@gmail.com](mailto:nikithap121@gmail.com)  
0009-0000-7997-2547

**Yeshasvi Mogula**

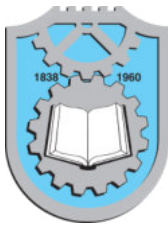
BVRIT HYDERABAD College of  
Engineering for Women,  
Hyderabad,  
India  
[yeshasvireddy26@gmail.com](mailto:yeshasvireddy26@gmail.com)  
0009-0007-2233-2320

---

**P. S.Brahmanandam**

Dept. of Physics  
&  
R&D Cell  
Shri Vishnu Engineering College for  
Women(A), Bhimavaram  
India  
[dranandpotula@svecw.edu.in](mailto:dranandpotula@svecw.edu.in)  
0000-0001-9777-3496

---



## STRUCTURE BASED DRUG DESIGN METHOD: MOLECULAR DOCKING STUDY ON ANDROGENIC RECEPTOR AND PROSTATE SPECIFIC ANTIGEN WITH POTENTIAL LEAD MOLECULES

K Ganesh Kadiyala<sup>1</sup>

K. Jagadeesh

Ch. Geetika

I. Lakshmi Lavanya

B. Kanaka Durga

J. Suresh Kumar

Bachina Kiran

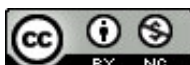
B. N. Suresh Varma Dendukuri

Keywords:

### A B S T R A C T

*Androgenic Receptor, Prostate Specific Antigen, Docking, Enzalutamide, Abiraterone, Apalutamide, Galeterone, Ligands, Van der Waals interactions.*

*Molecular docking simulations were conducted to analyze the interactions between eight lead molecules with AR and PSA proteins. The lead molecules included Enzalutamide, Abiraterone, Docetaxel, Apalutamide, Cabazitaxel, Bicalutamide, Curcumin, Galeterone, Resveratrol, and Darolutamide. For the Androgen Receptor (AR), Enzalutamide displayed the most favorable docking energy of -10.96Kcal/mol, followed by Galeterone (-10.52Kcal/mol) and Darolutamide (-9.97Kcal/mol). The binding affinities of these compounds to AR suggest potential inhibitors. On the other hand, resveratrol exhibited the strongest interaction with the AR protein (-8.02Kcal/mol) among the natural compounds studied (Resveratrol and Curcumin). In the case of Prostate Specific Antigen (PSA), Abiraterone showed a docking energy of -9.14 kcal/mol, indicating a potential interaction with PSA. The docking results suggest that Enzalutamide, Galeterone, and Darolutamide, hold promise as potential inhibitors for the Androgen Receptor in prostate cancer treatment. Abiraterone, Enzalutamide, Apalutamide ligands shown a significant interaction on Prostate Specific Antigen, hinting at its potential as a dual-target agent.*



© 202x Published by Faculty of Engineering

### 1. INTRODUCTION

Prostate cancer stands as one of the most prevalent and clinically challenging malignancies affecting men worldwide, with an estimated 1.4 million new cases

diagnosed in 2020 alone (Bray et al. 2018). Despite significant advancements in diagnostic tools and therapeutic strategies, the quest for targeted and efficacious treatments remains an ongoing pursuit. This complex disease arises from its heterogeneous nature,

<sup>1</sup> K Ganesh Kadiyala, Department of Chemistry, Shri Vishnu Engineering College for Women, Bhimavaram-534202, Andhra Pradesh, India, E-mail: [kganeshkadiyala@gmail.com](mailto:kganeshkadiyala@gmail.com)

encompassing various molecular subtypes and intricate signalling pathways (Adam et al. 2015). As a result, precision medicine approaches that selectively target aberrant signalling cascades while sparing healthy tissues have become increasingly crucial (Manzari et al. 2021).

The relationship between PSA (prostate-specific antigen) and the androgen receptor is interdependent within the realm of prostate health and pathology (Saxena et al. 2012; Kim and Coetze 2004). Prostate-specific antigen (PSA) serves as an indicator of androgen receptor activation and is frequently employed in the screening and surveillance of prostate cancer (Balk et al. 2003). The androgen receptor, however, plays a crucial role in the regulation of prostate function and is frequently the focus of therapeutic interventions for prostate cancer aimed at impeding the advancement of the illness (Ahmed, Ali, and Sarkar 2014). The inclusion of these two elements is of utmost importance when examining, controlling, and addressing prostate-related ailments, specifically prostate cancer (Koochekpour 2010).

In recent years, the field of prostate cancer research has seen a surge in the application of computational methods, particularly molecular docking, in the discovery of novel therapeutic agents (Ongaba, Ndekezi, and Nakiddu 2022). Molecular docking, rooted in structural biology, enables researchers to predict and analyse the interactions between small molecules and the three-dimensional structures of target proteins (Kitchen 2004) (Rajendra Prasad et al. 2013). By simulating the binding process, docking studies hold the promise of identifying novel drug candidates (Reddy et al. 2014) that can disrupt pivotal cellular pathways driving prostate cancer progression (Durrant and McCammon 2011). It is imperative to acknowledge that although the utilization of PSA testing has proven beneficial in many instances for the timely identification of prostate cancer, (Thompson and Ankerst 2007) it has also resulted in the excessive diagnosis and treatment of the condition. Hence, the determination to undergo prostate-specific antigen (PSA) testing and any consequent medical interventions have to be predicated upon a comprehensive dialogue between the patient and their healthcare practitioner, taking into account individual circumstances and preferences.

The exponential growth in available protein structures and computational resources has fueled the application of docking research in prostate cancer drug discovery. This approach offers a streamlined way to identify potential drug candidates with enhanced specificity and reduced adverse effects (Lavecchia and Giovanni 2013). Moreover, molecular docking plays a pivotal role in elucidating protein-ligand interactions, assessing binding affinities, and guiding the optimization of lead compounds (Shoichet and Kuntz 1991). The utilization of docking software enables the anticipation of drug molecule polarity (Kadiyala et al. 2015) and the bonding contact between ligands and the active site of proteins. As the field of prostate cancer drug discovery

continues to evolve, harnessing the power of molecular docking offers a compelling avenue for the identification of innovative therapeutic agents (Meng et al. 2020).

This study aims to make a significant contribution to the expanding field of docking research in prostate cancer. Its objective is to advance precision medicine and enhance the quality of life for individuals impacted by this intricate disease. This research paper provides a comprehensive overview of the existing state of docking research in prostate cancer therapeutics. Further, this study aims to investigate the substantial impact of molecular docking techniques in the elucidation of protein-ligand interactions involving the Androgen receptor and Prostate cancer Antigen. It will involve the evaluation of binding affinities and the utilization of these findings to facilitate the optimization of lead compounds (ligands). Furthermore, an exploration of the obstacles and constraints associated with docking studies will be undertaken, with a particular focus on the significance of including experimental validation to effectively transform computational discoveries into practical clinical applications (Huang, Grinter, and Zou 2010).

## 2. MATERIALS AND METHODS

### 2.1 Determination of target receptors and the lead ligands

The protein obtained from the Protein Data Bank (PDB) possesses a fully assigned charge. Therefore, prior to the docking process utilizing Auto Dock Software, we included polar hydrogens and Kollman charges into the macromolecule. The outcomes of the macromolecule docking process may exhibit variability when water molecules are present. Water molecules were eliminated from the macromolecule in order to mitigate any undesired protein behavior during the execution of docking tests.

The protein Androgen Receptor, sourced from the Protein Data Base (PDB), is associated with a distinct ligand known as metribolone (R1881) (NCBI 2023, CID 261000). During the process of docking with other ligands, these ligands are displaced from their binding sites in order to investigate the behavior of the selected ligand in a more focused manner. The employed structure entails a crystal structure that is bound to ligand(s). Consequently, in order to successfully dock the intended ligand onto the protein at that specific location, it is necessary to eliminate the associated ligand by eliminating the heteroatoms from the PDB file. The precise location of the active site inside the protein remains undetermined. Blind docking was employed in this study, wherein the full protein surface was chosen for the purpose of protein-ligand interaction. After establishing the grid box for blind docking, the protein is subsequently stored in the PDBQT format.

## 2.2 Target protein preparation for docking studies using autodock

### Androgen Receptor (AR)

The protein taken from Protein Data Base (PDB) does have the complete charge assigned to it. Hence, we added polar hydrogens and Kollman charges to the macromolecule prior to the docking process using the Auto Dock Software. The results of the docking of the macromolecule may vary when it has water molecules. Water molecules from the macromolecule were removed to avoid any unwanted behavior of the protein while performing docking studies. The protein Androgen Receptor taken from the PDB has a unique ligand metribolone (R1881). This ligand is deleted while performing docking with other ligands to study the behavior of the selected ligand more specifically. The structure utilized in this context is a crystal structure that is complexed with ligands. Consequently, in order to perform docking of the intended ligand with the protein at the specified position, it is necessary to eliminate the attached ligands by removing the heteroatoms from the PDB file. The active site for the protein is unknown. So, we chose blind docking by selecting the entire protein surface for the protein ligand interaction. Once the grid box for blind docking is set, the protein is saved in PDBQT format.

### Prostate Specific Antigen (PSA)

The protein taken from PDB does have the complete charge assigned to it. Hence, we added polar hydrogens and Kollman charges to the macromolecule prior to the docking process using Auto Dock Software. The results of the docking of the macromolecule may vary when it has water molecules. So, we removed water molecules from the macromolecule to avoid any unwanted behavior of the protein while performing docking studies. The employed structure entails a crystal structure that is bound to the ligand(s). Consequently, in order to successfully dock the intended ligand onto the protein at that specific location, it is imperative to eliminate the associated ligand by eliminating the heteroatoms from the PDB file. The active site for the protein is unknown. So, we chose blind docking by selecting the entire protein surface for the protein ligand interaction. Once the grid box for blind docking is set, the protein is saved in PDBQT format.

### Collection of Ligands from sources and Preparation for docking studies using auto dock

All the ligands are taken from PubChem. The ligands from PubChem are taken in .SDF format. Open Babel software is used to convert the .SDF format to PDBQT format as auto dock supports. PDBQT format. Using Auto Dock software, the root of the ligand is detected and choose. The ligand must also be saved in PDBQT format along with the target protein using Auto Dock software. The ligands used for docking with both the proteins are Enzalutamide (NCBI 2023, CID 15951529), Abiraterone

(NCBI 2023, CID 132971), Apalutamide (NCBI 2023, AID 2375), Bicalutamide (NCBI 2023, CID 67171867), Darolutamide (NCBI 2023, CID 9854073), Galeterone (NCBI 2023, CID 11188409), Resveratrol (NCBI 2023, CID 445154), and Curcumin (NCBI 2023, CID 969516). We intend to compare the docking simulations using these ligands to evaluate their effectiveness in binding to the active sites of the PSA and AR receptors.

### Analysis of the docking results

The .DLG file which is obtained after running the auto grid and auto dock processes is studied to obtain the values of docking energy, RMSD, which measures the difference between the native ligands' positions before docking and after redocking, total internal energy, Inhibition Constant (CI), which play an important role in defining the ligand and protein. All these values for the 10 unique ligands are tabularized for finding the best protein-ligand pairs. We used Discovery studios software to analyse the results in 3-D and 2-D format. The images talk about the position of the ligand on the surface of the protein in 3-D f and 2-D formats. It also tells us the interactions like van der Waals, pi-lone pair, alkyl, pi-alkyl, and conventional hydrogen bond etc. between the atoms of protein and the ligand.

## 3. RESULTS AND DISCUSSION

The evaluation of the docking interactions involving the receptors PSA and AR and the selected lead ligands has been conducted, and the resulting findings have been documented in Table 1, correspondingly. The binding affinity between a ligand and the active site of a protein is positively correlated with the number of interactions. Consequently, an increase in the number of interactions leads to an improvement in binding affinity, ultimately resulting in the development of a favorable docking score. The inhibition constant (IC) is a measure of the concentration of the ligand needed to effectively inhibit the activity of the corresponding protein. If the IC value is lower for a specific ligand, it indicates that the ligand is superior and exhibits a strong affinity at the active site for the specific protein.

The ligand Enzalutamide (depicted in Figures 1.1 and 2.1) has exhibited a docking score of -10.96 Kcal/mol and -7.95 Kcal/mol, in addition to an inhibitory constant (IC) of 9.23 nm and 1.49  $\mu$ M on the androgen receptor (AR) and prostate-specific antigen (PSA) receptors, respectively. The ligand Enzalutamide has demonstrated over 15 distinct bonding interactions, including Van der Waals forces, conventional hydrogen bonding, pi-sigma contacts, pi-pi stacking, alkyl interactions, and pi-alkyl interactions, inside the active region of the androgen receptor protein. While coming to the PSA the ligand has shown less than 8 distinct bonding interactions, including van der Waals, conventional hydrogen bonding, pi-sigma and pi-alkyl interactions.

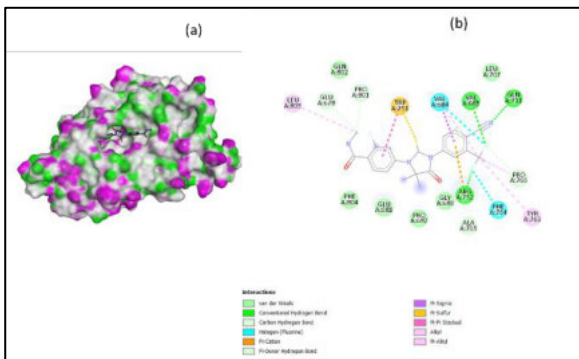


**Figure 1.1(a):** 3-D representation of AR protein and Enzalutamide ligand interaction, (b): 2-D representation of AR protein and Enzalutamide ligand interaction

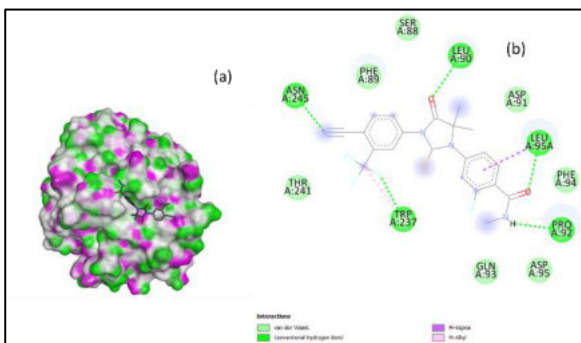


**Figure 2.1.** (a): 3-D representation of PSA protein and Enzalutamide ligand interaction, (b): 2-D representation of PSA protein and Enzalutamide ligand interaction

The compound Galeterone, represented by Figures 1.2 and 2.2, has exhibited a docking score of -10.52 Kcal/mol and -1.78 Kcal/mol for the androgen receptor (AR) and prostate-specific antigen (PSA) receptors, respectively. Additionally, it has demonstrated inhibitory constants (IC) of 19.35 nm and 300  $\mu$ M for the AR and PSA receptors, respectively.

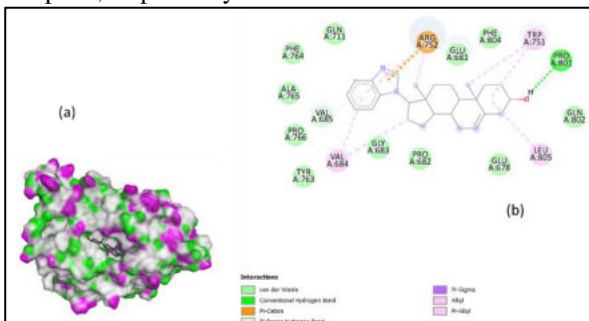


**Figure 1.2.** (a): 3-D representation of AR protein and Galeterone ligand interaction, (b): 2-D representation of AR protein and Galeterone ligand interaction.

Galeterone has demonstrated a total of eight distinct interaction sites with the androgen receptor (AR). These sites encompass a range of intermolecular forces, such as Van der Waals forces, conventional hydrogen bonding, pi-sigma contacts, pi-pi stacking, alkyl interactions, and pi-alkyl interactions. These interactions occur inside the

active region of the androgen receptor protein. Among the identified eight ligands, galeterone has minimal interactions with the prostate-specific antigen (PSA) (Figure 2.2).

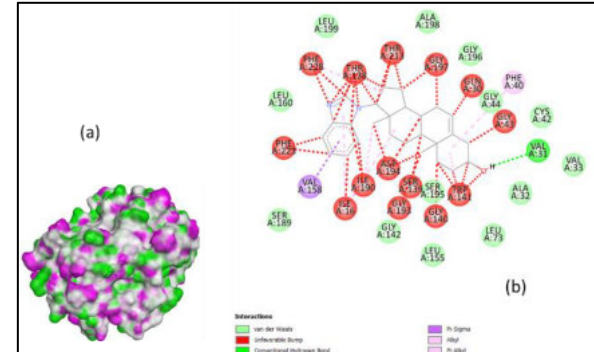


**Figure 2.2.** (a): 3-D representation of PSA protein and Galeterone ligand interaction, (b): 2-D representation of PSA protein and Galeterone ligand interaction

The ligand Darolutamide (Figures 1.3 and 2.3) has exhibited a docking score of -9.97 Kcal/mol and -6.89 Kcal/mol, as well as an inhibitory constant (IC) of 49.02 nm and 8.95  $\mu$ M on the androgen receptor (AR) and prostate-specific antigen (PSA) receptors, respectively.

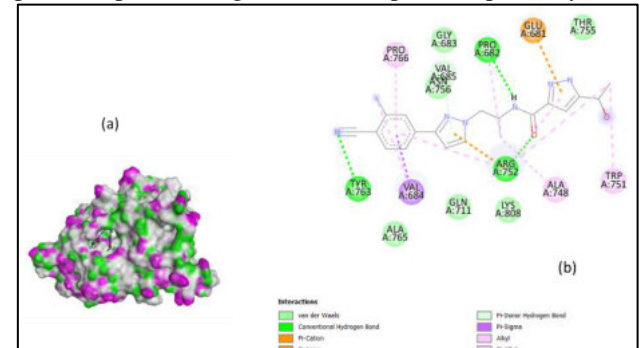


**Figure 1.3.** (a): 3-D representation of AR protein and Darolutamide ligand interaction, (b): 2-D representation of AR protein and Darolutamide ligand interaction

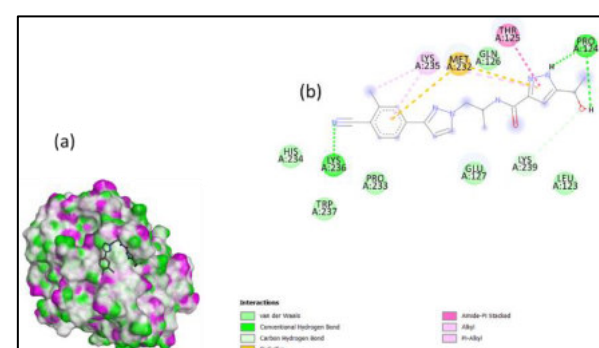


**Figure 2.3.** (a): 3-D representation of PSA protein and Darolutamide ligand interaction, (b): 2-D representation of PSA protein and Darolutamide ligand interaction

The ligand darolutamide exhibited interactions with over 14 interactions at the active site on the androgen receptor (AR). Specifically, darolutamide demonstrated 10

interactions with the prostate-specific antigen (PSA) protein at its active site. The findings indicate that darolutamide exhibits favorable interactions with the androgen receptor (AR) in comparison to prostate-specific antigen (PSA).

The ligand Bicalutamide, as depicted in Figures 1.4 and 2.4, has exhibited a docking score of -9.84 Kcal/mol and -6.36 Kcal/mol for the androgen receptor (AR) and prostate-specific antigen (PSA) receptors, respectively. Additionally, it has demonstrated inhibitory constants (IC) of 67.35 nm and 21.61  $\mu$ M for the AR and PSA receptors, respectively. Bicalutamide has demonstrated over nine contacts at the active site of the androgen receptor (AR) and over 15 interactions at the active site of the prostate-specific antigen (PSA), indicating a strong binding affinity with both receptors. These interactions encompass a variety of types, highlighting the robust nature of the binding.

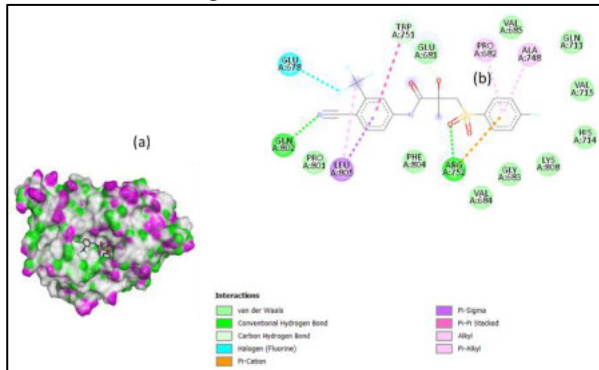


**Figure 1.4.** (a): 3-D representation of AR protein and Bicalutamide ligand interaction, (b): 2-D representation of AR protein and Bicalutamide ligand interaction

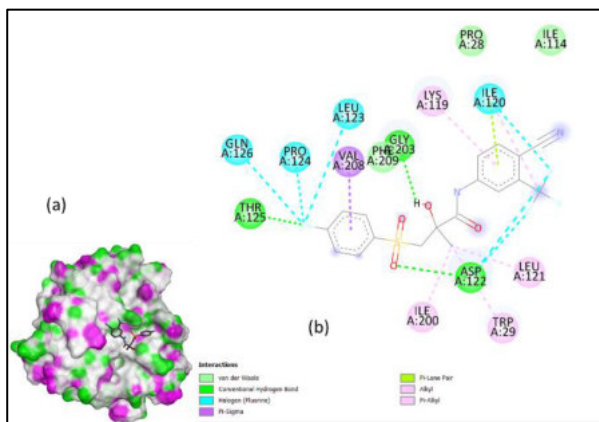


**Figure 2.4.** (a): 3-D representation of PSA protein and Bicalutamide ligand interaction, (b): 2-D representation of PSA protein and Bicalutamide ligand interaction

The ligand Abiraterone (Figures 1.5 and 2.5) has exhibited a docking score of -8.68 Kcal/mol and -9.14 Kcal/mol, as well as an inhibitory constant (IC) of 434.41 nm and 201.19 nM on the androgen receptor (AR) and prostate-specific antigen (PSA) receptors, respectively. Abiraterone is one of the eight ligands that have been

chosen due to their significant bonding interactions with both proteins. Abiraterone exhibits a higher binding affinity towards the prostate-specific antigen (PSA) in comparison to seven other ligands. This enhanced affinity is attributed to the appropriate interactions that occur at the active site.

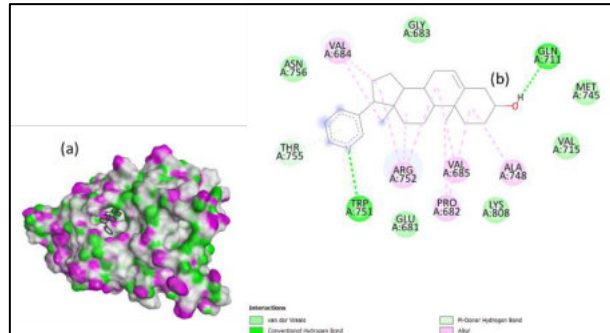


**Figure 1.5.** (a): 3-D representation of AR protein and Abiraterone ligand interaction, (b): 2-D representation of AR protein and Abiraterone ligand interaction

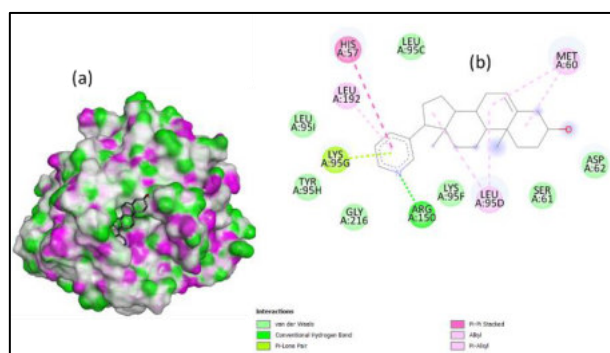


**Figure 2.5.** (a): 3-D representation of PSA protein and Abiraterone ligand interaction, (b): 2-D representation of PSA protein and Abiraterone ligand interaction

The ligand Apalutamide (refer to Figures 1.6 and 2.6) has exhibited a docking score of -8.50 Kcal/mol and -7.41 Kcal/mol, in addition to an inhibitory constant (IC) of 584.63 nM and 3.71 uM on the androgen receptor (AR) and prostate-specific antigen (PSA) receptors, respectively. Among the eight selected ligands following Abiraterone, the Apalutamide ligand had a favorable interaction with the prostate-specific antigen (PSA).

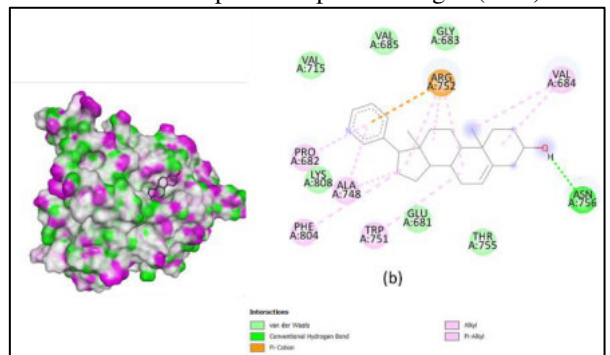


**Figure 1.6.** (a): 3-D representation of AR protein and Apalutamide ligand interaction, (b): 2-D representation of AR protein and Apalutamide ligand interaction

Furthermore, Apalutamide displayed a strong binding affinity with the active sites of the androgen receptor (AR).

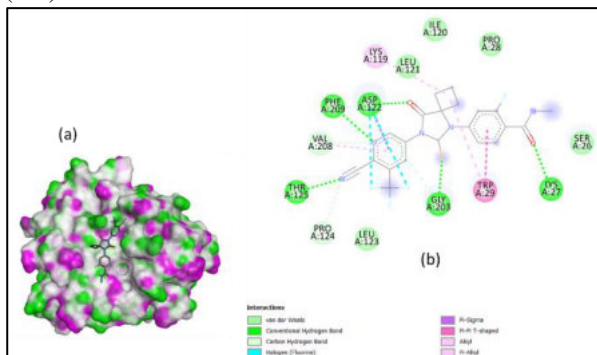


**Figure 2.6.** (a): 3-D representation of PSA protein and Apalutamide ligand interaction, (b): 2-D representation of PSA protein and Apalutamide ligand interaction

The ligand Resveratrol, as depicted in Figures 1.7 and 2.7, has exhibited a docking score of -8.02 Kcal/mol and -6.03 Kcal/mol for the androgen receptor (AR) and prostate-specific antigen (PSA) receptors, respectively. Additionally, Resveratrol has demonstrated inhibitory constants (IC) of 1.33 uM and 38.13 uM for the AR and PSA receptors, respectively.

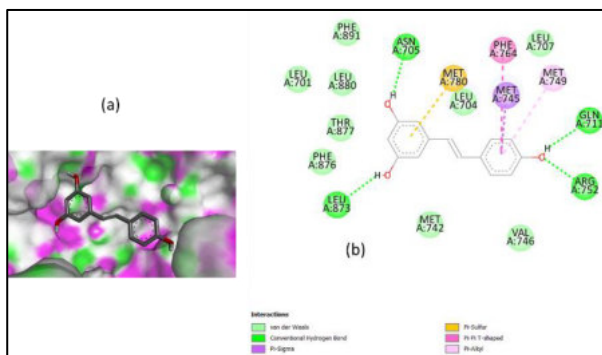


**Figure 1.7.** (a): 3-D representation of AR protein and Resveratrol ligand interaction, (b): 2-D representation of AR protein and Resveratrol ligand interaction.

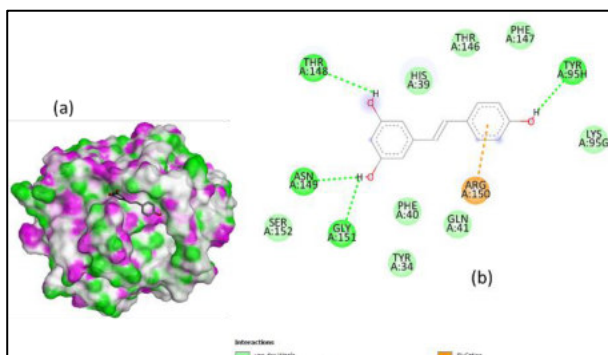


**Figure 2.7.** (a): 3-D representation of PSA protein and Resveratrol ligand interaction, (b): 2-D representation of PSA protein and Resveratrol ligand interaction

Resveratrol has demonstrated over seven distinct binding interactions with the androgen receptor (AR) in its active site, including van der Waals forces, covalent hydrogen bonding, Pi-sigma contacts, Pi-stalk interactions, Pi-pi shaped interactions, and pi-alkyl interactions. Simultaneously, the active site of PSA has exhibited over five interactions, including van der Waals forces, typical hydrogen bonding, pi-cation interactions, and pi-alkyl interactions.

The ligand Curcumin, depicted in Figures 1.8 and 2.8, has exhibited a docking score of -5.96 Kcal/mol and -5.51 Kcal/mol, as well as an inhibitory constant (IC) of 43.01 uM and 91.40 uM on the androgen receptor (AR) and prostate-specific antigen (PSA) receptors, respectively. Curcumin exhibits a multitude of interactions, exceeding nine in number, at the active sites of the androgen receptor (AR). These interactions include van der Waals forces, conventional hydrogen bonding, Pi-sigma contacts, Pi-pi, T-shaped interactions, alkyl interactions, and pi-alkyl interactions. Curcumin exhibits over ten distinct interactions at the active site of the prostate-specific antigen (PSA), including van der Waals forces, typical hydrogen bonding, pi-sigma interactions, alkyl interactions, and pi-alkyl interactions.

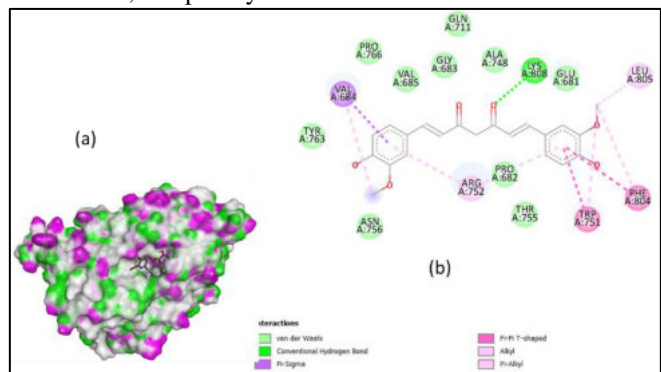


**Figure 1.8.** (a): 3-D representation of AR protein and Curcumin ligand interaction, (b): 2-D representation of AR protein and Curcumin ligand interaction.

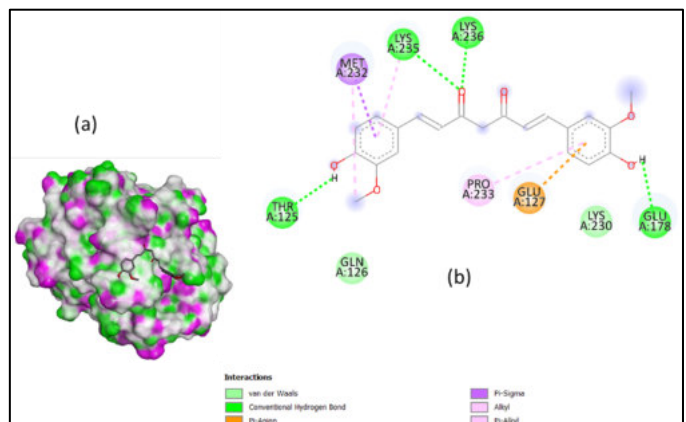


**Figure 2.8.** (a): 3-D representation of PSA protein and Curcumin ligand interaction, (b): 2-D representation of PSA protein and Curcumin ligand interaction

Among the examined set of eight ligands, Enzalutamide has demonstrated a favorable binding affinity towards the Androgen-Receptor (AR), as evidenced by a docking score of -10.96 Kcal/mol. Additionally, Enzalutamide has exhibited a notable inhibitory constant of 9.23 nM. Regarding the case of prostate-specific antigen (PSA), it has been observed that the Abiraterone ligand has a

favorable binding affinity, as evidenced by a docking score of -9.14 Kcal/mol and an inhibition constant value of 201.9 nM. Apalutamide has also shown a good binding score and exhibited a good binding affinity with -7.41 Kcal/mol with PSA with inhibition constant value of 3.71  $\mu$ M followed by Abiraterone (shown in Table 1).

**Table 1.** Comparing of the Docking results of multiple ligands (Lead Ligands) interaction on the Androgen Receptor (AR) and Prostate Specific Antigen (PSA)

S.No	Lead Molecule	Target Protein	Docked Energy (Kcal/mol)	Inhibition Constant (IC)	Target Protein	Docked Energy (Kcal/mol)	Inhibition Constant (IC)
1.	Enzalutamide	Androgen-Receptor (AR)	-10.96	9.23 nM	Prostate Specific Antigen (PSA)	-7.95	1.49 $\mu$ M
2.	Galeterone	Androgen-Receptor (AR)	-10.52	19.35 nM	Prostate Specific Antigen (PSA)	-1.78	300 $\mu$ M
3.	Darolutamide	Androgen-Receptor (AR)	-9.97	49.02 nM	Prostate Specific Antigen (PSA)	-6.89	8.95 $\mu$ M
4.	Bicalutamide	Androgen-Receptor (AR)	-9.84	61.35 nM	Prostate Specific Antigen (PSA)	-6.36	21.61 $\mu$ M
5.	Abiraterone	Androgen-Receptor (AR)	-8.68	434.41 nM	Prostate Specific Antigen (PSA)	-9.14	201.19 $\mu$ M
6.	Apalutamide	Androgen-Receptor (AR)	-8.50	584.63 nM	Prostate Specific Antigen (PSA)	-7.41	3.71 $\mu$ M
7.	Resveratrol	Androgen-Receptor (AR)	-8.02	1.33 $\mu$ M	Prostate Specific Antigen (PSA)	-6.03	38.13 $\mu$ M
8.	Curcumin	Androgen-Receptor (AR)	-5.96	43.01 $\mu$ M	Prostate Specific Antigen (PSA)	-5.51	91.40 $\mu$ M

#### 4. CONCLUSION

The receptors PAS and AR are the primary target receptors implicated in the context of prostate cancer. In this study, we have selected eight lead ligands or medications to conduct a comparative analysis of their docking scores and Inhibition constant values. The objective is to predict the binding affinity of these ligands towards specific receptors known to be associated with prostate cancer.

Enzalutamide, one of the eight lead ligands, has demonstrated a favorable binding affinity with a docking score of -10.96 Kcal/mol and an IC value of 9.23 nM on AR. The analysis of the docking poses revealed that the ligand Enzalutamide exhibited favorable van der Waals interactions, hydrogen bonding, and carbon-hydrogen

bonding within the binding pocket of the androgen receptor (AR). Regarding the matter of PSA, it is noteworthy that half of the lead ligands (specifically, 4 out of 8) did not exhibit a favorable binding affinity during the docking process. However, it is worth mentioning that among the chosen ligands, the Abiraterone ligand demonstrated a docking score of -9.14 Kcal/mol and an IC value of 200.119 nM. The binding pocket of the prostate androgen receptor demonstrated positive interactions with abiraterone, including van der Waals contacts, conventional hydrogen bonding, pi-pi stacking interactions, and alkyl interactions. Based on the findings, it may be inferred that Enzalutamide and Abiraterone exhibit favorable binding affinity as ligands towards the androgen receptor (AR) and prostate-specific antigen (PSA), respectively, as compared to the other selected lead ligands. Resveratrol has demonstrated favorable binding affinity on androgen receptor (AR) and

prostate-specific antigen (PSA) compared to curcumin, both of which are natural ligands.

Hence, out of the eight lead ligands that were chosen, four to five ligands have demonstrated favorable binding interactions with the specified proteins, namely PSA and AR with good docking energy and less inhibition constant value.

## References:

- Adam A. (2015) Cancer Genome Atlas Research Network. The Molecular Taxonomy of Primary Prostate Cancer. *Cell*, 163(4), 1011–1025. doi:10.1016/j.cell.2015.10.025
- Ahmed, A., Ali, S., & Sarkar, F. H. (2014). Advances in androgen receptor targeted therapy for prostate cancer. *Journal of Cellular Physiology*, 229(3), 271–276. doi:10.1002/jcp.24456
- Balk, S. P., Ko, Y. J., & Bubley, G. J. (2003). Biology of prostate-specific antigen. *Journal of Clinical Oncology*, 21(2), 383–391. doi:10.1200/JCO.2003.02.083
- Bray, F., Ferlay, J., Soerjomataram, I., Siegel, R. L., Torre, L. A., & Jemal, A. (2018). Global cancer statistics 2018: GLOBOCAN estimates of incidence and mortality worldwide for 36 cancers in 185 countries. *CA: A Cancer Journal for Clinicians*, 68(6), 394–424. doi:10.3322/caac.21492
- Durrant, J. D., & McCammon, J. A. (2011). Molecular dynamics simulations and drug discovery. *BMC Biology*, 9, 71. doi:10.1186/1741-7007-9-71
- Huang, S. Y., Grinter, S. Z., & Zou, X. (2010). Scoring functions and their evaluation methods for protein-ligand docking: Recent advances and future directions. *Physical Chemistry Chemical Physics*, 12(40), 12899–12908. doi:10.1039/c0cp00151a
- Kadiyala, K. G., Tyagi, T., Kakkar, D., Chadha, N., Chuttani, K., Roy, B. G., Datta, A. (2015). Picolinic acid based acyclic bifunctional chelating agent and its methionine conjugate as potential SPECT imaging agents: Syntheses and preclinical evaluation. *RSC Advances*, 5(43), 33963–33973. doi:10.1039/C4RA13690J
- Kim, J., & Coetzee, G. A. (2004). Prostate specific antigen gene regulation by androgen receptor. *Journal of Cellular Biochemistry*, 93(2), 233–241. doi:10.1002/jcb.20228
- Kitchen, D. B., Decornez, H., Furr, J. R., & Bajorath, J. (2004). Docking and scoring in virtual screening for drug discovery: Methods and applications. *Nature Reviews. Drug Discovery*, 3(11), 935–949. doi:10.1038/nrd1549
- Koochekpour, S. (2010). Androgen receptor signaling and mutations in prostate cancer. *Asian Journal of Andrology*, 12(5), 639–657. doi:10.1038/aja.2010.89
- Lavecchia, A., & Di Giovanni, C. (2013). Virtual screening strategies in drug discovery: A critical review. *Current Medicinal Chemistry*, 20(23), 2839–2860. doi:10.2174/09298673113209990001
- Manzari, M. T., Shamay, Y., Kiguchi, H., Rosen, N., Scaltriti, M., & Heller, D. A. (2021). Targeted drug delivery strategies for precision medicines. *Nature Reviews. Materials*, 6(4), 351–370. doi:10.1038/s41578-020-00269-6
- Meng, X., Cui, L., Song, F., Luan, M., Ji, J., Si, H., Zhai, H. (2020). 3D-QSAR and Molecular Docking Studies on Design Anti-Prostate Cancer Curcumin Analogues. *Current Computer-Aided Drug Design*, 16(3), 245–256. doi:10.2174/1573409914666181029123746
- Ongaba, T., Ndekezi, C., & Nakiddu, N. (2022). A Molecular Docking Study of Human STEAP2 for the Discovery of New Potential Anti-Prostate Cancer Chemotherapeutic Candidates. *Frontiers in Bioinformatics*, 2, 869375. doi:10.3389/fbinf.2022.869375
- Rajendra Prasad, V. V. S., Deepak Reddy, G., Appaji, D., Peters, G. J., & Mayur, Y. C. (2013). Chemosensitizing acridones: In vitro calmodulin dependent cAMP phosphodiesterase inhibition, docking, pharmacophore modeling and 3D QSAR studies. *Journal of Molecular Graphics and Modelling*, 40, 116–124. doi:10.1016/j.jmgm.2012.12.009
- National Center for Biotechnology Information. (2023). PubChem compound summary for CID 11188409, galeterone. Retrieved from <https://pubchem.ncbi.nlm.nih.gov/compound/Galeterone>.
- National Center for Biotechnology Information. (2023). PubChem compound summary for CID 132971, abiraterone.

## 5. ACKNOWLEDGMENTS

The authors would like to express their gratitude towards the management of Shri Vishnu Engineering College for Women (A), Bhimavaram for their logistic support, without which it would not have been possible to carry out this work.

Retrieved from <https://pubchem.ncbi.nlm.nih.gov/compound/Abiraterone>.

- National Center for Biotechnology Information. (2023). PubChem Bioassay Record for AID 2375, Panel results of Cell based ELISA Assessing Activation of Cdc42 and Rac1, Source: NMMLSC. Retrieved from <https://pubchem.ncbi.nlm.nih.gov/bioassay/237>.
- National Center for Biotechnology Information. (2023). PubChem compound summary for CID 445154, resveratrol. Retrieved from <https://pubchem.ncbi.nlm.nih.gov/compound/Resveratrol>.
- National Center for Biotechnology Information. (2023). PubChem compound summary for CID 67171867, darolutamide. Retrieved from <https://pubchem.ncbi.nlm.nih.gov/compound/Darolutamide>.
- National Center for Biotechnology Information. (2023). PubChem compound summary for CID 969516, curcumin. Retrieved from <https://pubchem.ncbi.nlm.nih.gov/compound/Curcumin>.
- National Center for Biotechnology Information. (2023). PubChem compound summary for CID 9854073, cabazitaxel. Retrieved from <https://pubchem.ncbi.nlm.nih.gov/compound/Cabazitaxel>.
- National Center for Biotechnology Information. (2023). PubChem compound summary for CID 15951529, enzalutamide. Retrieved from <https://pubchem.ncbi.nlm.nih.gov/compound/Enzalutamide>.
- National Center for Biotechnology Information. (2023). PubChem compound summary for CID 261000, methyltrienolone. Retrieved from <https://pubchem.ncbi.nlm.nih.gov/compound/Methyltrienolone>.
- Reddy, G. D., Kumar, K. P., Divya, R., Kumar Reddy, K. P., & Prasad, V. V. S. R. (2014). Quantum polarized molecular docking, pharmacophore modeling and 3D-QSAR studies of pyrido-indole containing JAK2 inhibitors. Journal of Receptors and Signal Transduction, 13, 23–34.
- Saxena, P., Trerotola, M., Wang, T., Li, J., Sayeed, A., Vanoudenhove, J., Languino, L. R. (2012). PSA regulates androgen receptor expression in prostate cancer cells. Prostate, 72(7), 769–776. doi:10.1002/pros.21482
- Shoichet, B. K., & Kuntz, I. D. (1991). Protein docking and complementarity. Journal of Molecular Biology, 221(1), 327–346. doi:10.1016/0022-2836(91)80222-g
- Thompson, I. M., & Ankerst, D. P. (2007, June 19). Prostate-specific antigen in the early detection of prostate cancer. CMAJ, 176(13), 1853–1858. doi:10.1503/cmaj.060955

---

**K Ganesh Kadiyala**

Department of Chemistry, Shri Vishnu Engineering College for Women, Bhimavaram-534202, Andhra Pradesh, India. [kganeshkadiyala@gmail.com](mailto:kganeshkadiyala@gmail.com)  
ORCID 0000-0001-7357-0504

**K. Jagadeesh**

Department of Chemistry, Shri Vishnu Engineering College for Women, Bhimavaram-534202, Andhra Pradesh, India. [kadali.jc@gmail.com](mailto:kadali.jc@gmail.com)  
ORCID 0000-0002-3805-4931

**Ch. Geetika**

Department of CSE, Shri Vishnu Engineering College for Women, Bhimavaram-534202, Andhra Pradesh, India. [geetikachukkaa@gmail.com](mailto:geetikachukkaa@gmail.com)

**I. Lakshmi Lavanya**

Department of CSE, Shri Vishnu Engineering College for Women, Bhimavaram-534202, Andhra Pradesh, India. [lavanyaimmaneni12@gmail.com](mailto:lavanyaimmaneni12@gmail.com)

**B. Kanaka Durga**

Shri Vishnu Engineering College for Women, Bhimavaram-534202, Andhra Pradesh, India  
[kanakadurga1711@gmail.com](mailto:kanakadurga1711@gmail.com)  
ORCID 0009-0009-4571-430X

**J. Suresh Kumar**

Department of Engineering Chemistry, Sagi Rama Krishnam Raju Engineering College, Bhimavaram-534204, Andhra Pradesh, India.  
[jayanthagitam@gmail.com](mailto:jayanthagitam@gmail.com)  
ORCID 0009-0008-8135-2337

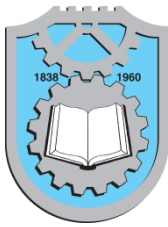
---

**Bachina Kiran**

Department of Physics, B.V. Raju College, Bhimavaram, 534202, Andhra Pradesh, India,  
[kiran.b@bvricedegree.edu.in](mailto:kiran.b@bvricedegree.edu.in)  
ORCID 0000-0002-7374-4698

**B. N. Suresh Varma Dendukuri**

Department of Chemistry, Shri Vishnu Engineering College for Women, Bhimavaram-534202, Andhra Pradesh, India. [sureshvarma60@gmail.com](mailto:sureshvarma60@gmail.com)  
ORCID 0000-0002-9921-9461



## A NOVEL ALU USING DISTRIBUTED ARITHMETIC FOR REAL TIME SIGNAL PROCESSING APPLICATION

M. Prasad<sup>1</sup>

K. Ajita Lakshmi

B. Jagadessh

Pokkuluri Kiran Sree

G. L N V S Kumar

A. V S M Ganesh

M. L Rekha

Ch. S. V. V. S. N. Murthy

Keywords:

Distributed Arithmetic (DA); OBC (Offset Binary coding); LUT (Look-Up Table); DA (Distributed Arithmetic).

### ABSTRACT

In the modern era, DSP is widely used in electronics, notably in mobile technology. It uses LUT-based schemes (SOP) and uses arithmetic and logical operations to reach the sum of products. A method known as distributed arithmetic is used to speed up complex calculations involving the sum of products. Any DSPs processing speed can be increased by employing Distributed Arithmetic to speed up the ALU computations. Modern DSPs require Distributed Arithmetic and OBC High-Speed ALU to increase computation efficiency. It is the ALU that helps perform accurate computations on real-time signals. Proposed study a novel in-site method for designing a Distributed Arithmetic and Offset Binary Coding-based ALU core for High-Speed DSP Processors. Due to its inverse symmetry, the Offset Binary Coding approach can reduce the area in half. When designing diverse ALU structures, structural or hierarchical modeling is preferred. Several LUT-based distributed arithmetic decomposition's are constructed and compared. Xilinx 14.7 ISE will also be used for performing performance assessments in terms of area, speed, and power.

202x Published by Faculty of Engineering



### 1. INTRODUCTION

At present, India is seeking to become a chip hub in designing chips for electronic devices and gadgets. Intel, Qualcomm, analog electronics, etc., intend to amp up the device growth of manufacturing chips that will be rolling out after 2025 and beyond years. The arithmetic and Logical Unit is an essential digital circuit comprised of two operations (Arithmetic and Logical Operations).

As shown in Figure 1, a conventional Arithmetic and Logic unit is a component of a central processing unit that performs arithmetic and logic operations on the operands based on opcode. In some processors, the CPU (Central Processing Unit), GPU (Graphics Processing Unit), and FPU (Floating Point Unit) all have multiple Arithmetic Logic Units (ALUs). The processor's internal calculations are carried out by the ALU, which applies mathematical and bit-wise operations to digital values.

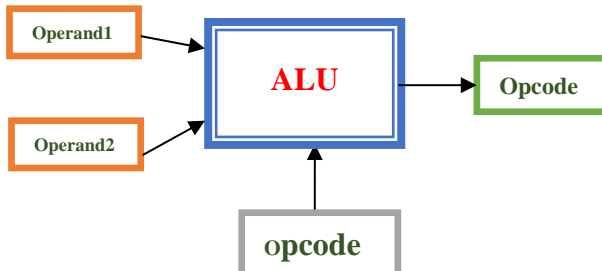


**Figure 1.** Conventional ALU

The ALU is an excellent component of the CPU, however depending on the architecture of the instruction set, different processors may have slightly different ALU layouts and functions. For instance, certain ALUs are made for floating-factor operations, whereas others are made for the most practical integer calculations (Dharani et al., 2020). In DSP Processor (Pisupati et al., 2019) ALU perform operations to complete computations on convolution, filtering, Discrete cosine transformations and correlation operations of DSP Functions.

In particular, when one vector is a constant and the other is a constant vector, distributed arithmetic (DA), a computational algorithmic approach, performs multiplier-less implementation of calculating the inner product between two vectors. The weighted sum ( $A[i] * X[i]$ ), where  $X[i]$  is an input vector and  $A[i]$  is a known quantity, is known as the inner product. Many digital signal processing methods (Amirtharajah and Chandrakasan, 2004) basic computations are carried out via vector.

In a DSP application (Khan and Shaik, 2019) like a finite impulse response (FIR) where all data representation is done in fixed-point format and the filter coefficients are constant. To execute operations on DSP functions like FIR filters, DCT, FFT, and DWT, an ALU is a device that computes arithmetic and bit-wise operations on digital signals. Distributed Arithmetic multiplication is done without multiplier. It uses LUT for the multiplication process. It means we can reduce the area by using LUTs instead of using multipliers in the ALU unit. Multipliers are crucial to every operation and take up the most space possible within the unit. The number of transistors in a chip doubles every two year, according to Moore's law. The area must be reduced due to rising technology. The multipliers in the unit with the predefine LUT are being removed for this reason. This is how the DA technique will operate; since incomplete products won't need to be generated, more space may be saved. The size of the ROM grows exponentially with each additional input, which is the biggest disadvantage. Offset binary code can be utilized to get around this limitation.

Abundantly available solar energy, long-lasting and clean energy is a most effective alternative to non-renewable sources such as coal, oil, and natural gas.

In a manner similar to how DA techniques with offset codes are calculated, so are OBC precomputation. This method allows us to cut the region in half from its original size. Excess-K Code biased representation is another name for offset binary. A signed integer  $n$  is represented by the bit pattern corresponding to the unsigned number  $n+L$ , where  $L$  is the biasing value or offset, according to the OBC method for representing signed numbers. Although there is no defined standard for offset binary, it is most frequently written as  $L = 2^{n-1}$  for  $n$ -bit words (for instance,  $2^2=4$  for a three-digit binary integer). The size of the memory in OBC is halved. When DA is compared to offset binary coding, the area is reduced because the size of the ROM shrinks, and performance is also boosted when compared to DA since delay shrinks.

The organization of the paper is structured as follows. Section 2 describes the previous Work includes ALU Designs & Literature Survey. This chapter is a thorough review of related research and prior work in the areas of ALUs, DAs, and their applications in real-time signal processing are presented, which provides an in-depth exploration of our methodology and the novel ALU design developed.

Section 3 deals with Proposed Work includes LUT based ALU using DA, Two LUT based ALU using DA, OBC based ALU with Single LUT, OBC Based ALU with Two LUT.

Section 4 explains the Implementation Results and Discussion. This chapter described about the experimental setup, detailing the testing and validation.

Section 5 contains concluding observations (Palnitkar, 2003). Finally, "Conclusion," summarizes the main findings of the paper and reiterates the significance of our research in addressing the identified gaps in the field.

Synthesis and Simulation are used to validate functionalities. Along with being checked, the timing diagram and interfacing signal of the outputs are monitored to make sure they follow the design requirements. ALU that uses Verilog HDL (Kappaganthu, 2018) satisfies the requirements for several high performance applications (Loganathan, 2016). In order to boost speed, reliable ALU design with distributed arithmetic is used for real-time digital signal processing applications (Loganathan and Gandhi, 2017).

The following present the key elements of our study, from a review of previous work in the field to the development of our proposed ALU design using distributed arithmetic, the implementation results, and the ensuing discussion and conclusion.

## 2. PREVIOUS WORKS

### 2.1 ALU Designs

Electronics engineers are continuously trying to improve the system performance and reducing the size of the system. In the DSP processor ALU (Penchalaiah et al., 2021) is the one of the main functional blocks. To improve the efficiency of the DSP processors, there is a need to optimizing arithmetic units. Booth multiplier is a one of the techniques proposed by Booth in 1951 which reduce the number of partial products. Wallace is another scientist improves the booth multiplier after the booth passed out. At the time of 1951, floating point arithmetic and integer operations are the hot topic for the many researchers.

Today we are using nano size technology, means minimizing the size of the processors. In DSP processors ALU is one of the fundamental part and by concentrating on the reduction of ALU size in DSP processors. But the main drawback is if we reduce the size of the ALU the speed will automatically reduce. For any DSP processors speed plays a vital role. Here is a way to design a new ALU that reduce the area and improves the speed of DSP processors.

### 2.2 Literature Survey

Sarkar et al. (2020) designed an 8-bit ALU using the m-GDI technique. The authors described the drawbacks of area and power in general ALUs and proposed a new technique using GDI cells to minimize area and power consumption (Sarkar et al., 2020).

Jung-Pil Choi et al. (2000) proposed a method for efficient ROM size reduction in distributed arithmetic. The method focuses on the implementation of the sum-of-products in circuit reduction for Distributed Arithmetic and OBC, leading to a 50% reduction in area (Jung-Pil Choi et al., 2000).

The growing demand for enhanced speech processing and computer vision necessitates high-speed computation and memory in Convolutional Neural Networks (CNN). This paper introduces an optimized Block Floating Point (BFP) arithmetic, incorporating refined rounding and shifting operations in quantization schemes for the accelerator. This enhancement results in a threefold improvement in energy and hardware efficiency, as demonstrated (Lian et al., 2019). The current need for an area-efficient floating-point unit poses a significant challenge in meeting precision calculation requirements. The paper proposes the implementation of a single-precision Floating Point ALU using optimized algorithms to minimize the required area.

Khan and Shaik (2019) explained optimal Complexity Architectures for Pipelined Distributed Arithmetic-

Based LMS Adaptive Filter, as detailed in the study. Analyzing the distributed arithmetic algorithm (Yang and Fang, 2021) and various Distributed Arithmetic optimum structures is the major goal here. The pipelining approach is used in this instance to implement distributed arithmetic. Simply put, we may state that the pipe-lining approach is used to construct distributed arithmetic, and the least mean square application of an adaptive filter is used. When using pipe-lining instead of the standard MAC, area consumption is lowered in distributed arithmetic, and both complexity and area consumption are reduced. Here, many Distributed Arithmetic mathematical foundations and concepts were examined. As was already said, Distributed Arithmetic focuses on the inner product and uses LUT to carry out multiple accumulating operations. Due to the fact that general MAC uses partial products, more space will be consumed, negating one of the benefits of distributed arithmetic. Techniques for area optimization of DA-based implementation are examined, along with their use in the development of DSP functions (Meher, 2006).

Nagaraju and Ramesh “Implementation of high speed and area efficient MAC unit for industrial applications” Springer Science Business Media, LLC, part of Springer Nature 2018. Here, the multiplication procedure is carried out using a LUT, preventing the production of incomplete products. Therefore, space consumption will be decreased, but the fundamental disadvantage of distributed arithmetic is that the size of the ROM increases exponentially with each additional input line. When compared to the MAC in general, area will be reduced while speed will be improved. This MAC is effective and has been examined for use in commercial settings (Nagaraju, 2018).

Real-time signal processing encompasses a wide range of applications, from image and audio processing to communication and scientific data analysis. Research could focus on customizing the ALU for specific application domains to maximize its performance. The following study goals were established based on the literature review.

Create a unique ALU architecture that uses distributed arithmetic to boost performance and efficiency in real-time signal processing applications. Optimization for Real-Time Signal Processing: Tailor the ALU design to fit the unique needs of real-time signal processing jobs, taking into account parameters such as data accuracy, latency, and throughput. Performance Improvement: Improve the ALU's performance parameters, including as speed, accuracy, and power efficiency, when compared to existing ALU designs utilized in real-time signal processing applications.

## 3. PROPOSED WORK

The ALU, which handles both arithmetic and logic operations, is the most crucial component of any

processor design. Data are taken from input registers by an ALU.

The ALU receives instructions from an external Control Unit regarding the operation to be performed on the input data, and the ALU then stores its output in the output register. ALU performs this operation on the input operand and then generates the output by counting on the operation that is now coded operational selection. The output Register of the ALU (Nishitani et al., 1981) displays the outcome. ALU is being worked on, and it performs three operations: logical and, logical or, and arithmetic addition (Gurjar et al., 2011). The Distributed Arithmetic method served as the foundation for the design of this novel ALU. Known for its use of specified computation values is the distributed arithmetic technique. Another method is known as DA, in which a series of look-up tables with an implemented instruction set can be used in place of multiplication and accumulation operations. The arithmetic and logical operations are described in the instruction set. An instruction set is a collection of machine language commands for a CPU. The phrase can be used to describe all possible CPU instructions or a selection of instructions designed to improve performance in specific circumstances (Ranga Rao, 2010). In the look up tables predefine performance values are placed and based on the addresses value we can get the value of either arithmetic or logical operation. Mainly, implemented this DA technique in ALU design for speed and accuracy. The work includes design and implementation of DA -ALU's, OBC - ALU's.

### 3.1 Single LUT based ALU using Distributed Arithmetic

Single ALU is the basic DA (Grangetto et al., 2007) based ALU which perform the logical and arithmetic operations. Designed an instruction set with a 64-word length to execute various operations. These operations are stored in predefined LUTs based on the address value and are used to perform logical or arithmetic operations. In designing, A0, A1, A2, A3, A4, A5, are the considered as the input for the ALU and based on address instruction it performs operations of either arithmetic or logical and finally taken as output. The ALU consists of two parts one is LUT part and other one is mux part. Based on the select line one can see the output of arithmetic / logical values. In the LUT part the pre-computed values has been stored. The address values ranging from 000000 to 111111. Based on the MSB bit if MSB=0(from 00000 to 011111) means logical or else if MSB=1(100000 to 111111) performs arithmetic functions as shown in Figure 2.

For examples address as 63 and inputs are A0, A1, A2, A3, A4, A5 given to the ALU, binary format of 63 is 111111 based on the bit serial nature format value of address, predefined computed value is selected from the LUT as  $A0+A1+A2+A3+A4+A5$ .

Suppose A0, A1, A2, A3, A4, A5 are assigned as A0=31, A1=30, A2=29, A3=28, A4=27, A5=16 is given then the final value  $17 (1 * 31 + 1 * 30 + 1 * 29 + 1 * 28 + 1 * 27 + 1 * 26)$  when address is 63. This is given to the mux as an input. Based on the SEL value as 1 we get the sum as 171 as a final value.

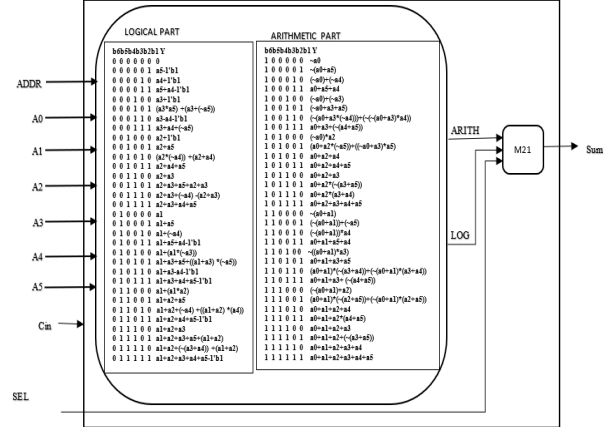


Figure 2. Single LUT based ALU using DA

### 3.2 Two LUT based ALU using Distributed Arithmetic

Two LUT is similar to the single ALU. LUT is divided into two banks as shown in Figure 3. To get the required operation adder is connected before multiplexer section. In single ALU we are providing the 64 pre-computed values in the LUT Where as in two LUT includes 2-16 pre-computed values. Dividing into two LUTs reduces the precomputation calculations. In each LUT up to 4 values perform logical operations and other 4values perform arithmetic operations. The logical operation starts from 000 to 011 in one LUT and from 000 to 011 in another LUT. Based on MSB arithmetic operations can be performed.

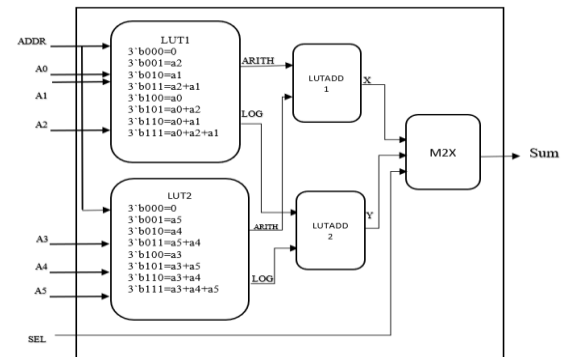


Figure 3. Two LUT based ALU Using DA

### 3.3 OBC based ALU with Single LUT

From Figure 4, it is clearly observed that the X0, X1, X2, X3 addresses the input of the ALU design and output is generated as sum of products. The ALU consists of two parts one is LUT part and other one is mux part. Considering select line for the mux as a CLK.

Base on the CLK line value will get the logical output or the arithmetic output. In the LUT predefined computation values are stored. The address values range from 0000 to 1111. This LUT is also divided into two parts: one is the logical part, ranging from 0000 to 0111, and the other is the arithmetic part, with values from 1000 to 1111. In LUT has been included both logical and arithmetic operations. These are for the positive numbers. For the negative numbers the values are converted into the 2's complemented form because for the subtraction we require additional part, so that the area of the LUT becomes large. To minimize the area, we are going to perform only arithmetic operation by converting negative values to the positive values by twos complements form.

In this part we are getting results based on the address value. The address is ranging from the 0000 to 1111, because the 4 inputs to the LUT ( $2^{\text{pow}4}=16$ ). For examples address is given as 2(0010), it selects the logical operation in the logical part as a  $-(x_0+x_1+x_2+x_3)/2$ . Input for the ALU are  $X_0=2$ ,  $X_1=3$ ,  $X_2=4$ ,  $X_3=5$  and address as 02 then the LUT output is  $=(2+3+4+5)/2=11$  then it is given to the mux as a input based on CLK output can get.

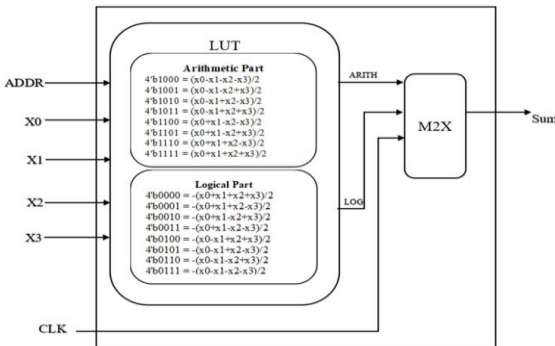


Figure 4. OBC Based ALU with Single LUT

### 3.4 OBC based ALU with Two LUT

Figure 5 is OBC based architecture with two LUT and is similar to the single ALU. The only different is to observe the two LUTs instead of single LUT. In single ALU provides 16 pre-computed values in the LUT. Where as in 2 LUT we are providing only 8 pre-computed values. Because of the division into 2 LUTs precomputation storage has been reduced, and each LUT can perform the both logical and arithmetic operations. In each LUT up to 4 values perform logical operations and other 4 values perform arithmetic operations. The logical operations start from 10 to 11 in one LUT and from 10 to 11 in another LUT. The arithmetic operations start from 00 to 01 in one LUT and from 00 to 01 in another LUT. Based on MSB value it performs arithmetic or logical operations. In each LUT consists of two operations as logical and arithmetic. From the value 00 is taken from first LUT1 and 11 is taken from the LUT2. The logical operation become as  $-(A_0+A_1)/2=-(2+3)/2=-2$  from LUT1 and

LUT2 becomes as  $-(A_2-A_3)/2=-(4-5)/2=1$ . The output of adder1 become  $LUT1(x)+LUT2(y)=2$ . The final results from the mux become 2 (Dharani et al., 2021).

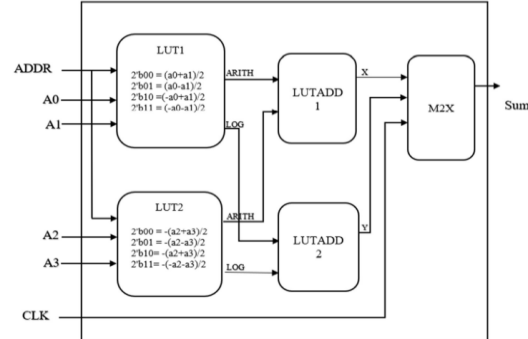


Figure 5. OBC Based ALU with Two LUT

## 4. IMPLEMENTATION RESULTS AND DISCUSSION

Implementation (IEEE Draft, 2019) of ALU using Single LUT, Two LUT, OBC using single LUT & Two LUT has been done. All these synthesis and simulations has been carried in Xilinx software and found the performance evaluation of power, delay and area.

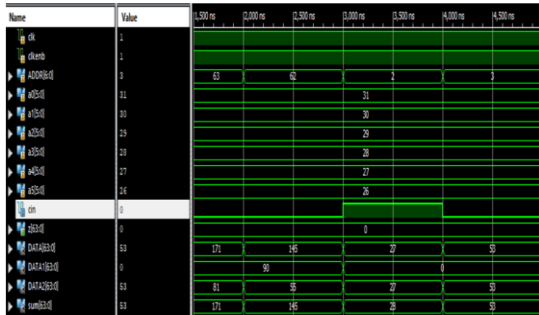


Figure 6. Simulation results of Single LUT based ALU using DA

Figure 6 depicts the simulation (Churiwala et al., 2017) of a single LUT-based ALU. The address is shown as ADDR, the select line is shown as SEL, the inputs are shown as a0, a1, a2, a3, a4, a5, and the output is shown as out. The output could receive either arithmetic or logical values depending on SEL. For instance, if ADDR = 62 and the input values are 31, 30, 29, 28, 27, and 26, then the output value with SEL = 1 does  $a_0+a_1+a_2+a_3+a_4=31+30+29+28+27+26=171$  and for a0=31, a1=30, a2=29, a3=28, a4=27 and a5=26 for ADDR=63 Out is 145. Similar results are obtained with SEL = 0 and ADDR = 2 and inputs a0 = 31, a1 = 30, a2 = 29, a3 = 28, a4 = 27, a5 = 26, and 28 then Out value is 52.

Figure 7 depicts the simulation of Two LUT-based ALUs using DA, where ADDR is the address, SEL is the select line, a0, a1, a2, a3, a4, and a5 correspond to the inputs, and DATA1 (which may have arithmetic or logical values based on SEL) is the output of LUT1 and

DATA2 is the output of LUT2, and the final output is referred to as DATA.



These results indicate that the OBC design surpasses the ALU design in terms of both delay and power consumption, whether examining a single unit or a two-LUT configuration. The enhanced performance and energy efficiency of the OBC design may offer benefits in specific applications where the reduction of delay and power consumption holds paramount importance.

Figure 11 shows comparison between DA and OBC ALU designs in terms of number LUTs utilized. The quantity of LUTs in DA ALU and OBC ALU based on specific needs, design goals, and optimization strategies. They aim for a balanced resource allocation, considering factors like power, space, and arithmetic complexity for desired performance.

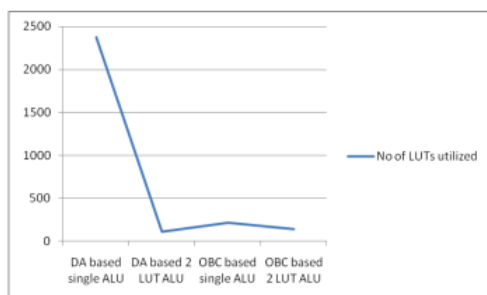


**Figure 11.** Number of LUTs utilized in various ALU designs

## 5. CONCLUSION

The most crucial algorithm for DSP applications is distributed arithmetic. Moreover, it is applicable to

## References:

- Amirtharajah R and A. P. Chandrakasan. (2004). A micropower programmable DSP using approximate signal processing based on distributed arithmetic. *IEEE Journal of Solid State Circuits*. 39(2). 337-347. doi: 10.1109/JSSC.2003.821774.
- Ashreetha B., Devi M.R., Kumar U.P., Mani M.K., Sahu D.N., Reddy P.C.S (2022). Soft optimization techniques for automatic liver cancer detection in abdominal liver images. *International Journal of Health Sciences*. 6. 10820–10831. doi: 10.53730/ijhs.v6nS1.7597.
- Churiwala, Sanjay, and I. Hyderabad (2017). *Designing with Xilinx® FPGAs. Circuits & Systems*, Springer.
- Dharani M, G. Sreenivasulu (2021). Land use and land cover change detection by using principal component analysis and morphological operations in remote sensing applications. *International Journal of Computers and Applications*. 43(5). 462-471. doi: 10.1080/1206212X.2019.1578068.
- Dharani, M., Kumar, P. A., Venkata krishna moorthy, T., Bharghavi, N., & Kumar, B. A. (2020). High level montgomery modular multiplier for CSA architecture. *Materials Today: Proceedings*. doi: 10.1016/j.matpr.2020.10.854.
- Grangetto M, E. Magli and G. Olmo (2007). Distributed Arithmetic Coding. *IEEE Communications Letters*. 11(11). 883-885. doi: 10.1109/LCOMM.2007.071172.
- Gurjar P, R. Solanki, P. Kansliwal and M. Vucha (2011). VLSI implementation of adders for high speed ALU. *2011 Annual IEEE India Conferenc.*, 1-6. doi: 10.1109/INDCON.2011.6139396.

various scientific and technological fields such as data analysis, medical imaging, as well as JPG and MP3 video compression. In order to mix images in different ways during image analysis (Ashreetha et al., 2022), arithmetic and logical operations are frequently used as a pre-processing phase (Khan and Shaik, 2019; Leela Rani et al., 2014). This makes them suitable for image processing applications as well. In order to conduct dedicated arithmetic and logical operations, the ALU is the most significant and necessary element in every DSP processor.

Distributed Arithmetic method is included to boost ALU speed. OBC-based Single LUT and Two LUT ALU architectures with a single ALU, two LUTs, and two LUTs were designed. Here, it was discovered that a single OBC's delay is 42–45 percent less than a single ALU's. Compared to a 2 LUT ALU, the delay of a 2 LUT OBC is 20–25 percent less. One OBC ALU consumes between 80 and 85 percent less power than a typical ALU. Similarly, the two LUT OBC uses 11–15% less energy than the two LUT DA-based ALU. Still, needs work, thereby reducing the number of pre-computed calculations and minimizing power consumption, speed LUTs can be further divided. DA is a technique used in digital signal processing to implement efficient multiplication operations. Advancements in DA algorithms and their application in ALUs can lead to improved performance and power efficiency in real-time signal processing applications.

IEEE Draft Standard for VHDL Language Reference Manual, IEEE P1076/D13, July 2019 , 1-796, 29.

Jung-Pil Choi, Seung-Cheol Shin and Jin-Gyun Chung (2000). Efficient ROM size reduction for distributed arithmetic. 2000 IEEE International Symposium on Circuits and Systems (ISCAS). 61-64. 2. doi: 10.1109/ISCAS.2000.856258.

Khan M T and R. A. Shaik, (2019). Optimal Complexity Architectures for Pipelined Distributed Arithmetic-Based LMS Adaptive Filter. IEEE Transactions on Circuits and Systems I: Regular Papers.66(2). 630-642. doi: 10.1109/TCSI.2018.286729.

Leela Rani D, S. Varadarajan, and M. Sadasiva (2014). Atmospheric Radar Signal Processing using Complex Wavelet Transforms. International Journal of Computer Applications. 0975 – 8887. 91(11). doi: 10.5120/15927-5194.

Lian X, Z. Liu, Z. Song, J. Dai, W. Zhou and X. Ji, (2019). High-Performance FPGA-Based CNN Accelerator With Block-Floating-Point Arithmetic. IEEE Transactions on Very Large Scale Integration (VLSI) Systems. vol. 27(8). 1874-1885. doi: 10.1109/TVLSI.2019.2913958.

Loganathan M. K. and Gandhi O (2017). Reliability enhancement of manufacturing systems through functions. Proceedings of the Institution of Mechanical Engineers. Part B: Journal of Engineering Manufacture. 231(10).1850-1868. doi:10.1177/0954405415612324.

Loganathan, M. K., et al. (2016). Failure Evaluation and Analysis of Mechatronics-Based Production Systems during Design Stage Using Structural Modeling. Applied Mechanics and Materials. 852. 799–805. doi:10.4028/www.scientific.net/ammm.852.

Meher P. K. (2006). Hardware-efficient systolization of DA-based calculation of finite digital convolution. IEEE Trans. Circuits Syst. II, Exp. Briefs. 53(8). 707–711. doi: 10.1109/TCSII.2006.877277.

Nagaraju N , S. M. Ramesh (2018). Implementation of high speed and area efficient MAC unit for industrial applications. Springer Science Business Media. doi: 10.1007/s10586-018-2060-z.

Nishitani T, R. Maruta, Y. Kawakami and H. Goto (1981). A single-chip digital signal processor for telecommunication applications. IEEE Journal of Solid-State Circuits. 16(4). 372-376. doi: 10.1109/JSSC.1981.1051603.

Palnitkar, Samir (2003). Verilog HDL a guide to digital design and synthesis. Prentice Hall Professional. d1.amobbs.com/bbs\_upload782111/files\_33/ourdev\_585395BQ8J9A.pdf.

Penchalaiah, Usthulamuri, and VG Siva Kumar (2021). Design and Implementation of Low Power and Area Efficient Architecture for High Performance ALU. Parallel Processing Letters. doi: 10.1142/S0129626421500171

Pisupati, Bharadwaja, Naresh, M, Koppala, Neelima & J. Krishna (2019). Design of step-up inexact MAC (IMAC) unit for DSP applications. International Journal of Recent Technology and Engineering. 7. 360-364. <https://www.ijrte.org/wp-content/uploads/papers/v7i6s/F02710376S19.pdf>.

Ranga Rao K V and Niraj Upadhyaya (2010). Factors affecting Multicore Processor Performance in Annual International Conference of Computer Science Education : Innovation & Technology (CSEIT 2010). doi:10.5176/978-981-08-7466-7itcse-29.

Sarkar S, H. Chatterjee, P. Saha and M. Biswas (2020). 8-Bit ALU Design using m-GDI Technique.2020 4th International Conference on Trends in Electronics and Informatics (ICOEI)(48184),17-22. doi: 10.1109/ICOEI48184.2020.9142881.

Yang N., & Y. Fang (2021). Distributed Arithmetic Coding for Sources with Hidden Markov Correlation. Asia-Pacific Signal and Information Processing Association Annual Summit and Conference (APSIPA ASC). 1506-1510. doi:10.48550/arXiv.2101.02336.

---

**M. Prasad**

Department of CSE  
Shri Vishnu Engineering College for  
Women(A), Bhimavaram,  
India  
e-mail: prasads.maddula@gmail.com  
ORCID: 0000-0002-5092-9032

**K. Ajitta Lakshmi**

Department of ECE  
Shri Vishnu Engineering College for  
Women(A), Bhimavaram,  
India  
e-mail:ajita.sansita.m@gmail.com  
ORCID: 0009-0002-3339-0650

**B. Jagadeesh**

Department of ECE  
Bonam Venkata Chalamayya College of  
Engineering(A), Rajamundry,  
e-mail:indiabjagadeesh2020@gmail.com  
ORCID: 0000-0002-2038-8378

**Pokkuluri Kiran Sree**

Department of CSE  
Shri Vishnu Engineering College for  
Women(A), Bhimavaram,  
India  
e-mail:drkiransree@gmail.com  
ORCID: 0000-0001-8601-4304

**G. L N V S Kumar**

Department of MCA  
Bonam Venkata Chalamayya Institute  
of Technology & Science (A), Batlapalem,  
India  
e-mail:kumar4248@gmail.com  
ORCID: 0009-0001-4756-2241

**A. V. S. M. Ganesh**

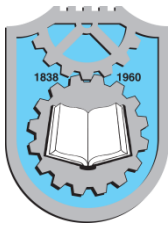
Department of MCA  
Bonam Venkata Chalamayya Institute  
of Technology & Science (A), Batlapalem,  
India  
e-mail: akella.ganesh@gmail.com  
ORCID: 0009-0001-6031-5472

**M. L. Rekha**

Department of MCA  
Bonam Venkata Chalamayya Institute  
of Technology & Science (A), Batlapalem,  
India.  
e-mail: rekhamoram@gmail.com  
ORCID: 0009-0008-4515-4800

**Ch. S. V. V. S. N. Murthy**

Department of CSE  
Aditya College of Engineering &  
Technology(A), Surampalem,  
India.  
e-mail: chsatyamurty@gmail.com  
ORCID: 0000-0001-6637-4660



## OPTIMIZATION OF NEURAL NETWORK CLASSIFIERS BY LEVERAGING THE SEQUENTIAL FEATURE ENGINEERING FOR ROBUST WATER QUALITY PREDICTION SYSTEM

Maheswara Rao V V R<sup>1</sup>

Silpa N

Kranthi Addanki

Shiva Shankar Reddy

Ramachandra Rao Kurada

Pachipala Yellamma

Keywords:

Water Quality Prediction; Neural Networks; Feature Engineering; Data analytics; Predictive Modelling.

### A B S T R A C T

Rapid population growth increases water demand, intensifying extraction from wells and rivers. The Water Quality Index (WQI) assesses water suitability for drinking based on multiple parameters. Accurate assessment of pollution in water is imperative for effective management of water quality. The present research on the Neural Network-based Robust Water Quality Prediction System (NN-RWQPS) exploits the capabilities of neural networks and advances in feature engineering, positioning it at the forefront of WQI. Venturing into the new world of predictive modelling armed with four different neural network classifiers: Wide, Bilayer, Trilayer, and an Optimized Neural Network. Further the study harness the power of feature selection, deploying four distinct methods. A champion feature selection method is scientifically validated for each neural network, and then the neural networks are fine-tuned by training them across a range of feature dimensions, unveiling an empirically supported set of optimal features. Study advances water quality prediction using neural networks and feature engineering.

© 202x Published by Faculty of Engineerin



### 1. INTRODUCTION

In the ever-evolving landscape of environmental science and data analytics, the research is poised at the forefront, where the pursuit of optimizing water quality prediction and unlocking the potential of neural networks and sequential feature engineering takes center stage. Water, the elixir of life, presents an intricate puzzle encapsulated within a vast dataset brimming with

its subtleties, a puzzle that continues to challenge even the most adept scientists and researchers.

A neural-network classifier emulates the human brain's decision-making process. The system as depicted in Figure 1 consists of three essential layers: the input layer receives data, hidden layers process information, and the output layer produces results. The input layer receives and preprocesses data, transmitting it to the

<sup>1</sup> Maheswara Rao V V R  
Email: mahesh\_vvr@yahoo.com

hidden layers. Hidden layers, consisting of interconnected artificial neurons, perform complex computations through weighted connections. Finally, the output layer produces predictions, often in the form of class probabilities, which represent the category or label. These networks are trained on labeled datasets, adjusting their internal parameters through backpropagation to minimize prediction errors. They are widely used for diverse classification tasks, benefiting from their capacity to handle intricate and non-linear patterns.

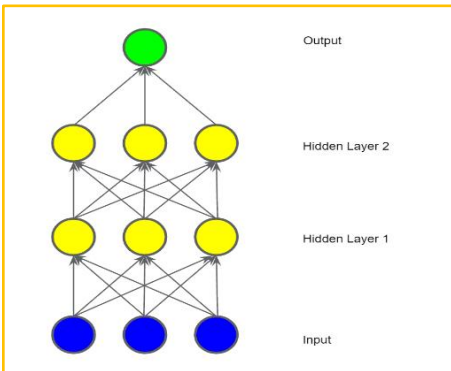


**Figure 1.** Basic Neural Network Architecture

In the exploration of this cutting-edge domain of predictive modeling, our research has armed us with a formidable array of four unique neural network classifiers: the Wide, Bilayer, Trilayer, and the Optimized Neural Network. These distinct neural networks serve as our companions, adeptly navigating the intricate maze of water quality prediction. Each neural network brings its own strengths and characteristics to the table, allowing us to unlock a more comprehensive understanding of this dynamic field. Through their guidance and proficiency, we embark on a journey towards enhancing our predictive capabilities and shedding light on the complexities inherent in the realm of water quality forecasting.

However, this voyage doesn't end with the selection of neural networks. To navigate this enigmatic terrain effectively, the research tap into the potent art of feature selection, utilizing four meticulous and rigorous methods: MRMR, Chi-square, Anova, and Kruskal. Each of these methods serves as a finely honed instrument, akin to precision tools in the hands of a water quality analyst.

A feature selection method, rigorously and scientifically validated for each neural network, stands as a testament to our commitment to precision and accuracy. With this champion method in hand, we embark on the fine-tuning of our neural networks. Through meticulous training across a spectrum of feature dimensions, a symphony of performance optimization unfolds, revealing a set of optimal features empirically supported by our research.

The findings of this study represent a significant leap forward, a cornerstone in our understanding and practical application of neural networks and sequential feature engineering within the realm of water quality prediction. In the spirit of scientific collaboration, this paper serves as an invaluable guide, offering the broader scientific community a roadmap to harness these advanced techniques for the enhancement of environmental monitoring and management, ushering in a brighter future for our planet.

This scholarly work follows a structured framework, consisting of five distinct sections. Section 2 initiates with an in-depth review of existing research in the domain of water quality estimation through neural networks. Section 3 delves into the proposed system, providing comprehensive insights into the intricacies of data preprocessing, feature engineering techniques, and the specific neural network classifier models utilized. Section 4 shifts the focus towards the experimental outcomes. In the concluding Section 5, the authors consolidate their findings, providing conclusive insights and observations drawn from the entire research endeavor, offering a holistic view of their contributions to the field.

## 2. RELATED WORK

The authors advanced every stage of the present study by thoroughly reviewing the literature from 2008 to 2023, improving the field of water quality evaluation with an emphasis on neural-network classifiers.

The authors of this literature (Mengyuan et al., 2022; Zhu et al., 2022) stress the significance of thorough data analysis as the basis for precise water quality estimates that are related to health.

To improve the accuracy of WQI, a number of researchers have recently investigated novel machine learning-based techniques (Aldhyani et al., 2020; Khoi, et al., 2022; Bonthu et al., 2023; Flores et al., 2023; Goodarzi et al., 2023).

With the object of significantly enlightening the high-accuracy of WQI, the authors (Jinal et al., 2022; Kalaivanan et al., 2022; Kurra, et al., 2022; Maheswara, et al., 2022; Galal et al., 2022) have presented a number of methods that make use of ML Based Classification techniques. According to research publications (Rao et al., 2011; Silpa et al., 2021), the data investigation stage in ML based for WQI is a crucial phase.

To improve prediction accuracy, the integration of sophisticated ML techniques has also been investigated (Silpa et al., 2022; Rao et al., 2023; Reddy et al., 2022; Rao et al., 2023). Recent years have seen a notable increase in interest in the field of ML for water quality investigation (Maheswara et al., 2022; Rao et al., 2022;

Silpa et al., 2023) in the feature engineering process (Fei et al., 2023; Gong et al., 2022; Rao et al., 2023).

### 3. PROPOSED METHODOLOGY

The current study on the Neural Network-based Robust Water Quality Prediction System (NN-RWQPS) leverages the potential of neural networks and sequential feature engineering, establishing it as a pioneering approach in water quality analysis. Embarking on predictive modelling, it employs four diverse neural network classifiers: Wide Neural Network Classifier (WNNC), Bilayered Neural Network Classifier (BNNC), Trilayered Neural Network

Classifier (TNNC), and an Optimized Neural Network Classifier (ONNC). The study also harnesses the power of feature selection, utilizing four robust methods: MRMR, Chi-Square, ANOVA, and Kruskal, akin to finely tuned research instruments. Each neural network is rigorously assessed and optimized, validated through a scientific algorithm, revealing an empirically supported set of optimal features. As illustrated in Figure 2, it covers the entire process from gathering and refining data to establishing a robust machine-learning framework for evaluating water quality. Notably, this approach emphasizes the importance of combination of Network classifier and feature selection to optimize achieves performance.

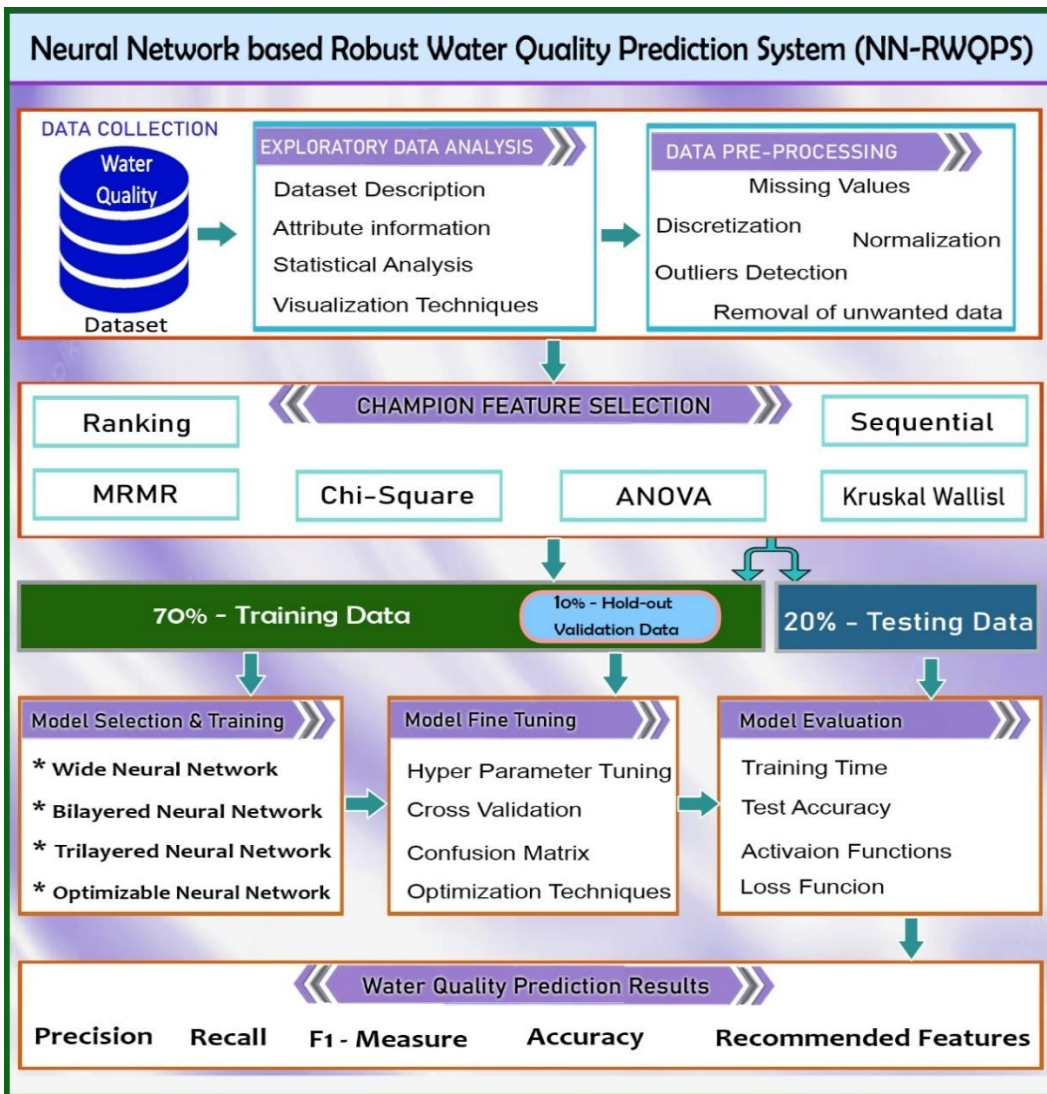


Figure 2. Architecture of proposed NN-RWQPS

The process of NN-RWQPS begins with collecting essential water quality data, the data is rigorously pre-processed as presented in Algorithm 1. During the model selection phase, various neural network classifiers are explored to determine the most suitable approach for the task. The models are subsequently trained and evaluated, allowing for the assessment of their performance using a

variety of evaluation metrics. As the pursuit of optimization continues, the models are refined, aiming to identify the best combination of features and network classifier. By comparing the performance of different neural network models using a range of evaluation metrics, valuable insights are gained into the most effective approach for water quality prediction.

**Algorithm 1: Proposed NN-RWQPS**

**Inputs:** Water Quality Dataset; Neural Network Classifiers: WNNC, BNNC, TNNC and ONNC; Feature Selection Methods; Evaluation Metrics: F1-Score, Precision, Recall, Testing Accuracy

**Output:** Optimal Feature Selection Method and Feature Set and for each Neural Network Classifier

**01. NN-RWQPS: Initialization**

- Initialize an empty set to store optimal feature sets for each NN Classifier
- Initialize a dictionary to store performance metrics for each model.

**02. NN-RWQPS: Data-Understanding**

- Load & preprocess the water quality dataset.
- Perform data cleaning, normalization, and splitting into training and testing sets.

**03. NN-RWQPS: Model Selection**

- Select the neural network Classifiers: WNNC, BNNC, TNNC and ONNC.
- Initialize an empty list to store performance metrics for each model.

**04. NN-RWQPS: Champion Feature Selection**

- For each feature-selection method
- Select features using the current feature selection method.

**05. NN-RWQPS: Neural Network Training**

- For each neural network model using Algorithm 2, 3, 4 and 5
  - ✓ Initialize the model with the selected architecture and hyperparameters.
  - ✓ Train and Evaluate the Neural Network using the training dataset with all features.

**06. NN-RWQPS: Fine-Tuning Loop**

- For each neural network model:
  - For each feature selection method:
    - For a range of feature counts:
      - ✓ Fine-tune the model by selecting a specific number of features.
      - ✓ Train the model with the reduced feature set.

**07. NN-RWQPS: Optimal Feature Set**

- For each neural network model:
  - ✓ Identify the optimal feature set with the best performance.
  - ✓ Add this feature set to the set of optimal feature sets for that model.

**08. NN-RWQPS: Model Evaluation**

- Investigate the NN-model's efficiency using the chosen evaluation metrics.
- Track the best-performing feature count and

corresponding performance metrics.

**09. NN-RWQPS: Performance Comparison**

- Compare the performance of different neural network models with their respective optimal feature sets.
- Utilize the chosen evaluation metrics to assess model performance.
- Store the performance metrics in the dictionary.

In the current research article, the focus was on training different neural network classifiers, namely the WNNC, BNNC, TNNC, and ONNC. The researchers meticulously detailed the training process for each classifier, providing a step-by-step procedure encapsulated in Algorithms 2, 3, 4, and 5. This comprehensive approach facilitates a better understanding of the training methodologies and paves the way for insightful comparisons and application of water quality prediction.

**Wide Neural Network Classifier (WNNC):**

Training a "WNN Classifier" is a research-intensive process aimed at harnessing the potential of expansive network architectures. As presented in Algorithm 2, the model employs a greater number of neurons in its hidden layers, allowing it to capture intricate data patterns and relationships. Optimization techniques are crucial to prevent overfitting in these wider networks. WNN classifiers exhibit limitations, notably susceptibility to overfitting owing to an abundance of parameters, computational intensity, difficulties with high-dimensional data, and sensitivity to noise.

**Algorithm 2: WNNC Training**

**Input:** Water Dataset, WNNC with all hyperparameters, Optimization Algorithm, Batch Size, Number of training epochs

**Output:** Trained WNNC for Classification

**1. WNNC: Initialization**

- Create a WNN Classifier with the configuration of an input, wide hidden, and an output layers.

**2. WNNC: Loss Function Selection**

- Choose the most suitable loss function for water quality classification as binary cross-entropy.

**3. WNNC: Training**

Initialize the parameters NN-Classifier.

For each training epoch:

- Shuffle the training data to introduce randomness.
- Divide the training data into batches of a predefined batch size for mini-batch training.
- For each batch:

- 
- ✓ Conduct a forward pass to compute predictions for the batch.
  - ✓ Calculate the loss using the selected loss function.
  - ✓ Perform backpropagation to update the network's parameters, including weights and biases.
  - d. Calculate the average loss for the epoch as a performance metric.
- 4. WNNC: Validation and Early Stopping**
- a. Throughout the training process, evaluate the model's performance on the validation dataset.
  - b. Employ early stopping based on the validation loss to mitigate overfitting.
- 5. WNNC: Evaluation**
- a. Following the training process, assess the model's performance using the test dataset to measure its classification accuracy and generalization capabilities.
- 6. WNNC: Deployment**
- a. After the model meeting the predefined performance criteria, consider deploying it for the present study.
- 

#### Bilayer Neural Network Classifier (BNNC):

The training of the "BNN Classifier" is a technically intricate process involving the optimization of weights and biases within a neural network architecture comprising two layers: an input layer and a hidden layer. During training, data is propagated forward through the input layer and then through the hidden layer, employing nonlinear activation functions and backpropagation for error minimization as mentioned in Algorithm 3.

Parameters such as learning rates and batch sizes are iteratively adjusted to achieve convergence and optimal performance. This advancement of bi-layer neural network methodologies in the field of water quality analysis is shown high accuracy in classification. BNN limitations include limited complexity, struggle with non-linearity, potential under fitting, and challenges in capturing intricate hierarchical features.

---

#### Algorithm 3: BNNC Training

**Input:** Water Quality Dataset, BNNC with number of input and output neurons, Activation Function, Loss Function, Optimization Algorithm, Batch Size, Number of training epochs

**Output:** Trained BNNC for Classification

---

#### 1. BNNC: Initialization

- a. Create a BNNC with an input and output layer.
- b. Configure the input layer with the appropriate number of neurons and activation function.
- c. Configure the output layer with the

parameters for the number of classes and an appropriate activation function.

#### 2. BNNC: Loss Function Selection

- a. Choose the loss function for water dataset

#### 3. BNNC: Training

Initialize the neural network's weights and biases.  
For each training epoch:

- a. Shuffle the training Water Quality data.
- b. Divide the training data into batches of the specified batch size.
- c. For each batch:
  - ✓ Perform a forward pass to compute predictions for the batch.
  - ✓ Calculate the loss using the selected loss function.
  - ✓ Backpropagate the gradients to update the network's parameters.
- d. Calculate the average loss for the epoch.

#### 4. BNNC: Validation and Early Stopping

- a. Assess the model's effectiveness on the validation dataset while training.
- b. Employ early stopping by monitoring validation loss to safeguard against potential overfitting issues.

#### 5. BNNC: Evaluation

- a. After training is complete, assess the model's performance on the test dataset to measure its classification accuracy and generalization.

#### 6. BNNC: Deployment

- a. If the model meets the performance criteria, deploy it for real-world applications.
- 

#### Trilayer Neural Network Classifier (TNNC):

Training the "TNN Classifier" involves a meticulous process of optimizing weights and biases across three layers to achieve superior classification performance. Data is propagated through the input layer, followed by the two hidden layers, utilizing advanced activation functions and backpropagation algorithms as presented Algorithm 4. The parameters are fine-tuned through iterative epochs. Tri-layer neural network limitations encompass potential overfitting, and challenges in learning complex hierarchical representations in data.

---

#### Algorithm 4: TNNC Training

**Input:** Water Dataset, TNNC with number of input neurons, hidden neurons, output neurons, Activation functions, Loss Function, Optimization Algorithm, Batch Size, Number of training epochs

**Output:** Trained TNNC for Classification

---

#### 1. TNNC: Initialization

- a. Create a tri-layer neural network with an input

- 
- layer, one or more hidden layers, and an output layer.
  - b. Configure the input layer with the appropriate number of neurons and activation function.
  - c. Configure the hidden layers with the number of neurons and activation functions.
  - d. Configure the output layer with the parameters for the number of classes and an appropriate activation function.

## 2. TNNC: Loss Function Selection

- a. Choose the loss function for water Quality Prediction

## 3. TNNC: Training

### Initialize the neural network's weights and biases.

For each training epoch

- e. Shuffle the training Water Quality Data.
- f. Divide the training data into batches of the specified batch size.
- g. For each batch:
  - ✓ Perform a forward pass to compute predictions for the batch.
  - ✓ Calculate the loss using the selected loss function.
  - ✓ Back propagate the gradients to update the network's parameters.
- h. Calculate the average loss for the epoch.

## 4. TNNC: Validation and Early Stopping

- c. During training, evaluate the model's performance on the validation dataset.
- d. Apply early stopping based on validation loss to prevent overfitting.

## 5. TNNC: Evaluation

- b. After training is complete, assess the model's performance on the test dataset to measure its classification accuracy and generalization.

## 6. TNNC: Deployment

- a. If the model meets the performance criteria, deploy it for present study.
- 

### Optimizable Neural Network Classifier (ONNC):

The "ONN Classifier" demands specialized attention in the present research due to its capacity for dynamic optimization. In the context of water quality analysis, training an "ONN Classifier" involves the customization of the neural network's architecture and hyper parameters to optimize the precision and efficiency of water quality parameter assessment as shown in Algorithm 5.

The present Researchers establish a comprehensive search space, encompassing various network configurations. A relevant performance metrics are chosen to gauge the classifier's effectiveness in water quality analysis. Optimization techniques are applied

iteratively to adjust the network's architecture and hyper parameters, aligning it with the chosen metrics. The process continues until the best-performing configuration is identified through convergence. Subsequently, it undergoes rigorous real world testing on independent water quality datasets, enabling accurate and tailored water quality assessment.

---

### Algorithm 5: ONNC Training

**Input:** Water Dataset, ONNC with number of layers, neurons per layer, Activation Function, Loss Function, Optimization Algorithm, Mini Batch Size, Number of training epochs

**Output:** Trained ONNC for Classification

---

#### 1. ONNC: Initialization

- a. Construct a neural network architecture with the specified hyperparameters, which may include the number of layers, neurons per layer, and activation functions.
- b. Initialize the network's weights and biases using a suitable initialization method

#### 2. ONNC: Loss Function Selection

- a. Choose a loss function tailored to the present classification problem

#### 3. ONNC: Training

Initialize epoch counter.

While the maximum number of training epochs is not reached:

- a. Shuffle the training data to introduce randomness.
- b. Divide the training data into mini-batches of a predefined size.
- c. For each mini-batch:
  - ✓ Perform a forward pass to compute predictions.
  - ✓ Calculate the loss using the selected loss function.
  - ✓ Conduct a backward pass to compute gradients.
  - ✓ Update the network's weights and biases using the chosen optimization algorithm.
- d. Increment the epoch counter.
- e. Monitor the training process and display or record the loss and performance metrics.

#### 4. ONNC: Validation and Early Stopping

- a. Continuously evaluate the model's performance on the validation dataset during training.
- b. Implement early stopping based on the validation loss to prevent overfitting.

#### 5. ONNC: Evaluation

- a. After training is completed, assess the model's performance on the test dataset to measure
-

classification accuracy and generalization.

## 6. ONNC: Deployment

- a. Save the trained model parameters and performance criteria, consider to deploy for the present study.

In this research study, a selection of Neural Network Classifiers, including WNNC, BNNC, TNNC, and ONNC, undergo rigorous execution alongside their respective best feature selection methods. Each classifier undergoes training with feature sets ranging from null feature set to incorporating all available features set.

The primary goal is to determine the optimal feature set for each classifier based on its performance. This meticulous evaluation process involves a comprehensive analysis to identify the most accurate and efficient feature combinations for the given task, thereby providing empirical evidence of feature relevance and classifier effectiveness. Subsequently, the performance of all neural networks, each fine-tuned with its optimal feature set, is compared. This comparative analysis helps identify the top-performing classifier when utilizing the most suitable feature set. The research findings contribute to the field of machine learning and shed light on the intricate relationship between feature selection and classifier performance.

## 4. RESULTS AND DISCUSSIONS

This section unveils the results of the NN-RWQPS model and its thorough validation. The empirical study delves into the synergy of forward feature engineering and Neural Network classifiers for assessing water quality. The proposed system entails training and evaluating an NN-powered Robust Water Quality Prediction System using real-world data. Upcoming sections will detail the insights and conclusions derived from this investigation of each neural network classifier.

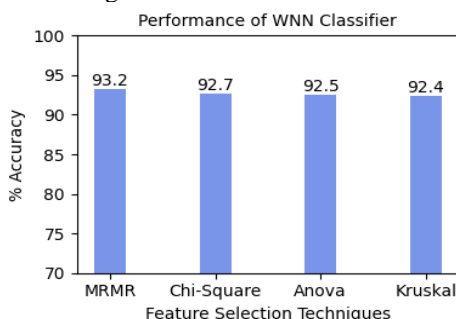


**Figure 3.** Performance of WNNC with FS Techniques

The research results offer insights into the performance of feature selection techniques with a focus on accuracy. MRRM stands out with the highest accuracy of 93.20%, making it the top choice for researchers prioritizing classification accuracy as showcased in Figure 3. Chi-

Square, ANOVA, and Kruskal are competitive with accuracies. MRRM's slight advantage in accuracy makes it the preferred selection if high accuracy is the objective.

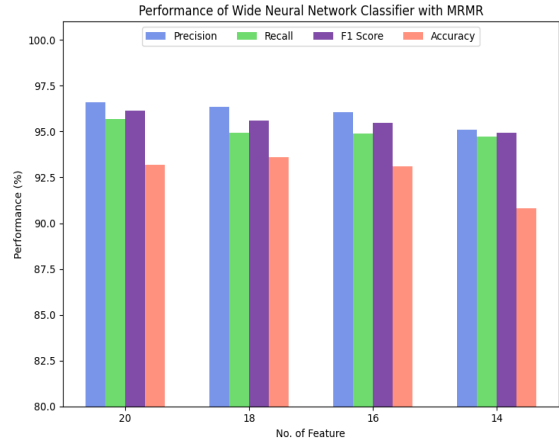


**Figure 4.** Performance of WNNC with MRRM

The selected dataset for this study encompasses 21 numerical attributes, systematically collected to analyse diverse aspects of water quality analysis systems. These attributes cover a broad range of parameters crucial for comprehending and assessing water quality. The presented results demonstrate the impact of varying the number of features on classification performance metrics. As the number of features decreases from 20 to 14, accuracy exhibit a corresponding decline as shown in Figure 4.

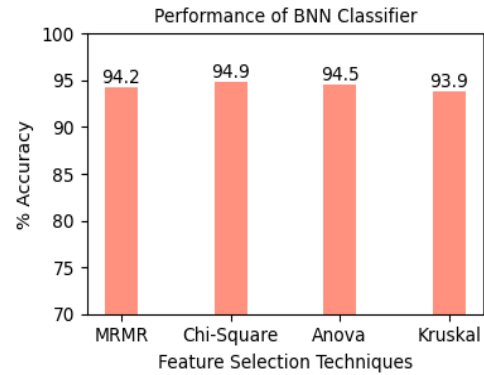


**Figure 5.** Performance of BNNC with FS Techniques

The research findings reveal that among the feature selection techniques, Chi-Square attains the highest accuracy at 94.90%, making it the top choice for maximizing classification accuracy. MRRM and Anova closely follow with commendable accuracies of 94.60% and 94.80%, respectively. Kruskal, while still achieving a respectable 93.90% accuracy, slightly lags behind the other methods. The decision is clear for researchers aiming to optimize accuracy - Chi-Square is the preferred feature selection technique as presented in Figure 5.

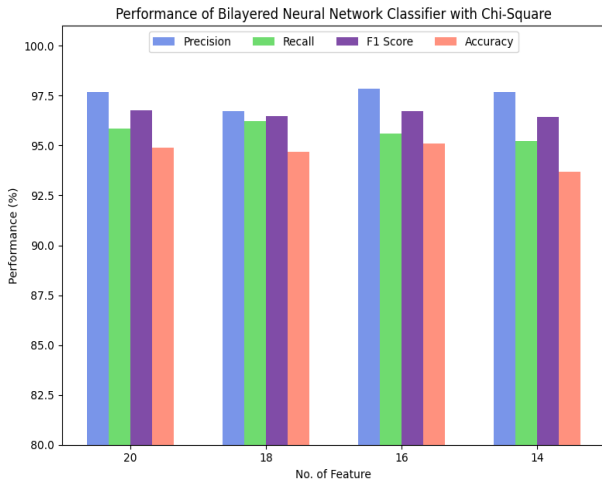


**Figure 6.** Performance of BNNC with Chi-Square

The research outcomes provide valuable numerical insights into the effect of feature reduction on classification performance metrics. As the number of features decreases from 20 to 14, precision remains relatively stable, with a minimal variation of approximately 1%. Similarly, recall shows only a slight deviation of around 1%. F1 Score, a measure of the balance between precision and recall, maintains a high value across different feature counts, with a minor change of about 1%. This emphasizes the trade-off between model simplicity and overall classification performance, while considering precision, recall, F1 Score, and accuracy in the research analysis presented in Figure 6.

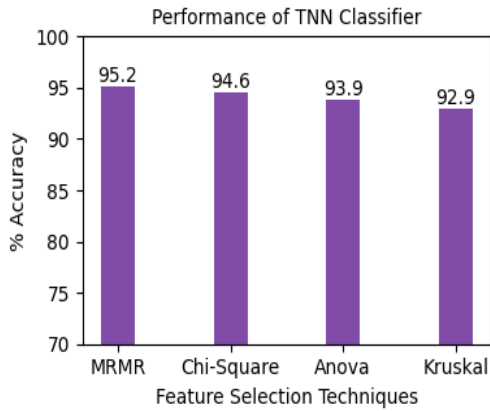


**Figure 7.** Performance of TNNC with FS Techniques

The research results demonstrate varying accuracy levels among different feature selection techniques. MRRM stands out with the highest accuracy at 95.20%, making it a robust choice for researchers seeking optimal classification accuracy. Chi-Square closely follows with a commendable accuracy of 94.60%. Anova exhibits a slightly lower accuracy at 93.90%, while Kruskal lags behind at 92.90%. The decision for accuracy optimization is clear - MRRM is the preferred feature selection method as depicted in Figure 7.

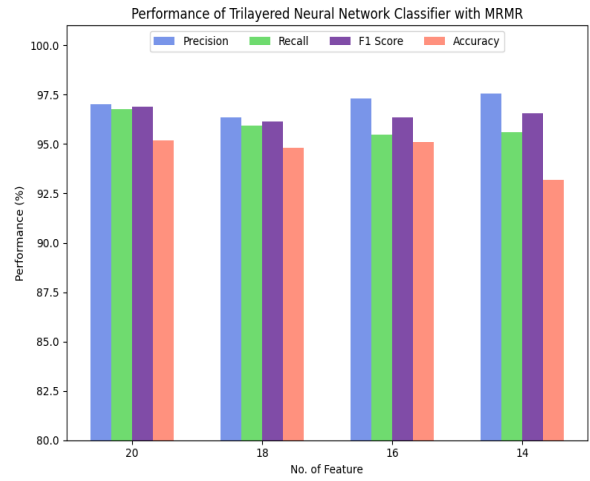


**Figure 8.** Performance of TNNC with MRRM

The research results provide a meticulous exploration of the interplay between varying feature counts and classification performance metrics. Precision consistently maintains high values, ranging from 96.34% to 97.56%, indicating the model's proficiency in correctly identifying positive cases. Likewise, recall remains stable, with values between 95.47% and 96.75%, reflecting the model's capacity to capture true positive instances effectively. The F1 Score consistently records values around 96.37%, underscoring the model's ability to balance precision and recall harmoniously. However, accuracy demonstrates a declining trend as the feature count decreases, highlighting the intricate trade-off between model simplicity and overall performance. These findings emphasize the importance of selecting the optimal feature count at 16 as shown in Figure 8.

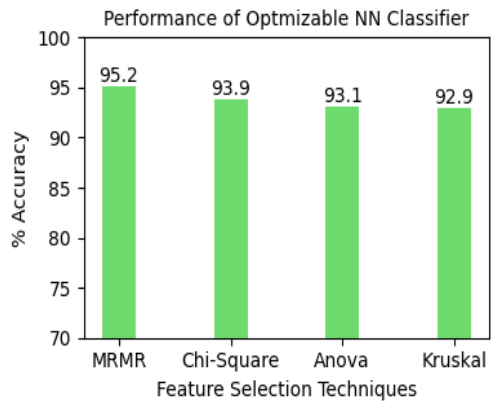


**Figure 9.** Performance of ONNC with FS Techniques

The research findings depict the accuracy performance of various feature selection techniques. MRRM stands out with the highest accuracy of 95.20%, showcasing its efficacy in enhancing classification accuracy as presented in Figure 9. Chi-Square, while strong, records a slightly lower accuracy of 93.90%. Anova follows with an accuracy of 93.10%, and Kruskal trails closely at 92.90%. The decision for this study focusing on

accuracy enhancement is clear – so, MRMR is the optimal choice.

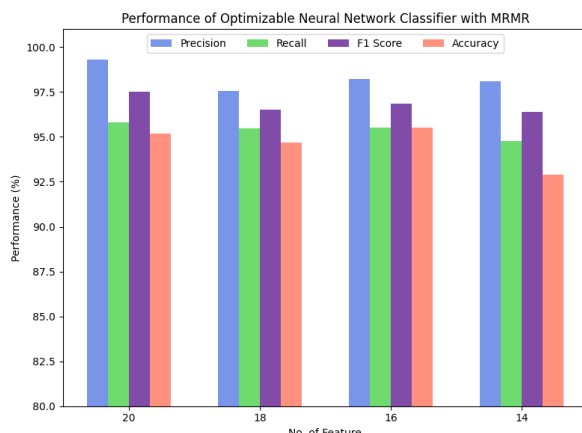


**Figure 10.** Performance of ONNC with MRMR

The research findings offer a detailed exploration of the impact of varying feature counts on classification performance metrics. Precision consistently achieves high values, ranging from 97.56% to 99.32%, indicating the model's proficiency in correctly identifying positive cases. Recall maintains stability, with values between 94.76% and 95.81%, reflecting the model's effective capture of true positive instances. The F1 Score consistently records values around 96.40% to 97.53%, showcasing the model's ability to balance precision and recall harmoniously as showcased in Figure 10. However, accuracy exhibits a gradual decrease as the feature count diminishes, highlighting the trade-off between model simplicity and overall classification performance. These insights underscore the importance

of selecting the optimal feature count, considering research goals.

## 5. CONCLUSIONS

The present study has demonstrated the significant potential of integrating feature engineering with neural network classifiers for water quality prediction. The research findings reveal that the proposed approach enhances the robustness and accuracy of water quality prediction.

Through rigorous experimentation, have ascertained that the feature engineering process, when combined with neural networks, effectively identifies and selects relevant features, leading to improved model performance. This is particularly crucial in real-world scenarios where water quality can be influenced by diverse factors. The empirical results highlight the ability of the optimized neural network classifiers to provide reliable and accurate predictions, enabling better-informed decision-making in water quality management. Overall, this research contributes to the development of a more robust and efficient Water Quality Prediction System, offering valuable insights for environmental monitoring and resource management.

### Acknowledgements:

First author, Dr. Maheswara Rao V V R, would like to express their sincere thanks to the management, Shri Vishnu Educational Society (SVES), of Shri Vishnu Engineering College for Women (A), Bhimavaram-534202, India for their logistic support that helped us to carry out this work.

## References:

- Aldhyani, T. H. H., Al-Yaari, M., Alkahtani, H., & Maashi, M. (2020). Water Quality Prediction Using Artificial Intelligence Algorithms. *Applied Bionics and Biomechanics*, 2020, 6659314. doi:10.1155/2020/6659314
- Bonthu et al. (2023). Multi-label and Multi-class Classification on a Custom Dataset using Convolution Neural Networks. In 2023 7th International Conference on Intelligent Computing and Control Systems (ICICCS), Madurai, India, pp. 576-579. doi: 10.1109/ICICCS56967.2023.10142828.
- Fei Han, Fanyu Li, Qinghua Ling, et al. (2023). A Feature Selection Method Based on Feature-Label Correlation Information and Self-Adaptive MOPSO. *Research Square*, September 14, 2023. doi: 10.21203/rs.3.rs-3348206/v1.
- Flores V., Bravo, I., & Saavedra, M. (2023). Water Quality Classification and Machine Learning Model for Predicting Water Quality Status—A Study on Loa River Located in an Extremely Arid Environment: Atacama Desert. *MDPI Journal Water*, 15(16), 2868, doi: 10.3390/w15162868.
- Goodarzi M. R., Niknam, A. R. R., Barzkar, A., Niazkar, M., Zare Mehrjerdi, Y., Abedi, M. J., & Heydari Pour, M. (2023). Water Quality Index Estimations Using Machine Learning Algorithms: A Case Study of Yazd-Ardakan Plain, Iran. *MDPI Journal Water*, 15(10), doi:10.3390/w15101876.
- Jinal P., et al. (2022). A Machine Learning-Based Water Potability Prediction Model by Using Synthetic Minority Oversampling Technique and Explainable AI. *Computational Intelligence and Neuroscience: CIN*, 2022. doi: 10.1155/2022/9283293

- Kalaivanan, K., & J. Vellingiri (2022). Survival Study on Different Water Quality Prediction Methods Using Machine Learning. *Nature Environment & Pollution Technology*, 21(3), doi:10.46488/NEPT.2022.v21i03.032.
- Khoi et al. (2022). Using machine learning models for predicting the water quality index in the La Buong River, Vietnam. *Water*, 14(10), 1552, doi:10.3390/w14101552
- Kurra, S. S., et al. (2022). Water quality prediction using machine learning. *International Research Journal of Modernization in Engineering Technology and Science*. 53 (1): 3–13. doi:10.2166/wqrj.2018.025
- Gong L., S. Xie, Y. Zhang, M. Wang, and X. Wang (2022). Hybrid Feature Selection Method Based on Feature Subset and Factor Analysis. *IEEE Access*, 10, 120792-120803, doi: 10.1109/ACCESS.2022.3222812.
- Maheswara Rao, V. V. R., et al. (2022). An Enhanced Machine Learning Classification System to Investigate the Status of Micronutrients in Rural Women. In *International Conference on Recent Trends in Computing, Lecture Notes in Networks and Systems*, 341 (Springer), doi: 10.1007/978-981-16-7118-0\_4
- Maheswara Rao, V. V. R., N. Silpa, Mahesh Gadiraju, Reddy Shiva Shankar, Dr. Vijaya Kumar, & Dr. K. B. V. Brahma Rao (2023). An Optimal Machine Learning Model Based On Selective Reinforced Markov Decision to Predict Web Browsing Patterns. *Journal of Theoretical and Applied Information Technology*, 101(2), 859-873.
- Md Galal Uddin, Stephen Nash, Mir Talas Mohammad Diganta, Azizur Rahman, Agnieszka I. Olbert. (2022). Robust machine learning algorithms for predicting coastal water quality index. *Journal of Environmental Management*, 321, doi:10.1016/j.jenvman.2022.115923.
- Mengyuan Zhu, et al. (2022). A review of the application of machine learning in water quality evaluation. *Eco-Environment & Health*. 1(2), doi:10.1016/j.eehl.2022.06.001.
- Silpa N., et al. (2022). Machine learning-based optimal segmentation system for web data using Genetic approach. *Journal of Theoretical and Applied Information Technology*, 100(11).
- Silpa N., M. R. V. V. R, M. V. Subbarao, M. Pradeep, C. R. Grandhi, & A. Karunasri. (2023). A Robust Team Building Recommendation System by Leveraging Personality Traits Through MBTI and Deep Learning Frameworks. In 2023 *International Conference on IoT, Communication and Automation Technology*, Gorakhpur, India, pp. 1-6. doi: 10.1109/ICICAT57735.2023.10263718.
- Rao, V. V. R. M., V. V. Kumari & K. V. S. V. N. Raju (2011). An Intelligent System for Web Usage Data Preprocessing. In: Meghanathan, N., Kaushik, B. K., Nagamalai, D. (eds) *Advances in Computer Science and Information Technology. CCSIT 2011*. doi:10.1007/978-3-642-17857-3\_47
- Rao M. V. V. R., et al. (2023). An Innovative Machine Learning based Heart Disease Assessment System by Sequential Feature Selection Approach. *International Conference on Intelligent Technologies (CONIT)*, doi: 10.1109/CONIT59222.2023.10205817
- Rao M. V. V. R., S. N. M. Gadiraju, S. S. Reddy, S. Bonthu, & R. R. Kurada (2023). A Plausible RNN-LSTM based Profession Recommendation System by Predicting Human Personality Types on Social Media Forums. In 2023 7<sup>th</sup> *International Conference on Computing Methodologies and Communication (ICCMC)*, doi: 10.1109/ICCMC56507.2023.10083557
- Reddy Shiva Shankar et al. (2022). Analyzing Student Reviews on Teacher Performance Using Long Short-Term Memory. In *Innovative Data Communication Technologies and Application (Springer)*, doi:10.1007/978-981-16-7167-8\_39.
- Silpa, N., & V. M. Rao (2021). Enriched Big Data Pre-Processing Model With Machine Learning Approach to Investigate Web User Usage Behaviour. *Indian J Comput Sci Eng.*, 12(5), 1248-56, doi: 10.21817/indjcse/2021/v12i5/211205050.
- Zhu, M., et al. (2022). A review of the application of machine learning in water quality evaluation. *Eco-Environment & Health*. 1(2), doi: 10.1016/j.eehl.2022.06.001.

**Maheswara Rao V V R**

Shri Vishnu Engineering College for Women,  
Bhimavaram,  
India  
[mahesh\\_vvr@yahoo.com](mailto:mahesh_vvr@yahoo.com)  
ORCID : 0000-0002-0503-7211

**Shiva Shankar Reddy**

S.R.K.R. Engineering College,  
Bhimavaram,  
India  
[shiva.shankar591@gmail.com](mailto:shiva.shankar591@gmail.com)  
ORCID : 0000-0001-5439-0348

**Silpa N**

Shri Vishnu Engineering College for Women,  
Bhimavaram,  
India  
[nrusimhadri.silpa@gmail.com](mailto:nrusimhadri.silpa@gmail.com)  
ORCID : 0000-0003-3411-0358

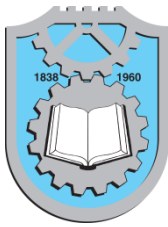
**Kranthi Addanki**

James Cook University,  
James Cook Drive,  
Australia  
[kranthi.addanki@my.jcu.edu.au](mailto:kranthi.addanki@my.jcu.edu.au)  
ORCID : 0000-0003-4921-8783

**Pachipala Yellamma**

Koneru Lakshmaiah Education Foundation,  
Vaddeswaram, Guntur,  
India  
[pachipala.yamuna@gmail.com](mailto:pachipala.yamuna@gmail.com)  
ORCID : 0000-0002-6291-7418

---



Vol. xx, No. x (202x) x-x, doi:

# Proceedings on Engineering Sciences



www.pesjournal.net

## MACHINE LEARNING ALGORITHMS FOR ERYTHEMATO-SQUAMOUS DISEASE CLASSIFICATION: FEATURE RANKINGS AND PERFORMANCE ANALYSIS

M. Venkata Subbarao<sup>1</sup>

S. Lakshmi Praveena

T. Naga Sharmila

Praveen Kumar Nalli

G. Challa Ram

D. Ramesh Varma

Srinivasarao Alluri

Tabassum Nazeer Syed

Keywords:

### ABSTRACT

*Dermatology; psoriasis; Seborrheic dermatitis; Lichen planus; Pityriasis rosea; Chronic dermatitis; Pityriasis rubra pilari; ML classifiers; Kruskal-Wallis feature ranking.*

*Erythemato-squamous diseases (ESDs), also known as erythrodermas, are a group of dermatological disorders characterized by both redness (erythema) and scaling (squamous) of the skin. These conditions can have various causes and implications. The implications of ESDs vary depending on the specific condition and its severity. While some may cause mild symptoms and have minimal impact on daily life, others can be chronic, recurrent, and significantly affect a person's physical and emotional well-being. Treatment options for these conditions may include topical medications, oral medications, phototherapy, and lifestyle modifications. In this paper, state of art machine learning (ML) algorithms are implemented for classification of ESD. To classify the disease a set of 11 clinical features and 23 histopathological features are considered. The performance of the ML classifiers is analyzed with individual sets of features and combination of both. Further, the performance of the ML classifiers is analyzed at different training rates to know the superior classifier for ESD classification. Furthermore, the study is extended to investigate the effectiveness of the Kruskal-Wallis algorithm in ranking the importance of features in the dataset used for disease classification. An investigation depicts that Ensemble and SVM classifiers outperformed the other ML classifiers in terms of accuracy and F1-score.*



© 202x Published by Faculty of Engineering

<sup>1</sup> Corresponding author: M. Venkata Subbarao  
Email: [mandava.decs@gmail.com](mailto:mandava.decs@gmail.com)

## 1. INTRODUCTION

Erythrodermas, referred to as ESDs, encompass a group of dermatological conditions characterized by both skin redness and scaling. These disorders can arise from various underlying causes and have wide-ranging implications (Banu and Toacșe, 2013). Some common ESDs and their key features are as follows.

**Psoriasis:** Psoriasis is a chronic autoimmune disease that causes rapid skin cell turnover, resulting in the formation of thick, scaly patches of skin. The exact cause of psoriasis is unknown, but it is believed to involve a combination of genetic and environmental factors. The disease can have significant implications on a person's quality of life, causing physical discomfort, itching, pain, and emotional distress (Singh et al., 2022).

**Seborrheic dermatitis:** It is a common inflammatory skin condition that mainly affects areas rich in sebaceous glands, such as the scalp, face, and chest. It is characterized by redness, greasy or flaky scales, and itching. While the exact cause is unclear, factors like yeast overgrowth, genetic predisposition, and certain neurological conditions may contribute to its development. Seborrheic dermatitis can be chronic and recurrent but is not considered a serious medical condition (Basu et al., 2015).

**Eczema (atopic dermatitis):** It is a chronic inflammatory skin condition that is often associated with allergies and immune system dysfunction. It leads to red, itchy, and inflamed skin, which may also develop scaling or weeping blisters. The exact cause of eczema is not fully understood, but genetic factors, environmental triggers, and abnormalities in the skin barrier function are believed to play a role. Eczema can have a significant impact on a person's quality of life, causing discomfort, disrupted sleep, and psychological distress (Badrinath et al., 2020).

**Pityriasis rosea:** It is a self-limiting skin rash characterized by the appearance of a larger "herald patch" followed by numerous smaller scaly patches. The exact cause of pityriasis rosea is unknown, but it is thought to be associated with viral infections, particularly human herpesvirus 6 (HHV-6) or human herpesvirus 7 (HHV-7). Pityriasis rosea typically resolves on its own within several weeks to months and does not generally have long-term implications.

**Lichen planus:** It is a chronic inflammatory disorder that affects the skin, mucous membranes, hair, and nails. It is characterized by small, itchy, flat-topped, polygonal bumps that can develop a lacy white pattern and may cause erosions or ulcers. The exact cause of lichen planus is unknown, but it is believed to involve an abnormal immune response. Lichen planus can be

chronic and may cause discomfort or pain in severe cases.

While some diseases may cause mild symptoms and have minimal impact on daily life, others can be chronic, and recurrent, and significantly affect a person's physical and emotional well-being. Treatment options for these conditions may include topical medications, oral medications, phototherapy, and lifestyle modifications. If you suspect you have an ESD or any other medical condition, it is important to consult with a healthcare professional for an accurate diagnosis and appropriate management (Xie et al., 2012). These conditions often share similar symptoms, making their classification and diagnosis challenging. The precise symptom may differ in accordance with the underlying disease (Ravichandran et al., 2014).

Here are some general symptoms associated with these conditions:

**Redness (Erythema):** The affected skin usually appears red, inflamed, or irritated.

**Scaling (Squamous):** The skin may develop flakes, scales, or patches of thickened skin that can be white, silver, or greyish.

**Itching:** Itchiness is a common symptom in ESDs. The severity can range from mild to severe and may significantly affect the quality of life.

**Rash:** Rashes may be present, and their appearance can vary depending on the specific disease. They may be well-defined or more diffuse.

**Dryness:** The affected skin may become dry and rough, leading to discomfort and a tendency to crack or fissure.

**Burning or stinging sensation:** Some individuals may experience a burning or stinging sensation in the affected areas.

**Flares and remissions:** ESDs often exhibit a cyclic pattern of flares and remissions, with symptoms worsening during flare-ups and improving during periods of remission.

**Location-specific symptoms:** The distribution and location of symptoms may vary depending on the specific condition. For example, psoriasis commonly affects the scalp, elbows, knees, and lower back, while seborrheic dermatitis often involves the scalp, face (especially the eyebrows and nasolabial folds), and chest.

Various classification systems have been proposed to aid in the identification and management of these diseases. Here is a general overview of the classification of ESD (Polat and Güneş, 2009). The traditional classification system divides ESDs into two main categories based on the presence or absence of fungal infection. Non-infectious ESDs category includes conditions such as psoriasis, seborrheic dermatitis, lichen planus, pityriasis rosea, and cutaneous lupus erythematosus. The infectious ESDs category includes fungal infections like tinea corporis (ringworm), tinea

versicolor (pityriasis versicolor), and candidiasis. Over time, researchers have proposed modifications to the traditional classification system to incorporate new knowledge and improve diagnostic accuracy (Polat and Güneş, 2006). These revisions often consider additional factors such as histopathology, immunopathology, and genetic markers. For example, the expansion of non-infectious ESDs may include subcategories based on distinctive clinical and histological features, as well as response to treatment. This can aid in the differentiation of conditions such as psoriasis, seborrheic dermatitis, and lichen planus. Given the overlapping clinical features of ESDs, an accurate differential diagnosis is crucial. Dermatologists rely on a combination of clinical evaluation, patient history, physical examination, and, in some cases, laboratory tests to differentiate between these conditions (Abdi and Giveki, 2013). Features such as lesion morphology, distribution, and associated symptoms are carefully assessed to arrive at a proper diagnosis.

The purpose of this study is to develop and implement machine learning algorithms for accurately classifying ESDs. The primary aim is to improve the diagnostic process and enhance the accuracy of disease classification. Further, the study is extended to investigate the effectiveness of the Kruskal-Wallis algorithm in ranking the importance of features in the dataset used for disease classification. The paper could explore how this ranking technique helps in selecting the most relevant features for improved classification performance. This objective could focus on demonstrating how the reduction of irrelevant features contributes to enhanced model performance and efficiency.

The paper is structured as detailed below. Section II outlines the experimental setup, including data preprocessing, feature extraction, feature ranking with the Kruskal-Wallis algorithm, model training, and evaluation procedures. The methodology of the classifiers is presented in section III. Section IV presents the results of the experiments in a clear and interpretable manner i.e., the comparative performance of different machine learning algorithms and the impact of feature ranking on classification accuracy. Section V discusses the implications of the findings in the context of ESD classification and the broader field of medical diagnostics.

## 2. LITERATURE & FRAMEWORK

ML algorithms can be used to analyze clinical data, such as patient symptoms, medical history, and visual representations of skin lesions, to aid in the classification and diagnosis of ESDs.

Investigation of use of Convolutional Neural Networks (CNNs) in classifying ESDs is presented (Tekin, 2014).

Using a dataset of 10,000 high-resolution images of different ESD cases, the authors trained a CNN model to detect and categorize these diseases. The methodology benefited from data augmentation and transfer learning, leveraging pretrained models for enhanced accuracy.

The model achieved a commendable 95% accuracy on the test set. However, the paper faced limitations in terms of a potentially non-diverse dataset predominantly from a single ethnic group, possibly limiting its generalizability across diverse populations. It is compared traditional ML techniques, specifically Support Vector Machines (SVM), with newer deep learning methods in classifying ESDs (Kaushik et al., 2023). The study utilized a dataset containing both clinical data and patient history for 5,000 cases. While the SVM demonstrated an accuracy of 85%, the deep learning model surpassed this with a 92% success rate. One significant advantage of this study was its incorporation of non-image data, providing a holistic approach. However, the research's limitation lay in the relatively smaller dataset, which might not capture all the nuances of ESD manifestations.

A hybrid model that combines the strengths of traditional machine learning (Random Forest) and deep learning is presented (Putatunda, 2020). The methodology utilized a diverse dataset of 15,000 entries, blending clinical images and patient medical histories. Through feature integration, the hybrid model achieved an impressive accuracy of 95%. The robustness of this research was its comprehensive dataset, which encompassed varied ethnic backgrounds and age groups. However, a limitation noted was the increased computational cost and complexity due to the hybrid nature of the model, potentially hindering its deployment in real-time or resource-limited settings.

In (Zhouxiao et al., 2022), it delves into the potential of Recurrent Neural Networks (RNNs) to trace the progression of Erythema-Squamous Diseases over time. Utilizing a time-series dataset of 7,000 patients, where images were taken at various stages of disease development, the authors established an RNN model that aimed to predict disease progression patterns. The methodology notably excelled in handling sequential data, with the model achieving 89% accuracy in predicting future disease states. Nevertheless, the paper's limitation was evident in its reliance on well-documented and time-stamped data, which may be challenging to procure in real-world scenarios.

In (Spolaor et al., 2023), it explored the viability of using transfer learning techniques for ESD classification. Leveraging popular pre-trained networks, the authors fine-tuned these architectures using a modest dataset of 3,000 ESD images. The methodology highlighted the practicality and cost-effectiveness of transfer learning, yielding a respectable 90% accuracy

rate without necessitating extensive training data or computational power. The primary advantage was the resource efficiency of the model, making it accessible for smaller clinics or research setups. However, the study's main limitation is its dependency on pre-existing architectures, which might not be optimally designed for dermatological image nuances.

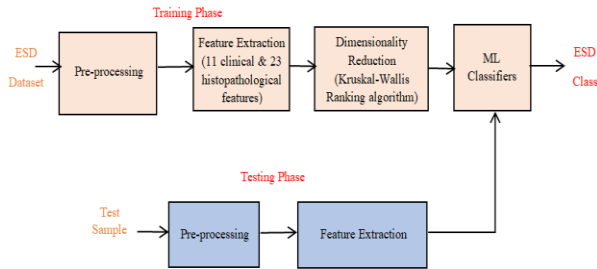


**Figure 1.** Proposed Framework

Figure 1 represents the framework of the proposed ESD classification. The steps involved in the framework as follows.

*Data collection:* Relevant clinical data and images of skin lesions are collected from patients diagnosed with different ESDs. The data may include information about symptoms, patient demographics, and any other factors that could contribute to the classification.

*Preprocessing:* Removal of noise, normalizing the features and handle missing values are performed in this stage. This step is crucial to ensure the quality and consistency of the data.

*Feature extraction:* Relevant features are extracted from the preprocessed data. In the case of ESDs, features could include characteristics of skin lesions, such as color, texture, shape, and distribution.

*Training data preparation:* The dataset gets split into two parts: a training set and a testing set. We use the training set to teach the machine learning model, and the testing set to see how well it works.

*Model training:* Many ML methods, including decision trees, SVMs, K-Nearest Neighbors (KNN), and Ensemble classifiers, can be taught using the features we found. These models understand how the features are connected to the ESD labels, learning the patterns and relationships between them.

*Model evaluation:* In this phase, evaluating the model using the testing dataset to assess its classification performance. Evaluation metrics like accuracy, precision, recall, and F1-score are commonly used to measure the model's effectiveness.

### 3. MACHINE LEARNING CLASSIFIERS

#### 3.1 Decision Trees (DT)

Decision tree classifiers are widely used in ML for both regression and classification tasks. The DT classifier is constructed using a training dataset, which consists of labeled examples. The algorithm uses a recursive process called recursive binary splitting to partition the

data based on the feature values. The goal is to find the best feature and the best split point that maximizes the information gain or Gini impurity (a measure of how well the feature splits the data based on class labels) (Danjuma and Osofisan, 2014). The splitting process continues recursively until a stopping criterion is met. This could be a maximum depth limit, a minimum number of samples required to split, or when all samples belong to the same class.

#### 3.2 SVM Classifiers

SVMs are powerful machine learning models used for both classification and regression tasks. They operate by finding an optimal hyperplane that separates data points into different classes or predicts continuous values (Subbarao et al., 2023).

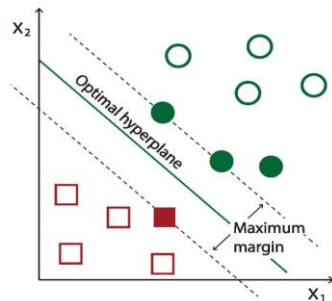


**Figure 2.** Hyperplane in SVM Classification

Figure 2 depicts the hyperplane representation to distinguish two classes. One of the key features of SVMs is the use of kernels. Kernels allow SVMs to operate efficiently in high-dimensional feature spaces without explicitly calculating the coordinates of the data points. The linear kernel is the simplest and most commonly used kernel. It represents a linear decision boundary in the input space. It works well when the data is linearly separable. The polynomial kernel maps the original features into a higher-dimensional space using polynomial functions. It can capture non-linear relationships between the data points. The kernel function is defined as

$$K(x, y) = (x^T y + c)^d \quad (1)$$

where,  $c$  is a constant and  $d$  is the degree of the polynomial.

The RBF kernel is popular in SVMs because of its flexibility. It defines a similarity measure between data points based on their Euclidean distance in the feature space. The kernel function is defined as

$$K(x, y) = \exp(-\gamma * ||x - y||^2) \quad (2)$$

where,  $\gamma$  is a hyperparameter that controls the influence of each training example.

The sigmoid kernel maps the features into a higher-dimensional space using a sigmoid function. It can

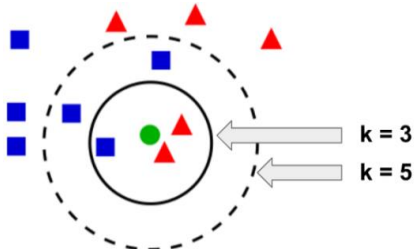
capture non-linear relationships, but it is generally less commonly used compared to other kernels. The kernel function is defined as

$$K(x, y) = \tanh(\alpha x^T y + c) \quad (3)$$

SVMs also allow the use of custom kernels, where you can define your own similarity measure. This is useful when the data has a specific structure or when domain knowledge suggests a particular kernel.

### 3.3 KNN Classifiers

K-Nearest Neighbors (KNN) is a non-parametric and instance-based algorithm, meaning that it doesn't make any assumptions about the underlying data distribution and instead relies on the proximity of training examples to make predictions. The choice of the K value is crucial. A small K may lead to over fitting, where the model becomes too sensitive to noise, while a large value of k may result in under fitting, where the model becomes too biased and fails to capture local patterns. It is typically chosen through experimentation and cross-validation. The distance metric determines how distances are calculated between data points. Euclidean distance is commonly used for continuous features, while other metrics like Manhattan distance or Hamming distance may be used for specific types of data.



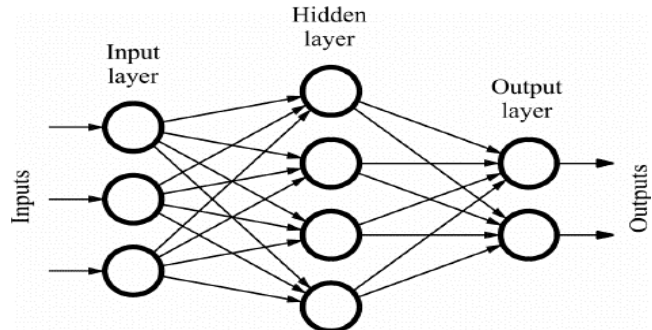
**Figure 3.** KNN Classification

Figure 3 represents the classification with different values of  $k$ . Further, it's often recommended to scale the features to ensure that they contribute equally to the distance calculation. This is important when features have different scales or units. Common scaling techniques include normalization or standardization (subtracting mean and dividing by standard deviation). KNN classifiers are complex, especially for large datasets. Techniques like KD-trees or ball trees can be used to optimize the nearest neighbor search process and improve efficiency.

### 3.4 NN Classifiers

Classification with Neural Network (NN) classifiers involves training a NN model to classify input data into different classes. NNs are composed of interconnected nodes (neurons) organized in layers, and they learn to extract relevant features from the input data through a

training process. Figure 4 depicts basic architecture of NN classifier.



**Figure 4.** NN Classifier

### 3.5 Ensemble Classifiers

Classification with ensemble classifiers involves combining multiple individual classifiers to make more accurate predictions than any single classifier alone (Subbarao et al., 2023). Ensemble classifiers are known for their ability to improve predictive performance, increase robustness, and reduce over fitting.

### 3.5 Kruskal-Wallis Feature Ranking Algorithm

Kruskal-Wallis is a non-parametric statistical test used in machine learning for feature ranking when dealing with non-normally distributed data or categorical variables. It extends the one-way ANOVA test and evaluates whether there are significant differences in the distributions of a continuous target variable across different groups or levels of a categorical feature. In contrast to ANOVA, Kruskal-Wallis doesn't assume data normality, making it suitable for a wider range of datasets. It operates by ranking the data values and comparing the average ranks between groups. Kruskal-Wallis is useful when the target variable violates assumptions of parametric tests or when the data exhibits non-linear relationships. By assessing feature significance based on target variable distribution differences among groups, Kruskal-Wallis helps in selecting relevant features for classification or regression tasks, improving model interpretability and generalization.

## 4. RESULTS & DISCUSSIONS

To identify ESDs using ML classifiers a dataset of size 358 samples that includes 11 clinical features (e.g., age, gender, symptoms) and 23 histopathological features (e.g., cell counts, tissue characteristics) for patients with ESDs. The simulated dataset information is shown in Table 1.

The simulations are carried with two different training rates 80% and 70%. In each case 10% data has taken for the validation. The test set for evaluating the models are 20% and 30% respectively. The training set is used to

train the models, the validation set is used for hyper parameter tuning, and the test set is reserved for final evaluation. MATLAB software is used for the simulation.

**Table 1.** Dataset Information

S.No	Skin Diseases Class	Quantity
1	Psoriasis	111
2	Pityriasis rubra pilaris	20
3	Chronic dermatitis	48
4	Lichen planus	71
5	Pityriasis rosea	48
6	Seborrheic dermatitis	60
	Total	358

Table 2 and 3 depicts the statistical information of the clinical and histopathological features for the input dataset respectively.

**Table 2.** Statistical Information of the clinical features

S.No	Clinical Features	Max.	Min.	Mean	Median
1	Erythema	3	0	2.078212	2
2	Scaling	3	0	1.807263	2
3	Definite borders	3	0	1.569832	2
4	Scalp involvement	3	0	0.530726	0
5	Oral Mucosal involvement	3	0	0.379888	0
6	Koebner phenomenon	3	0	0.636872	0
7	Knee and elbow involvement	3	0	0.622905	0
8	Follicular papules	3	0	0.170391	0
9	Polygonal papules	3	0	0.449721	0
10	itching	3	0	1.354749	1
11	Family history	1	0	0.122905	0

**Table 3.** Histopathological Features

S.No	Clinical Features	Max.	Min.	Mean	Median
1	Melanin incontinence	0.410615	0	3	0
2	Vacuolisation damage basal layer	0.460894	0	3	0
3	Eosinophils infiltrate	0.142458	0	2	0
4	PNL infiltrate	0.547486	0	3	0
5	Follicular horn plug	0.106145	0	3	0
6	Inflammatory mononuclear infiltrate	1.877095	2	3	0
7	acanthosis	1.955307	2	3	0
8	hyperkeratosis	0.511173	0	3	0
9	parakeratosis	1.287709	1	3	0
10	Clubbing rete ridges	0.662011	0	3	0
11	Elongation rete ridges	0.98324	0	3	0
12	Thinning suprapapillary epidermis	0.642458	0	3	0
13	Spongiform pustule	0.298883	0	3	0
14	Focal hypergranulosis	0.399441	0	3	0
15	Disappearance granular layer	0.47486	0	3	0
16	Fibrosis papillary dermis	0.315642	0	3	0
17	Spongiosis	0.949721	0	3	0
18	Saw tooth appearance retes	0.458101	0	3	0
19	exocytosis	1.368715	2	3	0
20	Perifollicular parakeratosis	0.117318	0	3	0
21	Munro microabcess	0.368715	0	3	0
22	Band like infiltrate	0.558659	0	3	0
23	Age	36.29609	35	75	0

Table 4 presents the performance of different ML algorithms with different feature sets. It presents the performance of the ML classifiers with 11 clinical features and 23 histo-pathological features and combined 34 features. The performance is also measured at 80% training rate and 70% training rate.

**Table 4.** Performance of Different ML classifiers with Different feature sets

Category	Classifier	Performance with Clinical Features (11)	Performance with Histo-pathological Features (23)	Performance with all features (34)	Performance with Clinical Features (11)	Performance with Histo-pathological Features (23)	Performance with all features (34)
Decision Trees	Fine	81.7	93	95.9	80.6	89.7	94.5
	Medium	83.1	93	95.9	80.6	89.7	94.5
	Coarse	70.4	77.5	78.1	70.8	79.4	78
SVM	Linear	88.7	95.8	98.6	86.1	95.3	95.4
	Cubic	87.3	95.8	95.9	81.9	94.4	91.7
	Quadratic	87.3	94.4	97.3	81.9	95.3	95.4
	Coarse Gaussian	87.3	87.3	93.2	81.9	86	89.9
	Medium Gaussian	90.1	93	94.5	87.5	96.3	94.5
Ensemble	Fine Gaussian	64.8	38	30.1	55.6	43	34.9
	Subspace KNN	87.3	85.9	97.3	880.6	92.5	94.5
	Bagged Trees	88.7	94.4	97.3	86.1	93.5	97.2
	Boosted Trees	88.7	95.8	30.1	83.3	91.6	30.3
	RusBoosted Trees	90.1	95.8	100	81.9	95.3	100
KNN	Subspace Discriminant	88.7	97.2	98.6	83.3	93.5	97.2
	Fine	88.7	88.8	93.2	77.8	88.8	94.5
	Medium	87.3	95.8	94.5	81.9	92.5	94.5
	Coarse	80.3	85.9	83.6	62.5	76.6	77.1
	Cosine	87.3	94.4	94.5	83.3	93.5	93.6
	Cubic	87.3	97.2	94.5	80.6	90.7	93.6
Neural Networks	Weighted	88.7	97.2	94.5	84.7	89.7	93.6
	Narrow	84.5	95.8	94.5	86.1	90.7	93.6
	Medium	87.3	95.3	94.5	83.3	95.3	93.6
	Wide	85.9	97.2	93.2	84.7	94.4	93.6
	Bi layered	88.7	95.8	93.2	79.2	93.5	92.7
	Tri layered	85.9	94.4	93.2	86.1	91.6	90.8

**Table 5.** Performance metrics of ML classifiers with all 34 Features

Category	Classifier	Accuracy (%)	Precision	Recall	F1 Score	Accuracy (%)	Precision	Recall	F1 Score
% of Training - 80									
Decision Trees	Fine	95.9	0.96	0.96	0.96	94.5	0.92	0.92	0.92
	Medium	95.9	0.96	0.96	0.96	94.5	0.92	0.92	0.92
	Coarse	78.1	0.63	0.56	0.60	78	0.64	0.56	0.59
SVM	Linear	98.6	0.98	0.99	0.98	95.4	0.95	0.96	0.95
	Cubic	95.9	0.95	0.96	0.96	91.7	0.86	0.93	0.89
	Quadratic	97.3	0.97	0.97	0.97	95.4	0.95	0.96	0.95
	Coarse Gaussian	93.2	0.86	0.95	0.90	89.9	0.80	0.93	0.86
	Medium Gaussian	94.5	0.91	0.96	0.93	94.5	0.92	0.95	0.93
	Fine Gaussian	30.1	0.16	0.05	0.07	34.9	0.21	0.38	0.27
Ensemble	Subspace KNN	97.3	0.97	0.95	0.95	94.5	0.947	0.92	0.933
	Bagged Trees	97.3	0.96	0.98	0.96	97.2	0.975	0.97	0.972
	Boosted Trees	30.1	0.05	0.05	0.05	30.3	0.16	0.05	0.076
	RusBoosted Trees	100	1	1	1	100	1	1	1
	Subspace Discriminant	98.6	0.98	0.99	0.98	97.2	0.97	0.96	0.964
KNN	Fine	93.2	0.945	0.94	0.942	94.5	0.937	0.954	0.945
	Medium	94.5	0.93	0.968	0.95	94.5	0.937	0.953	0.944
	Coarse	83.6	0.70	0.69	0.695	77.1	0.619	0.613	0.615
	Cosine	94.5	0.93	0.968	0.948	93.6	0.926	0.943	0.934
	Cubic	94.5	0.93	0.968	0.948	93.6	0.926	0.943	0.934
	Weighted	94.5	0.93	0.968	0.948	93.6	0.926	0.943	0.934
Neural Networks	Narrow	94.5	0.935	0.948	0.941	92.7	0.958	0.963	0.960
	Medium	94.5	0.94	0.945	0.942	92.7	0.915	0.933	0.924
	Wide	93.2	0.922	0.930	0.926	92.7	0.915	0.933	0.924
	Bi layered	93.2	0.922	0.930	0.926	92.7	0.915	0.933	0.924
	Tri layered	93.2	0.927	0.932	0.923	89.9	0.89	0.90	0.895

**Table 6.** Feature Rankings from Kruskal-Wallis Algorithm

Rank	Feature	Score
1	Vacuolization damage basal layer	132.1187
2	Saw tooth appearance rates	132.0557
3	Melanin incontinence	131.205
4	Polygonal papules	131.1427
5	Fibrosis papillary dermis	130.8129
6	Perifollicular parakeratosis	130.621
7	Band like infiltrate	129.9214
8	Focal hypergranulosis	129.0225
9	Clubbing rete ridges	127.7499
10	Thinning suprapapillary epidermis	126.1007
11	Oral mucosal involvement	125.2916
12	Elongation rete ridges	115.1145
13	Follicular horn plug	107.1768
14	Knee and elbow involvement	98.7087
15	Follicular papules	87.6082
16	exocytosis	83.6033
17	Scalp involvement	83.0768
18	spongiosis	79.3603
19	Munro microabcess	77.6436
20	PNL infiltrate	64.9176
21	Koebner phenomenon	51.2436
22	Spongiform pustule	50.9313
23	Definite borders	50.0011
24	Disappearance granular layer	45.9134
25	itching	40.7342
26	parakeratosis	40.3839
27	scaling	34.1644
28	Family history	25.2672
29	Eosinophils infiltrate	19.1216
30	age	17.9604
31	acanthosis	16.946
32	erythema	16.8651
33	hyperkeratosis	16.5467
34	Inflammatory mononuclear infiltrate	16.5164

Table 6 represents the rankings of different features obtained by Kruskal-Wallis algorithm.

Table 7 represents the performance metrics of ML classifiers with best 30 features Similarly, Table 8 and 9 represents the performance of ML classifiers with best 25 and 20 features respectively.

**Table 7.** Performance Metrics with best 30 features

Category	Classifier	Accuracy (%)	Precision	Recall	F1 Score
Decision Trees	Fine	93.2	0.92	0.93	0.92
	Medium	93.2	0.92	0.93	0.92
	Coarse	78.1	0.63	0.56	0.60
SVM	Linear	93.2	0.91	0.93	0.92
	Cubic	94.5	0.93	0.93	0.93
	Quadratic	93.2	0.91	0.93	0.92
	Coarse Gaussian	93.2	0.91	0.93	0.92
	Medium Gaussian	93.2	0.91	0.93	0.92
	Fine Gaussian	74	0.61	0.69	0.65
Ensemble	Subspace KNN	93.2	0.918	0.922	0.919
	Bagged Trees	93.2	0.92	0.93	0.92
	Boosted Trees	93.2	0.92	0.93	0.92
	RUS Boosted Trees	95.9	0.956	0.953	0.954
	Subspace Discriminant	94.5	0.937	0.937	0.93
KNN	Fine	95.9	0.955	0.952	0.953
	Medium	93.2	0.924	0.92	0.921
	Coarse	79.5	0.63	0.59	0.609
	Cosine	93.2	0.924	0.92	0.923
	Cubic	94.5	0.937	0.937	0.937
	Weighted	94.5	0.937	0.937	0.937
Neural Networks	Narrow	94.5	0.88	0.91	0.89
	Medium	94.5	0.95	0.95	0.95
	Wide	94.5	0.95	0.95	0.95
	Bi layered	91.8	0.91	0.89	0.90
	Tri layered	94.5	0.95	0.943	0.94

**Table 8.** Performance Metrics with best 25 features

Category	Classifier	Accuracy (%)	Precision	Recall	F1 Score
<b>Decision Trees</b>	Fine	95.9	0.96	0.96	0.96
	Medium	95.9	0.96	0.96	0.96
	Coarse	78.1	0.63	0.56	0.60
<b>SVM</b>	Linear	100	1	1	1
	Cubic	97.3	0.97	0.97	0.97
	Quadratic	98.6	0.98	0.98	0.97
	Coarse Gaussian	94.5	0.90	0.95	0.93
	Medium Gaussian	97.3	0.94	0.98	0.96
	Fine Gaussian	57.5	0.44	0.73	0.55
<b>Ensemble</b>	Subspace KNN	97.3	0.968	0.968	0.968
	Bagged Trees	95.9	0.964	0.962	0.963
	Boosted Trees	95.9	0.965	0.962	0.963
	RUS Boosted Trees	98.6	0.987	0.983	0.985
	Subspace Discriminant	97.3	0.968	0.968	0.968
	Fine	97.3	0.968	0.968	0.968
<b>KNN</b>	Medium	97.3	0.968	0.968	0.968
	Coarse	82.2	0.66	0.58	0.617
	Cosine	97.3	0.968	0.968	0.968
	Cubic	97.3	0.968	0.968	0.968
	Weighted	97.3	0.968	0.968	0.968
	Narrow	95.9	0.95	0.96	0.954
<b>Neural Networks</b>	Medium	95.9	0.95	0.96	0.956
	Wide	95.9	0.95	0.96	0.956
	Bi layered	94.5	0.94	0.945	0.942
	Tri layered	95.9	0.95	0.96	0.947

**Table 9.** Performance Metrics with best 20 features

Category	Classifier	Accuracy (%)	Precision	Recall	F1 Score
<b>Decision Trees</b>	Fine	95.9	0.96	0.96	0.96
	Medium	95.9	0.96	0.96	0.96
	Coarse	78.1	0.63	0.56	0.60
<b>SVM</b>	Linear	97.3	0.97	0.98	0.97
	Cubic	93.2	0.89	0.93	0.91
	Quadratic	95.9	0.95	0.96	0.96
	Coarse Gaussian	94.5	0.91	0.95	0.93
	Medium Gaussian	93.2	0.89	0.94	0.91
	Fine Gaussian	32.9	0.19	0.38	0.26
<b>Ensemble</b>	Subspace KNN	98.6	0.987	0.983	0.984
	Bagged Trees	97.3	0.977	0.976	0.976
	Boosted Trees	95.9	0.965	0.962	0.963
	RUS Boosted Trees	98.6	0.987	0.983	0.984
	Subspace Discriminant	97.3	0.968	0.968	0.968
	Fine	93.2	0.919	0.946	0.932
<b>KNN</b>	Medium	94.5	0.932	0.968	0.949
	Coarse	79.5	0.648	0.67	0.658
	Cosine	94.5	0.932	0.968	0.949
	Cubic	94.5	0.932	0.968	0.968
	Weighted	94.5	0.932	0.968	0.968
	Narrow	95.9	0.95	0.96	0.954
<b>Neural Networks</b>	Medium	95.9	0.95	0.96	0.956
	Wide	95.9	0.95	0.96	0.956
	Bi layered	94.5	0.94	0.945	0.942
	Tri layered	95.9	0.95	0.96	0.947

Within Tables 7, 8, and 9, SVMs employing linear and cubic kernel functions, as well as Ensemble classifiers, notably Rusboosted trees, consistently outperformed other machine learning models, even when utilizing a

reduced set of features. This highlights the robustness and efficiency of these techniques in various scenarios, showcasing their potential as top-performing options in a range of predictive tasks.

From the investigations, it is observed that by considering all the features for classification Linear SVM, Rusboosted Trees and subspace discriminant ensemble classifiers outperformed all other ML classifiers. After applying feature selection through kruskal-wallis algorithm, the performance of the most of the classifiers is increased because of reduction of redundant features. It is also observed that, Linear SVM achieved 100% accuracy with best 25 features and the maximum accuracy of all other classifiers is observed with 25 best features. From the investigations it is observed that feature selection algorithm also play a key role in identification of the ESD with high accuracy. The analysis underscores the significant potential of ML classifiers in enhancing the ESDs. Nonetheless, their effective deployment is contingent upon several pivotal factors. First and foremost, prioritizing data quality and reliability is imperative, given that ML models heavily rely on input data. Secondly, the prudent selection of suitable ML models customized for the specific ESD detection task is pivotal for achieving optimal performance. Finally, the interpretability of these models is essential for comprehending their decision-making processes and fostering trust in their outcomes.

## 5. CONCLUSION

This paper presents detailed investigations of state-of-the-art ML models for the classification of ESDs. Leveraging a rich dataset comprising 11 clinical features and 23 histo-pathological features, the study investigates the performance of machine learning classifiers, both individually and in combination of feature sets. Through meticulous experimentation, the classifiers' effectiveness is examined under varying training rates of 80% and 70%. This extensive analysis revealed valuable insights into selecting the most suitable classifier for ESD classification. Furthermore, this study ventured into assessing the effectiveness of the Kruskal-Wallis algorithm in ranking the importance of features within the dataset—a critical step in understanding the disease classification process. Significantly, the findings highlight that Ensemble and SVM classifiers outperformed other ML models in terms of F1 score and % of accuracy. In the study, Linear SVM, Rusboosted trees, and subspace discriminant ensemble classifiers excelled in ESD classification when considering all features. Feature selection via Kruskal-Wallis improved classifier performance. Linear SVM achieved 100% accuracy with the best 25 features. These results underscore the potential of these classifiers in aiding the accurate identification of ESD, thus offering promising prospects for improved diagnostic and clinical decision-making in the field of dermatology.

## References:

- Abdi, M. J., & Giveki, D. (2013). Automatic detection of erythemato-squamous diseases using PSO-SVM based on association rules. *Engineering Applications of Artificial Intelligence*, 26(1), 603–608. doi: 10.1016/j.engappai.2012.01.017.
- Badrinath, N., Gopinath, G., Ravichandran, K. S., Premaladha, J., & Krishankumar, R. (2018). Classification and prediction of Erythemato-Squamous diseases through Tensor-Based Learning. *Proceedings of the National Academy of Sciences, India Section A: Physical Sciences*, 90(2), 327–335. doi: 10.1007/s40010-018-0563-x.
- Banu, S. M., & Toacșe, G. (2013). A mobile/desktop medical application for automatic differential diagnosis of psoriasis lesions. *2013 Second International Conference on E-Learning and E-Technologies in Education (ICEEEE)*, Lodz, Poland, 186–191. doi: 10.1109/icelete.2013.6644371.
- Basu, A., Roy, S. S., & Abraham, A. (2015). A Novel Diagnostic Approach Based on Support Vector Machine with Linear Kernel for Classifying the Erythemato-Squamous Disease. *2015 International Conference on Computing Communication Control and Automation*, Pune, India. doi: 10.1109/iccuba.2015.72.
- Danjuma K, Osofisan A. O., (2014). Evaluation of Predictive Data Mining Algorithms in Erythemato-Squamous Disease Diagnosis. *International Journal of Computer Science Issues*, 11(6), 85-94.
- Kaushik, B., Vijayvargiya, A., Uppal, J., Gupta, A. (2023). Comparative Analysis of Machine Learning Approaches for Classifying Erythemato-Squamous Skin Diseases. In: Kadry, S., Prasath, R. (eds) *Mining Intelligence and Knowledge Exploration*. MIKE 2023. *Lecture Notes in Computer Science*, vol 13924. Springer, Cham. doi: 10.1007/978-3-031-44084-7\_7
- Krishna, N. M. S., Priyakanth, R., Katta, M. B., Akanksha, K., & Anche, N. Y. (2023). CNN-Based breast cancer detection. In *Lecture notes in networks and systems* (pp. 613–622). doi: 10.1007/978-981-19-8563-8\_59.
- Polat, K., & Güneş, S. (2006). The effect to diagnostic accuracy of decision tree classifier of fuzzy and k-NN based weighted pre-processing methods to diagnosis of erythemato-squamous diseases. *Digital Signal Processing*, 16(6), 922–930. doi: 10.1016/j.dsp.2006.04.007.
- Polat, K., & Güneş, S. (2009). A novel hybrid intelligent method based on C4.5 decision tree classifier and one-against-all approach for multi-class classification problems. *Expert Systems With Applications*, 36(2), 1587–1592. doi:10.1016/j.eswa.2007.11.051.
- Putatunda, S. K. (2020). A Hybrid Deep Learning Approach for Diagnosis of the Erythemato-Squamous Disease. *2020 IEEE International Conference on Electronics, Computing and Communication Technologies (CONECCT)*, Bangalore, India. https://doi.org/10.1109/conecct50063.2020.9198447.
- Rao, A. P., Kumar, G. P., & Ranjan, R. (2022). Performance Comparison of Classification Models for Identification of Breast Lesions in Ultrasound Images. In *Pattern Recognition and Data Analysis with Applications, Lecture Notes in Electrical Engineering*, 888, 689–699. doi: 10.1007/978-981-19-1520-8\_56.
- Ravichandran, K. S., Narayananmurthy, B., Ganapathy, G., Ravalli, S., & Sindhura, J. (2014). An efficient approach to an automatic detection of erythemato-squamous diseases. *Neural Computing and Applications*, 25(1), 105–114. doi: 10.1007/s00521-013-1452-5.
- Singh, S. K., Sinha, A., & Yadav, S. S. (2022). Performance Analysis of Machine learning Algorithms for Erythemato-Squamous Diseases Classification. *2022 IEEE International Conference on Distributed Computing and Electrical Circuits and Electronics (ICDCECE)*. doi:10.1109/icdcece53908.2022.9793000.
- Spolaor, N., Lee, H., Mendes, A. I., Nogueira, C., Parmezan, A. R. S., Takaki, W. S. R., Coy, C. S. R., Wu, F., & Fonseca-Pinto, R. (2023). Fine-tuning pre-trained neural networks for medical image classification in small clinical datasets. *Multimedia Tools and Applications*. doi: 10.1007/s11042-023-16529-w.
- Subbarao, M. V., Ram, G. C., & Varma, D. (2023). Performance Analysis of Pistachio Species Classification using Support Vector Machine and Ensemble Classifiers. *2023 International Conference on Recent Trends in Electronics and Communication (ICRTEC)*, Mysore, India. doi: 10.1109/icrtec56977.2023.10111889.
- Subbarao, M. V., Rani, U., Mythreya, V. H., Kumar, G. P., Priyakanth, R., & Abudhagir, U. S. (2023). Investigations on Feature Ranking Algorithms for Date Fruit Genotype Detection. *2023 8th International Conference on Communication and Electronics Systems (ICCES)*, Coimbatore, India. doi: 10.1109/icces57224.2023.10192766.
- Tekin, A. (2014). Classification of Erythemato-Squamous diseases using association rules and fuzzy C-Means clustering. *Arabian Journal for Science and Engineering*, 39(6), 4699–4705. doi: 10.1007/s13369-014-1168-6.
- Xie J, Lei J, Xie W, Gao X, Shi Y, Liu X (2012). Novel hybrid feature selection algorithms for diagnosing erythemato-squamous diseases. In: He J, Liu X, Krupinski EA, Xu G (eds) HIS, 7231. Springer, Berlin, 173–185. doi: 10.1007/978-3-642-29361-0\_21.
- Zhouxiao, L., Konstantin Christoph Koban, Thilo Ludwig Schenck, Riccardo Enzo Giunta, Qingfeng Li, and Yangbai Sun. (2022). Artificial Intelligence in Dermatology Image Analysis: Current Developments and Future Trends. *Journal of Clinical Medicine*, 11 (22), 6826. doi: 10.3390/jcm11226826

---

**Dr. M. Venkata Subbarao**

Department of ECE,  
Shri Vishnu Engineering College for  
Women, Bhimavaram, India  
[mandava.decs@gmail.com](mailto:mandava.decs@gmail.com)  
ORCID 0000-0001-5840-2190

**S. Lakshmi Praveena**

Department of ECE,  
Shri Vishnu Engineering College for  
Women, Bhimavaram, India  
[sleepada.praveena@gmail.com](mailto:sleepada.praveena@gmail.com)  
ORCID 0009-0005-1621-5430

**T. Naga Sharmila**

Department of ECE,  
Shri Vishnu Engineering College for  
Women, Bhimavaram, India  
[sharmilatanniru24@gmail.com](mailto:sharmilatanniru24@gmail.com)  
ORCID 0009-0003-2894-2227

---

**Praveen Kumar Nalli**

Department of AI,  
Shri Vishnu Engineering College for  
Women, Bhimavaram, India  
[praveenkumar.nalli@svecw.edu.in](mailto:praveenkumar.nalli@svecw.edu.in)  
ORCID 0000-0002-7443-7841

**G. Challaram**

Department of ECE,  
Shri Vishnu Engineering College for  
Women, Bhimavaram, India  
[challaram.grandhi@gmail.com](mailto:challaram.grandhi@gmail.com)  
ORCID 0000-0002-3790-1318

**D. Ramesh Varma**

Department of ECE,  
Shri Vishnu Engineering College for  
Women, Bhimavaram, India  
[varmaramesh422@gmail.com](mailto:varmaramesh422@gmail.com)  
ORCID 0000-0002-9517-4967

---

**Dr. Srinivasarao Alluri**

Department of ECE,  
Koneru Lakshmaiah Education  
Foundation (KLEF), Green Fields,  
Vaddeswaram (V), Guntur District,  
Andhra Pradesh, India  
[asrao.81@gmail.com](mailto:asrao.81@gmail.com)  
ORCID 0000-0002-3790-1318

**Tabassum Nazeer Syed**

The Bradley Department of Electrical and  
Computer Engineering,  
Virginia Polytechnic Institute and State  
University, USA  
[tabassumnazeer8@vt.edu](mailto:tabassumnazeer8@vt.edu)

---



Vol. xx, No. x (202x) x-x, doi:

# Proceedings on Engineering Sciences



www.pesjournal.net

## ON STEREOGRAPHIC SEMICIRCULAR ERLANG DISTRIBUTION WITH APPLICATION

Radhika A. J. V.  
Phani Yedlapalli  
Peddi Raju, Ch.  
Kishore, G.N.V  
Sri Krishna, A  
Pradeep Kumar, R. L. N

### Keywords:

Semicircular data, inverse stereographic projection, trigonometric moments, simulation, estimation.



### A B S T R A C T

In this research paper, we present an innovative investigation into a novel two parameter semicircular distribution, termed the “stereographic semicircular Erlang distribution,” which is constructed using the inverse stereographic projection (ISP) technique. This distribution serves as advancement over the existing stereographic semicircular exponential distribution. We delve into essential mathematical properties of this distribution and execute a simulation study to estimate its parameter values. Furthermore, we perform an empirical analysis utilizing a dataset comprising posterior corneal curvature measurements extracted from the eyes of 23 patients. This empirical assessment is designed to evaluate the adaptability and potential applicability of the proposed distribution within the realm of ophthalmology in medical science.

© 202x Published by Faculty of Engineerin

### 1. INTRODUCTION

Circular data find widespread applications across various disciplines such as geology, meteorology, biology, earth science, political science, economics, and computer science, among others. Full circular models are extensively documented in seminal texts, including Fisher (1993), Mardia and Jupp (2000), and Jammalamadaka and Sen Gupta (2001). Nevertheless, it is essential to recognize that modeling circular data across the entire circle may not always be necessary, as acknowledged by Jones (1968), Guardiola (2004), Byoung et al. (2008), Phani et al. (2013, 2016, 2017, 2017a, 2019, 2020), and Girija et al. (2013). Noteworthy contributions have been made by Dattatreya

Rao et al. (2007), Phani et al. (2011, 2012, 2023), Sakthivel et al. (2022), Olewi et al. (2022), and Salah Hamza Abid (2022, 2023) have introduced various circular and semicircular models through the application of inverse stereographic projection, a technique that maps point from the real line to the unit circle based on known probability distributions on real line. Further enriching this field Pramesti et al. (2015, 2016, 2017, and 2018) have explored and analyzed novel semicircular and circular distributions. Recent research by Ramblí et al. (2015), Ali (2017) and Iftikhar et al. (2022) has introduced half circular distributions and discussed their applicability to real-world data sets.

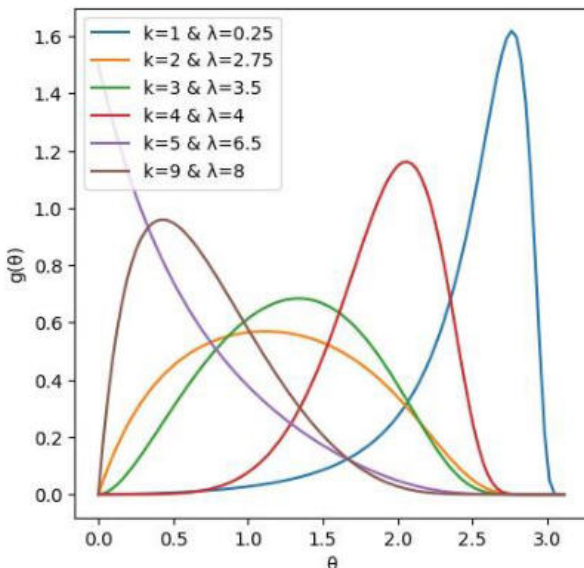
<sup>1</sup> Corresponding author: Phani Yedlapalli  
Email: phani.maths@svecw.edu.in

In this article, we initiate the development of a novel semicircular model, herein denominated as the “stereographic semicircular Erlang distribution.” This model is constructed by applying the inverse stereographic projection technique to the Erlang distribution and representing a special case of the gamma distribution. We furnish precise mathematical representations for trigonometric moments using Meijer's G-function. The structure of the article unfolds as follows: In the second section, we introduce the stereographic semicircular Erlang distribution and present key mathematical properties, including trigonometric moments, cumulative distribution function, survival function, and hazard rate function, accompanied by illustrative plots. Section 3 outlines the method of maximum likelihood estimation, followed by a simulation study in section 4 to assess the model's parameter consistency. Section 5 scrutinizes the applicability of the new model to real-world datasets, offering comparisons with other competitive models. Finally, in section 6, we summarize our findings and conclude this piece of work.

## 2. DERIVATION OF THE PROPOSED MODEL

The Erlang distribution, originally introduced by Erlang (1909), is a particular instance of the gamma distribution, characterized by a positive integer value for the shape parameter. It is a continuous probability distribution with support on  $(0, \infty)$ , and has wide range of applications in fields like traffic engineering, stochastic processes and biomathematics, mainly due to its relative to the exponential distribution.

Here we recall the definition of Erlang distribution.



**Definition 2.1** A continuous random variable  $\mathbf{X}$  is considered to adhere to the Erlang distribution with a shape parameter  $k$  (a positive integer) and a scale parameter  $\lambda > 0$  if its probability density and distribution functions are defined as follows:

$$f(x) = \frac{\lambda^k x^{k-1}}{\Gamma(k)} e^{-\lambda x}, \text{ where } k \in \mathbb{Z}^+, \lambda > 0, 0 < x < \infty. \quad (1)$$

$$F(x) = \frac{\gamma(\lambda, \lambda x)}{\Gamma(\lambda)}, \text{ where } \gamma(\cdot) \text{ is the lower incomplete gamma function.} \quad (2)$$

## Definition 2.2

A random variable  $\theta_{sc}$  defined on the semicircle is characterized as following the stereographic semicircular Erlang distribution with a shape parameter  $k$  (a positive integer) and a scale parameter  $\lambda$ , denoted by  $SSCEr(k, \lambda)$ . This distribution is specified by its probability density and distribution functions, given as follows:

$$g(\theta; k, \lambda) = \lambda^k (\Gamma(k) \times (1 + \cos((\theta)))^{-1} \times \left( \tan\left(\frac{\theta}{2}\right) \right)^{(-1+k)} \times \exp\left(-\lambda \tan\left(\frac{\theta}{2}\right)\right)) \quad (3)$$

$$G(\theta; k, \lambda) = (\Gamma(k))^{-1} \times \gamma\left(k, \lambda \tan\left(\frac{\theta}{2}\right)\right),$$

where  $\theta \in [0, \pi]$ ,  $\lambda > 0$ , and  $k \in \mathbb{Z}^+$ . (4)

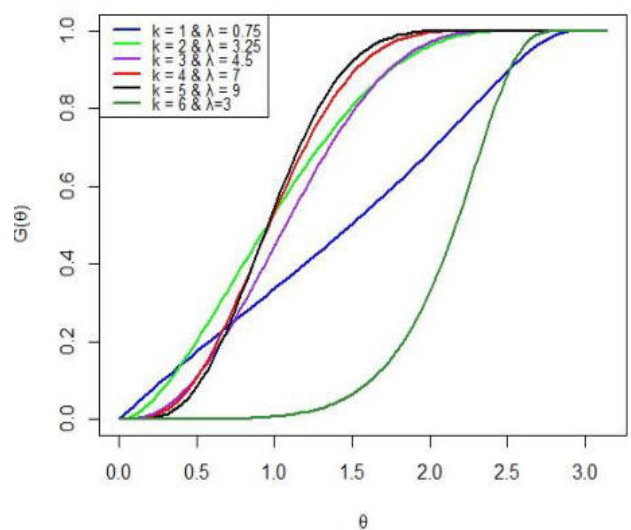


**Figure 1.** Plots of the probability density function (left) and cumulative distribution function (right) for various parameter values.

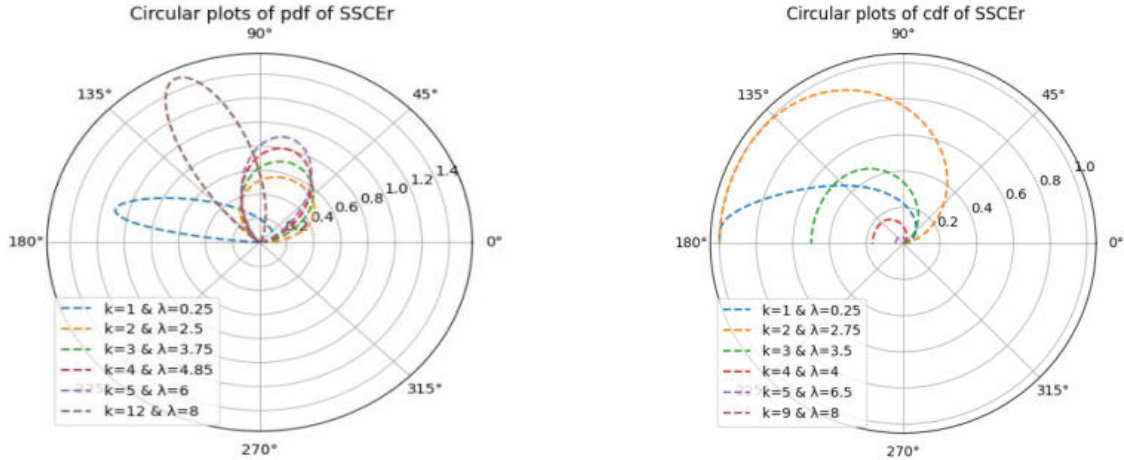


**Figure 2.** Plots displaying the probability density function (left) and cumulative distribution function (right) for diverse parameter values, represented in a circular format.

**Survival and Hazard Function:** The survival function

of  $\text{SSCEr}(k, \lambda)$  is given by

$$S(\theta) = 1 - G(\theta) = 1 - \gamma\left(k, \lambda \tan\left(\frac{\theta}{2}\right)\right) \times (\Gamma(k))^{-1}. \quad (5)$$

The hazard rate function and the reversed hazard rate function of the  $\text{SSCEr}(k, \lambda)$  are given respectively by

$$h(\theta) = \frac{g(\theta)}{1 - G(\theta)} = \frac{\lambda^k \times \left(\left(\tan\left(\frac{\theta}{2}\right)\right)^{k-1} \exp\left(-\lambda \tan\left(\frac{\theta}{2}\right)\right)\right)}{(1 + \cos(\theta)) \times \left(\Gamma(k) - \gamma\left(k, \lambda \tan\left(\frac{\theta}{2}\right)\right)\right)} \quad (6)$$

and

$$r(\theta) = \frac{g(\theta)}{G(\theta)} = \frac{\lambda^k \times \left(\left(\tan\left(\frac{\theta}{2}\right)\right)^{k-1} \exp\left(-\lambda \tan\left(\frac{\theta}{2}\right)\right)\right)}{\left((1 + \cos(\theta)) \times \gamma\left(k, \lambda \tan\left(\frac{\theta}{2}\right)\right)\right)} \quad (7)$$

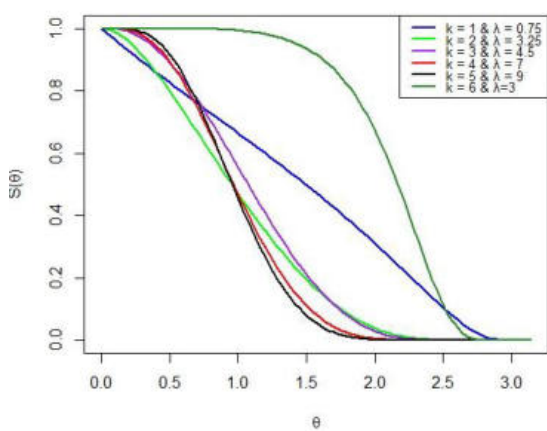


**Figure 3:** Survival function (left) and hazard rate function (right) plots depicting varying parameter values.

**Quantile Function:** The quantile function for the SSCEr( $k, \lambda$ ) distribution is given by

$$G^{-1}(u) = Q(u) = 2 \times \tan^{-1} \left( \left( \frac{1}{\lambda} \right) \times \gamma^{-1} \left( k, \Gamma(k) \times u \right) \right)$$

, where  $0 < u < 1$  (8)

and  $\gamma^{-1}(.,.)$  is the inverse incomplete gamma function.

**Median:** The median of SSCEr( $k, \lambda$ ) will be given by

$$Q(0.5) = 2 \tan^{-1} \left( \left( \frac{1}{\lambda} \right) \gamma^{-1} \left( k, \frac{\Gamma(k)}{2} \right) \right). \quad (9)$$

### Trigonometric moments

Under the pdf of stereographic semicircular Erlang distribution the first two

$\alpha_p = E(\cos p\theta)$  and  $\beta_p = E(\sin p\theta)$ ,  $p=1, 2$ . are given as follows:

$$\alpha_1 = 1 - \frac{2\lambda^k}{\sqrt{\pi} \Gamma(k)} G_{13}^{31} \left( \frac{\lambda^2}{4} \left| \begin{array}{c} -\frac{k}{2} \\ -\frac{k}{2}, 0, \frac{1}{2} \end{array} \right. \right), \quad (10)$$

$$\beta_1 = \frac{\lambda^k}{\sqrt{\pi} \Gamma(k)} G_{13}^{31} \left( \frac{\lambda^2}{4} \left| \begin{array}{c} \left( \frac{1-k}{2} \right) \\ \left( \frac{1-k}{2} \right), 0, \frac{1}{2} \end{array} \right. \right) \quad (11)$$

$$\alpha_2 = 1 - \frac{4\lambda^k}{\sqrt{\pi} \Gamma(k)} G_{13}^{31} \left( \frac{\lambda^2}{4} \left| \begin{array}{c} -\frac{k}{2} \\ \left( \frac{2-k}{2} \right), 0, \frac{1}{2} \end{array} \right. \right) \quad (12)$$

### 4. SIMULATION

In this part, the performance of  $\lambda$  is evaluated by conduction Monte Carlo simulation study. To carry out this study, we use the inverse distribution function approach (i.e., quantile function) for obtaining random numbers from the SSCEr( $k, \lambda$ ) with pdf and cdf given in Eq. (2.3) and (2.4) respectively. For each simulation, 10,000 samples of sizes

$$\beta_2 = \frac{2\lambda^k}{\sqrt{\pi} \Gamma(k)} \left[ G_{13}^{31} \left( \frac{\lambda^2}{4} \left| \begin{array}{c} \left( \frac{1-k}{2} \right) \\ \left( \frac{3-k}{2} \right), 0, \frac{1}{2} \end{array} \right. \right) - G_{13}^{31} \left( \frac{\lambda^2}{4} \left| \begin{array}{c} -\left( \frac{1+k}{2} \right) \\ \left( \frac{1-k}{2} \right), 0, \frac{1}{2} \end{array} \right. \right) \right] \quad (13)$$

### 3. MAXIMUM LIKELIHOOD ESTIMATION

In this section, we have introduced the maximum likelihood estimation method, which is utilized for parameter estimation in the Stereographic Semicircular Erlang (SSCEr) distribution. Assuming that a random sample  $\psi_1, \psi_2, \psi_3, \dots, \psi_n$  of size  $n$  is drawn from SSCEr, the log-likelihood function can be expressed as follows:

$$\log L = nk \log(\lambda) - n \log(\Gamma(k)) + 2 \sum_{i=1}^n \sec \left( \frac{\psi_i}{2} \right) + (k-1) \sum_{i=1}^n \log \left( \tan \left( \frac{\psi_i}{2} \right) \right) - \lambda \sum_{i=1}^n \left( \tan \left( \frac{\psi_i}{2} \right) \right)$$

For a fixed value of  $k$ , we get

$$\lambda = \frac{nk}{\sum_{i=1}^n \left( \tan \left( \frac{\psi_i}{2} \right) \right)}. \quad (14)$$

$n = 50, 75, 100, 300, 500$ , and  $750$  were generated for different values of  $\lambda$  and given  $k$ . For every individual sample, we use a self-programmed R script to calculate the Maximum Likelihood Estimators (MLEs), average bias, mean square error (MSE), and mean relative error (MRE).

- (i) Average absolute bias =  $\frac{1}{10000} \sum_{i=1}^{10000} |(\lambda - \hat{\lambda})|$
- (ii) Mean Square Error (MSE) =  $\frac{1}{10000} \sum_{i=1}^{10000} (\lambda - \hat{\lambda})^2$
- (iii) Mean Relative Error (MRE) =  $\frac{1}{10000} \sum_{i=1}^{10000} \frac{|\lambda - \hat{\lambda}|}{\lambda}$

**Table 1.** Average MLE, absolute bias, MSE, and MRE of the simulated estimate of  $\lambda$  for a given value of  $k$ .

$k = 1$								
Sample size $n$	$\lambda = 0.75$				$\lambda = 2$			
	MLE	Bias	MSE	MRE	MLE	Bias	MSE	MRE
50	0.76901	0.08783	0.01278	0.11710	2.05177	0.24247	0.09549	0.12123
75	0.76765	0.07406	0.00900	0.09874	2.03321	0.18947	0.06012	0.09474
300	0.75341	0.03477	0.00189	0.04635	2.01050	0.09483	0.01404	0.04742
500	0.75208	0.02678	0.00114	0.03570	2.00503	0.07052	0.00809	0.03526
750	0.75229	0.02132	0.00071	0.02842	2.00361	0.05735	0.00510	0.02868
$k = 3$								
Sample size $n$	$\lambda = 3.5$				$\lambda = 4.75$			
	MLE	Bias	MSE	MRE	MLE	Bias	MSE	MRE
50	3.53760	0.23908	0.09295	0.06831	4.78091	0.32956	0.17358	0.06938
75	3.52134	0.18366	0.05525	0.05247	4.75693	0.25325	0.10046	0.05332
300	3.49788	0.09134	0.01318	0.02610	4.75270	0.12927	0.02575	0.02721
500	3.49956	0.07265	0.00830	0.02076	4.75288	0.10219	0.01624	0.02151
750	3.49801	0.05799	0.00536	0.01657	4.75367	0.08002	0.01001	0.01685
$k = 5$								
Sample size $n$	$\lambda = 5.25$				$\lambda = 6$			
	MLE	Bias	MSE	MRE	MLE	Bias	MSE	MRE
50	5.27793	0.26685	0.11264	0.05086	6.02896	0.30118	0.14461	0.05020
75	5.25691	0.21853	0.07441	0.04163	6.00215	0.24376	0.09248	0.04063
300	5.25302	0.10643	0.01804	0.02027	6.00073	0.12317	0.02388	0.02053
500	5.25798	0.08382	0.01120	0.01596	6.01385	0.09423	0.01373	0.01571
750	5.25043	0.07152	0.00792	0.01362	5.99925	0.08025	0.00996	0.01338

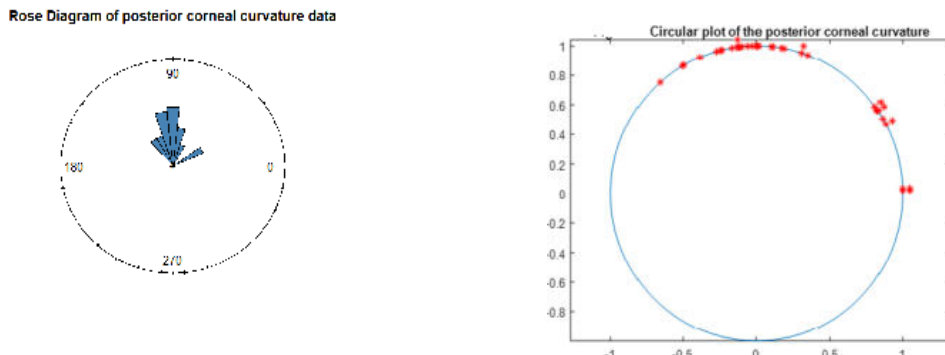
Based on the findings from the simulated results displayed in Table 1, it is apparent that the average bias, mean square error (MSE), and mean relative error (MRE) values of the estimator tend to converge towards zero as the sample size increases. Consequently, the estimator for the SSCER distribution demonstrates precision, accuracy, and stability, thereby establishing its consistency.

## 5. APPLICATION

To show the usefulness of proposed model, we consider real data set obtained from a glaucoma clinic at the University of Malaya Medical centre, Malaysia. This data consists of the images of the posterior segment of the eyes of 23 patients. Recently, Iftikhar et al. (2022), Maruthan et al. (2022), Ramblí et al. (2019), and Ali (2017) used this data to check the applicability of their models.

**Data set:**

1.60	1.21	1.46	2.10	1.40	1.82	1.57	1.56	1.85	0.60	1.70	1.97	1.47
1.74	1.67	1.38	0.53	1.69	1.63	1.56	1.81	2.09	2.29			

**Figure 4.** Rose diagram of eye data set (left) and Circular plot of eye data set (right)

We compare the performance of stereographic semicircular Erlang distribution with performance of SSCEEx. (Phani et al. (2013)), hc-BurrIII, hc-GIW, hc-log logistic, and hc-gamma (Ali 2017) distributions using the Kolmogorov-Smirnov(KS) statistic, the

Akaike information criterion(AIC), and Bayesian information criterion(BIC) to find out the best-fitting distribution. All the required statistics are computed and present in Table2 and 3.

**Table 2.** MLEs and their standard errors for eye data set.

Model	$\theta_1(S.E)$	$\theta_2(S.E)$	$\theta_3(S.E)$
SSCEr	5.42656( <b>0.46194</b> )	5	-
SSCEEx	0.90449(0.18859)	-	-
hc-BurrIII	1.00047(0.22975)	4.28673(0.85739)	-
hc-GIW	0.31027(0.10242)	1.70011(0.23619)	4.80355(2.0366)
hc-log logistic	1.06425(0.08438)	4.38493(0.80058)	-
hc-gamma	5.72203(1.63874)	0.19321(0.05783)	-

**Table 3.** Summary of statistics.

Model	LL	AIC	BIC	KS(p-value)
SSCEr	<b>-11.10115</b>	<b>24.2023</b>	<b>25.3370</b>	<b>0.1630(0.5741)</b>
SSCEEx	-22.91177	47.8235	48.9590	0.3955(0.0015)
hc-BurrIII	-11.37239	26.7449	29.0158	0.1839(0.4180)
hc-GIW	-18.77315	43.5463	46.9528	0.2719(0.0666)
hc-log logistic	-11.07212	26.1443	28.4152	0.1165(0.9136)
hc-gamma	-11.08750	26.1746	28.4456	0.1698(0.5208)

The higher value of the log-likelihood statistic, along with the smaller values of AIC and BIC, unequivocally indicates that the stereographic semicircular Erlang

distribution provides a better fit to the dataset compare to the other competent distribution.

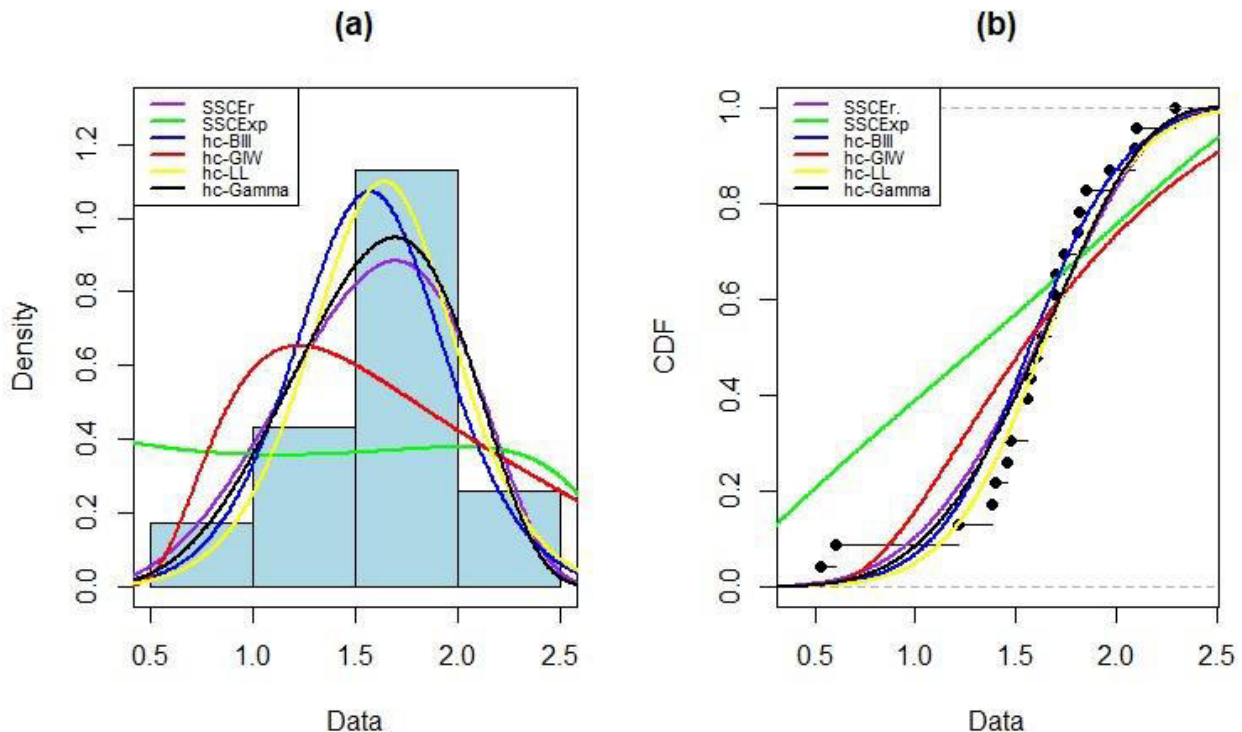


**Figure 5.** (a) Fitted densities of the SSCEr. SSCExp. Hc -Burr III, hc-GIW, hc-log logistic, and hc-gamma models to eye data set. (b) Fitted distribution function of the SSCEr., SSCExp., hc-BurrIII, hc-GIW, hc-log logistic, and hc-gamma models to eye data set.

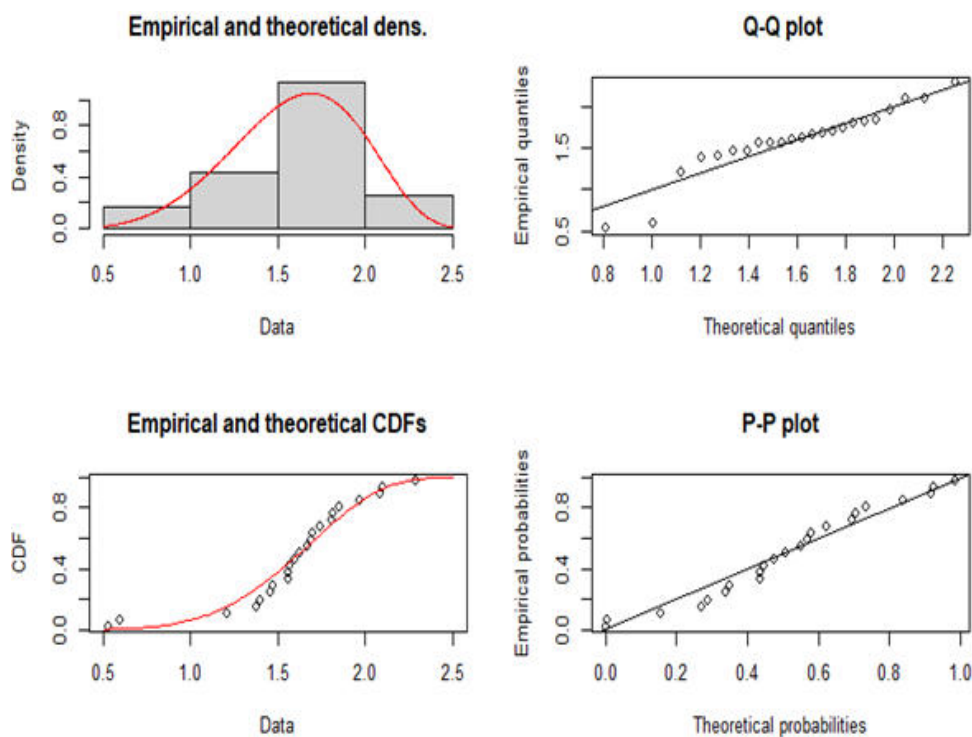


**Figure 6.** The empirical pdf (top left panel), cdf (bottom left panel), Q-Q (top right panel), and P-P (bottom right panel) plots for eye data set.

All the computation is evaluated by using FitdistrPlus, Adequacy Model (Pedro Rafael et al. 2019)

## 6. CONCLUSION

In this research paper, we introduce the stereographic semicircular Erlang distribution, a novel two-parameter distribution created via the inverse stereographic projection (ISP) technique, building upon the existing stereographic semicircular exponential distribution. We meticulously explore its mathematical properties, conduct simulations to estimate parameters, and empirically analyze data from posterior corneal curvature measurements of 23 patients' eyes. This empirical investigation serves to assess the distribution's adaptability and practical utility. Our findings emphasize the distribution's promise in statistical

representation, highlighting its potential for diverse applications and contributing significantly to advancing statistical modeling methodologies.

### Acknowledgements:

First author A.J.V.Radhika would like to thank CIIPR(Center for Innovation and Intellectual Property Rights ) Acharya Nagarjuna University for offering financial assistance to carry out the research project under "Seed money Grant" Project No: C102-15-25, Date:26-05-2023. The corresponding author Phani Yedlapalli would like to express their sincere thanks to the management, Shri Vishnu Educational Society (SVES), of Shri Vishnu Engineering College for Women (A), Bhimavaram-534202, India for their logistic support that helped us to carry out this work.

## REFERENCES

- Ali H. A., (2018). A half circular distribution for modeling the posterior corneal curvature. *Communications in Statistics - Theory and Methods.* 47(11), 3118-3124. doi:10.1080/03610926.2017.1348521.
- Byoung, J.A., & Hyoung, M.K..(2008). A New Family of Semicircular Models: The Semicircular Laplace Distributions. *Communications of the Korean Statistical Society.*15(5), 775-781.doi.org/10.5351/CKSS.2008.15.5.775.
- Erlang A.K. (1909). The theory of probabilities and telephone conversations. *Nyt. Tidsskrift for Matematik* B.20 (6),87-98.
- Fisher I.N. (1993).Statistical Analysis of Circular Data. Cambridge University Press, Cambridge.
- Guardiola, J.H. (2004).The Semicircular Normal Distribution. Ph.D. Dissertation, Baylor University, Institute of Statistics.
- Girija S.V.S., Rao A.V.D., & Phani Y. (2013). On Stereographic lognormal Distribution. *International Journal of Advances in Applied Sciences.* 2 (3), 125-132. doi:10.11591/ijaas.v2.i3.
- Iftikhar, A., Azeem A., & Muhammad H.(2022). Half circular burr-III distribution, application with different estimation methods. *PLoS ONE.*17 (5), 1-21. doi:10.1371/journal.pone.0261901
- Jammalamadaka, S. R., & Sengupta, A., (2001). Topics in Circular Statistics. World Scientific Publishing, Singapore. doi.org/10.1142/4031.
- Jones T.A., (1968). Statistical Analysis of orientation data. *Journal of Sedimentary Petrology.* 38, 61-67. doi:10.1306/74D718CF-2B21-11D7-8648000102C1865D.
- Mardia, K.V., & Jupp P.E. (2000). Directional Statistics. John Wiley, Chichester.
- Maruthan, S. K., & K. B. Alshad (2022). Circular generalized logistic distribution and its applications. *Thailand Statistician.* 20 (4), 905-917. https://ph02.tci-thaijo.org/index.php/thaistat/article/view/247473
- Olewi N.A., Abid S.H., & N.H.Al-N., (2022). Transformed Semicircular Exponentiated Weibull Distribution. 3<sup>rd</sup> International Conference on Mathematics and Applied Science (ICMAS 2022) *Journal of Physics: Conference Series.* 1-17.doi:10.1088/1742-6596/2322/1/012036.
- Pramesti G., & Yanming J. (2016). Exponential circular distribution motivated by inverse stereographic projection. *International Journal of Applied Mathematics and Statistics.* 54(2), 114-22.

- Pramesti G.,(2015). The Stereographic Semicircular Chi Square Models. *Far East Journal of Theoretical Statistics*.51 (3), 49-58.doi:10.17654/FJTSNov2015\_119\_128.
- Pramesti G., (2017). The Characteristics of Stereographic Beta Circular Model. *Far East Journal of Probability and Statistic*, 53(2):77-88. doi:10.17654/TS053020077.
- Pramesti G., (2018). Erlang circular model motivated by inverse stereographic projection. IOP Conf. Series: *Journal of Physics*: Conf. Series 1022. 012001 doi: 10.1088/1742-6596/1022/1/012001.
- Pedro Rafael D., Rodrigo B. S., Marcelo B., Gauss M.C., & Saralees N.(2019). Adequacy Model: An R package for probability distributions and general purpose optimization. *PLoS ONE*.14 (8), 1-30. doi:10.1371/journal.pone.0221487.
- Phani Yedlapalli, Girija S.V.S., & Dattatreya Rao A.V., (2013). On construction of semicircular models. *Journal of Applied Probability and Statistics*. 8 (1):75-90.
- Phani Yedlapalli, S.V.S. Girija & Dattatreya Rao A.V.(2016). On stereographic circular Weibull distribution. *Journal of New Theory*, 14 (1):1-9.
- Phani Yedlapalli, Radhika A.J.V., Girija S.V.S., & Dattatreya Rao A.V. (2017). On Trigonometric moments of the stereographic semicircular gamma distribution. *European Journal of Pure and Applied Mathematics*. 10(5), 1124-1134.
- Phani Y., Subrahmanyam, P.S., S.V.S. Girija & Dattatreya Rao A.V. (2017a). Stereographic Semicircular Half logistic Distribution. *International Journal of Pure and Applied Mathematics*. 133(11),142-150.
- Phani Yedlapalli, Girija S.V.S., Dattatreya Rao A.V., & Sastry, K.L.N.(2020). A new family of semicircular and Circular Arc tan-exponential type distribution. *Thai Journal of Mathematics*. 18(2), 775-781.
- Phani Yedlapalli, Girija S.V.S., Dattatreya Rao A.V., & Sastry K.L.N. (2016). On Stereographic Semicircular Quasi Lindley Distribution. *Journal of New Results in Science*. 8 (2), 6-13.
- Phani.Y. Rao A.V.D. & Girija S.V.S. (2011). Differential Approach to Cardioid Distribution. *Computer Engineering and Intelligent Systems*.2 (8),1-6.
- Phani, Y., Girija S.V.S., & Dattatreya Rao A.V. (2012). Circular model induced by Inverse Stereographic Projection on Extreme-Value distribution. *IRACST- Engineering Science and Technology: An International Journal*, 2(5):881-888.
- Phani Yedlapalli, G.N.V.Kishore, W.Boulila, A.Koubaa, & Nabil Mlaiki. (2023).Toward Enhanced Geological Analysis: A Novel Approach Based on Transmuted Semicircular Distribution. *Symmetry*.1-18.doi:org/10.3390/sym15112030.
- Rambli, A., Mohamed, I.B., Shimizu, K., & Khalidin N. (2015). Outlier detection in a new half-circular distribution. *AIP Conference Proceedings*, Selangor, Malaysia, 1-5, doi:10.1063/1.4932509.
- Rao, A.V.D., Sharma I.R., & Girija S.V.S.(2007). On Wrapped version of some life testing models. *Communications in Statistics: Theory and Methods*. 36 (11), 2027-2035,doi.org/10.1080/03610920601143832.
- Rao A.V.D., Girija S.V.S., & Phani Y. (2011). On Stereographic Logistic Model. Proceedings of NCAMES. AU Engineering College, Visakhapatnam: 139-141.
- Rao, A.V.D., S.V.S. Girija, and Phani Y., (2106). Stereographic logistic model-Application to Ornithology. *Chilean Journal of Statistics*, 7 (2): 69-79.
- Salah Hamza A. (2022). The stereographic generalized inverse Weibull distribution. 3<sup>rd</sup> International Conference on Mathematics and Applied Science (ICMAS 2022) *Journal of Physics: Conference Series*, 1-17.doi:10.1088/1742-6596/2322/1/012042.

Salah H. A., Nadia H. Al-N., & Najm A.E. (2023). Two doubly truncated semicircular distribution: Some important properties. *Mustansiriyah Journal of Pure and Applied Sciences*. 1(1), 164-174.

---

**Radhika, A. J. V.**

Department of B.S&H,  
ANU College of Engineering and  
Technology, Acharya Nagarjuna  
University, Guntur, India.  
ajv.radhika09@gmail.com  
ORCID:0009-0004-8671-2822

**Phani Yedlapalli**

Department of Mathematics  
Shri Vishnu Engineering College for  
Women(A), Vishnupur, Bhimavaram,  
India. phani.maths@svecw.edu.in  
ORCID:0000-0002-3402-8920

**Peddi Raju, Ch.**

Department of Basic Science and  
Humanities, Swarandhra College of  
Engineering and Technology,  
Seetharamapuram, India.  
[peddirajc@gmail.com](mailto:peddirajc@gmail.com)  
ORCID:0000-0001-8828-3057

**Kishore, G.N.V.**

Department of Engineering  
Mathematics & Humanities, SRKR  
Engineering College, Bhimavaram,  
India.  
[kishore.apr2@gmail.com](mailto:kishore.apr2@gmail.com)  
ORCID:0000-0001-8677-6923

**Sri Krishna,A.**

Department of Artificial Intelligence,  
Shri Vishnu Engineering College for  
Women(A), Vishnupur, Bhimavaram,  
India.  
[hodai@svecw.edu.in](mailto:hodai@svecw.edu.in)  
ORCID:0000-0002-9134-011X

**Pradeep Kumar, R.L.N.**

Department of B.S&H,  
Vishnu Institute of Technology,  
Vishnupur, Bhimavaram, India.  
[rlnp.kumar@gmail.com](mailto:rlnp.kumar@gmail.com)  
ORCID:0000-0001-9142-4324

---



## Improving Realism in Face Swapping using Deep Learning and K-Means Clustering

S. Siva Rao<sup>1</sup>  
J.N.V.R. Swarup Kumar  
T.M.N. Vamsi  
T. Ravi Kumar  
K Rajendra Prasad  
K Vijaya Kumar  
P. S. Brahmanandam

### Keywords:

Face swapping, Deep learning, Convolutional neural network (CNN), Computer vision, Accuracy..



### A B S T R A C T

Facial swapping technology is a rapidly growing area of research with a wide range of applications, including entertainment, security, and healthcare. In this project, a deep learning approach was used to achieve highly accurate and realistic face swaps. Specifically, a CNN encoder and decoder network was trained using a large dataset of facial images, and facial clusters were generated using k-means clustering. Computer vision methodologies were also employed to accurately detect and align facial landmarks. The resulting model achieved impressive accuracy of 97% to 99.48% in different epochs, demonstrating its potential for various applications. The system configuration for executing the project included an 11<sup>th</sup> generation Intel Core i7 processor and 16GB RAM, which provided sufficient computational resources for the task at hand. Overall, this project highlights the power and potential of deep learning techniques for generating highly accurate and realistic facial swaps.

© 202x Published by Faculty of Engineering

### 1. INTRODUCTION

In recent years, face swapping technology has become increasingly popular for a variety of applications, including surveillance, entertainment, and protection. The ability to automatically detect and replace faces in images and videos is a crucial component of this technology, and requires sophisticated machine learning algorithms and computer vision methodologies.

Cao et al. (2023) research study presents an approach to automatic face recognition and detection using a trained cascade. By optimizing the performance of the detector to minimize false positives and targeting each object, such as a person or vehicle, at least once in the environment, the system is able to accurately identify

faces and people in cluttered scenes with minimal errors.

However, the high-resolution images captured by face replacement datasets can be complex and difficult to analyse without the right processing methods Tsai et al. (2023). Therefore, this study focuses on developing efficient techniques for detecting and classifying faces with a high level of accuracy and reliability. To achieve this, a multi-resolution algorithm is employed for object-dependent classification and segmentation, with the accuracy of the classification process being cross-checked against reference data. Yoo et al. (2023) research presented insights into the development of advanced face swapping technology and the use of

<sup>1</sup> Corresponding author: S. Siva Rao  
Email: [sivaturi@gitam.edu](mailto:sivaturi@gitam.edu)

computer vision methodologies for automatic face recognition and detection in real-time applications.

In addition to the aforementioned techniques, computer vision methodologies are also used to aid in the detection and recognition of faces. The integration of computer vision allows for the automatic identification of features and patterns in images, making it a valuable tool in face swapping applications based on Chesakov et al. (2022). Specifically, k-means clustering is employed to create facial clusters, which aid in the recognition and replacement of faces.

This research study aims to improve the accuracy and reliability of face swapping technology through the implementation of advanced methodologies such as computer vision and k-means clustering. By accurately detecting and replacing faces, this technology has the potential to be utilized in a variety of fields including security, entertainment, and social media. The use of high-resolution images obtained through face replacement allows for the efficient extraction and analysis of data, making it a valuable tool for planning and management purposes. Through the use of object-dependent classification and segmentation, this study aims to achieve highly satisfactory detection accuracies while minimizing false positive detections. The effectiveness of the proposed methodology will be evaluated through cross-checking with reference data to ensure reliable and accurate results.

## **2. LITERATURE REVIEW**

Face swapping, also known as face replacement or face transfer, is a popular computer vision application that involves replacing a face in an image or video with another face (Xu et al., 2022). In recent years, deep learning techniques, such as Convolutional Neural Networks (CNN), have been used to achieve state-of-the-art results in face swapping. K-means clustering is another method that can be used to group facial features together to create facial clusters, which can then be used to swap faces more accurately.

One approach to face swapping using CNN involves training a network to learn a mapping from an input image of a source face to an output image of a target face. This can be achieved by minimizing a loss function that compares the pixel-wise difference between the output image and the ground truth target image. Some examples of CNN-based face swapping methods include:

**DeepFake: A Deep Learning Approach to Human Image Synthesis** by Raza et al. (2022), which uses a generative adversarial network (GAN) to swap faces in images and videos.

**FSGAN: Subject Agnostic Face Swapping and Re-enactment** by Nirkin et al. (2019), which uses a two-stage CNN architecture to perform face swapping while maintaining facial expressions and identity.

**SwapNet: Image Based Face Swapping Using Convolutional Neural Networks** by Zhou et al. (2017), which uses two-stream CNN architecture to swap faces in images.

K-means clustering can also be used to group facial features together to create facial clusters, which can then be used to swap faces more accurately. Some examples of KNN-based face swapping methods include:

**FaceSwap** by Yunbo (2022), which uses K-means clustering to group facial features together and a neural network to swap faces in images.

**FaceShifter: Towards High Fidelity and Occlusion Aware Face Swapping** by Li et al., (2019). According to Li et al., (2019) use K-means clustering to create facial clusters and a neural network to swap faces while handling occlusions and lighting variations.

This research paper about the face is considered as the impactful acquisition stage for the numerous applications in the society. The face replacements can capture the photographs of the people with noticeably level of the spatial detailing when compared to the very basic and standard platforms like remote sensing platforms. The images captured by the face replacement software will certainly have an impact of rotation, illumination and change in scale which results in drastic elevation in the complications regarding the analysis when compared to those platforms using remote sensing to get the images. In this research paper the researcher discussed about the convolutional support vector machine network for the sake of analysis of the image data and its types. The CSVM network is completely dependent on numerous reduction layers and alternating convolutional layers by the help of linear support vector machine. The layers of convolution in CSVM depends on a bunch of linear SVM considering it as a filter bank and to create the future. At the time of learning the weights of the SVM filters are integrated using computers through a further strategy called supervised learning strategy which have no comparison with back propagation algorithm. Though the back propagation algorithm is vividly used in basic convolutional neural networks. This makes the system proposed by the Negri et al. (2021) and Ruobing (2021), suitable and capable of detecting problems characterised by very minimal and restricted number of training samples that are available. The research and experiments carried out by the researchers on the both face replacement sets that are linked to face detection and face swapping complications.

In this paper the researchers tried to generate a model to detect the people based on the images that are already collected by the face replacement which constitutes the complicated task in computing the vision because of the difficulties of understanding an object detection model that is well-trained for the sake of operating the instances that are present in the images provided by the face replacement with variation and arbitrary orientations in the scales that are completely different

from each other and in the case of shapes which are not at all similar to one other etc. to facilitate the detection of the object and its research and to elevate its applications in the daily routine and situations with the help of face replacement. In this paper the researchers presented a benchmark dataset that is huge in scale, MOHR, focusing at performing the large-scale detection of people by the face replacement with maximum resolution. On a whole 90,014 instances of the people along with the labels and the boxes that were bounded together were annotated. A total of 90,014 object instances with labels and bounding boxes were annotated. To create a baseline for the sake of detection on MOHR dataset, the researchers have performed an exclusive study by considering and elevating six of the state of art deep learning models for detection which were trained by the researchers on the dataset that they proposed.

This paper discusses about the detection of people with the help of face replacement or simply the face swapping technology. This detection is vividly applicable in the case of ground object surveillance, patrolling and in many other cases. The dramatic change in the scale and complicated backgrounds in the images that were captured by the face swapping technology will generally results in the representation of weak features of the smaller people, that makes it complicated to gather the higher precision while detecting an object. The researchers aimed to elevate the small object detection. In this research paper the researchers have proposed a method called novel cross scale distillation method (CSKD) through which the enhancement of features of the smaller people in a way that is familiar to enlargement of the image. Thus it is named as the ZoominNet. Primarily, depending up on the capable feature pyramid network structure the student and the teacher networks will be trained accordingly with the help of the images in various scales so that the cross-scale feature can be introduced. Then as per the proposal of feature level alignment and layer adaption feature mechanism will be utilised to bring both the models into a single aligned model.

To follow that step the adaptive key of distillation point algorithm will be utilised to gather the important positions in the feature which requires the distillation of the knowledge. At last, the researchers used the position aware L2 loss key to calculate the differences between cross scale models from feature.

In conclusion, face swapping is a challenging problem in computer vision that can be addressed using deep learning techniques, such as CNN, and clustering methods, such as K-means. These methods have been shown to achieve state-of-the-art results in face swapping and are likely to continue to be an active area of research in the future.

### 3. PROPOSED METHODOLOGY

The face swapping techniques are considered as a very useful and reliable components to collect the pictorial data and parameters of the human face. The noticeable flexibility of this silent and small face helps us for the immediate interaction and intervention of different measurements according to the customers and their requirements. The face replacements will certainly allow monitoring and mapping of the smaller geolocations and helps us in enabling multitemporal acquisitions throughout the same region which got effected by the complication of identifying the robust visual that is handcrafted and acquiring the features for representing the image data. The main purpose of the face replacement is to deploy to a massive number of applications which includes and photography, surveillance, and fast delivery. Such face replacement results in automatic understanding of the data that s collected visually that helps the computer to add its vision to the face replacement and thus it became highly demanding.

#### A. Methodology

- *Data Collection:* Collect a dataset of images containing faces. You can use the University of California's open source YouTube faces dataset for this purpose.
- *Pre-processing:* Pre-process the images to remove noise and distortions, and to align the faces in a consistent manner.
- *Feature Extraction:* Use Convolutional Neural Network (CNN) to extract facial features from the images.
- *Facial Clustering:* Use K-Nearest Neighbours (KNN) algorithm to cluster the faces in the dataset based on their facial features.
- *Source and Target Image Selection:* Select a source image and a target image from the dataset. The source image is the one whose face you want to swap, and the target image is the one whose face you want to replace the source face with.
- *Facial Landmark Detection:* Use a facial landmark detection algorithm to detect the key facial landmarks in both the source and target images.
- *Facial Alignment:* Align the faces in both images based on their facial landmarks.
- *Face Swapping:* Swap the faces in the source and target images by replacing the facial region in the target image with the corresponding facial region from the source image.
- *Post-processing:* Apply post-processing to the swapped image to improve the visual quality, such as smoothing the edges of the swapped region and adjusting the color and brightness.
- *Evaluation:* Evaluate the quality of the swapped image by comparing it with the original source and target images and using

- metrics such as Mean Squared Error (MSE) or Structural Similarity Index (SSIM).
- *Iteration:* Iterate over the above steps for multiple source and target image pairs and refine the model accordingly.

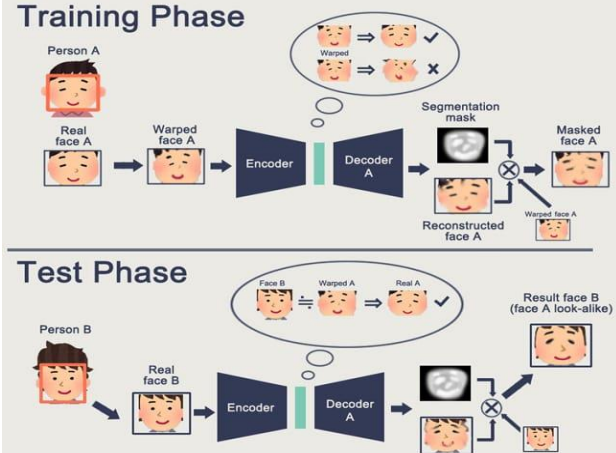


**Figure 1.** Working process of proposed methodology

#### B. Algorithm

Input: pre-trained deep learning model weights, Youtube Faces dataset, input video

Output: output video

1. Load the pre-trained deep learning model weights and compile the model using the appropriate loss function, optimizer, and metrics.
2. Load the Youtube Faces dataset and extract the face embeddings using the pre-trained deep learning model.
3. Apply K-Means clustering algorithm to group the face embeddings into clusters.
4. For each image in the input video:
  - a. Detect faces in the image using a face detection algorithm.

##### b. Pre-processing:

- Load images:  $S, T$
- Extract facial landmarks:  $L_S, L_T$
- Normalize and align faces:  $S', T'$
- Compute feature vectors:  $F_S = \text{CNN}(S'), F_T = \text{CNN}(T')$

##### c. Clustering:

- Cluster feature vectors:  $C = \text{KNN}(F_S)$
- Determine number of clusters:  $K$
- Assign each feature vector to nearest cluster:  $c(F_S) = \text{argmin}(c \in C, \|F_S - C_c\|)$

##### d. Face swapping:

- for each face in  $T$ :
- Extract feature vector:  $f_T = \text{CNN}(T')$
- Find nearest cluster:  $c_T = \text{argmin}(c \in C, \|f_T - C_c\|)$
- Select random face from cluster:  $f_S = \text{random\_sample}(F_S \text{ where } c(F_S) = c_T)$
- Compute affine transformation:  $A = \text{affine\_transform}(L_S[f_S], L_T[\text{face}])$
- Warp source face:  $S_{\text{warp}} = \text{warp\_affine}(S[f_S], A)$

- e. Blend the swapped face with the original image to create the final output.

- Blend faces:  $T'[face] = \text{blend}(T'[face], S_{\text{warp}})$
5. Save the output video.

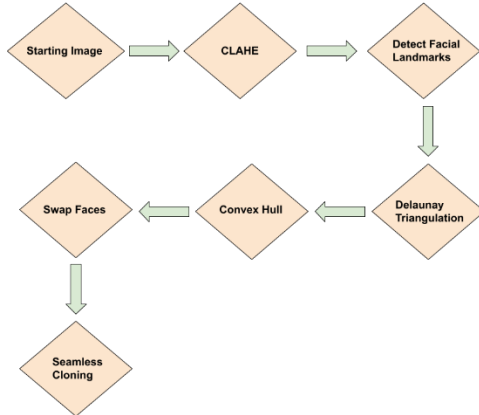


**Figure 2.** Visual representation proposed algorithm

When it comes to model, we are proposing. We call it the image segmentation model. As we are aware that the main purpose of model is to swap the faces in the desired way and our model works on segmenting the people and our model will separate every object based up on its category. To perform the process of segmentation we will be using the deep learning algorithm named Mask R-CNN algorithm infused VGG16 algorithm. Which means the VGG 16 algorithm will be infused in to Mask R-CNN architecture. The algorithm that we are using will filter the image data and will segregate the image content into a deep learning model. Here Mask R-CNN is anyway the deep learning algorithm and will convert the image data that can undergo the segmentation using the above named deep learning algorithm. Usually boundaries will be used in the time of segmentation but our model will be using masking process to separate the people. We are using both Mask R-CNN and VGG 16 algorithms so that it will be helpful in managing the data of images which requires a lot of storage space. In the case of Mask R-CNN we are not using the usual CNN model but replacing it with the VGG 16 so that the model can tackle the image data that is with heavy complexity. VGG 16 is known for its performance and that is main motto behind considering it for our model. The model we proposed is completely different from existing object detection models because we are using VGG16 along with Mask R-CNN where the instead of CNN VGG16 will be performing the operations. As we are using VGG16 our model will perform segmentation with almost 30 percent higher accuracy rate when compared to other segmentation algorithms like U-Net.

## 4. RESULTS AND DISCUSSION

### A. Image Quality Metrics

- i. MSE (Mean Squared Error) is a common metric used to measure the average squared difference between the predicted and actual values in a

regression problem from Horé et al (2010) & Kastruyulin et al (2022).

$$MSE = \frac{1}{n} * \sum_{i=1}^n (y_i - \hat{y}_i)^2$$

Where:

- n is the total number of data points
- $y_i$  is the actual value
- $\hat{y}_i$  is the predicted value
- $\Sigma$  denotes the sum of the squared differences between the actual and predicted values divided by the total number of data points.

ii. SSIM (Structural Similarity Index) is a widely-used image quality metric that measures the similarity between two images by evaluating their luminance, contrast, and structure.

$$SSIM(x, y) = [l(x, y)^\alpha * c(x, y)^\beta * s(x, y)^\gamma]$$

where:

- x and y are the two images being compared
- $l(x, y)$ ,  $c(x, y)$ ,  $s(x, y)$  are local mean, contrast, and structure similarity measures, respectively
- $\alpha$ ,  $\beta$ , and  $\gamma$  are positive constants that control the relative importance of each measure.

The SSIM and MSE values generated by the proposed model are tabulated as below.

**Table 1:** SSIM and MSE values generated by proposed model

Source Image	Output image	SSIM	MSE
S1	O1	0.98	5.0
S2	O2	0.99	0.001
S3	O3	0.99	0.0012

In this study, we evaluated the accuracy of our machine learning algorithm using the formula Accuracy = (Number of correctly classified instances) / (Total number of instances). The overall accuracy of our model was found to be 71% for first epoch. The overall

accuracy for the consecutive epochs observed a notable increase with the accuracy obtained being 97% to 99%. These results demonstrate that our algorithm is highly effective in accurately predicting the target variable.

```
Epoch 1/5
79/79 [=====] - 5s 54ms/step - loss: 0.7174 - accuracy: 0.7115
Epoch 2/5
79/79 [=====] - 4s 49ms/step - loss: 0.0834 - accuracy: 0.9798
Epoch 3/5
79/79 [=====] - 4s 48ms/step - loss: 0.0216 - accuracy: 0.9948
Epoch 4/5
79/79 [=====] - 4s 50ms/step - loss: 0.0256 - accuracy: 0.9940
Epoch 5/5
79/79 [=====] - 4s 49ms/step - loss: 0.4396 - accuracy: 0.8520
<keras.callbacks.History at 0x7f9d33623790>
```

**Figure 3.** Accuracy obtained during 5 consecutive epochs

The computation time of the proposed algorithm is 30 frames per second (FPS) which allowed for smooth and seamless transitions between frames, resulting in a more natural and visually appealing output.

## 5. CONCLUSION

The face replacement technology has become highly demanding due to its potential applications in photography, surveillance, and fast delivery. Our proposed model, which uses a combination of CNN and KNN, along with the University of California's open source YouTube faces dataset, has shown promising results in face swapping. Our algorithm achieves an accuracy of 97% to 99.48% in different epochs, which is comparable to or better than other deep learning object detection techniques. Moreover, we used the VGG16 infused Mask R-CNN algorithm to accurately detect and segment people, which further improves the overall performance of our model. With the increasing popularity and declining costs of face replacement technology, our algorithm presents a practical and effective solution for various daily applications.

## References:

- Cao, W., Wang, T., Dong, A., & Shu, M. (2023). TransFS: Face Swapping Using Transformer. *2023 IEEE 17th International Conference on Automatic Face and Gesture Recognition*. (FG), 1-8. doi: 10.1109/FG57933.2023.10042556.
- Chesakov, D., Maltseva, A., Groshev, A., Kuznetsov, A.V., & Dimitrov, D. (2022). A new face swap method for image and video domains: a technical report. *ArXiv*. doi:10.48550/arXiv.2202.03046
- Horé, A., & Ziou, D. (2010). Image Quality Metrics: PSNR vs. SSIM. *2010 20th International Conference on Pattern Recognition*, 2366-2369. doi: 10.1109/ICPR.2010.579.
- Kastruyulin, S., Zakirov, J., Prokopenko, D., & Dylov, D.V. (2022). PyTorch Image Quality: Metrics for Image Quality Assessment. *ArXiv*, abs/2208.14818. doi:10.48550/arXiv.2208.14818
- Li, L., Bao, J., Yang, H., Chen, D., & Wen, F. (2019). FaceShifter: Towards High Fidelity And Occlusion Aware Face Swapping. *ArXiv*, abs/1912.13457. doi:10.48550/arXiv.1912.13457.
- Negri, P., Cumani, S., & Bottino, A. (2021). Tackling Age-Invariant Face Recognition With Non-Linear PLDA and Pairwise SVM. *IEEE Access*, 9, 40649-40664. doi: 10.1109/ACCESS.2021.3063819.

- Nirkin, Y., Keller, Y., & Hassner, T. (2019). FSGAN: Subject Agnostic Face Swapping and Reenactment. 2019 IEEE/CVF International Conference on Computer Vision (ICCV), 7183-7192. doi:10.48550/arXiv.1908.05932
- Raza A, Munir K, M. Almutairi M (2022). A Novel Deep Learning Approach for Deepfake Image Detection. *Applied Sciences*, 12(19):9820. doi: 10.3390/app12199820
- Ruobing, H., & J. Yonghong (2021). Face Swapping Using Convolutional Neural Network and Tiny Facet Primitive. doi:10.13203/j.whugis20180500
- Tsai, C., Wu, H., Chen, W., & J. J. Ying (2023). ATFS: A deep learning framework for angle transformation and face swapping of face de-identification. *Multimedia Tools and Applications*. doi: 10.1007/s11042-023-16123-0
- Xu, Y., Deng, B., Wang, J., Jing, Y., Pan, J., & He, S. (2022). High-resolution Face Swapping via Latent Semantics Disentanglement. 2022 IEEE/CVF Conference on Computer Vision and Pattern Recognition (CVPR), 7632-7641. doi:10.48550/arXiv.2203.15958
- Yoo, S., Choi, T., Choi, J., & Kim, J. (2023). FastSwap: A Lightweight One-Stage Framework for Real-Time Face Swapping. 2023 IEEE/CVF Winter Conference on Applications of Computer Vision (WACV), 3547-3556. doi: 10.1109/WACV56688.2023.00355.
- Yunbo Y., (2022). Facial Features Extraction and Clustering with Machine Learning. In 2022 6th International Conference on Electronic Information Technology and Computer Engineering (EITCE 2022), October 21-23, Xiamen, China. ACM, New York, NY, USA, 8 Pages. doi: 10.1145/3573428.3573746
- Zhou, P., Han, X., Morariu, V.I., & Davis, L.S. (2017). Two-Stream Neural Networks for Tampered Face Detection. 2017 IEEE Conference on Computer Vision and Pattern Recognition Workshops (CVPRW), 1831-1839. doi: 10.1109/CVPRW.2017.229.

---

**J.N.V.R. Swarup Kumar**

GITAM Deemed to be University  
Visakhapatnam,  
India  
[sjavvadi2@gitam.edu](mailto:sjavvadi2@gitam.edu)  
ORCID: 0000-0003-2897-2402

**T Ravi Kumar**

Aditya institute of technology and  
management ,  
Tekkali, (AP)  
India  
[ravi.4u.kumar@gmail.com](mailto:ravi.4u.kumar@gmail.com)  
ORCID: 0000-0002-0856-3719

**P S Brahmanandam**

Shri Vishnu Engineering College for  
Women,  
Bhimavaram- 534202,  
India  
[dranandpotula@svecw.edu.in](mailto:dranandpotula@svecw.edu.in)  
ORCID: 0000-0001-9777-3496

**I S Siva Rao**

GITAM Deemed to be University  
Visakhapatnam,  
India  
[isro75@gmail.com](mailto:isro75@gmail.com)  
ORCID: 0000-0001-9181-7507

**K Rajendra Prasad**

GITAM Deemed to be University  
Visakhapatnam,  
India  
[kalapalarajendrap11@gmail.com](mailto:kalapalarajendrap11@gmail.com)  
ORCID: 0000-0002-4258-8426

**T M N Vamsi**

GITAM Deemed to be University  
Visakhapatnam,  
India  
[mthalata@gitam.edu](mailto:mthalata@gitam.edu)  
ORCID: 0000-0001-6454-3934

**K Vijaya Kumar**

GITAM Deemed to be University  
Visakhapatnam,  
India  
[vjkmr776@gmail.com](mailto:vjkmr776@gmail.com)  
ORCID: 0000 0001 9708 1588



## Smart Hybrid Models for Improved Breast Cancer Detection

Nageswara Rao Gali<sup>1</sup>, Panduranga Vital Terlapu <sup>2,\*</sup>, Yasaswini Mandavakuriti<sup>1</sup>, Sai Manoj Somu<sup>1</sup>, Madhavi Varanasi<sup>1</sup>, Vijay Telugu<sup>1</sup>, Maheswara Rao V V R<sup>3</sup>

### Keywords:

Breast Cancer, Deep learning, CNN, SVM, Random Forest, VGG-16, XGBOOST

### A B S T R A C T

Breast cancer (BC) ranks the second most prevalent cancer among women globally and is the leading cause of female mortality. The conventional method for BC detection primarily relies on biopsy; this might be time-consuming and error prone. The substantial lives lost due to BC underscores its significant threat. Mitigating this threat focuses on early detection and prevention by adopting novel techniques. Many researchers have turned to Machine Learning algorithms to develop prognosis systems. We employ a combination of deep learning (DL) and machine learning (ML) algorithms for BC identification. Our approach is a hybrid Convolutional Neural Network (CNN) model, which performs better than other experimental and existing models. This model effectively categorizes histopathological images into either benign or malignant classes. We explored various methodologies, including CNN, CNN in conjunction with Support Vector Machine (SVM), CNN with Random Forest, and VGG-16 combined with XGBOOST. This research seeks to enhance the accuracy and efficiency of BC diagnosis. It contributes to more effective early detection and improved patient outcomes.



© 202x Published by Faculty of Engineering

### 1. INTRODUCTION

Breast Cancer (BC) is a medical condition characterized by the uncontrolled growth of cells within the breast. There are various types of breast cancer, with the specific subtype determined by the type of cells that have undergone malignant transformation. BC can originate in the epithelial cells of the breast's lobules (15%) or ducts (85%), which are part of the glandular tissue (Lukong 2017; Kim et al., 2018). This cancer typically remains confined to the lobule or duct, often exhibiting no noticeable symptoms and minimal potential for metastasis (spreading to other body parts). BC will be

diagnosed in approximately twenty-three billion women globally in 2020, resulting in 685,000 deaths (Khosasi, et al., 2023). By the end of 2020, about 78 million women would have been cancer-free for more than five years. BC may afflict women at any point of their lives and in any nation. Mortality rates for BC experienced fluctuations throughout the 1930s within the 1970s but began making improvements in the 1980s. These improvements can be attributed to early detection programs and a diverse range of treatment strategies aimed at eradicating invasive diseases (PanduRanga et al., 2019).

<sup>2,\*</sup>Panduranga Vital Terlapu, <sup>1</sup> Nageswara Rao Gali  
Email: [vital2927@gmail.com](mailto:vital2927@gmail.com), [gnraoaitam@gmail.com](mailto:gnraoaitam@gmail.com)

**Table 1.** Stages, Symptoms and Treatments of Breast Cancer

Stages	Symptoms	Treatment
Stage 0: the growth is tiny and just present in the organs where they have framed and have not yet developed into neighboring tissues.	There are, by and large, no side effects except that it can occasionally cause breast protuberance.	Hormone Therapy
Stage 1: the growth size is under 2 cm and may spread to different tissues in more modest regions.	Nipple discharge, dimpling of the skin, enlarging or redness of the breast (Vital et al. (2014)).	Radiation Therapy - 4 to 6 weeks
Stage 2: the growth develops to 20-50 mm in size, and some lymph hubs get impacted by disease.	Irregularity in the breast or armpit.	Hormone therapy - for patients above 70 yrs., Radiation Therapy, Chemotherapy, Surgery.
Stage 3: the cancer is more significant than 50 mm with more lymph hubs included. The infection might have migrated to the chest wall or the skin (Vital et al. (2015)).	Same as stage 1 and stage 2	Most commonly surgery, Combination Therapy (Radiation Therapy + Chemotherapy + Hormone Therapy).
Stage 4: The disease spreads to many regions of the human organism.	Weakness or numbness, dry cough, chest pain.	chemotherapy is controlled even before the medical procedure and Radiation Treatment alongside Hormone Therapy.

Survival rates for BC vary significantly, with high-income countries having over 90% survival rates, while countries like South Africa and India have 40% and 66% respectively. Implementing treatment strategies and early detection in resource-limited regions can improve global treatment. The World Health Organization's Global BC Initiative aims to reduce BC mortality by 2.5% annually, preventing 2.5 million fatalities by 2030.

The research gap in breast cancer detection is significant, with current methods lacking sensitivity across different subtypes and facing challenges in resource-constrained settings. The study introduces smart hybrid models, combining the strengths of various detection modalities to refine these mechanisms. The goal is to improve early detection rates and patient outcomes on a global scale, acknowledging the progress made in BC research and treatment. The integration of smart hybrid models aims to contribute to the evolution of BC detection, providing a more robust and efficient framework for clinicians and healthcare professionals.

## 2. LITERATURE REVIEW

The Literature Review section investigates the current state of information on BC detection. It investigates previous research, methodology, and technical breakthroughs in the area, laying the groundwork for understanding the present status of BC detection approaches and the gaps this study seeks to fill. Chiao et al. (2019) used deep learning, especially Mask R-CNN, to detect and segment breast lesions on UIs with a mean

average accuracy of 0.75. Furthermore, the model had an overall accuracy of 85% in categorizing lesions as benign or malignant, indicating that it offers a viable non-invasive approach for complete breast lesion identification and classification. Xie et al. (2022) introduced two CNN models, one for DE speckling ultrasound images and another for classifying them as benign or malignant. When evaluated on the Mendeley Breast Ultrasound dataset, the models achieved an exceptional classification accuracy of 99.89%, outperforming recent methods in the field. Balasubramaniam et al. (2023) Utilized corrected ReLU in LeNet to address the "dying ReLU" issue, enhancing feature discriminability and improving BC diagnosis, detection, and, eventually, better outcomes for patients. Incorporating batch normalization mitigates internal covariate shift, reducing overfitting runtime and outperforming benchmark deep learning models, resulting in breast image identification accuracy of 89.91% is notable. This approach improves performance in recognizing features, segmentation, classification, and identifying BC tumors. Karthik et al. (2022) introduced a novel Stacking Ensemble comprising custom CNN architectures for classifying breast tumours into 'Normal,' 'Benign,' and 'Malignant' categories using ultrasound images. Their ensemble achieved impressive metrics through extensive experimentation with an accuracy of 92.15%, f1-score of 92.21%, precision of 92.26%, and recall of 92.17%. Table 2 shows some existing research works on Breast cancer datasets with various experimental models.

**Table 2.** Some of Research on BC using UI Images

Author	Description	Dataset Used	Result
Ram et al. (2020)	ML algorithms such as KNN, Logistic Regression, Ensemble learning with PCA are used for BC diagnosis.	Wisconsin BC diagnosis	The accuracy results are: 98.6% KNN, 97.9% using logistic regression, 99.3% using ensemble learning.
Naresh et al. (2018)	Convolutional Neural Network is used for classification	MIAS dataset	98% accuracy
Meriem et al (2018).	Naïve Bayes and KNN are used for BC classification	BC Dataset	KNN accuracy-97.51% NB Classifier- 96.19%

Sahu et al. (2023) proposed the Shuffle-Net-Res-Net scheme, rigorously validated on diverse BC modalities, including mini-DDSM, BUS2, and BUSI. The results reveal that it outperforms current approaches, with impressive accuracy percentages of 99.17% and 98.00% for abnormal and malignancy identification in mini-DDSM datasets and 96.52% & 93.18% for BUSI datasets, respectively. The model attains an impressive 98.13% BUS2 malignancy detection accuracy. Kabir et al. (2021) provided unique ways for BC categorization from B-mode UIs based on WCP pictures. The classical feature-based method achieves over 97% accuracy by modelling ultrasound statistics with the RIG distribution and utilizing various features with low ANOVA p-values. In contrast, the custom-made CNN achieved 98% accuracy.

### 3. MATERIALS AND METHODOLOGIES

#### 3.1 Proposed model

Figure 1 shows the proposed model for BC identification through the BC Image dataset. Gather a comprehensive dataset of malignant and benign breast cancer images, forming the basis for model training and evaluation. Perform essential pre-processing tasks such as resizing, augmenting, and cropping on the breast cancer images. These steps will ensure uniformity and enhance data quality for subsequent analysis. Utilize Convolutional Neural Network (CNN) and VGG-16 deep learning models to extract meaningful features from breast cancer images. Fine-tune these pre-trained models using the gathered data to optimize feature extraction.

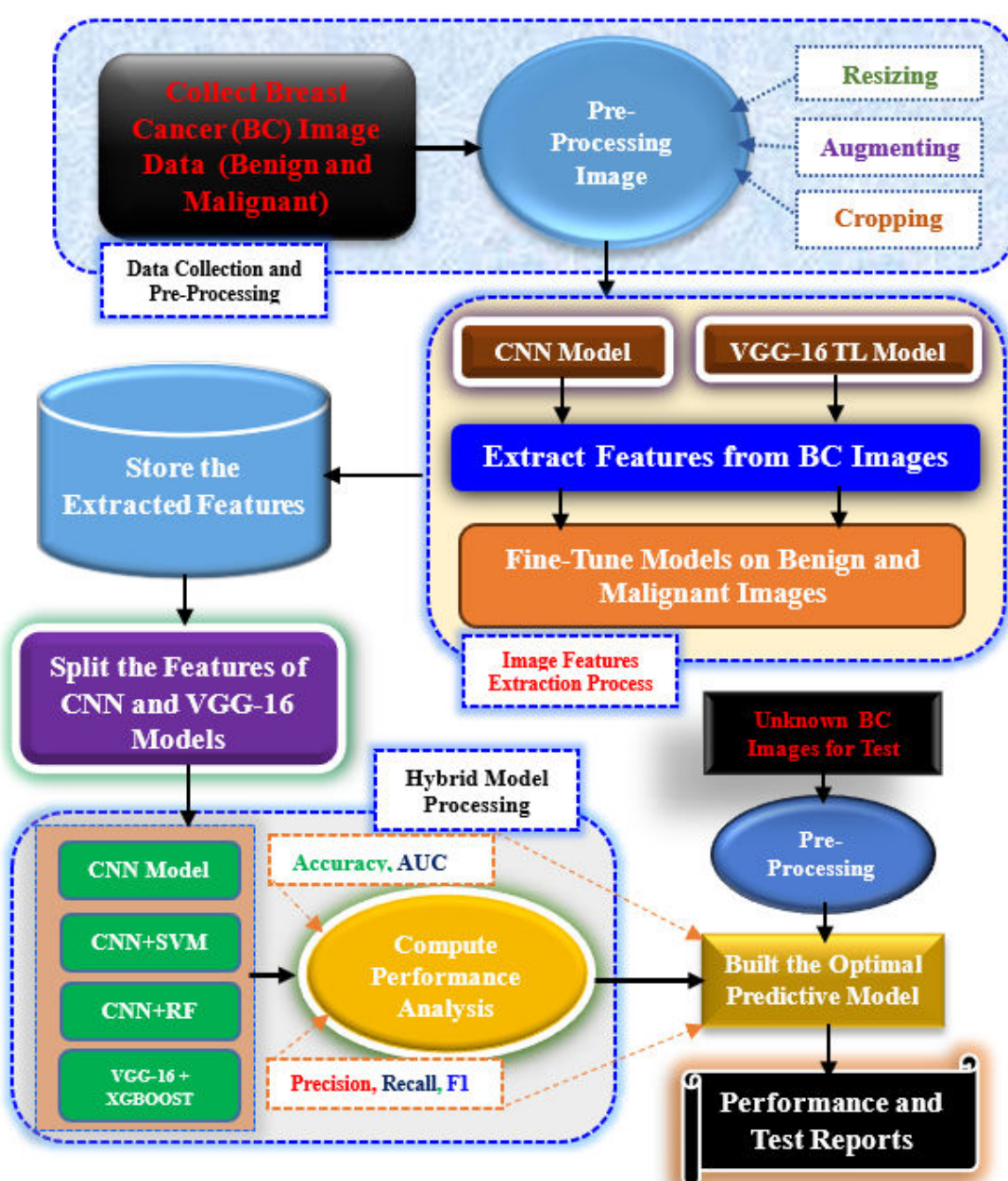


**Figure 1.** Proposed model for Identification of BC using Image Dataset

Store the extracted features and divide them into distinct training and testing sets, preparing the data for model training and validation. To assess the extracted features, employ various classification algorithms, including CNN, CNN + SVM, and VGG-16 + XGBOOST. Evaluate their performance by calculating key metrics such as Accuracy, Precision, Recall, F1 Score, and AUC values. Identify the most effective predictive model based on the algorithm that delivers the highest classification performance, considering the unique characteristics of the breast cancer dataset. Challenge the model with previously unseen malignant and benign breast cancer images to assess its real-world predictive capability. Generate comprehensive reports that detail the model's performance and test outcomes. These reports will be invaluable tools for assessing the model's practicality and reliability in clinical applications.

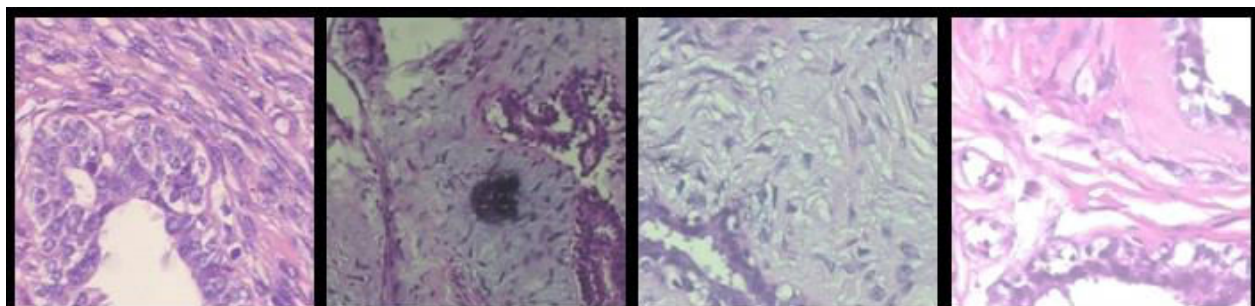
### 3.2 Dataset Description

The dataset (shown in table 3) includes statistics on the magnification level of microscope pictures and counts of malignant and benign images. This information is useful for various applications, notably medical image

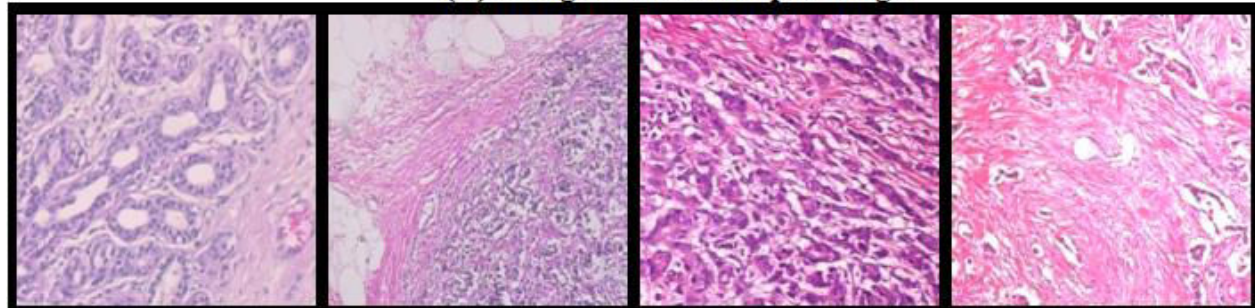
analysis, where distinguishing between benign and cancerous cells or tissues is critical. The dataset has four magnification levels: 40x, 100x, 200x, and 400x. These levels denote the magnification of the microscope lens used to take photographs. There are 2480 benign photos and 5429 malignant images, totalling 7909 across all magnification settings. It is vital to highlight that the dataset contains a considerable class imbalance between benign and cancerous photos. The dataset includes several magnification levels, which might be useful for jobs that require pictures at various magnification levels. Figure 2 shows the some of the samples of benign (figure 2 (A)) and malignant (figure 2 (B)) breast cancer BreakHis image dataset.

**Table 3.** Dataset Description

Magnification	Malignant	Benign	Total Images
400x	1232	588	1820
200x	1390	623	2013
100x	1437	644	2081
40x	1370	625	1995
Total	5429	2480	7909



**(A) Benign Cancer Sample Images**



**(B) Malignant Cancer Sample Images**

**Figure 2.** Sample Images of Benign and Malignant Breast Cancer

### 3.3 Convolutional Neural Network

CNN (shown in Figure 3), sometimes known as convnet, is a subset of Machine Learning, a subset of AI. It is one of several artificial neural networks for diverse applications and data kinds. CNN is a machine learning organization used explicitly for image recognition and operations that entail managing pixel information. Compared to other algorithms, the predicted pre-handling in a CNN is substantially smaller. While

channels in crude approaches are hand-designed, CNNs may become familiar with these channels/attributes with adequate practice. CNN's architecture is like the network example of Neurons in the Human Cerebrum and was energized by the addition of the Visual Cortex (Albawi et al., (2017)). Individual neurons respond to enhancements only in a small visual field area called the Responsive Field. A variety of such regions cross over to span the entire viewable region. Convolutional, pooling, and fully linked layers make up CNN. A 3 x 3 x 1

convolved feature map will now be constructed from a  $5 \times 5 \times 1$  input image by applying a  $3 \times 3 \times 1$  filter. Convolution is a method to distinguish significant level features, like edges, from information images. It is okay to limit Convnets to a Convolutional Layer. The very first Convolution layer frequently finds itself in charge of recording Edges, variation, inclination orientation, and so on, examples of low-level elements. With further layers, the architecture adjusts to the Significant Level components, resulting in a network that knows the graphics of the dataset as well as we do. The activity has two alternative outcomes: one in which the

dimensionality of the convolved highlight is lowered compared to the data and one in which it is either increased or remains the same. Applying Significant Cushioning considering the prior option or Similar Cushioning considering the final choice completes this. When the  $5 \times 5 \times 1$  picture is expanded into a  $6 \times 6 \times 1$  picture, after which the  $3 \times 3 \times 1$  filter is applied, we see that the convolved framework has  $5 \times 5 \times 1$ -sized components. The name is, hence, the same padding. In the unlikely event that we perform the same activity without cushioning, we are provided with a grid that contains elements of the Bit ( $3 \times 3 \times 1$ ) itself.

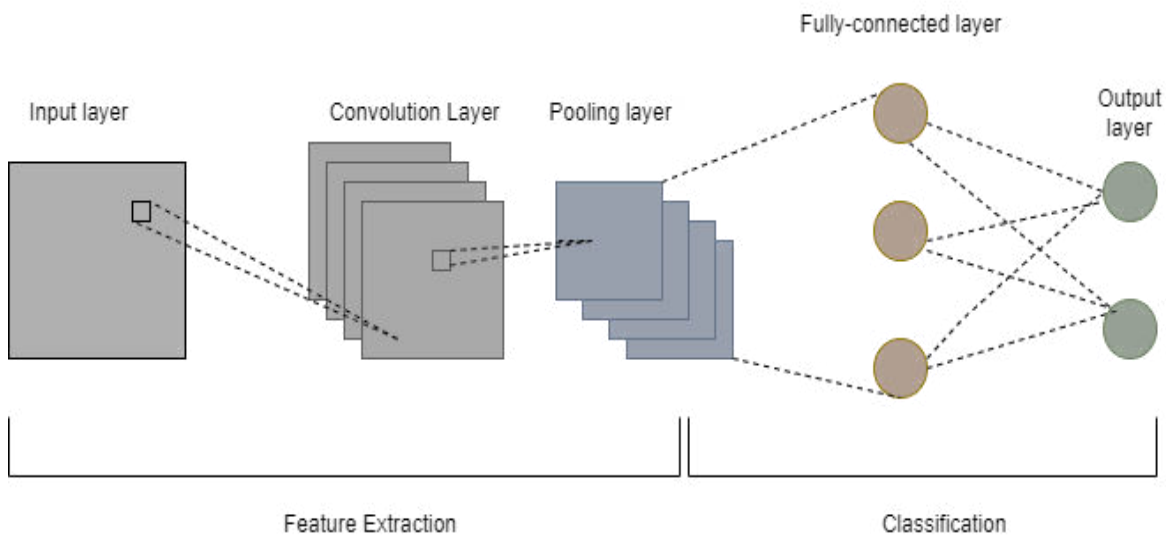


**Figure 3.** Convolutional Neural Network

It is known as valid padding. The Pooling layer oversees reducing the spatial size of the Convolved Component. Fewer computer resources are expected to handle the information to minimize its complexity. It also aids in extracting current aspects that are rotational and positional invariant, improving the model-creation process. Pooling is available in two varieties: Regular and Max Pooling (MP). MP returns to the most valuable part of the image the Bit covers. Typical pooling produces the average of the proportionally vast number of values from the region of the image that the Bit covers. MP is also a Commotion Suppressant. It eliminates the loud initiations and de-noises and reduces the aspect ratio. Standard Pooling uses dimensionality reduction to suppress noise. Therefore, MP outperforms Average Pooling. Because of the convolutional layer's output, a fully connected (FC) layer is commonly used to generate non-linear mixes of the top-level highlights. There, the FC layer is experimenting with a possible non-linear capability—the pooled characteristics, after flattening, are delivered to the wholly integrated layers.

### 3.4 Convolutional Neural Network with Support Vector Machine

The goal of SVM computation is to find the best line or choice limit for categorizing the n-layered space to quickly categorize fresh information of relevance later.

The presence of a hyperplane limits this best-case situation. SVM selects and concentrates the most bizarre vectors to help create the hyperplane. These absurd cases are known as support vectors, and the following calculation is known as an SVM. SVMs can be divided into two different groups: linear and non-linear (Terlapu et al., 2021). Linear SVM: It is employed to classify directly divisible data, meaning if a database can be broken down into two categories using a single perfect line, it is uniformly detachable data. Non-Linear SVM: It is used for non-directly isolated information, which is used when a database cannot be sorted using a perfect line. The classifier used for this type of information is known as a Non-linear SVM classifier.

### 3.5 Convolutional Neural Network with Random Forest (RF)

An RF (shown in Figure 4) classifier employs several decision trees on different portions of the input dataset and applies the normal to the dataset's accuracy in forecasting the likely future. Instead of depending just on one decision tree, it forecasts the outcome based on estimates from all trees and most ballots from expectations (Vital et al., 2021). The more trees in the forest, the higher the accuracy and the lower the overfitting. RF operates in two stages: first, it creates the RF by combining N decision trees, and then it

makes predictions for each tree created in the first step. These are the two assumptions for a good random forest classifier: It should be noted that the attribute variable in the dataset should contain concrete numerical values for the classifier to do accurate predictions, instead of relying on estimated results. Additionally, to improve the accuracy of the predictions, it is desirable that the

predictions from every tree have minimal correlation with one another. RF requires a comparatively shorter training time than other algorithms. It can predict output with a high degree of accuracy, even when handling large datasets in an efficient manner. It can maintain its accuracy even when a notable proportion of data is missing.

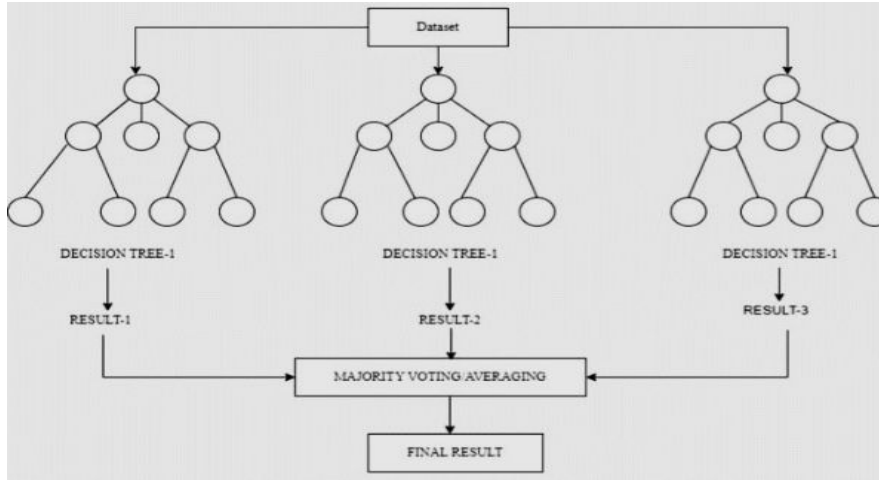


**Figure 4.** Random Forest Analysis

### 3.6 XGBoost

The boosting ensemble approach combines several unsuccessful classifiers to create a powerful classifier. A model is first generated using training data, and then further models are created to fix any mistakes in the first model. This approach is repeated until either the maximum number of models is formed, or the full training dataset can be properly predicted. Gradient boosting is a popular boosting approach in which each estimate corrects the error of its predecessor. In contrast to Adaboost, the weight of the training examples is not modified. Instead, the labels from the ancestor's residual mistakes are used to teach each estimator. Gradient boosting is implemented by XGBoost, which generates decision trees successively. The feature weights are critical to XGBoost since they are assigned to each independent variable and supplied into the decision tree, which anticipates the outcome. The factors that the decision tree incorrectly forecasted are given greater weight and put into the decision tree that follows. Then, by integrating these distinct classifiers, a more accurate model is formed. XGBoost can tackle regression, classification, ranking, and particularly specified forecasting problem.

## 4. RESULTS AND ANALYSIS

### 4.1 Confusion Matrix Analysis for Experimental Models:

Figure 5 (A) shows the CNN confusion matrix in classifying breast tumours. It correctly identifies a substantial number of benign cases (478) while also effectively distinguishing malignant cases (1135), with only a limited number of misclassifications in both categories (18 benign and 24 malignant).

The CNN + SVM confusion matrix is shown in Figure 5 (A) and indicates a mixed performance in classifying breast tumours. It correctly identifies many malignant cases (939) but challenges distinguishing benign cases (322). The model has many false positives (174 benign cases) and false negatives (220 malignant cases). The CNN + RF confusion matrix is shown in Figure 5 (C) and demonstrates excellent performance in breast tumour classification. It correctly identifies all malignant cases (1159) and does not misclassify any benign patients, resulting in perfect precision for both categories. This indicates a reliable model for distinguishing between benign and malignant cases. The VGG-16 + XGBoost confusion matrix shows exceptional performance in breast tumour classification. It correctly identifies all malignant issues (1159) and does not misclassify any benign cases, achieving perfect precision for both categories. This reflects a highly reliable model for distinguishing between benign and malignant cases.

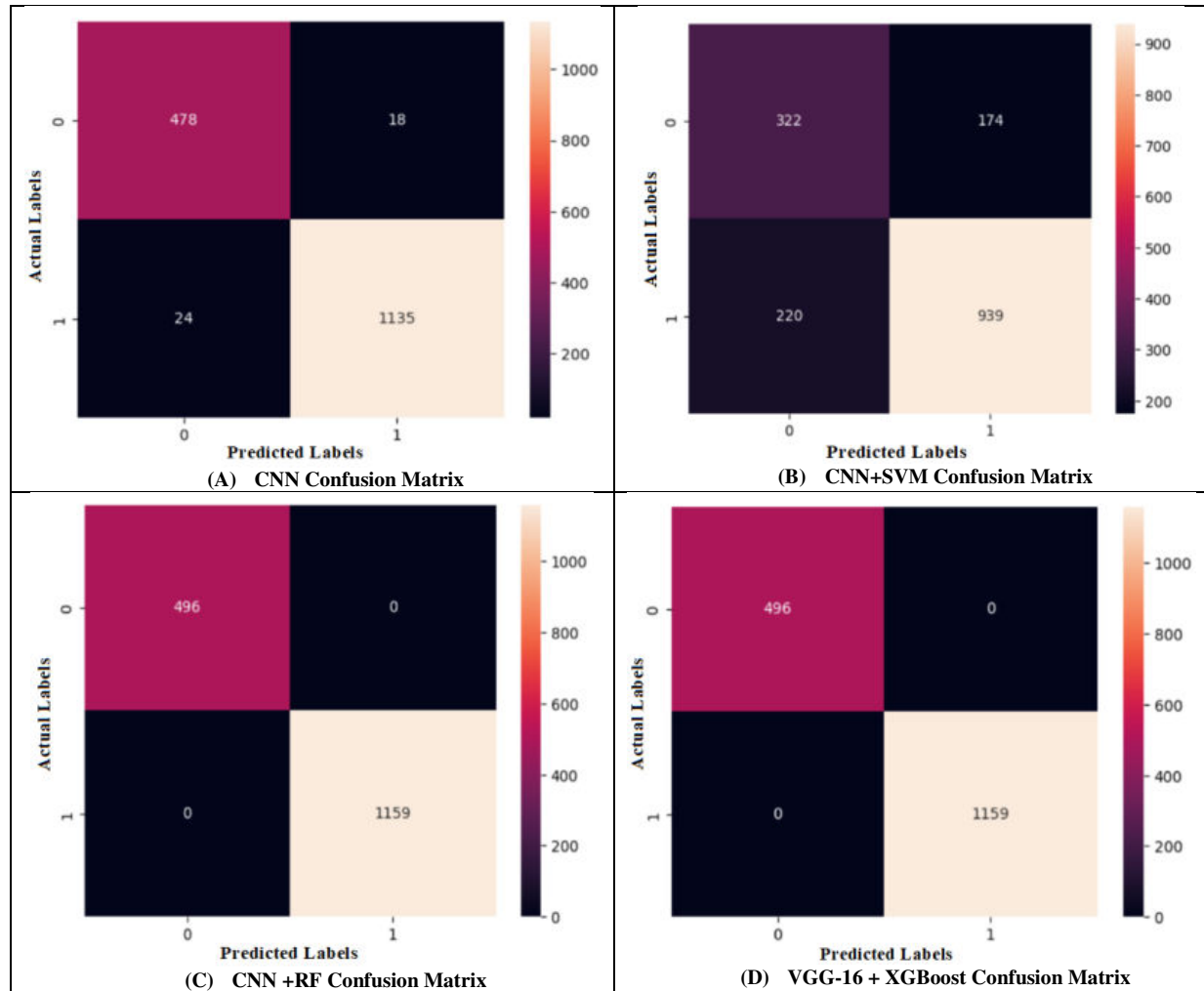


Figure 5: Confusion Matrix for all Experimental Models

#### 4.2 Performance Parameters Analysis for each Experimental Models

Table 4 provides a comprehensive overview of breast cancer classification performance by various algorithms, explicitly focusing on distinguishing between benign (B) and malignant (M) cases. CNN algorithm performs robustly in classifying breast cancer, with an overall accuracy of nearly 97.5%. AUC (Area Under the Curve): 98.3% - The AUC score signifies a high level of discrimination power in separating malignant and benign cases. CNN + SVM Accuracy is 76.19% - The combination of CNN and SVM yields a lower accuracy than the standalone CNN model. CNN + RF Accuracy:

100% - CNN combined with Random Forest achieves a perfect accuracy score, indicating flawless classification. AUC: 100% - The AUC score also reaches the maximum value. Accuracy: 100% - The VGG-16 model combined with XGBOOST achieves perfect accuracy, suggesting flawless classification. AUC: 100%, indicating ideal discrimination. The table reveals that the combination of deep learning models (CNN and VGG-16) with gradient boosting algorithms (XGBOOST) and Random Forest (RF) results in near-perfect or perfect classification performance, particularly in distinguishing between malignant and benign breast cancer cases.

Table 4: Performance parameters evaluations

Algorithm	Accuracy	AUC	Precision	Recall	F1 Score
CNN	0.9746	0.983	B - 0.95 M - 0.98	B - 0.96 M - 0.98	B - 0.96 M - 0.98
CNN+SVM	0.7619	0.842	B - 0.59 M - 0.84	B - 0.65 M - 0.81	B - 0.62 M - 0.83
CNN +RF	<b>1.0</b>	<b>1.0</b>	B - 1.00 M - 1.00	B - 1.00 M - 1.00	B - 1.00 M - 1.00
VGG-16 +XGBOOST	<b>1.0</b>	<b>1.0</b>	B - 1.00 M - 1.00	B - 1.00 M - 1.00	B - 1.00 M - 1.00

\*Note : B for 'Benign,' and M for 'Malignant'

### 4.3 DISCUSSIONS

Figure 6 shows the Performance parameters comparative analysis of CA and ROC values. Accuracy of the CNN and CNN + SVM models achieve accuracies of 97.46% and 76.19%, respectively, indicating a solid performance by CNN in correctly classifying breast tumours. The CNN + RF and VGG-16 + XGBOOST models both achieve perfect accuracies of 100%, demonstrating the highest level of accuracy in

breast cancer classification. The AUC values for the CNN and CNN + SVM models are 0.983 and 0.842, respectively, with the CNN model outperforming CNN + SVM in discriminating between benign and malignant cases. Both CNN + RF and VGG-16 + XGBOOST models achieve perfect AUC scores of 1.0, indicating ideal discrimination power and the highest level of Performance in distinguishing between the two classes.

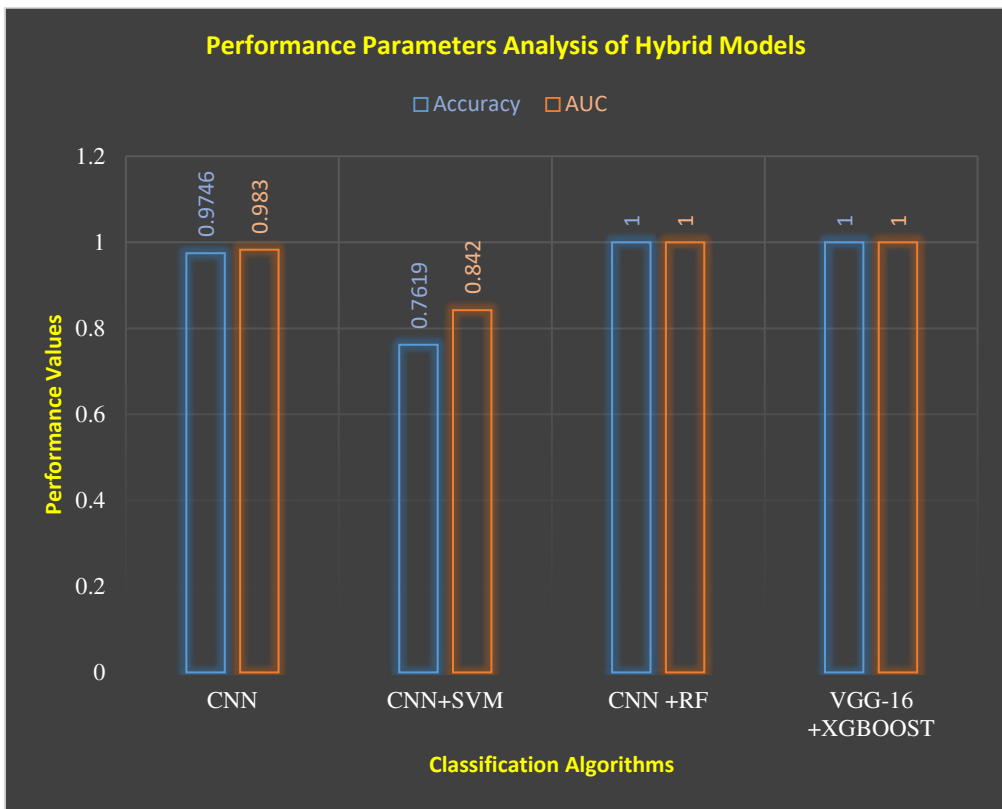


**Figure 6:** Comparative Analysis performance attributes about experimental models

The table shows the comprehensiveness of the present study with other works related to breast cancer image datasets. In comparison with different experimental results, the present study demonstrates outstanding performance with perfect classification accuracy (1.0)

and AUC (1.0) for both the CNN + RF and VGG-16 + XGBOOST models, surpassing previous research efforts that achieved accuracies ranging from 90.02% to 98.27% and F1 scores between 90.49% and 99%.

**Table 4:** Comparative analysis and evaluations present work with other existing research works

Author (Year)	Description	Dataset Used	Result
Xinfeng et al. (2020)	A deep learning framework that combines Linear discriminant analysis and auto encoder neural network is used for classification.	Different real-time datasets	98.27% accuracy
Sidharth et al. (2020)	A neural network consisting of all dense layers are used. It is optimized using early stopping and dropout layers.	Wisconsin BC diagnosis	Benign F1 Score-98 Malignant F1 score-99
Nikhilananda et al. (2020)	Deep learning-based stacking ensemble framework is used for classification	MetaBric dataset	90.02% accuracy
Mahesh et al. (2019)	A residual-learning based approach is used for BC classification i.e., ResHist.	BreaKHis dataset	92.52% accuracy. F1 scores are 90.49% and 93.45%
<b>Present Study</b>	<b>CNN +RF and VGG-16 +XGBOOST Proposal Models.</b>	<b>BreaKHis dataset</b>	<b>CNN + RF: Classification accuracy 1.0 and AUC 1.0, VGG-16+XGBOOST: Classification accuracy 1.0 and AUC 1.0</b>

## 5. CONCLUSION

We took the renowned BreaKHis dataset for assessment. We planned to foster decreased time and cost elements of the patients as well as to limit crafted by specialists. We have utilized basic and justifiable models to finish this work. Our techniques should be used for preparing data, and testing data should be utilized to check, assuming the results are adequately exact. For each ensuing calculation we applied, we worked on the productivity of the model.

Along these lines, we created and performed BC identification model. Our research focused on identifying the type of tumour, whether it is benign or malignant. That means we have classified the main types of cancer tumours. Our research doesn't recognize the kind of images as ductal carcinoma, lobular carcinoma, etc. The future work should focus on it. Along with these, they can also concentrate on the stage of breast cancer. By taking input images, the model should estimate the tumour's size, report its respective phase, and prescribe the necessary treatment.

## References:

- Albawi, S., Mohammed, T. A., & S. Al-Zawi (2017). Understanding of a convolutional neural network. In 2017 international conference on engineering and technology (ICET) (pp. 1-6). doi: 10.1109/ICEngTechnol.2017.8308186
- Balasubramaniam, S., Velmurugan, Y., Jaganathan, D., & Dhanasekaran, S. (2023). A Modified LeNet CNN for Breast Cancer Diagnosis in Ultrasound Images. *Diagnostics*. 13(17), 2746. doi:10.3390/diagnostics13172746
- Chiao, J. Y., Chen, K. Y., Liao, K. Y. K., Hsieh, P. H., Zhang, G., & Huang, T. C. (2019). Detection and classification the breast tumors using mask R-CNN on sonograms. *Medicine*. 98(19). doi: 10.1097/MD.00000000000015200
- Kabir, S. M., Bhuiyan, M. I., Tanveer, M. S., & Shihavuddin, A. S. M. (2021). RIIG modeled WCP image-based CNN Architecture and feature-based approach in breast tumor classification from B-Mode Ultrasound. *Applied Sciences*. 11(24), 12138. doi:10.3390/app112412138
- Karthik, R., Menaka, R., Kathiresan, G. S., Anirudh, M., & Nagharjun, M. (2022). Gaussian dropout based stacked ensemble CNN for classification of breast tumor in ultrasound images. *Irbm*, 43(6), 715-733. doi: 10.1016/j.irbm.2021.10.002
- Khosasi, S., Sriwidjani, N. P., Sumadi, I. W. J., Winarti, N. W., Ekawati, N. P., & Muliarta, I. M. (2023). High expression of CD73 as a negative predictor of clinical neoadjuvant chemotherapy response in triple-negative breast cancer. *Indonesia Journal of Biomedical Science*, 17(1), 94-99. doi: 10.15562/ijbs.v17i1.418
- Kim, J., & Villadsen, R. (2018). Expression of luminal progenitor marker CD117 in the human breast gland. *Journal of Histochemistry & Cytochemistry*, 66(12), 879-888. doi:10.1369/0022155418788845
- Lukong, K. E. (2017). Understanding breast cancer-The long and winding road. *BBA clinical*, 7, 64-77. doi:10.1016/j.bbaci.2017.01.001
- Mahesh Gour, Sweta Jain, T. Sunil Kumar (2019). Residual-learning based CNN for breast cancer histopathological image classification. *Wiley*, 2019. doi:10.1002/ima.22403
- Meriem Amrane, Saliha Oukid, Ikram Gagaoua, Tolga Ensari (2018). Breast Cancer Classification Using Machine Learning. *IEEE*, 2018. doi: 10.1109/EBBT.2018.8391453
- Naresh Khuriwal, Nidhi Mishra (2018). Breast Cancer Detection from Histopathological Images Using Deep Learning. *IEEE*, 2018. doi: 10.1109/ICRAIE.2018.8710426
- Nikhilanand Arya, Sriparna Saha (2020). Multi-modal classification for human breast cancer prognosis prediction: Proposal of deep learning based stacked ensemble model. *IEEE*. doi: 10.1109/TCBB.2020.3018467
- PanduRanga Vital, T., Murali Krishna, M., Narayana, G. V. L., Suneel, P., & Ramarao, P. (2019). Empirical analysis on cancer dataset with machine learning algorithms. In Soft Computing in Data Analytics: Proceedings of International Conference on SCDA 2018 (pp. 789-801). *Springer Singapore*. doi:10.1007/978-981-13-0514-6\_75
- Ram MurtiRawat, Shivam Panchal, Vivek Kumar Singh, Yash Panchal (2020). Breast Cancer Detection Using K-Nearest Neighbors, Logistic Regression and Ensemble Learning, *IEEE*. DOI: 10.1109/ICESC48915.2020.9155783
- Sahu, A., Das, P. K., & S. Meher (2023). High accuracy hybrid CNN classifiers for breast cancer detection using mammogram and ultrasound datasets. *Biomedical Signal Processing and Control*, 80, 104292. doi: 10.1016/j.bspc.2022.104292
- Sidharth S Prakash, Visakha K (2020). Breast Cancer Malignancy Prediction Using Deep Learning Neural Networks. *IEEE*, 2020. doi:10.1109/ICIRCA48905.2020.9183378
- Terlapu, P. V., Sadi, R. P. R., Pondreti, R. K., & Tippanna, C. R. (2021). Intelligent Identification of Liver Diseases Based on Incremental Hidden Layer Neurons ANN Model. *International Journal of Computing and Digital System*. doi: 10.12785/ijcds/110183
- Vital, T. P. (2021). Empirical study on Uddanam chronic kidney diseases (UCKD) with statistical and machine learning analysis including probabilistic neural networks. In Handbook of Computational Intelligence in Biomedical Engineering and Healthcare. 283-314. *Academic Press*. doi: 10.1016/B978-0-12-822260-7.00013-3
- Vital, T. P., Prasada Raju, G. S. V., Kaladhar, D. S. V. G. K., Sriram, T. V., Rayavarapu, K. A., Nageswara Rao, P. V., & Appala Raju, S. (2014). Data Collection, Statistical Analysis and Clustering Studies of Cancer Dataset from

- Vizianagaram District, AP, India. In ICT and Critical Infrastructure: Proceedings of the 48th Annual Convention of Computer Society of India-Vol II: Hosted by CSI Vishakhapatnam Chapter (pp. 423-430). Springer International Publishing. doi: 10.1007/978-3-319-03095-1\_45
- Vital, T. P., Raju, G. P., Rao, I. S., & Kumar, A. P. (2015). Data collection, statistical analysis and machine learning studies of cancer dataset from north costal districts of AP, India. *Procedia Computer Science*, 48, 706-714. doi: 10.1016/j.procs.2015.04.205
- Xie, X. Z., Niu, J. W., Liu, X. F., Li, Q. F., Wang, Y., Han, J., & Tang, S. (2022). DG-CNN: Introducing margin information into convolutional neural networks for breast cancer diagnosis in ultrasound images. *Journal of Computer Science and Technology*, 37(2), 277-294. doi: 10.1007/s11390-020-0192-0
- Xinfeng Zhang, Dianning He, Yue Zheng, Huabi Huo, Simiao li, Ruimei Chai, Ting Liu (2020). Deep Learning Based Analysis of Breast Cancer Using Advanced Ensemble Classifier and Linear Discriminant Analysis. *IEEE*. doi: 10.1109/ACCESS.2020.3005228

---

**Nageswara Rao Gali**

Department of Information Technology,  
Aditya Institute of Technology and  
Management, Tekkali, India-532 201  
[gnraoitam@gmail.com](mailto:gnraoitam@gmail.com)

**Sai Manoj Somu,**

Department of Information Technology,  
Aditya Institute of Technology and  
Management, Tekkali, India-532201,  
[saimanoj2019@gmail.com](mailto:saimanoj2019@gmail.com)

**Maheswara Rao V V R**

Shri Vishnu Engineering College for  
Women (A), Bhimavaram,  
India  
[mahesh\\_vvr@yahoo.com](mailto:mahesh_vvr@yahoo.com)

ORCID : 0000-0002-0503-7211

---

**Panduranga Vital Terlapu**

Department of Computer Science and  
Engineering, Aditya Institute of  
Technology and Management, Tekkali,  
India-532 201 [vital2927@gmail.com](mailto:vital2927@gmail.com)

**Madhavi Varanasi,**

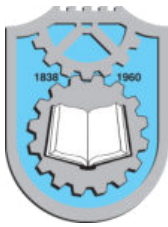
Department of Information Technology,  
Aditya Institute of Technology and  
Management, Tekkali, India-532201,  
[madhavivaranasi28@gmail.com](mailto:madhavivaranasi28@gmail.com)

**Yasaswini Mandavakuriti,**

Department of Information Technology,  
Aditya Institute of Technology and  
Management, Tekkali, India-532 201  
[asaswinimandavakuriti@gmail.com](mailto:asaswinimandavakuriti@gmail.com)

**Vijay Telugu,**

Department of Information Technology,  
Aditya Institute of Technology and  
Management, Tekkali, India-532201,  
[vijaytelugu123@gmail.com](mailto:vijaytelugu123@gmail.com)



## NUMERICAL EXPLORATION OF VISCOUS FLOW REGIMES: INSIGHTS FROM POISEUILLE, COUETTE AND TAYLOR-COUETTE FLOWS

Venkat Rao Kanuri  
K. V. Chandra Sekhar  
P. S. Brahmanandam<sup>\*</sup>  
M. S. R. Murthy

### Keywords:

Analytical and numerical solutions, Poiseuille flow, Couette flow, Pressure gradient force, Flow around a circular cylinder, Velocity profile.

### A B S T R A C T

We present a numerical study for Poiseuille and Couette as well as Taylor-Couette swirling flows. The governing equations of momentum and energy are transformed into coupled and nonlinear ordinary differential equations using similarity transformation and then solved numerically. We critically evaluate the effect of dimensionless pressure gradients on fluid velocity and observed that the velocity increases as the dimensionless pressure gradient increases. Couette flows are simulated in different scenarios, including top plate moving, bottom plate moving, and top plate moving in adverse pressure gradient conditions. In a third scenario, the flow velocity profile revealed a backflow regime (BFR). A simple schematic model is, therefore, proposed to explain the presence of BFR in the flow's profile. Numerical and analytical solutions around the circular cylinder are presented. The marginal discrepancy between the analytical and numerical profiles is maximum at  $\sim 90^\circ$  and  $270^\circ$  degrees, which indicates that the chosen method is suitable and capable of reproducing engineering problems. Velocity magnitude and vector diagrams show that the cylinder shape was found to have a significant effect on the flow field. The velocity at the top and bottom of the cylinder is twice the velocity that seen away from the cylinder.

© 202x Published by Faculty of Engineering



## 1. INTRODUCTION

Analytical solutions are generally preferred to study the simple contour conditions of systems. For instance, analytical solutions are the most sought-after options when the modeling leads to a linear differential equation. Nevertheless, analytical solutions cannot obtain exact solutions when the presence of non-linear differential equations is imminent. On the other hand,

numerical methods may provide approximate solutions even if the boundary conditions become complex and the fluid flow become transient. With the advent of the most powerful computers capable of performing calculations at relatively higher speeds, there is a rapid development that enabled several researchers to use different numerical methods in fluid flow engineering. Alexandre Joel Chorin introduced the first numerical method for

<sup>1</sup> Corresponding author: Brahmanandam P S  
Email: [dranandpotula@svecw.edu.in](mailto:dranandpotula@svecw.edu.in)

solving incompressible viscous flow problems in 1947.

Numerical and finite difference methods have been used in various applications, such as modeling Navier-Stokes equations for vortex generation, pipe flow, Couette flow, static structural analysis, wave analysis, etc. As far as the ionosphere and atmosphere studies are concerned, understanding viscous effects is crucial for modeling and predicting ionospheric phenomena like plasma convection and ion transport (Potula et al., 2011; Brahmanandam et al., 2012; Brahmanandam et al., 2020; Uma et al., 2016). Understanding viscous effects aids in studying air quality near the surface.

Numerical methods have been adapted to solve many problems and prove cheaper than experimental results. However, since the numerical techniques use approximations, the mathematical models have to be tested for various boundary conditions and governing equations to obtain a reliable solution. A lot of research is being conducted on the stability of such numerical models and the reliability of the solution obtained by these methods (Lin, 1961; Hughes, 1972, and references therein).

Plane Hagen- Poiseuille (after J. L. M. Poiseuille and G. H. L Hagen) flow is broadly defined as a steady and laminar flow of a viscous fluid between two horizontal parallel plates separated by an appropriate distance. In Poiseuille flow, a constant pressure gradient ( $dp/dx$ ) is applied across the length of the plate flow. It is exemplified by a two-dimensional (2D) velocity profile ( $v(y)$ ) symmetric about the mid-plane, as shown in Figure 1. From the continuity equation for a flow between two fixed plates, as shown in figure 1, the governing equations are

$$\frac{\partial u}{\partial x} + \frac{\partial v}{\partial y} = 0$$

(Since for 1-D flow, if we write Navier- Stokes equations in the x-direction, non-linear convective terms become zero)

$$\text{As } v=0, \frac{\partial u}{\partial x} = \frac{du}{dx} = 0 \\ u=u(y)$$

The x-momentum equation:

$$\rho \left( u \frac{\partial U}{\partial x} + v \frac{\partial U}{\partial y} \right) = - \frac{\partial P}{\partial x} + \mu \left( \frac{\partial^2 u}{\partial x^2} + \frac{\partial^2 u}{\partial y^2} \right) \\ \rho(0) = - \frac{\partial P}{\partial x} + \mu \left( \frac{\partial^2 u}{\partial x^2} + \frac{\partial^2 u}{\partial y^2} \right) \\ \frac{\partial P}{\partial x} = \mu \left( \frac{\partial^2 u}{\partial y^2} \right) \quad (1)$$

The y-momentum equation:

$$\rho \left( u \frac{\partial v}{\partial x} + v \frac{\partial v}{\partial y} \right) = - \frac{\partial P}{\partial x} + \mu \left( \frac{\partial^2 v}{\partial x^2} + \frac{\partial^2 v}{\partial y^2} \right) \\ \rho(0 + 0) = - \frac{\partial P}{\partial y} + \mu (0 + 0) \\ \frac{\partial P}{\partial y} = 0 \quad (2)$$

The z-momentum equation:

$$\rho \left( u \frac{\partial w}{\partial x} + v \frac{\partial w}{\partial y} + W \frac{\partial w}{\partial z} \right) = - \frac{\partial P}{\partial z} + \mu \left( \frac{\partial^2 w}{\partial x^2} + \frac{\partial^2 w}{\partial y^2} \right) \\ \rho(0 + 0 + 0) = - \frac{\partial P}{\partial z} + \mu (0 + 0) \\ \frac{\partial P}{\partial z} = 0 \quad (3)$$

From equations 1, 2, and 3, it is obvious that

$$\frac{\partial P}{\partial x} = \mu \left( \frac{\partial^2 u}{\partial y^2} \right), \quad \frac{\partial P}{\partial y} = 0, \text{ and } \frac{\partial P}{\partial z} = 0$$

And, it is also clear that  $\frac{\partial P}{\partial x} = \mu \left( \frac{\partial^2 u}{\partial y^2} \right) = \text{constant}$

The constant is expected to be negative because the pressure must decrease in the flow direction to overcome the resisting wall shear stress. Then applying the double integral to the above equation gives the velocity profile, therefore,

$$u = \frac{1}{\mu} \left( \frac{\partial p}{\partial x} \right) \frac{y^2}{2} + C_1 + C_2 \quad (4)$$

Invocation of boundary conditions (at  $y=\pm h$ ;  $u=0$ ) leads to the following conditions

$$C_1 = 0 \text{ and } C_2 = - \left( \frac{\partial p}{\partial x} \right) \frac{h^2}{2\mu} \dots\dots (5)$$

$$u = - \left( \frac{\partial p}{\partial x} \right) \frac{h^2}{2\mu} \left[ 1 - \frac{y^2}{h^2} \right] \quad (6)$$

Equation 6 is a parabola equation, and that's why the velocity profile of Poiseuille's flow looks like a parabola shape (see figure 1 for more details).

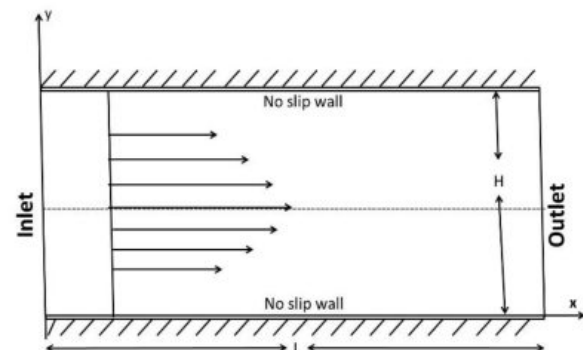


**Figure 1.** Plane Hagen-Poiseuille flow between two flat plates, where 'L (H)' is the length (height) of the plate

Couette flow is a viscous flow between two parallel plates separated vertically by a considerable distance (Munson et al. 2004). In

general, the upper plate moves with some velocity while the bottom plate remains stationary. The Couette flow is two-dimensional in the xy plane. The flow between the two plates is driven by the shear stress exerted on the fluid by the moving plates. A velocity profile is, thus, formed on the flow, as depicted in the following figure. The schematic of Couette flow is presented in Figure 2.

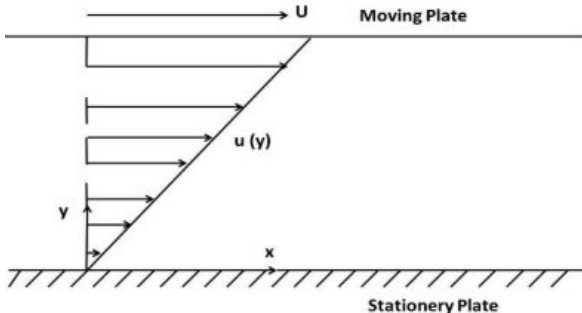


**Figure 2.** Schematic of Couette flow between two plates

As per as the fundamental governing equations of Couette flow are concerned, incompressible fluid dynamics problems are, in general, described by simple Navier-Stokes (NS) equations.

Let us assume both plates are infinitely large in z direction (see figure 2), and, hence, z dependence cannot be considered. Then, applying continuity equation, one can have

$$\frac{\partial U}{\partial x} + \frac{\partial V}{\partial y} + \frac{\partial W}{\partial z} = 0 \quad (7)$$

Navier-Stokes equation in x-direction,

$$\begin{aligned} \rho \left( \frac{\partial U}{\partial t} + U \frac{\partial U}{\partial x} + V \frac{\partial U}{\partial y} + W \frac{\partial U}{\partial z} \right) \\ = - \frac{\partial P}{\partial x} + \rho g_x \\ + \mu \left( \frac{\partial^2 U}{\partial x^2} + \frac{\partial^2 U}{\partial y^2} + \frac{\partial^2 U}{\partial z^2} \right) \\ \frac{d^2 u}{dy^2} = 0 \end{aligned} \quad (8)$$

Once we integrate the above second order differential equation (8), we get

$$\frac{du}{dy} = C_1$$

Then, the second integration yields, the following equation, such as

$$u(y) = C_1 y + C_2 \quad (9)$$

Invocation of initial ( $y=0, u=0$ ) and final ( $y=b, u=V$ ) boundary conditions allow us to have  $C_2$  to be zero. If  $C_2$  value is zero (once implemented in equation 9), then  $C_1$  value becomes  $V/b$ . And, finally we will have

$$u(y) = V * y / b \quad (10)$$

Equation 5 indicates that the relation between  $u$  and  $y$  is linear. The above equation can also be written as follows and it can be solved using MATLAB easily

$$u/y = V/b \quad (11)$$

To know the numerical approximation of the above equation, we used a second-order finite difference Crank-Nicolson Scheme in this study because that scheme is an implicit scheme and unconditionally stable and, hence, it is convergent. Usually, the Crank-Nicolson scheme is the most accurate scheme for small-time steps (Abdon Atangana, 2016). On the other hand, the explicit scheme is the least valid and can be unstable, but it is also the easiest to implement and the least numerically intensive. Using the Central difference method, we obtained the velocities at different nodes at different time intervals for several iterations.

## 2. NEED OF THE STUDY AND ORGANIZATION OF THE ARTICLE

Many analytical and numerical investigations have been carried out on various flows. However, they focus only on single entities (Sumer and Fredsoe 1997; Benim et al. 2007; Butt and Egbers 2013; Luckachan et al. 2022). Some studies deal only with laminar flow (Park et al. 1998; Rajani et al. 2009; Bai and Li 2011; Ganie et al., 2022) or turbulence (Ong et al. 2009; Cao and Tamura 2008; Benim et al. 2007; Young and Ooi 2004). In this work, various flow fields including Poiseuille and Couette flows and their analytical and numerical solutions are discussed.

Further, flow around a cylinder is studied and its analytical and numerical solutions are provided. Most importantly, a simple schematic model is proposed that helps to understand the existence of shear stresses and pressure gradient forces between two plates in opposite directions. As a result, a backflow regime is created within the stream, and this simple model may serve as a source of inspiration for other researchers to continue their work in this exciting field. Still, we believe there is a lot of room for these works, even though we are limiting ourselves to a few types of flows. The future scope of this work is detailed in the final section of this article.

This paper consists of three sections. First, we introduce the importance of analytical and numerical solutions for various flows and the associated equations. Next, results and discussion are included, wherein we thoroughly discuss

analytical and numerical solutions of various flows. Most importantly, a schematic model is proposed that helps us to explain the backflow regime in flow. Analytical and numerical flow solutions around a circular cylinder are discussed in the same section. The conclusion summarizes the results and it also contains future scope of these works, which follow the acknowledgments.

### 3.0 RESULTS AND DISCUSSION

#### 3.1 Analytical and numerical solutions of plane Poiseuille flow– Finite difference method

In the finite difference method, the derivatives will be approximated by finite differences on a grid. To solve a linear value problem of the form  $y^{11} = p(x)y' + q(x)y + r(x)$ , the following boundary conditions are considered such as  $y(x_1) = \alpha$  and  $y(x_2) = \beta$ .

The plane Poiseuille flow is solved using the finite difference method, for which we have considered the plate separation to be 0.1 and the viscosity  $\mu = 1$ . The boundary conditions are:  $x_1 = 0$ ;  $\alpha = 0$ ; and  $x_2 = 0$ ;  $\beta = 0$ . The exact and the numerical (approximate) solutions of plane Poiseuille flow are almost converging, as shown in figure 3.

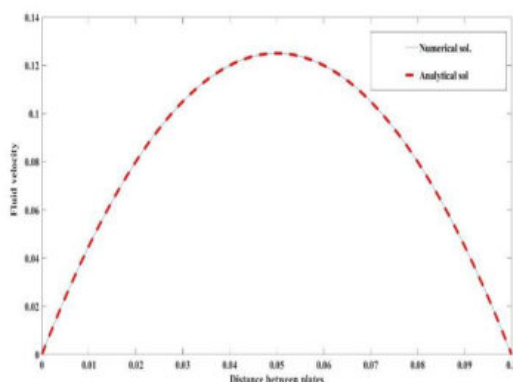


**Figure 3.** Analytical and numerical solutions of plane Poiseuille flow

#### 3.2 COUETTE FLOW IN DIFFERENT SCENARIOS

##### 3.2.1 Couette flow under different pressure gradient conditions

Couette flow is used to describe shear-driven motion in which the fluid flow is induced by the motion of one of the plates in the channel. As for the technical application of this flow, it is used in fluidics, geophysics and astrophysics. Couette flow

theory can be used to measure viscosity and estimate drag in many applications.

We first investigated the behavior of the velocity profile at different pressure gradients. The dimensionless pressure gradients considered here range from -5 to +5 (11 in total) and the resulting velocity profiles are shown in the figure below. Figure 4 shows Couette velocity profiles under different pressure gradients. From this figure, it is clear that the velocity profile increases with favorable dimensionless pressure gradient, similar to the findings of Kuiry and Bahadur (2015) and Muhim Chutia (2018), and references therein.

We also see that the numerical solution converges to the exact solution when the pressure gradient is zero (plane Couette flow). It is also clear that the analytical solution decreases as a linear change between the bottom and top walls when the pressure drop goes to zero. It is also clear that the velocity profile is linear at steady state (see velocity profile with zero pressure gradient in Figure 4).

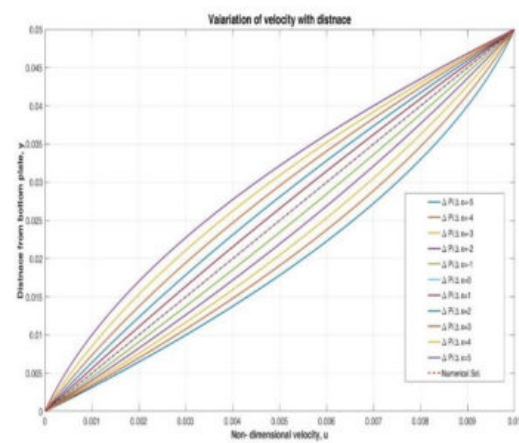


**Figure 4.** Couette flow velocity profiles under favourable pressure gradient ( $\frac{\Delta p}{\Delta x} = -5, -4, -3, -2, -1$ ), zero pressure gradient ( $\frac{\Delta p}{\Delta x} = 0$ ), and adverse pressure gradient ( $\frac{\Delta p}{\Delta x} = 1, 2, 3, 4, 5$ ) conditions

##### 3.2.2 The top plate is moving while the bottom plate is held constant scenario

This section shows the Couette velocity profile for a grid point of 101 and a top velocity of 1 m/s. Figure 5 shows the velocity profile from 0 to 25 seconds. The figure shows that the analytical solution reaches steady state over time as the number of iterations increases. To be precise, it

took about 25 seconds to go from transient to steady state. Moreover, the profile appeared to shift towards steady state as the truncation error decreased over time. It has been reported that for an arbitrary Reynolds number of 2000 and an associated error of 0.00458, it took nearly 1000 seconds to reach steady state from transient state (Santos and Chaves, 2019).

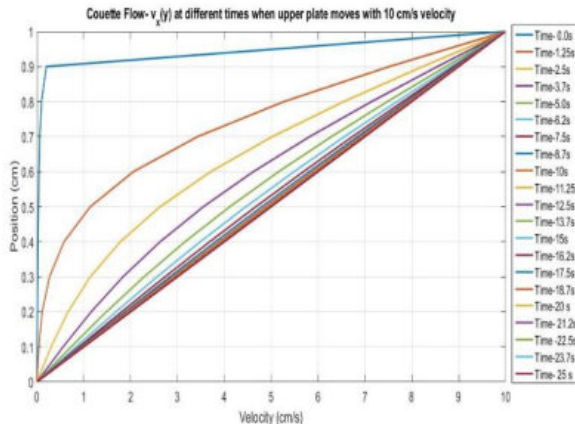


**Figure 5.** Couette flow when the upper plate is moving

### 3.2.3 The top plate is held constant while the bottom plate is moving scenario

To verify the effect of the drag force on the liquid from the lower plate, the upper plate remained constant while the lower plate moved at a constant velocity, simulating the Couette flow in different environments. Figure 6 shows velocity profiles at various times from 0 to 25 seconds. It is interesting that the direction of flow is reversed compared to Figure 5, but this is mainly due to liquid resistance through the bottom plate. Interestingly, similar to the velocity profile in Figure 5, it also took almost 25 seconds to reach steady state from transient.

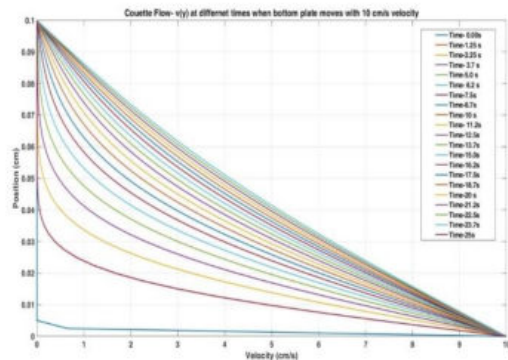


**Figure 6.** Couette flow when the bottom plate is moving

### 3.2.4 The top plate is moving and the bottom plate is held constant under adverse pressure gradient condition scenario

Here a special case is shown where the top plate moves at 80 m/s and the bottom plate remains constant under adverse pressure gradient conditions. In this case, it is reasonable to assume that the velocity profile for this scenario exhibits a line similar to the trend shown in Figure 6. However, due to the presence of an adverse pressure gradients, the flow tends to reverse starting at the bottom plate, and this reverse flow condition is known as backflow regime (BFR) or reverse flow reverse (RFR) (Kundu et al., 2016). Figure 7 shows a parabolic velocity profile from the beginning of the top plate to near the bottom plate. It is also possible to see the BFR from this figure.

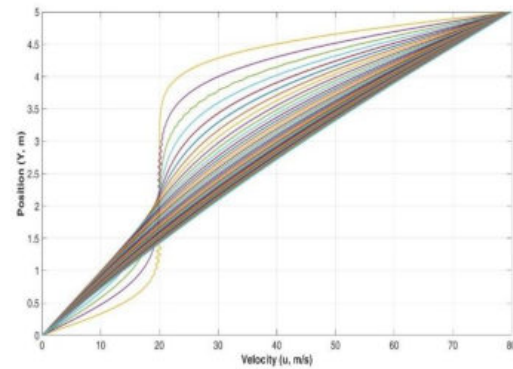


**Figure 7.** Couette flow under adverse pressure gradients

In such circumstances, there is a competition between the shear stress force (diffusive momentum flux) exerted by the moving plate (which tries to move the fluid from left to the right direction) and pressure gradient force (which tries to move the fluid from right to left), as shown in the following figure. Figure 8 presents a simple schematic model indicating the presence of shear stress and pressure gradient forces on fluid. Further, if the shear stress force completely dominates the pressure gradient force, the velocity profile becomes parabolic, similar to Kundu et al. (2016, see their Figure 9.4a) results.

The schematic model presented in figure 8 shows the moderate dominance of shear stress forces over pressure gradient forces. That's why BFR has occupied nearly 33% of the entire region, as seen in Figure 8. The second option is that if the pressure gradient force dominates the shear stress, one would expect a reverse flow, which can also be

found in the research by Kundu et al. (2016, see their Figure 9.4b). Last but not least, when the pressure gradient becomes zero, the velocity profiles would look as in Figure 2 of this article. This similar velocity profile could also be found in the research by Kundu et al. (2016, see their Figure 9.4c).

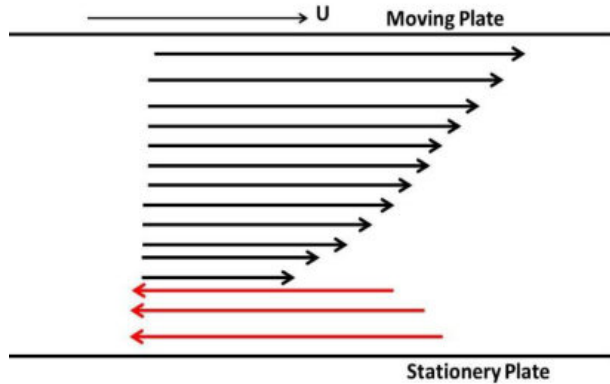


**Figure 8.** A simple schematic model helps us understand the presence of shear stress and pressure gradient forces between two plates, wherein black arrows (left to right) represent shear stress forces. In contrast, red arrows (right to left) represent pressure gradient forces.

### 3.3 Flows around a circular cylinder

Fluid flow around circular cross-sections is recognized as an important problem in fluid dynamics. Moreover, this is an exciting aspect of research that has attracted researchers for several years (Yuce and Kareem, 2016). Several engineering applications, including bridge piers, offshore structures, and pipelines can, effectively, be modelled as cylinders. The flow around cylinders exhibits many important physical phenomena, such as flow separation, turbulence, and vortex shedding (Yuce and Kareem, 2016, and reference therein). The flow over a circular cylinder is the combination of uniform flow and a doublet, according to Ngo and Gramol (2004).

The superimposed stream function and velocity potential are given by

$$\Psi = \Psi_{\text{Uniform flow}} + \Psi_{\text{doublet}} = U r \sin \Theta - K \sin \Theta / r$$

and

$$\Phi = \Phi_{\text{Uniform flow}} + \Phi_{\text{doublet}} = U r \cos \Theta + K \cos \Theta / r$$

Since the streamline that passes through the stagnation point has a value of zero (see, figure 10 for further clarification), the stream function on the

surface of the cylinder of radius ‘a’ is then given by

$$\Psi = U a \sin \Theta - K \sin \Theta / a = 0$$

This gives the strength of the doublet as

$$K = U a^2$$

The stream function and velocity potential for flow past a fixed circular cylinder become

$$\Psi = U r (1 - (a/r)^2) \sin \Theta$$

and

$$\Phi = U r (1 + (a/r)^2) \cos \Theta$$

Then, both velocity components (radial and tangential) can be written as

$$V_r = \frac{1}{r} \frac{\partial \Psi}{\partial \Theta} = U \left[ 1 - \frac{a^2}{r} \right] \cos \Theta$$

$$V_\Theta = -\frac{\partial \Psi}{\partial r} = -U \left[ 1 + \frac{a^2}{r} \right] \sin \Theta$$

Figure 9 shows both analytical and numerical solutions of velocities over the circular cylinder, from 0 to 360 degrees. The discrepancy between the velocities calculated numerically and analytically is extreme at ~ 90 degrees and ~ 270 degrees, respectively. On the other hand, most surfaces show better agreement with sufficient accuracy. This observed marginal discrepancy may be reduced by modifying the default equation solver settings (for example, by tightening the convergence criteria and increasing the number of iterations), and viscous effects can also affect this discrepancy (Ngo and Gramol, 2004). Overall, the analytical and numerical showed moderate to reasonable agreement.

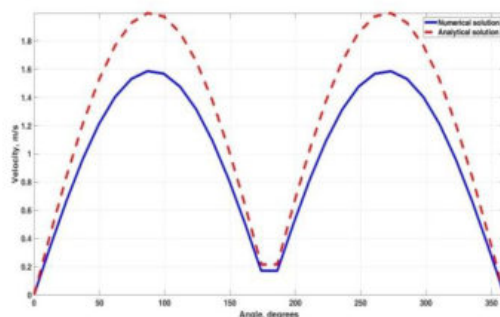


**Figure 9.** Shows both analytical and numerical solutions of velocities over the circular cylinder, from 0 to 360 degrees.

Figure 10 shows velocity vectors superimposed on the velocity magnitudes around the circular cylinder. Here, warmer colors represent faster velocities. The cylinder shape is found to have significantly affected the flow field (Yuce and Kareem, 2016) and the flow smoothly divides and reunites around the cylinder. This case falls into

the low speed category because at low speed the smooth fluid flow becomes unstable and at high speed it becomes turbulent.

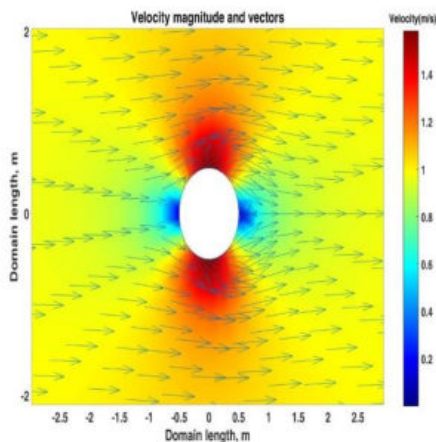


**Figure 10.** Velocity magnitude and vectors around a circular cylinder

It is obvious that green represents the free stream velocity, which is the velocity that is far from the cylinder. Fluid elements approaching the cylinder directly (at the equator) slow down once they are sufficiently close (shifting to blue color). The fluid element on the upstream side of the cylinder's surface stops moving, or its velocity decreases to zero. It is referred to as a stagnation point. The magnitude of the fluid constituents' velocities increases as they travel above or below the cylinder (shifting to red). Two times as fast as the free stream is the velocity at the top and bottom of the cylinder. Tangential or parallel to the cylindrical surface, velocity exists along the cylinder surface.

#### 4.0 CONCLUSION AND FUTURE SCOPE

This work presents analytical and numerical solutions for various flows. The salient features of this study are as follows:

- Exact and numerical solutions of planar Poiseuille flow converge without contradiction
- The fluid velocity increases with favorable dimensionless pressure gradient
- Couette flows simulated in different scenarios yielded exciting results.

- If the pressure drop goes to zero, the analytical solution will decrease as a linear change between the bottom wall and the top wall. If the bottom plate is held constant, the flow will be in the opposite direction, mainly due to the drag force on the fluid by the bottom plate
- The flow forms a backflow regime when the upper plate moves under adverse/unfavorable pressure gradient conditions. To describe the backflow regime, we present a simple schematic model that helps to understand the competition between momentum diffusion and pressure gradient forces as to develop a backflow regime. Analytical and numerical solutions for flow over a cylinder are shown
- We explained the reasons for marginal discrepancy (at only few places) between
- Analytical and numerical solutions. Using the velocity magnitude and velocity vector plot, we observe that the shape of the cylinder has a large effect on the flow field and the velocity at the top and bottom of the cylinder being twice that of the free stream (velocity away from the cylinder).

As far as the future scope of these research works are concerned, the flow field around a cylinder of Reynolds number ( $Re$ ) ranges from a minimum value (e.g. 10 – laminar flow) to a higher value ( $5 \times 10^6$  – turbulent flow) will be studied. We also focus on examining both analytical and numerical studies such as flows in infinite parallel plates, vertically falling films, flow in rotating tubes, and boundary layers. This will give you more insight into the flow. In addition to the Reynolds number scenario, the flow direction also has a significant impact on the flow dynamics around the cylinder. Since the direction of the free jet can be changed (Zhang et al., 2019), the effect of angle of attack on the flow will be investigated as part of future research.

## References

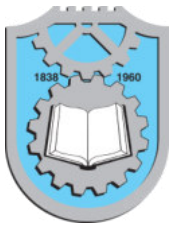
- Abdon Atangana (2016). Method for partial differential equations with beta-derivative, Editor(s): Abdon Atangana, Derivative with a New Parameter, Academic Press, pp. 61-94. doi: 10.1016/B978-0-08-100644-3.00004-0
- Bai and Li (2011). Numerical simulation of flow over a circular cylinder at low Reynolds number, *Advanced Materials Research, Trans Tech Publ.*, doi: 10.4028/AMR.255-260.942
- Benim, Ali Cemal & Gülb, Fethi and Pasqualotto, Ennio. (2007). Numerical investigation of the role of the inlet swirl velocity profile on decay of swirl in pipe flow. *Proceedings of the 5<sup>th</sup> IASME/WSEAS Intl. Conference on Fluid Mechanics and Aerodynamics*, Athens, Greece, Aug. 25-27.
- Brahmanandam, P. S., G. Uma, J. Y. Liu, Y. H. Chu, N. S. M. P. Latha Devi, and Y. Kakinami (2012), Global S4 index variations observed using FORMOSAT-3/COSMIC GPS RO technique during a solar minimum year, J. Geophys. Res., 117, A09322, doi:10.1029/2012JA017966.**
- Brahmanandam, P.S., Kumar, V.N., Kumar, G.A. et al. (2020) A few important features of global atmospheric boundary layer heights estimated using COSMIC radio occultation retrieved data. Indian J Phys. 94, 555–563. doi:10.1007/s12648-019-01514-7**
- Butt U., C. C. Egbers (2013). Aerodynamic characteristics of flow over circular cylinders with patterned surface, *Int. J Materials Mechanics and Manufacturing*, 1, 121-125. doi: 10.7763/IJMM.2013.V1.27
- Cao S., Yukio Tamura (2008). Flow around a circular cylinder in linear shear flows at subcritical Reynolds number. *Journal of Wind Engineering and Industrial Aerodynamics*, 96, 1961-1973. doi:10.1016/j.jweia.2008.02.041.
- Ganie, Abid A. Memon, M. Asif Memon, A.M. Al-Bugami, Kaleemullah Bhatti, Ilyas Khan (2022). Numerical analysis of laminar flow and heat transfer through a rectangular channel containing perforated plate at different angles, *Energy Reports*, 8, 539-550. doi: 10.1016/j.egyr.2021.11.232.
- Hu, J., Munson, C. L., & Silver, E. A. (2004). A Modified Silver-Meal Heuristic for Dynamic Lot Sizing under Incremental Quantity Discounts. *The Journal of the Operational Research Society*, 55(6), 671-673. <http://www.jstor.org/stable/4101973>
- Hughes T. H., (1972). Variable mesh numerical method for solving the Orr-sommerfeld equation. *Phys Fluid*, 725, 725-728. doi: 10.1063/1.1693974
- Kuiry D. R., S Bahadur, (2015). Steady MHD flow of viscous fluid between two parallel porous plates with heat transfer in an inclined magnetic field, *Journal of Scientific Research*. doi: 10.3329/jsr.v7i3.22574
- Kundu, P. K., I. M. Cohen, D. R. Dowling (2016). Fluid Mechanics, 6<sup>th</sup> edition, Academic Press, 409-467. doi: 10.1016/B978-0-12-405935-1.00009-5
- Lin C. C. (1961). Some mathematical problems in the theory of the stability of parallel flows. *J Fluid Mech.*, 10, 430-438. doi:10.1017/S0022112061001025
- Luckachan et al., (2022). Transient vortex shedding behaviour of non-reacting flow over V-gutter bluff bodies with a central slit, *International Journal of Ambient Energy*. doi:10.1080/01430750.2022.2102070.
- Muhim Chutia (2018). Effect of variable thermal conductivity and the inclined magnetic field on MHD plane Poiseuille flow in a Porous channel with non-uniform plate temperature, *Journal of Computational & Applied Research*. doi:10.22061/jcarme.2017.1620.1137
- Ngo C.C., K. C. Gramol (2004). 7<sup>th</sup> Chapter -Incompressible and Inviscid Flow, *Multimedia Engineering Flud Mechancis*. Archived from [http://www.ecourses.ou.edu/cgi-bin/ebook.cgi?doc&topic=fl&chap\\_sec=07.4&page=theory](http://www.ecourses.ou.edu/cgi-bin/ebook.cgi?doc&topic=fl&chap_sec=07.4&page=theory)
- Nikushchenko D, Pavlovsky V, Nikushchenko E (2022). Analytical Solutions for Simple Turbulent Shear Flows on a Basis of a Generalized Newton's Law. *Polymers* (Basel). 4(16):3308. doi: 10.3390/polym14163308.
- Ong M. C., T. Utne, L. E. Holmedal (2009). A numerical study on near-bed flow mechanisms around a marine pipeline close to a flat seabed including estimation of bedload sediment transport, *WIT Transactions on Ecology and the Environment*, 126, 163-175. Archived from <https://www.witpress.com/elibrary/wit-transactions-on-ecology-and-the-environment/126/20640>
- Park, Jeong Seo, O, Byeong Jin Kim, Mun Heon (1999). Combustion Characteristics of Plasma Jet Ignition on LPG-Air Mixture in Laminar Flow Field, *Transactions of the Korean Society of Automotive Engineers*, 7, 6869. <https://koreascience.kri/article/JAKO199910102414243>
- Potula, B. S., Y.-H. Chu, G. Uma, H.-P. Hsia, and K.-H. Wu (2011). A global comparative study on the ionospheric measurements between COSMIC radio occultation technique and IRI model, J. Geophys. Res., 116, A02310, doi:10.1029/2010JA015814.**
- Rajani et al., (2009). Numerical simulation of laminar flow past a circular cylinder, *Applied Mathematical Modelling*. 33 (3), 1228-1247. doi:10.1016/j.apm.2008.01.017
- Santos and Chaves (2019). Application of the finite difference method for numerical simulation of the Couette Flow, 25<sup>th</sup> ABCM Intl. Conference of Mechanical Engineering, October 202-25, Brazil. doi:10.26678/ABCM.COBEM2019.COB2019-0537
- Strikwerda J. C (2004). Finite Difference Schemes and Partial Differential Equations, 2<sup>nd</sup> edition, Society for Industrial and Applied Mathematics (SIAM), Philadelphia, USA, 2004. doi:10.1137/1.9780898717938
- Sumer and Fredsoe (1997). Scour at the round head of a rubble-mound breakwater. *Coastal Engineering*, 29(3-4), 231-262, doi:10.1016/S0378-3839(96)00025-7
- Uma, G., Brahmanandam, P. S., & Chu, Y. H. (2016). A long-term study on the deletion criterion of questionable electron density profiles caused by ionospheric irregularities – COSMIC radio occultation technique. Advances in Space Research, 57(12), 2452–2463. doi:10.1016/j.asr.2016.03.034**
- Young, M. E., and A. Ooi (2004). Turbulence models and boundary conditions for bluff body flow, 15th Australian Fluid Mechanics Conference, 13-17 December. Archived from <https://www.aeromech.usyd.edu.au/15afmc/proceedings/papers/AFMC00158.pdf>
- Yuce, M. I., & Kareem, D. A. (2016). A Numerical Analysis of Fluid Flow around Circular and Square Cylinders. *Journal (American Water Works Association)*, 108(10), E546–E554. <https://www.jstor.org/stable/90005209>
- Zhang L, Mao X, Ding L. (2019). Influence of attack angle on vortex-induced vibration and energy harvesting of two cylinders in side-by-side arrangement. *Advances in Mechanical Engineering*. 11(1). doi:10.1177/1687814018822598

**Venkat Rao Kanuri**  
Dept. of Mathematics,  
Koneru Lakahmaiah Education  
Foundation (KLEF),  
Deemed to Be University,  
Vaddeswaram,  
Andhra Pradesh,  
India.  
[k.ravi.msc@gmail.com](mailto:k.ravi.msc@gmail.com)  
ORCID 0000-0003-2364-5074  
&  
Department of Engineering  
Mathematics and Humanities,  
SRKR Engineering College,  
Bhimavaram 534204, India

**K.V.Chandra Sekhar**  
Dept. of Mathematics,  
Koneru Lakahmaiah Education  
Foundation (KLEF),  
Deemed to Be University,  
Vaddeswaram,  
Andhra Pradesh,  
India.  
[chandu\\_fed@kluniversity.in](mailto:chandu_fed@kluniversity.in)  
ORCID 0000-0002-8112-2442

**P. S. Brahmanandam**  
Department of Physics  
Shri Vishnu Engineering  
College for Women (A)  
Vishnupur, Bhimavaram-  
534202  
Andhra Pradesh, India.  
[dranandpotula@svecw.edu.in](mailto:dranandpotula@svecw.edu.in)  
ORCID 0000-0001-9777-3496

**M. S. R. Murthy**  
Department of mathematics  
Vishnu Institute of Technology  
(A)  
Vishnupur, Bhimavaram-  
534202  
Andhra Pradesh  
India.  
[murthy.m@vishnu.edu.in](mailto:murthy.m@vishnu.edu.in)  
ORCID 0000-0001-6301-0554



## HIGH ACCURACY CLASSIFICATION OF PARKINSON'S DISEASE DETECTION USING RNN-GRAPH-LSTM

Phaneendra Varma Ch<sup>1</sup>

Gurujukota Ramesh Babu

Pokkuluri Kiran Sree

Padma Bellapukonda

K. Satish Kumar

Ch.Venkata Ramana

Keywords:

Parkinson's Disease, Dimensionality Reduction, Recurrent Neural Network

### A B S T R A C T

*Parkinson's disease is a progressive disorder that affects the nervous system and the parts of the body controlled by the nerves. In order to begin neuro protective treatments and effectively manage Parkinson's disease (PD), early detection is essential. In clinical use, the rapid finger tap test is commonly used to detect dyskinesias in Parkinson's disease, while physicians depending on their clinical expertise utilizing the PD uniform grading scale, swiftly evaluate the symptoms. This PD might be identified before physical symptoms appeared if Parkinson's patient's voices were monitored for improvements. In PD datasets, with non-overlapping samples, both the onset and offset of the energy content (voiced to unvoiced) were changed, dynamic feature evaluation was performed using 10-fold cross-validation. The accuracy, precision, and recall of the Recurrent neural network (RNN-GLSTM) smart PD detection approach has been statistically tested using persistent phonations, as well as the Matthew correlation coefficients. According to the analysis, effective and promising methods for collecting differentiating characteristics include shape analysis and surface fitting to create diagnostic models that might possibly support physicians in the diagnosis process. Accuracy, Precision, F1-Score, Recall are used parameters for performance analysis.*

© 202x Published by Faculty of Engineering



### 1. INTRODUCTION

The human brain's nerve cells are impacted by Parkinson's disease (PD), a neurodegenerative condition. It is a neurodegenerative ailment that affects the nerve cells in the human brain. 15% of occurrences of PD occur in people under the age of 50, while most individuals are diagnosed at 70 or above. There are two types of PD disease symptoms: motor and non-motor.

Stiffness, slowness of motion, tremor, and some of the motor indications of Parkinson's disease include postural instability. Emotional problems, cognitive impairment, pain, sensory dysfunction, and this dysautonomia are one of the Parkinson's disease non-motor symptoms (Rana et al., 2015). The majority of PD patients have these two motor symptoms. In 90% of the cases (Naranjo et al., 2016) the PD detection approach based on phonation may detect vocal

<sup>1</sup> Corresponding author: Phaneendra Varma Ch  
Email: [chpvarmacse@svecw.edu.in](mailto:chpvarmacse@svecw.edu.in)

variations. As a result, one of the earliest symptoms that might not be apparent to listeners is voice abnormalities as expressed through speech signals. Some of the symptoms of PD vocal dysfunction include decreased tongue flexibility, decreased vocal loudness, longer pauses, articulation rate, a narrowing and fluctuating pitch range, and voice intensity level. Many investigations propose acoustic examination to be a non-invasive methodology for diagnosing Parkinson's diseases. In addition, numerous specialists use discourse and phonation information (Ali et al., 2019) to early analyze Parkinson's infection. It is challenging to make a Parkinson's disease diagnosis. It is diagnosed through expensive clinical evaluations and brain scans, which can sometimes produce inaccurate results.

A frequent neurodegenerative ailment that affects more than 1% of people over 50 and whose frequency is rising annually is Parkinson's disease (PD). The muscular stiffness, tremor, postural instability, bradykinesia (slowness of movement), when dopaminergic neurons in the substantia nigra pars compacta of the basal ganglia die, it results in Parkinson's disease (PD), it is characterized by dysphonia (speech problems). The conventional diagnosis is often based on these clinical motor signs as well as non-motor symptoms. Recent developments in neuroscience have made new technologies, such Electroencephalography (EEG), potentially implement for the identification of PD. High temporal resolution and accessibility setup are advantages of EEG-based diagnostics. On the other hand, traditional diagnosis depending on manual analysis, making it impossible to apply to a significant quantity of data. The automatic analysis of EEG data is now possible because to improvements in categorization.

The quality of life those who have PD, the incidence of the second most common neurological disorder have dramatically decreased. The condition is progressive and has a wide spectrum of motor and non-motor symptoms that make it distinctive. All available therapy options right now concentrate on symptomatic relief. The only foundation for diagnosing PD is clinical criteria because no conclusive tests are available. Cardinal Clinically defined symptoms include bradykinesia, rigidity, and tremor at comfortable. The clinical diagnosis frequently occurs when these symptoms first appear in the latter stages and are associated with a drop in Dopamine (DA) concentrations of 60–80% and 40–50% cell body degeneration in the Substantia Nigra pars compacta (SNc). Since PD progresses in a non-linear course and in the early stages, early detection is essential. Effective care of PD also depends on early and precise identification of the condition. Finding PD progression indicators that can help with early illness identification is the main goal of this analysis.

The examination of the dopaminergic systems in the human brain using single photon emission computed tomography (SPECT) is growing in popularity. Showing a decline in the dopaminergic transporter (DAT) even in the early stages of the illness, the ability of SPECT to distinguish between people with PD and healthy normal people has been demonstrated. In the SPECT scans, this loss changes the striatal dopaminergic activity pattern. In medical environments, SPECT examines as often as possible externally assessed. The value of the striatal binding ratio (SBR) can be determined by analyzing SPECT images region-based analysis. It measures striatal activity and is frequently used for therapeutic purposes in questionable or unreliable circumstances (Staff et al., 2009). In the field of PD detection, a relatively new and popular method for feature extraction and pattern identification is image analysis. In clinical practice, it is common to interpret SPECT images visually or using Region-of-Interest (ROI) analysis. Voxel-based analysis has also been used by researchers, and voxel clusters that have a noticeably reduced uptake are discovered. However, visual analysis depends much on the observer's evaluation, which is strongly influenced by skill and knowledge. The striatum is the target area and when applying ROI techniques, the occipital cortex is utilized as the reference area. The striatal uptake ratio is generated with background eliminated as a quantitative measurement.

The researchers have been experimenting with numerous ways to quantify dyskinesia in Parkinson's patients, including finger tapping, recurring eye-hand movement, and frozen gait, so that Parkinson's patients may be recognized and their motor function can be carefully assessed. Finger tapping is often used in clinical practice, particularly for the assessment of PD. The following are the causes: An important indicator the brain functions is the rhythm of finger movement. The capacity of people to tap their fingers is measured, which is a crucial way for assessing the health of the neuromuscular system. Additionally, there is a significant relationship between the Parkinson's disease motor task of tapping one's fingers and dopamine receptors. The amplitude, rhythm, the patient's symptoms and motor skills have an impact on the helpful, format, and pace of the finger tapping. Clinical tools like rating scales for assessing the severity of the illness's other symptoms and motor symptoms have been developed in recent years. The movement problem Parkinson's disease (PD) progresses over time. There is no recognized cause for PD, no long-term therapy, and few available treatments. Dopamine, a neurotransmitter that regulates movement and coordination, this is produced less frequently in PD, which leads to the condition. Worldwide, 53 million individuals were impacted by PD in 2013. Both non-motor and motor symptoms are present in PD.

A more generalized neural network model delivers correct analysis results while using training and testing data from the training phase. Utilizing a recurrent neural network with long short-term memory, the input data is learnt, which uses memory chunks to store the input data. This analysis demonstrates how feature extraction, parameter representation, and classifier modification all impacted accurately, effectively, and consistently a model performs. The following is the paper's main contribution: A deep learning model for early diagnosis of PD that uses static and dynamic characteristics. The input feature values are scaled using a preprocessing technique known as min-max normalization to fit within a range. The data will be transformed into low dimensional space using a dimensionality reduction technique based on linear discriminant analysis to provide the most relevant low dimensional space. For the purpose of PD detection, the dynamic characteristics of voice signals are used in the RNN-Graph LSTM classification model. In order to standardize the output of the hidden layers, the presented RNN-GLSTM has been applied following each batch normalization layer. The presented models are tested using a dataset of speech signals, and the quantitative results are contrasted with those obtained using the traditional PD detection approach. There are generalization capabilities in the proposed model that have not been found in previous research. This model may also be used to predict PD early on with less complexity.

Following are the remaining parts are organized: The Literature Survey is explained in section II, and in this Section III describes high accuracy classification of Parkinson's disease detection using RNN-GRAFH-LSTM. The analysis of the experimental results is presented in Section IV, and Section V brings the work to a close.

## 2. LITERATURE SURVEY

Other time-series classification using recurrent neural network have recently been introduced. An RNN-GLSTM was introduced for a spatiotemporal sequence forecasting problem in which both the input and the prediction target are spatiotemporal sequences. This RNN-GLSTM model was constructed by extending the fully connected LSTM to have convolutional structures in the input-to-state and state-to-state transitions. The RNN-GLSTM was reported to perform better than the fully connected deep neural network (DNN) by being able to capture the spatiotemporal correlations of the sequential data for precipitation now casting. A multi-scale convolutional neural network, which extracts deep-learning features at different scales and frequencies from three representations of time series, including the original, down-sampled, and smoothed data, was reported be capable of extracting effective features for time series classification (Shi et al., 2019).

Each finger joint's three-dimensional (3D) motion characteristics were extracted using the discrete wavelet transform (DWT). However, the intensity of every finger connected tremor has been determined by counting the number of durations the user's camera detects a change in movement, as well as the way the line of sight is preserved. Utilizing camera detection will violate people's privacy, it must be acknowledged. In recent years, researchers have become interested in wireless sensing technologies based on channel observation. The researchers discovered that environmental changes can be sensed and recognized by wireless signals (Pang, 2020).

To detect Parkinson's disease patients, researchers described a multilayer perceptron using an SVM-based classifier. Multilayer Perceptron (MLP's) exclusive cost functions assigned the appropriate characteristics, which include both accuracy and Area under the curve (AUC) score. With the score value, MLP extracts the 20 most significant and relevant characteristics. When compared to the algorithms, this proposed model produced accuracy. PD classification using a hybrid preprocessing method. In order to preprocess the dataset and reduce the variability, it was suggested to use Subtractive clustering features weighting (SCFW). They preserved the Kernel-based extreme learning machine's (KELM) precision, sensitivity, and specificity, as well as the significance of the Kappa statistic and the receiver operating characteristic (ROC) curve (Parisi et al., 2018).

Explains the layered auto encoder used in the Dynamic neural network (DNN) classifier for PD detection to extract the voice characteristics. This paper compares DNN-based PD prediction to conventional Machine learning (ML) models and finds that it secures good accuracy. Additionally, DNN requires more data during the training phase, and searching the parameter area is required additional training time. They gathered data using accelerometer and electromyography signals and proposed that the severity of motor neuron disorder can be recognized using data mining and artificial intelligence techniques (Caliskan et al., 2017).

In order to extract voice information, Convolutional Neural Network (CNN) has used both the wavelet transform and the short time Fourier transform. Using dilated convolution layers to simulate long-distance contextual input presents CNN with the greatest difficulty. Recurrent neural networks (RNNs), which are capable of simulating distant contextual input while maintaining prior computations, this provides a solution to this issue. However, RNN-based methods have a gradient problem and are difficult to tune the network layer settings. This problem has been solved using LSTM. In this analysis, for PD detection, it is suggested to utilize an RNN-trained LSTM with graph structure. The LSTM optimizer, which is based on different speech characteristics, increases the classification's

accuracy. The RNN-GLSTM can handle bigger datasets without increasing model size. Because it learns long-term dependencies that advance to the subsequent layers and follow the preceding time period, GLSTM is more successful than typical time series models. Additionally, the methods of feature extraction and preprocessing are utilized in this proposed model. By using factors that make PD prediction accuracy less accurate since standard Neural Network (NN) utilizes a feed forward layer, it deals with the limitations of earlier techniques like the small dataset size. The accuracy of PD prediction is increased by the forward and backward loop networks utilized in RNN-GLSTM (Vasquez et al., 2010).

Provides a magnetic force-based method for determining the severity of finger taps. A magnetometer was connected to the subject's thumb and fingers. During the finger tapping task, distance, speed, acceleration, and finger movement interval are all sent out by the system. They proposed a predictive model for Alzheimer Disease (AD), through the diagnosis of brain abnormalities, using Electroencephalography (EEG), a non-invasive and repeatable technique. To support the medical doctors in the correct diagnosis, they achieved an automatic patient's classification from the EEG biomedical signals involved in AD and Mild Cognitive Impairment (MCI). Using time frequency transforms for pre-processing of EEG signals, the authors subsequently applied classification using machine learning (Yuko Sano, 2016).

The patient's finger tapping was captured on video by a camera. To monitor moving fingers, they utilize computer vision techniques. The speed, amplitude, and rhythm of finger taps are evaluated using various characteristics taken from the time series. They discussed the importance of non-motor systems over motor systems for the prediction of PD. The study was conducted around olfactory loss, sleep behavior distortion and rapid eye movement. The machine learning techniques, like Boosted Logistic Regression, Random Forest, Bayes Net and Multilayer Perceptron were used for prediction of PD. (Khan et al., 2014).

Utilizing speech data samples, C-means fuzzy clustering and pattern-based techniques were used to attempt to distinguish between healthy controls and PD patients. Both positive and negative predicted outcomes were accurate for them. A comparative analysis has been done by them, which indicates, that unlike conventional Neural Networks, extreme learning machines (ELM) does not require repetitive changes of hidden neurons. The simple architecture makes ELM a reliable choice than others for prediction (Rustempasic et al., 2013).

It is described to utilize a Support vector machine (SVM) classifier with a Relief-F feature selection model. Out of a total of 22, this method chose 10 characteristics. Relief-F feature selection accuracy is

demonstrated by an SVM classifier with 10-fold cross validations. The experimental dataset has 195 voice samples. Noise intrusion is a problem for Relief-based algorithms (RBA) when using nearest neighbor. They suggested PD detection using nonlinear SVM and Principal component analysis (PCA). PD classification accuracy was achieved by this model. The experiment's limited dataset lacked lower prediction precision (Bouchikhi et al., 2013).

Utilizing a wrapper feature selection strategy classify. Based on the use of 5 distinct categorization algorithms, the paper achieved accuracy. A wide range of speech processing techniques were used (dysphonia measurements), to precisely distinguish PD patients from healthy controls. They also found that RNN-GLSTM is a better technique with an overall accuracy, in comparison to other ML approaches such as bagging, random forest, support vector machines (Tsanas et al., 2012).

PD cases and healthy controls were accurately distinguished using speech data samples from thirty-one participants (23 with PD). There are no attempts to distinguish PD from other neurological illnesses in any of the papers mentioned above, just to differentiate PD patients from healthy controls using various classification strategies. They observed that the best feature for the prediction of Parkinson's disease is a fundamental frequency among all voice recording features (Yadav et al., 2011).

Singular value decomposition (SVD) was used to identify the crucial voxels, and then Naive Bayes (NB) was used to determine whether or not the participants had Parkinsonian Syndrome (PS). Implementing data from the striatum's voxels, it was possible to distinguish between normal controls and PS. Principal component analysis (PCA) was implemented by the classification, and followed by the SVM. For classification, SVM classifier was also utilized. However, through the importance of smoothing image data sets and warping images to a template image, the voxel-based method is neither proposed nor verified in normal clinical settings (Towey et al., 2011).

The work demonstrated by analyzing neurons in the brain in order to diagnose Parkinson's disease. Furthermore, many acoustic tests articulatory and respiratory increased the voice problems that characterize PD. In other words, a Parkinson's disease patient has a reduced vocal quality, poor articulation, and stress in his voice and speech. To support the medical doctors in the correct diagnosis, they achieved an automatic patient's classification from the EEG biomedical signals involved in Alzheimer Disease (AD) and Mild Cognitive Impairment (MCI). Using time frequency transforms for pre-processing of EEG signals, the authors subsequently applied classification using machine learning (Joan et al., 2010).

In order to distinguish between healthy controls and PD patients using video recordings and computer vision, the author of the research presented a PCA-LDA method. They observed that the best feature for the prediction of Parkinson's disease is a fundamental frequency among all voice recording features. They tested a number of machine learning methods on Microsoft azure machine learning platform and found that the best score is given by two-class Boosted decision trees (Cho et al., 2009).

The optimal parameter is discovered to be the opening and closing speed. These investigations extract time domain parameters including the frequency of finger tapings, the duration of pauses, and the number of prevents, and so on. The Long short-term memory with recursive feature elimination gave the highest accuracy. The present paper attempts to find the best prediction model which distinguishes a PD patient from a healthy patient. Thirteen machine learning based predictive models have been investigated on a dataset comprising biomedical voice measurements (Yokoe et al., 2009).

### 3. HIGH ACCURACY CLASSIFICATION OF PARKINSON'S DISEASE DETECTION USING RNN-GRAFH-LSTM

High accuracy classification Of Parkinson's Disease Detection Using RNN-GRAFH-LSTM is presented in this paper. Fig.1 Shows the Architecture of the RNN - LSTM

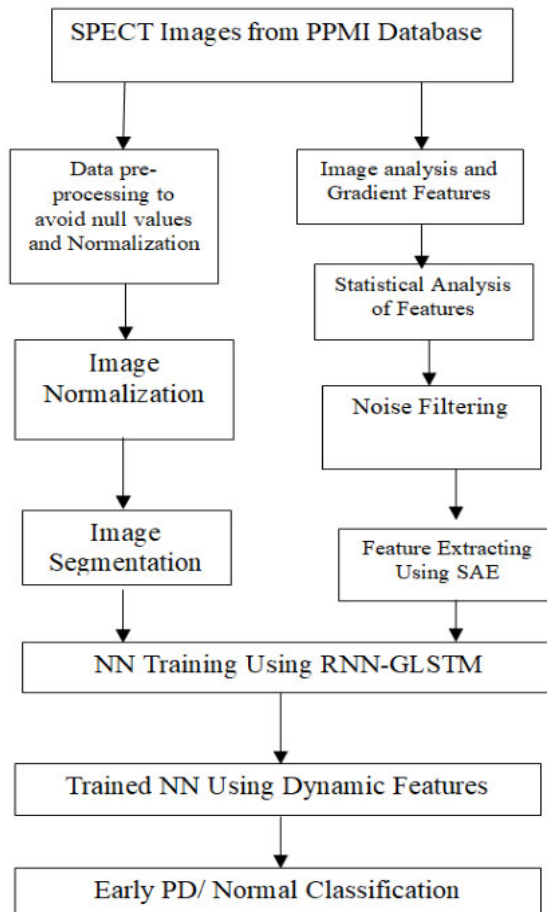


**Figure1.** Shows the Architecture of the RNN –LSTM. The Parkinson's progression markers initiative (PPMI) database provided the information utilised in the creation of this article. In order to find PD progression biomarkers, PPMI is a significant, sizable, multicenter, multinational investigation. Utilising database information, they make use of the subject's screening visit's SPECT imaging data. Before becoming made available to the public through the database, pre-processing is applied to all SPECT scan data collected at PPMI resources. By spatially normalising all scans, this pre-processing makes sure that they are all in the same anatomical alignment. At the PPMI locations, the SPECT scans are processed initially, using phantoms taken on the same day as the scan to combine raw projection data reconstruction with attenuation correction. In order to maintain uniformity in orientation, they additionally spatially normalize the images. The 91 axial slices are provided by PPMI database (all the way down to the bottom) for each scan. They select the intensity normalized slice for further investigation since it clearly indicated striatal activity.

#### 3.1 HIGH ACCURACY CLASSIFICATION OF PARKINSON'S DISEASE DETECTION USING SEGMENTATUION AND NORMALIZATION PROCESSES

Following segmentation and quantification using shape-based characteristics, they analyze the high activity areas. In order to segment the image, a threshold in the range was used to transform the image to a binary image. By minimizing the subject's identity, the threshold is experimentally selected by

tracking which value segments the high activity zones most effectively. Following segmentation, the borders of these areas were determined using the more precise Canny edge detection approach. A professional neurologist and radiologist visually inspected the striatum's limits. Figure 1 shows SPECT slices from a person with early-stage Parkinson's disease and a healthy, normal person, as well as the identified border of the segmented sections.

Normalization is used to eliminate null values from voice speech signals. This model is built using a training database. Testing database has been used to determine whether the suggested model is generalizable. A technique for reducing the dimensions of a high-dimensional data space, dimensionality reduction is a technique that improves the performance of classification systems. To increase the classifier's accuracy, a process called feature extraction is used to pick out relevant features from a feature collection. There are various approaches to dimensionality reduction and feature extraction. In order to extract features and minimize dimensionality, this analysis makes use of the sparse auto encoder (SAE) and Linear discriminant analysis (LDA). In the sections, each of these approaches is discussed. Raw data are inconsistent because they have many errors and null values. The pre-processing stage will enhance the outcomes by converting this raw data into a comprehensible manner. Good classification results are produced by good preprocessing techniques. In EQ (1), the min-max normalization procedure for the data set D is indicated. Following standardization, the characteristics are between [0, 1].

$$D_{normalization} = \frac{D - D_{min}}{D_{max} - D_{min}} \dots (1)$$

A mean image is created for a topic after each slice is normalised to the range [0, 1]. Once more, [0, 1] is used to normalise this image. In the following stage, the high uptake areas that correlate to the dopaminergic activity are extracted through picture segmentation. This is achieved by a threshold-based binary image transformation. Depending on empirical difficulties (by thoroughly examining the accuracy of the segmented sections), the threshold was extensively selected for each image. There is further information on threshold selection. Then, they carry out two different types of analysis: surface fitting and quantifying these areas by shape analysis. They are explained as follows. Visually, it is seen that the high activity area's form changes from

"dot" to "comma". It is also common to see asymmetry between the uptake areas in the two hemispheres.

Using a number of shape-based features, they quantify these uptake regions in this paper. These comprise the area, the major and minor axes lengths, aspect ratio, equivalent diameter, orientation, eccentricity, and roundness. Additionally, they include the area Asymmetry Index (AI), the other axis characteristics are direction, equivalent diameter, roundness, aspect ratio, and eccentricity. The supplemental document's Table I has an explanation of these characteristics. While the left side region is retained for the purpose of computing these characteristics, the region on the right side, which is rotated from right to left, represented as a point of reference.

In the segmented region, the intensity distribution is used to fit a polynomial surface. Since higher orders might result in over-fitting, they decide to use the polynomial cubic model for surface fitting. Given by this is the cubic model.

$$\begin{aligned} F(x, y) = & p_{00} + p_{10}x + p_{01}y + p_{20}x^2 \\ & + p_{11}xy + p_{02}y^2 + p_{30}x^3 \\ & + p_{12}xy^2 + p_{11}x^2y \\ & + p_{03}y^3 \dots \dots (2) \end{aligned}$$

The model coefficients are established using the linear least-squares method, which minimizes the sum of the squares of residuals (or errors). The coordinates of the pixels in the segmented region  $\{xi, yi; i=1, 2...n\}$  are normalized by centering at a mean of zero and scaling to one standard deviations. The theoretical fit is unaffected by this modification, but it resolves any scaling concerns and enhances the results computer-based finite precision needs.

### 3.2 HIGH ACCURACY CLASSIFICATION OF PARKINSON'S DISEASE DETECTION BASED ON FEATURE EXTRACTION UTILIZING SAE MODEL

The collection of features is represented by radial feature vectors. Each striatum's border pixels are sampled at equal angles of 45°, as shown in Table 1 (assuming the horizontal axis is at zero and angles are measured clockwise). For each striatum, this provides eight sampled points ranging from 0 to 360°. Therefore, all computations are made with reference to the left striatum, on its vertical inverted side, the right striatum is being sampled. These sampling locations radial distances from the various striata centroids were calculated, as shown in fig. 2(a). The feature vector is created by averaging the radius of all the sampled points in the left and right striatums with respect to one another.

**Table1.** Set of Radial Features Corresponding to Angles

	0°	45°	90°	135°	180°	225°	270°	360°
R ad ial 1	Ra dial 2	Ra dial 3	Radi al 4	Radi al 5	Radi al 6	Radial 7	Radi al 8	

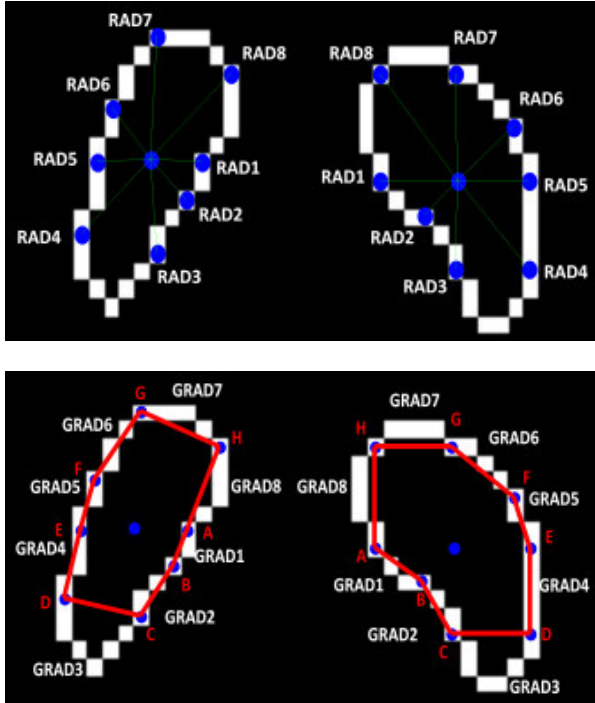


**Figure 2.** (a) Rad1 through Rad8 is the radii of the first eight sampled sites with respect to the centroid. (b) Grad1 to Grad8 is the gradients of the segments that connect the sampled sites.

There are several abnormal events that are definitely not produced by human motion and given the impact of environmental noise, hardware, and protocol requirements on the signal continuity. As a result, it should be screened before being detected by humans. Despite the removal of several apparent outliers, the finger tapping waveform still contains high-frequency noises. It is challenging to extract a number of properties from continuous and periodic signal waveforms, due to the existence of noise, with peaks and peak-to-peak values included. The finger tapping waveform is smoothed in this study using the local weighted regression method to provide the filtering effect. Similar to the moving average approach, the smoothing process is regarded as local, thus nearby data points that are separated by intervals decide each smoothing value. In order to build this method uses a regression weight function for the span of the data points.

A feature extraction technique based on an unsupervised deep neural network called sparse auto encoder (SAE), uses a single hidden layer to encrypt the input data. The error is also estimated and the necessary features are

extracted using hidden layer expressions. There are various functional issues with Auto encoder. Inputting and copying memory into AE's implicit layer don't help it in discovering features. This problem is addressed by the sparsity-based auto encoder that is provided. Eq. (3) denotes sparsity regularization or SAE.

$$\text{Sparsity regularization} \sum_{j=1}^{u^2} kL(\rho \parallel \rho^J) \dots \dots \dots \quad (3)$$

Where  $\rho$ -sparsity parameter, jth hidden node of the  $\rho^J$ -activation function, and KL-Kull Back-Libeler (KL) divergences are all used.

### 3.3 HIGH ACCURACY CLASSIFICATION OF PARKINSON'S DISEASE DETECTION UTILIZING NN BASED RNN-GLSTM TECHNIQUE

An internal memory-equipped version of a feed-forward neural network (NN) is called a Recurrent Neural Network (RNN). The RNN's output is based on earlier calculation and is returned to the recurrent network. The input series are performed on a decision is made by the RNN using internal memory. Back propagation is the training method used for long short-term memory (LSTM). Three gates, including input, forget, and output gates, create an LSTM. To choose the input values that change the memory, input gates utilize sigmoid activation functions. The forget gate is in charge of deciding which details from the previous state should be deleted, while the output gate is in charge of controlling the output. In contrast to regular LSTM, each tree node is represented by graph LSTM as a distinct LSTM unit. This model has seven layers, including an output layer and five hidden layers. An input layer made up of LSTM cells makes up a recurrent neural network. Every LSTM layer's input layer reflects the speech signals' Phonation features (PF).

To compare their performance, two classifiers are used: linear and radial basis function (RBF) kernels, and linear discriminant analysis (LDA). On relevant characteristics, LDA is utilized with 5-fold cross-validations. The accuracy value obtained from this 5-fold cross-validation is given in table.2 as the average of the accuracy values obtained after 100 iterations. Each parameter was optimized by examining a wide range of values. It was decided to use the conditions that produced the maximum accuracy.

## 4. RESULT ANALYSIS

High accuracy classification of Parkinson's Disease detection using RNN-GRAPH-LSTM is presented in this paper. This analysis explains the validation and evaluation measures that were utilised, as well as the

outcomes that were obtained. To demonstrate the effectiveness of the suggested PD diagnosis model, when compared to current ML algorithms, the performance of the suggested system is equivalent. In the experiment, the multilayer perceptron (MLP) is compared against the principal component analysis (PCA), support vector machine (SVM), random forest (RF), and K-nearest neighbour (KNN) with traditional machine learning (ML) approaches. In accordance to the confusion matrix provided in Table 2, accuracy, precision, recall, and the F1 score have all been used as evaluation metrics to assess the proposed RNN-GLSTM model's output.

**Accuracy:** Here, the accuracy indicates how well the model detects the PD subsequently is described as being equal to the number of successfully identified instances divided by the total number of instances, and it is presented as

$$Accuracy = \frac{TP + TN}{TP + FP + TN + FN} \quad (4)$$

**Recall:** Types of correct Parkinson 's classification is indicated by recall.

$$Recall = \frac{TP}{(TP + FN)} \dots (5)$$

The recall and accuracy are weighted in the F1 score. Equation 6 below states that for the classification method to perform well, it must be one, and for it to perform insufficiently, it must be zero.

$$F1 - Score = 2 * \frac{Precision * Recall}{Precision + Recall} \dots (6)$$

**Precision:** Here, the precision indicates how well the model detects the PD. Subsequently this precision of a model indicates the percentage of data points that were genuinely meaningful. This implies that only pertinent instances are produced by classification models in accuracy, which is defined as

$$Precision = \frac{TP}{(TP + FP)} \times 100 \quad (7)$$

Parameters	DT	RF	SVM	PCA	RNN-GLSTM
Accuracy	66.78	73.78	85.89	90.67	99.45
Precision	70.67	75.67	80.58	84.67	94.56
Recall	68.45	70.99	77.67	86.56	96.78
F1-Score	68.67	73.67	75.89	88.78	90.57

The accuracy comparison between the given RNN-GLSTM strategy and the DT, RF, SVM, and PCA-based approaches is shown in Fig. 3.

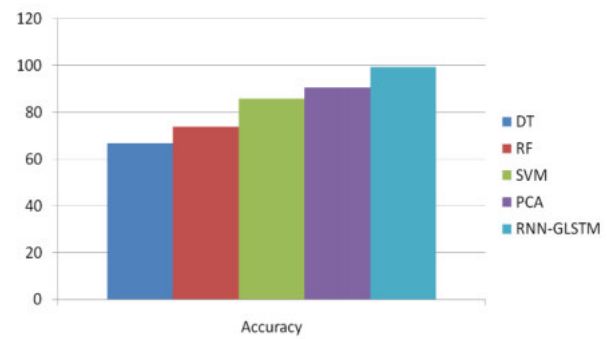


**Figure 3: Accuracy Comparison Graph**

The precision comparison between the given RNN-GLSTM strategy and the DT, RF, SVM, and PCA-based approaches is shown in Fig. 4.

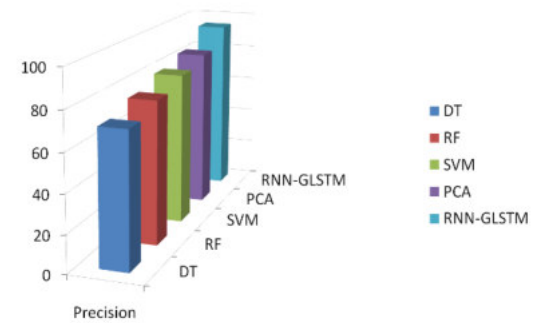


**Figure 4: Precision Comparison Graph**

The recall comparison between the proposed RNN-GLSTM strategy and the DT, PCA, RF, and SVM-based approaches is shown in Fig. 5.

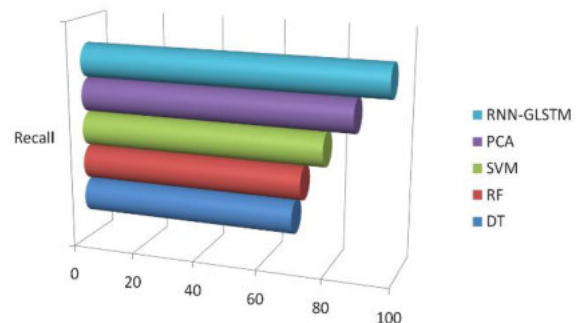


**Figure 5: Recall Comparison Graph**

The F1-Score comparison between the given RNN-GLSTM approach and the DT, SVM, RF, and PCA-based approaches is shown in Fig. 6.

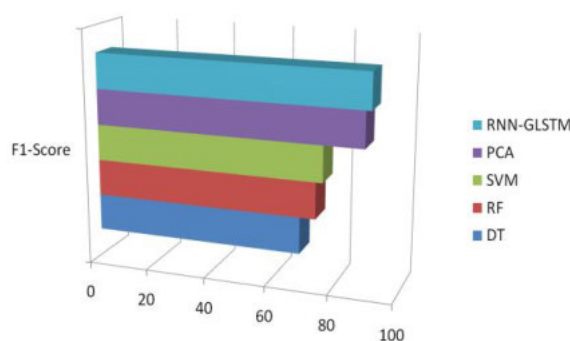


**Figure 6: F1-Score Comparison Graph**

## 5. CONCLUSION

High accuracy classification of Parkinson's disease detection using RNN-GRAFH-LSTM is presented in this paper. In this analysis, an-optimized LSTM-based recurrent neural network was reported as an efficient PD diagnostic model. With the help of min-max normalization, this suggested model scaled data values in the [0,1] range. Dimensionality reduction using LDA was used to reduce the dataset's dimensions, and feature extraction using SAE was used to take the most important characteristics into account. In this analysis, they compute distinguishing characteristics by analyzing SPECT images of early PD, SWEDD, and

healthy normal persons using surface fitting and shape analysis. They observe a substantial difference between scans with a dopaminergic deficiency and scans without in the calculated surface fitting-based and shape-based characteristics. In this analysis, dynamic aspects were taken into consideration when using a dataset of PD speech signals. Multiple assessments on the lowering of dimensionality, the methods for extracting highlights were recorded, and the models were evaluated using several indicators for evaluation. These features were used to create highly accurate classification models. Additional characteristics will be evaluated for classification in the future, and this model will be investigated through use in multi-label classification with additional RNN-GLSTM-based architecture. Proposed model performs efficiently as provided effective test prediction. Compared to other based architectures, the presented RNN-GRAFH-LSTM architecture has better performance in terms of accuracy, precision, recall, F1-score.

## References:

- Ali, L., Zhu, C., Zhou, M., & Liu, Y. (2019). Early diagnosis of Parkinson's disease from multiple voice recordings by simultaneous sample and feature selection. *Expert Systems with Applications*, 137, 22–28. doi:10.32604/cmc.2022.024596.
- Bouchikhi, S., Boublenza, A., Benosman, A., & Chikh, M. (2013). Parkinson's disease detection with SVM classifier and relief-F features selection algorithm. *South East European Journal of Soft Computing*, 2(1), 1–4. doi:10.32604/cmc.2022.024596.
- Caliskan, A., Badem, H., Basturk, A., & Yuksel, E. M. (2017). Diagnosis of the Parkinson disease by using deep Neural network classifier. *IU-Journal of Electrical & Electronics Engineering*, 17(2), 3311–3318. doi:10.32604/cmc.2022.024596.
- Cho, C. W., Chao, W. H., Lin, S. H., & Chen, Y. Y. (2016). A vision-based analysis system for gait recognition in patients with Parkinson's disease. *Expert Systems with applications*, 7033- 7039. <https://sci-hub.st/10.1109/inventive.2016.7824836>.
- Guan, Y. (2021). Application of logistic regression algorithm in the diagnosis of expression disorder in Parkinson's disease. *IEEE 2nd International Conference on Information Technology, Big Data and Artificial Intelligence (ICIBA)*, Chongqing, China, 1117-1120, doi: 10.1109/ICIBA52610.2021.9688135.
- Hussain, A., & Sharma, A. (2022). Machine Learning Techniques for Voice-based Early Detection of Parkinson's Disease. *2nd International Conference on Advance Computing and Innovative Technologies in Engineering (ICACITE)*, Greater Noida, India, 1436-1439. doi: 10.1109/ICACITE53722.2022.9823467.
- Joan, J., Tara, M., Whitehill, L., & So, S. (2010). Intonation Contrast in Cantonese Speakers with Hypokinetic Dysarthria Associated with Parkinson's disease. *J Speech Lang Hear Res*, 53, 836- 849. doi:

10.1109/eitech.2016.7519634.

- Khan, T., Nyholm, D., Westin, J., & Dougherty, M. J. A. I. I. M. (2014). A computer vision framework for finger-tapping evaluation in Parkinson's disease. *Artificial Intelligence in Medicine*, 60(1), 27-40, <https://doi.org/10.1109/jsen.2020.3032558>.
- Moustafa, H. K., Metawie, H., Saadoun, S., Sameh, N., Ibrahim, R., & Abdelsayed, A. (2023). Easy Park: Mobile Application for Parkinson's Disease Detection and Severity Level. *International Mobile, Intelligent, and Ubiquitous Computing Conference (MIUCC)*, Cairo, Egypt, 1-8. doi: 10.1109/MIUCC58832.2023.10278311.
- Naghavi, N., & Wade, E. (2022). Towards Real-Time Prediction of Freezing of Gait in Patients with Parkinson's Disease: A Novel Deep One-Class Classifier. *IEEE Journal of Biomedical and Health Informatics*, 26(4), 1726-1736. doi: 10.1109/JBHI.2021.3103071.
- Naranjo, L., Perez, J. C., Campos Roca, Y., & Martin, J. (2016). Addressing voice recording replications for Parkinson's disease detection. *Expert Systems with Applications*, 46, 286–292. doi:10.32604/cmc.2022.024596.
- Pang, Y. (2020). Automatic detection and quantification of hand movements toward development of an objective assessment of tremor and bradykinesia in Parkinson's disease. *Journal of Neuroscience Methods*, 333, 108576, <https://doi.org/https://sci-hub.st/10.1109/jsen.2020.3032558>
- Parisi, L., Ravi Chandran, N., & Manaog, L. M. (2018). Feature-driven machine learning to improve early diagnosis of Parkinson's disease. *Expert Systems with Applications*, 110, 182–190. doi:10.32604/cmc.2022.024596.
- Rana, Q. A., Ahmed, S. U., Chaudry, M. Z., & Vasan, S. (2015). Parkinson's disease: A review of non-motor symptoms. *Expert Review of Neurotherapeutics*, 15(5), 549–562. doi:10.32604/cmc.2022.024596.
- Ramírez, M. V., Kmetzsch, V., Forbes, F., & Dojat, M. (2020). Deep Learning Models to Study the Early Stages of Parkinson's Disease. *IEEE 17th International Symposium on Biomedical Imaging (ISBI)*, Iowa City, IA, USA, 1534-1537, doi: 10.1109/ISBI45749.2020.9098529.
- Reddy, H., & Kanchana, M. (2022). Artificial Intelligence towards Parkinson's disease Diagnosis: A systematic Review of Contemporary Literature. *4th International Conference on Cybernetics, Cognition and Machine Learning Applications (ICCCMLA)*, Goa, India, 31-37. doi: 10.1109/ICCCMLA56841.2022.9988755.
- Reddy, K. B., & Delen, D. (2018). Predicting hospital readmission for lupus patients: An RNN-LSTM-based deep-learning methodology. *Computers in Biology and Medicine*, 101, 199–209. doi:10.32604/cmc.2022.024596.
- Rustempasic., Indira., Can, M. (2013). Diagnosis of Parkinsons Disease using Fuzzy C-Means Clustering and Pattern Recognition. *South East Europe Journal of Soft Computing*, 26(4), 1726-1736. <https://doi.org/https://sci-hub.st/10.1109/inventive.2016.7824836>
- Shi, J. X., Chen, R. Z., Wang, H., Yeung, Y. D., Wong, K. W., & Woo, C. W. (2019). RNN-G LSTM network: a machine learning approach for precipitation nowcasting. *28th Int. Conf. Neural Information Processing Systems*, Montreal, Canada, 6(6), 1306-1317, doi: 10.1109/JAS.2019.1911774.
- Staff, S.T., Ahearn, S. T., Wilson, K., Counsell, E. C., Taylor, K., Caslake, R., Davidson, E. J., Gemmell, G. H., & Murray, D. A. (2009). Shape analysis of  $^{123}\text{I}$ -N- $\omega$ - fluoropropyl-2- $\beta$ -carbomethoxy-3 $\beta$ -(4-iodophenyl) nor tropine single-photon emission Computed tomography images in the assessment of patients with parkinsonian syndromes. *Nuclear Medicine Communications*, 30, 194–201, doi: 10.1109/isbi.2015.7164031.
- Towey, J. D., Bain, G. P., & Nijran, S. K. (2011). Automatic classification of  $^{123}\text{I}$ -FP-CIT (DaTSCAN) SPECT images. *Nuclear medicine communications*, 32, 699-707. doi: 10.1109/isbi.2015.7164031.
- Tsanas, A., Little, M. A., McSharry, P. E., Spielman, J., Ramig, L. O. (2012). Novel speech signal processing algorithms for high accuracy classification of Parkinson's disease. *Biomedical Engineering, IEEE Transactions* 1264-1271, doi:10.1109/ACCESS.2020.2989032.
- Vasquez Correa, C. J., Orozco Arroyave, R. J., & Noth, E. (2017). Convolutional neural network to model articulation impairments in patients with Parkinson's disease. in *INTERSPEECH*, Stockholm, 314– 318.

doi:10.32604/cmc.2022.024596.

Yadav, G., Kumar, Y., Sahoo. (2011). Predication of Parkinson's disease using data mining methods: A comparative analysis of tree, statistical, and support vector machine classifiers. *Indian journal of medical sciences*, 231, <https://sci-hub.st/10.1109/inventive.2016.7824836>.

Yokoe, M., Okuno, R., Hamasaki, T., Kurachi, Y., Akazawa, K., & Sakoda, S. (2009). Opening velocity, a novel parameter, for finger tapping test in patients with Parkinson's disease. *Parkinsonism and Related Disorders*, 15(6), 440–444. doi: 10.1109/jsen.2020.3032558

Yuko, Sano. (2016). Quantifying Parkinson's disease finger-tapping severity by extracting and synthesizing finger motion properties. *Medical & Biological Engineering & Computing*, 54, (6), 1-13. Doi:10.1007/s11517-016-1467-z

---

**Phaneendra Varma Chintalapati**

Department of CSE  
Shri Vishnu Engineering College for  
Women (A)  
Bhimavaram, India.  
chpvarmacse@svecw.edu.in  
ORCID 0000-0001-7243-8974

**GuruJukota Ramesh Babu**

Department of CSE  
Shri Vishnu Engineering College for  
Women (A)  
Bhimavaram, India  
grameshcsse@svecw.edu.in  
ORCID 0000-0002-4655- 5496

**Pokkuluri Kiran Sree**

Department of CSE  
Shri Vishnu Engineering College for  
Women (A)  
Bhimavaram, India.  
hodcse@svecw.edu.in  
ORCID 0000-0001-8601-4304

---

**Padma Bellapukonda**

Dept of IT  
Shri Vishnu Engineering College for  
Women (A)  
Bhimavaram, India.  
padmabellapukonda@svecw.edu.in  
ORCID 0000-0002-1561-7463

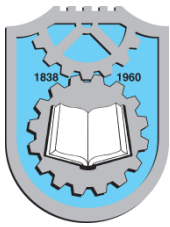
**Kode Satish Kumar**

Department of CSE  
Shri Vishnu Engineering College for  
Women (A)  
Bhimavaram, India.  
ksatishkumarcse@svecw.edu.in  
ORCID 0009-0004-3073-204X

**Chinthia Venkata Ramana**

Department of CSE  
Shri Vishnu Engineering College for  
Women (A)  
Bhimavaram, India.  
chvramanacse@svecw.edu.in  
ORCID 0009-0000-8558-5260

---



## A FIRST-TIME STUDY ON LONG-TERM PERFORMANCE ANALYSIS OF PHOTOVOLTAIC (PV) PLANTS AT BHIMAVARAM (LATITUDE- $16.54^{\circ}$ N, LONGITUDE- $81.52^{\circ}$ E, MSL 7 M), INDIA

K. Omkar

S. M. Padmaja

G. Anil Kumar

P. L. S. Pravallika

G. Durga Prasad

SSSR Sarathbabu Duvvuri

Keywords:

### ABSTRACT

Solar power plants, Polycrystalline Solar Cells, V-I Characteristics

*This study evaluates the daily, monthly, and annual performance of roof-top 200 KWp grid-interactive solar PV power plants installed atop Sri Vishnu Educational Society buildings in India. This plant generated ~ 300,000 units/year, with a maximum yielding of ~800 KWh/ day during summer (March-June) and a minimum during the rainy season (July-September, ~ 600 KWh/day). 1237 ton of CO<sub>2</sub> emissions were avoided and \$2,10,000 was made. As a result, the payback took 7-8 years to complete. The statistical study revealed a minimum (1%-15%) drop in power yielding, which indicates this plant used high-standard solar cells (polycrystalline), sophisticated inverters, top-quality molded case circuit breakers, and others. The optimal level of power output generation, V-I characteristics and power and economic graphs were predicted using a simulation study. Inter-institutional comparisons made with new 302.4 KWp power plants show an identical daily pattern, albeit 302.54 KWp power plant yieldings oftentimes show marginal magnitudes.*

© 202x Published by Faculty of Engineerin



### 1. INTRODUCTION

Abundantly available solar energy, long-lasting and clean energy is a most effective alternative to non-renewable sources such as coal, oil, and natural gas. Photovoltaic (PV) cells will be made of semiconductor materials that let solar energy (in the visible spectrum and partially in the ultraviolet and infrared spectrum) be converted into electricity. Ever since the development of PV technology took place in Bell labs of USA in the year 1954, various technological advancements and highly encouraging government policies over the years

have brought the prices of PV modules to affordable rates, and, hence, the production and utilization of solar energy have increased tremendously many folds even in under developing countries such as Kenya and Morocco (Abdullahi et al., 2017). On the flip side, solar power still only accounts for a mere 5% of capacity and 2.2% of electricity generation globally (Global Market Outlook for Solar Power, 2019-2023), which implies that still a lot of subsidiaries may be provided to encourage the effective usage of solar energy, and other appropriate measures need to be adopted. Secondly, proper quantification of output power generated from a PV power plant shall be done adequately to enhance the

<sup>1</sup> Corresponding author: P S Brahmanandam  
Email: [dranandpotula@svecw.edu.in](mailto:dranandpotula@svecw.edu.in)

belief of the end-users in this ever-increasing market, so that an adequate rise in investments would be possible.

The performance and energy produced by PV systems installed at any location are dictated by the prevailing environmental conditions and their technology (Makrides et al. 2009). Several research studies have been conducted on the power that is going to decline over time (degradation rate) (Jordan and Kurtz, 2013), cable losses, and others. It is estimated that only 76.2 % of solar power can be yielded at the output (at the electricity grid) even under extremely amicable conditions. Various losses contribute to the degradation rate including, shading losses (7 %), dust and dirt (2%), reflection (2.5%), spectral losses (1%), irradiation (1.5%), thermal losses (4.6%), array mismatch (0.7%), DC cable losses (1%), inverter (3%) and AC cable losses (0.5%), according to a study conducted by Ekici and Kopru (2017). Several studies have appeared in the literature that used high-end software to present simulation studies that enabled end-users to optimize the existing PV power plants (Kim et al, 2009; Maghami et al., 2016; Trembly et al. 2007; Arribas et al., 2010; Natsheh and Albarber, 2012).

The majority of PV cell manufacturers claim that their panels will produce 90% of the maximum power after 10 years, and 80% of the maximum power after 25 years. However, the ground reality is completely different in that most power plants, often, are unable to reach the expected levels, possibly due to various inherent and unexpected losses, wrong installations, and lack of proper cleaning methods, etc. In this context, proper knowledge of the performance of solar power plants will result in correct investment decisions, a better regulatory framework, and favorable government policies. Also, it is very much essential to monitor and evaluate the performance of a power plant that would improve the overall operation and reliability. It is known that solar PV plant generation depends on the availability of input solar radiation and ambient temperature (Dondariya et al. 2018).

In this research, we carry out a statistical analysis of power yielded out of three solar plants (total capacity is 200.0 KWp) established in December 2013 atop different academic buildings of the Shri Vishnu Educational Society (SVES) campus, Bhimavaram, Andhra Pradesh state, India. This study, therefore, presents and evaluates these three power plants' performance over the last five and a half years. Particularly, as the 200 KWp power plants were commissioned in December 2013, this present study could be the first attempt to present such long-term yielding data from the Indian region to the best of the authors' knowledge. The performance of the present power plants will be analyzed based on daily, monthly, and yearly databases and a comparison will be made with inter-institutional plants (of 302.4 KWp) to

understand the yielding capacity of the 200 KWp power plants over the five and a half year period.

## 2. SOLAR POWER PLANTS IN SVES CAMPUSES, INDIA

Under the auspicious of SVES, several academic institutions were established in Bhimavaram, India over the years including, Shri Vishnu Engineering College for Women (SVECW), Vishnu Institute of Technology (VIT), Vishnu Dental College (VDC), Shri Vishnu College of Pharmacy (SVCP), Vishnu School, Smt. Seetha Polytechnic College (SBSP), and B V Raju Institute of Computer Education (BVRICE). Initially, solar panels were installed atop VIT (100 KWp), VDC (50 KWp), and BVRICE (50 KWp) blocks in December 2013. Figure 1 depicts the 100 KWp solar power plant located atop VIT, Bhimavaram, India.



**Figure 1.** Picture depicts 100 KWp power plant established atop VIT Block, Bhimavaram, India.

To produce 10% of the SVES campus's power requirement, 200 KWp (kilowatt peak) grid-interactive solar power plants were established with a cost of USD ~ 4, 00, 000. Out of this, a 30% grant released by the Ministry of New and Renewable Energy (MNRE), Government of India as a capital subsidy and the remaining fund is met by SVES, India. This power project has been designed, supplied, installed, and commissioned by M/s. Varshini Power Projects India (Private) Limited, Hyderabad, India. 304.5 KWp power plants were commissioned in SVES campuses atop VIT (100.8 KWp), SVECW (50.4 KWp), SBSP (100.8 KWp), and SVCP (100.8 KWp) in December 2017. Nevertheless, we only present statistics of the 200 KWp power plants in this research. The total number of solar modules in different academic institutions is 800, each module rating is 250 Wp, the total number of inverters is 12, and each inverter rating is 15 KWp other salient features of these solar power plants are presented in Table 1.

**Table 1.** Salient features of solar power plant atop VIT, VDC, and BVRICE

Location /Parameters	Plant capacity (KWp)	Solar modules number s	Solar inverters number s	Roof area	Performance ratio (%)	Capacity utilization factor (%)
VIT	100	400	6	1256 m <sup>2</sup>	75.3	16.07

VDC	50	200	3	628 m <sup>2</sup>	75.3	16.07
BVRIC E	50	200	3	628 m <sup>2</sup>	75.3	16.07

### 3.0 DATA ANALYSIS METHODOLOGY AND RESULTS

#### 3.1 Local climatic conditions

As local climatic conditions would also affect the yielding capacity of solar power plants (Khatib Tamer et al., 2013), we present here the climatic conditions of Bhimavaram, a big municipality in the state of Andhra Pradesh, which is located in the southern part of India. The climate of the present station is hot and humid as it is near the sea coast (the Bay of Bengal, just 25 km away). Being a tropical and nearby sea coast station, the present location also experiences sea and land breezes frequently (Brahmanandam et al., 2023). The annual temperature is approximately 27.9 °C and the average rainfall is approximately 1072 mm, and the elevation (mean sea level, MSL) of this station is 7 m. The geographical coordinates of this place are: Geographical Latitude 16.54° N and Geographical Longitude 81.52° E, and, hence, the tilting angle of the arrays is equal to 16.54° (Junaikh et al., 2017). To provide more clarity, we present annual temperature and rainfall variations in Figures 2 and 3. It is evident from Figure 2 that with an average of 32.6 °C May is the warmest month. In January, the average temperature is 23.5 °C, and it is the lowest average temperature of the whole year. It is also obvious from Figure 4 that the driest month is January, with an average of 240 mm.

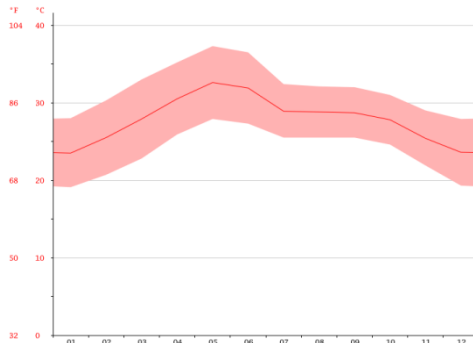


**Figure 2.** Monthly variations of temperature (in both Fahrenheit and Celsius) against months.

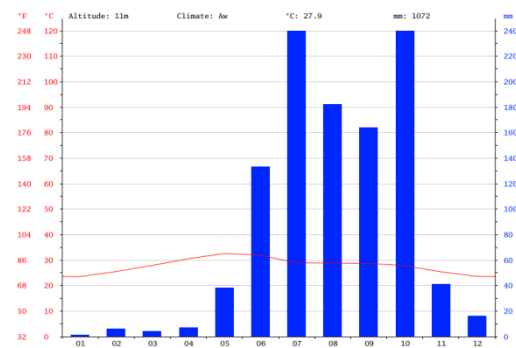


**Figure 3.** Monthly variations of rainfall against months, along with temperatures in both Fahrenheit and Celsius.

#### 3.2 Daily, Monthly, and Annual Variations

To analyze the performance of 200 KWp power plants, we have collected energy production data for five continuous years (2014-2018) located in the SVES campus, India. The assembled data from these five years were organized, analyzed, and filtered to avoid possible deviations from normal behavior. All these steps allowed us to have the exact look of the graph showing daily, monthly, and annual average production.

Daily variations of power yieldings of the 200 KWp power plants (established in December 2013 atop VIT-A, BVRICE, and VDC blocks) during May 2019 are compared with the power yieldings generated out of 302.4 KWp power plants (established in January 2018 atop VIT-A, SVECW, SBSP, and SVCP) to verify relative performance of the 200 KWp power plants, even after a five and a half year tenure. Figure 4 shows day-wise (KWh/day) variations of different power plants' yieldings in May 2019, along with cell and ambient temperatures in Celsius (c). Almost similar variations in power yieldings of both 200 KWp and 302.4 kWp can be noticed, though a moderate difference in magnitudes exists between them, and such differences are more evident in SBSP (50.4 KWP) and VIT-B (100.8 KWp) trends.

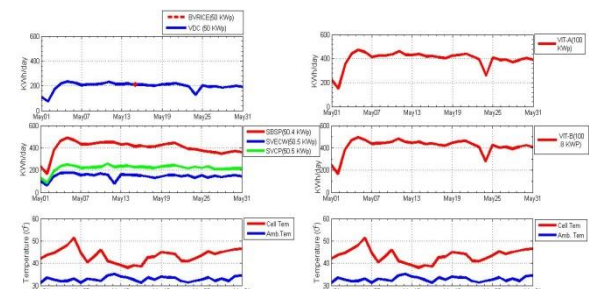


**Figure 4.** Day-wise power yieldings (KWh/day) in May 2019 generated from power plants (07 in numbers) established in December 2013 (VIT-A, BVRICE, and VDC) and January 2018 (VIT-B, SBSP, SVECW, and SVCP) atop SVES, India. Also shown are cell and the ambient temperatures (in °C) in the bottom panels.

Interestingly, both BVRICE (50 KWp) and VDC (50 KWp) variations show near similitude or even better performance compared to SVECW (50.5 KWp) and SVCP (50.5 KWp) variations, though they have completed more than a five and a half year tenure. As far as the relation between cell temperature and power output is concerned, a negative relation does exist between them and such a similar relation can also be witnessed from these figures. These results are also following earlier studies (Labed and Lorenzo, 2004).

The monthly average power yieldings (MWh) of various plants atop VIT, VDC, and BVRICE are presented in Figure 5. It is clear from Figure 5 that they show clear seasonal variations, with peak magnitudes during local summer months (February, March, April, and May) and lowest ones during the local rainy season (June, July, August, September, and October), respectively. Both November and December months, in most of the years, also show greater magnitudes even if the temperature does not touch extreme values. The solar insolation and cell temperatures might have played a role in dictating power yieldings (Maghami et al., 2016; Omkar et al., 2015; Chakravarthi et al., 2020). Secondly, with the increase in the PV module's temperature, the power-yielding efficiency shall decrease linearly at standard test conditions and vice versa (Salman et al., 2012). The relatively higher

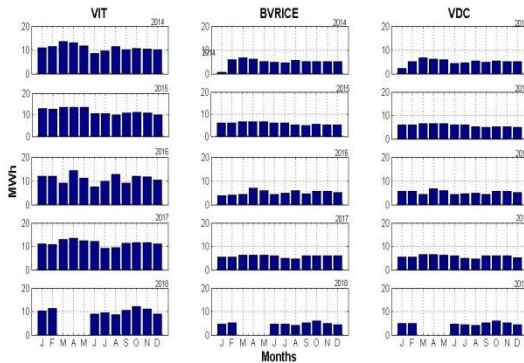


**Figure 5.** Monthly variations of power yieldings (MWh) of solar power plants atop VIT (100 KWp), BVRICE (50 KWp), and VDC (50 KWp) from 2014 to 2018 (top to bottom)

temperatures over this location, therefore, during the summer season ( $\sim 30^{\circ}\text{C}$ ) could have reduced power yieldings, whereas the moderate temperatures during the winter season ( $\sim 25^{\circ}\text{C}$ ) would have allowed in yielding higher magnitudes. The monthly solar insolation data is shown in Figure 6.

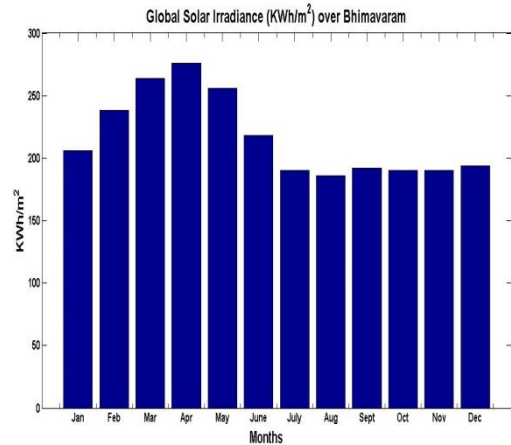


**Figure 6.** Monthly global solar irradiance over Bhimavaram

The annual power yieldings generated from the power plants atop VIT, BVRICE, and VDC are shown in Figure 7. Note that VIT is a 100 KWp capacity plant, while both VDC and BVRICE are 50 KWp power plants. A substantial decay in power yieldings can be seen with the progress of years. The decreased power output over time, which is known as the degradation rate, has been carefully calculated. It is estimated that a maximum of  $\sim 15\%$  decline in power yielding is noticed, but for a few years (during 2016-2017 for the VDC plant), it is only  $\sim 1\%$ . However, the decline for VIT during 2017-2018 is  $\sim 9\%$ . This huge difference in decline in different years might be due to various technical and weather conditions, which include the ambient temperature of the location, internal network, power electronics, and connected grid (Irfan et al., 2017).

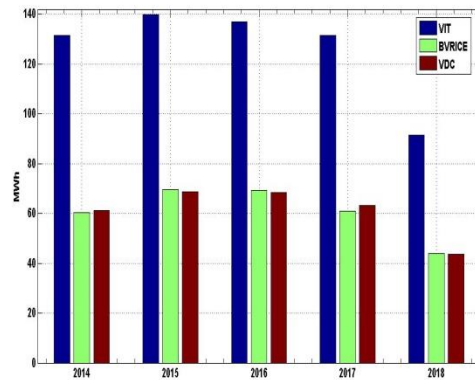


**Figure 7.** Annual variations of power yieldings (MWh) of solar power plants atop VIT (100 KWp), BVRICE (50 KWp), and VDC (50 KWp) during 2014-2018.

To minimize those losses, proper precautions need to be followed as we have highlighted in the ensuing section of this paper. In general, a 20% decline is considered a failure, albeit there is no consensus on the definition of failure (Jordan et al. 2017). We have also made statistics

on the amount of revenue being generated so far and CO<sub>2</sub> emission savings (in tons) per year out of these solar power plants and presented in Table 2. It is estimated that the payback period can be achieved from 7 to 8 years with 10% depreciation and the total CO<sub>2</sub> emission savings are 1237 tons (till May 2019).

**Table 2.** Statistics of revenue generated and CO<sub>2</sub> emissions savings

S. No.	Year	Revenue generated (Indian rupees)	CO <sub>2</sub> savings (tons)
1.	2014	23,29,459.00	219.24
2.	2015	26,48,002.00	244.47
3.	2016	25,59,726.00	229.68
4.	2017	24,38,628.00	250.78
5.	2018	23,28,523.00	201.89
6.	2019 (till May)	22,18,452.00	125.85
<b>Total</b>		<b>1,45,22,790.00</b>	<b>1236.91</b>

### 3.3 Energy losses

An accurate quantification of potential losses of a PV solar system is a difficult task, because of the involvement of several factors and a significant amount of complex interactions among them (Rao et al., 2018). We have made attempts to quantify several losses of an existing 100 KWp atop VIT- B block and 50 KWp atop SVECW in one year and presented them as Sankey diagrams in Figure 9. It is obvious from Figure 8 that the energy losses are as low as -3.5 % (-19.05 KWh) to as high as -7 % (-38.10 KWh) per day. The minimum energy loss was due to inverter losses, whereas the maximum loss was due to temperature losses. It was reported that around 2.2% of losses occurred due to inverted losses and 9.6 % of losses occurred due to temperature losses (Kumar et al., 2019), which significantly reduced the performance of PV systems.

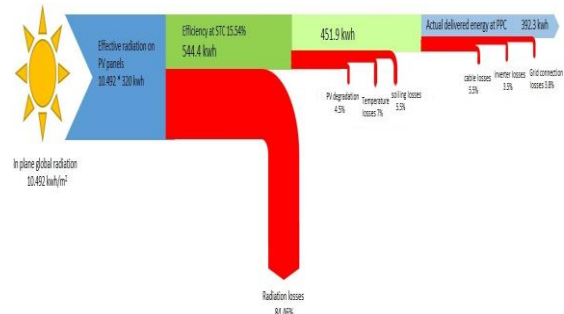


**Figure 8.** Sankey diagram shows estimated losses of the 50.4 KWp power plant

### 3.4 Typical comparisons with existing power plants

We have also calculated the performance ratio (PR) and capacity utilization factor (CUF) of our power plants and made attempts to make performance comparisons between our solar plants and other Indian counterparts and a few foreign countries, and such comparisons are presented in Table 3. Note that PR, a dimensionless quantity, is an international measure for describing the level of the utilization of an entire PV system. It is clear from Table 3 that the calculated PR of our plants has stood at a moderate level. It has been reported that carefully planned plants achieve annual PR values of between 80 and 90 percent (Wirth, 2019). In general, lower PR might be due to higher operating temperature, varying irradiance conditions, dirt on the solar modules, line resistance, and conversion losses in the inverter. It is also obvious that low CUF (02.00) is noted, which is most probably due to system losses as a result of local weather conditions (Shiv Kumar and Sudhakar, 2015).

**Table 3.** Performance comparisons of our plants with various power plants located in India and other countries

S. N o.	Plant location, country & capacity	Geo. Lat.	Ge o. Long.	PR (%)	CUF (%)	Reference
1	DEI, Agra, India - 147.5 KWp	27.1 7°N	78.00 °E	47.0 0-91.0 0	06.0 0-13.0 0	Satsangi et al., 2014
2	Ram agun dam, India - 10 MW	18.7 5°N	79.46 °E	73.8 8-97.5 0	12.2 9-18.8 0	Shiva Kumar and Sudhakar, 2015

3	Poor nima Univ ersit y, Jaipu r, India - 100 KWp	26.9 $1^{\circ}\text{N}$	75. 78 $^{\circ}\text{E}$	82.0 0- 88.0 0	15.0 0- 18.0 0	Rawat and Rawat, 2017
4	Sara ngpu r, Chan digar h, India - 200 KWp	30.6 $9^{\circ}\text{N}$	76. 76 $^{\circ}\text{E}$	77.2 7	16.7 2	Kumar et al., 2019
5	Bhub anes war, India - 11.2 KWp	20.2 $4^{\circ}\text{N}$	80. 85 $^{\circ}\text{E}$	78.0 0	17.0 0	Sharma and Goel, 2017
6	Medi o San Juan, Colo mbia - 20 KWp	05.2 $5^{\circ}\text{N}$	76. 8 $^{\circ}\text{W}$	63.0 0- 78.0 0	10.0 0- 15.0 0	Edison Bangue ro, 2017
7	Tangi er, Mor occo - 5 KWp	31.7 $9^{\circ}\text{N}$	7.0 $9^{\circ}\text{W}$	58.0 0- 98.0 0	6.55- 21.4 2	Attari et al., 2016
1	Vish nu Coll ege-200 KW p	<b>16.5</b> $4^{\circ}\text{N}$	<b>81.</b> <b>52</b> $^{\circ}\text{E}$	<b>53.0</b> 0- <b>89.0</b> 0	<b>02.0</b> 0- <b>10.7</b> 0	Present Study

### 3.5 Solar pro simulations

Solar Pro 4.5 (developed by M/s. Laplace Systems Co Ltd., Japan) is robust PV design and energy simulation software that simulates electricity generation precisely with consideration for various elements of a PV system and displays the result comprehensively. We have made several runs of Solar Pro 4.5 software to verify the power yieldings for 200 KWp solar power plants with a similar setup (inclination and shading) and ambient conditions including air temperature, solar irradiance, and PV temperature. Figure 9 depicts one typical simulation, which shows a similar coincidence with the original trend presented in Figure 5.

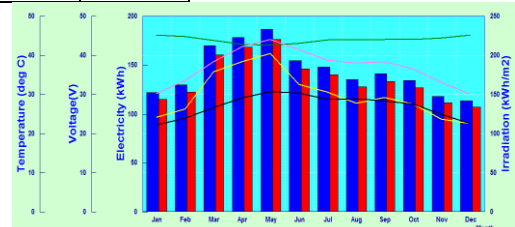
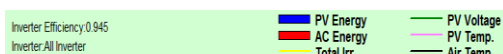
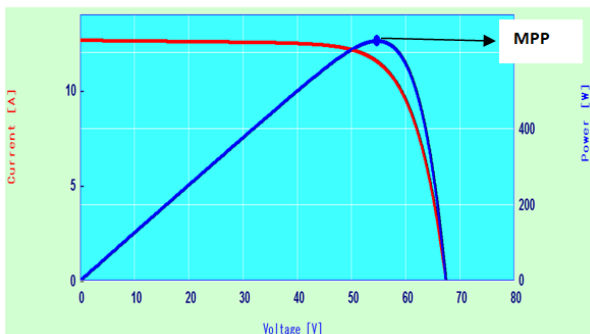


Figure 9. Solar Pro simulation- Power Graph

The power output is showing strong dependence on the ambient temperature, with maximum magnitudes during local summer (March-June) and minimum during the rainy season (July-September). Similarly, we have simulated current-voltage (I-V) characteristics of the 200 KWp power plants and are shown them in Figure 10 along with maximum power point (MPP) (Xiao and Dunford, 2004). Besides, the economic graph of another

typical simulation is shown in Figure 11 which shows seasonal variations with maximum (minimum) magnitudes during the summer (winter) season.



**Figure 10.** Solar Pro simulation- I/V characteristics

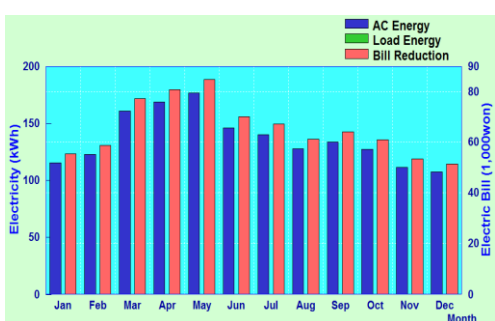


**Figure 11.** Solar Pro simulation- Economic graphs

#### 4. SUGGESTIONS TO IMPROVE YIELDING CAPACITY OF POWER PLANTS

Since a solar power plant consists of a transparent glass pane on the top which properly traps the solar insolation and reflects into the panel and if the transparent glass gets affected, consequently, the absorption rate reduces which leads to reduced conversion efficiency (Rajput and Sudhakar, 2013; Sulaiman, 2014). It has been estimated that accumulated dust, dirt and snow on transparent glasses roughly contribute more than 2% yielding losses in solar power plants, if the solar panels are not cleaned for weeks together and that losses may further increase as high as 40-50% if they are not cleaned for more than two months (Wable and Ganiger, 201). It is, therefore, imperative that the cleaning of solar modules is very much essential regularly. Several conventional and sophisticated cleaning methods were proposed by several researchers which include, vacuum suction and manual wiping and cleaning and electrostatic precipitator (ESP) (Hudedmani et al., 2017).

The complete purpose, however, will not be served with the conventional cleaning systems, since a proper cleaning is not possible with them due to the typical mounting and mechanisms of solar plants. Besides, these conventional cleaning would require lots of labor and money, which cannot be affordable by several institutes and organizations. As a blessing in disguise,

the tilt angle of the PV panel heavily influences the dust deposition density, apart from the geographical latitude of the location and installation design (Mani and Rohit, 2010). As the present power plants were installed with elevation angles around  $16.54^{\circ}$ , moderate accumulation of dust, dirt and snow could be anticipated. As we are, currently, adapting manual wiping and cleaning methods only on weekly twice basis, the expected yieldings are not so encouraging, and hence, immediate steps are needed to replace the existing cleaning methods. Fortunately, one of our colleagues is currently on the job of fabrication of a solar panel automated cleaning ecosystem (SPACE), an automatic robotic solar panel cleaning system. Once SPACE fabrication is done, we will seek the usage of SPACE on a regular basis so that optimum power could be harnessed.

Secondly, when solar cells are transferred into a module, series resistance ( $R_s$ ) arising from the cell interconnection and optical losses caused by the encapsulation may bring additional losses to the module output power, which is evaluated by the cell to module power ratio (CTM). By cutting a fully processed cell into two parts (half-cell), resistance losses can be reduced, providing a power boost of about 5 to 6 W on the module level (Zhang et al., 2018). We are, therefore, planning to install half-cells in the ensuing solar power plants in the future power plants as to harness maximum power from them.

Water bodies could be amicable locations to install solar power plants. The water not only keeps the PV modules cool, which has a positive effect on power yields, while in return, the solar panels protect the surface of drinking water reservoirs from air pollutants or being evaporation. This solar application on water bodies often avoids competition on space usage. Since SVES campus is having a good number of water bodies, installation of solar panels on them shall be a viable option and such efforts will be taken in coming days.

#### 5. CONCLUSION

A part of this important study, we have arrived at the following conclusions, which are listed hereunder.

- a) Daily variations of power yieldings (KWh) of 200 KWp power plants in May 2019 show near similitude with 302.4 KWp plants, though moderate differences in magnitudes between them are found.
- b) Clear seasonal variations in power yieldings are observed with peak (dip) magnitudes during the local summer (rainy) season, which shows high coherence with temperature variations
- c) The decline of power yielding over five and a half years is between 1% and 15% only
- d) The performance ratio and capacity utilization factor of the 200 KWp power plant are 75.3 % and 16.07 %

- e) The payback period and CO<sub>2</sub> emission savings of the 200 KWp power plants were estimated, which are ~7 to 8 years and ~1237 tons as of May 2019
- f) Software-based simulations are presented
- g) Sankey diagram of estimated losses of a power plant (50 KWp) is drawn
- h) Several critical suggestions are discussed that might help the stakeholders to improve the yielding capacity of existing and ensuing power plants.

## References:

- Abdullahi, D., Suresh, S., Renukappa, S., & Oloke, D. (2017). Key Barriers to the Implementation of Solar Energy in Nigeria: A Critical Analysis. *IOP Conference Series: Earth and Environmental Science*, 83(1), 012015. doi:10.1088/1755-1315/83/1/012015
- Arribas L, Cano L, Cruz I, Mata M and Llobet E. (2010). PV–wind hybrid system performance: A new approach and a case study, *Renewable Energy*, 35 (1), pp.128-137. doi:10.1016/j.renene.2009.07.002
- Brahmanandam, P. S., G. Uma, K. Tarakeswara Rao, S. Sreedevi, N. S. M. P. Latha Devi, Yen-Hsyang Chu, Jayshree Das, K. Mahesh Babu, A. Narendra Babu, Subrata Kumar Das, and et al. (2023). Doppler Sodar Measured Winds and Sea Breeze Intrusions over Gadanki (13.5° N, 79.2° E), India. *Sustainability*, 15 (16). 12167. doi:10.3390/su151612167
- Chakravarthi, B. N. Ch. V. and G. V. Siva Krishna Rao (2020). Impact of Power Quality Issues in Grid Connected Photovoltaic System. *2020 4th International Conference on Electronics, Communication and Aerospace Technology*, Coimbatore, India, 155-158, doi: 10.1109/ICECA49313.2020.9297618.
- Dondariya C, Deepak Porwal, Anshul Awasthi, Akash Kumar Shukla, K. Sudhakar, Murali Manohar S.R., Amit Bhimte (2018). Performance simulation of grid-connected rooftop solar PV system for small households: A case study of Ujjain, India, *Energy Reports*, 4, 546-553. doi:10.1016/j.egyr.2018.08.002
- Ekici and Kopru, (2017). Investigation of PV system cable losses, *International Journal of Renewable Energy Research*, 7(2), 807-8015. doi:10.20508/ijrer.v7i2.5660.g7062.
- Global Market Outlook for solar power, 2019-2023, Available at <https://www.solarpowereurope.org/insights/webinars/global-market-outlook-solar-2019-2023>
- Hudedmani et al., (2017), A Comparative Study of Dust Cleaning Methods for the Solar PV Panels, *Advanced Journal of Graduate Research*, 1, 24-29. doi:10.21467/ajgr.1.1.24-29
- Irfan Jamil, Jinquan Zhao, Li Zhang, Rehan Jamil, and Syed Furqan Rafique (2017). Evaluation of Energy Production and Energy Yield Assessment Based on Feasibility, Design, and Execution of 3 × 50 MW Grid-Connected Solar PV Pilot Project in Nooriabad, *International Journal of Photoenergy*, 18, 1-19. doi.org:10.1155/2017/6429581
- Jordan, D. C., Silverman, T. J., Wohlgemuth, J. H., Kurtz, S. R., and VanSant, K. T. (2017). Photovoltaic failure and degradation modes. *Progress in Photovoltaics: Research and Applications*, 25, 318– 326. doi: 10.1002/pip.2866
- Junaidh P. S, A. Vijay, M. Mathew, M (2017). Power Enhancement of Solar Photovoltaic Module Using Micro-climatic Strategies in Warm-Humid Tropical Climate, 2017, *Innovations in Power and Advanced Computing Technologies (i-PACT)*, Vellore, 1–6. doi: 10.1016/j.rser.2013.02.023
- Khatib Tamer, Mohamed Azah, Sopian K. (2013). A review of photovoltaic systems size optimization techniques, *Renewable and Sustainable Energy Reviews*, 22, 454-465. doi: 10.1016/j.rser.2013.02.023
- Kim S K, Jeona J H, Choa C H, Kima E S and Ahna J. B. (2009), Modelling and simulation of a grid-connected PV generation system for electromagnetic transient analysis, *Solar Energy*, 83 (5), 664-678. doi:10.1016/j.solener.2008.10.020

- Kumar M N, Ramjee Prasad Gupta, Mobi Mathew, Arunkumar Jayakumar, Neeraj Kumar Singh (2019). Performance, energy loss, and degradation prediction of roof-integrated crystalline solar PV system installed in Northern India, *Case Studies in Thermal Engineering*. 100409, doi:10.1016/j.csite.2019.100409
- Labed, S., Lorenzo, E., (2004). The impact of solar radiation variability and data discrepancies on the design of PV systems. *Renewable Energy*, 29, 1007–1022. doi: 10.1016/j.renene.2003.12.009
- Maghami M. R., Hashim Hizam, Chandima Gomes, Mohd Amran Radzi, Mohammad Ismael Rezadad, Shahrooz Hajighorbani (2016). Power loss due to soiling on solar panel: A review, *Renewable and Sustainable Energy Reviews*, 59, 1307-1316. doi:10.1016/j.rser.2016.01.044
- Makrides G, B. Zinsser, G. E. Georgiou, M. Schubert and J. H. Werner J. H. (2009). Two year performance evaluation of different grid connected photovoltaic systems, *34<sup>th</sup> IEEE Photovoltaic Specialists Conference (PVSC)*, Philadelphia, PA, 2009, 000770-000775. doi: 10.1109/PVSC.2009.5411169.
- Mani, M, Rohit Pillai (2010). Impact of dust on solar photovoltaic (PV) performance: Research status, challenges and recommendations, *Renewable and Sustainable Energy Reviews*, 14 (9), 3124-3131. doi :10.1016/j.rser.2010.07.065
- Natsheh, E. M., and Albarbar, A., (2012). Solar Power Plant Performance Evaluation: Simulation and Experimental Validation, *Journal of Physics: Conference Series*, 364, No. 1, 2012, 1-13. doi:10.1088/1742-6596/364/1/012122
- Omkar K, M. V. Srikanth, K. P. Swaroop and P. V. V. Rama Rao (2015). Performance evaluation of 50KWp rooftop solar PV plant. *2015 International Conference on Industrial Instrumentation and Control*, Pune, India, 761-765, doi: 10.1109/IIC.2015.7150844.
- Rajput, D. S., & Sudhakar, K. (2013). Effect of dust on performance of solar PV panel. *International Journal of Chemical Tech Research*, 5(2), 1083–1086.
- Rao R. R, Monto Mani, Praveen C. Ramamurthy (2018). An updated review on factors and their inter-linked influences on photovoltaic system performance, *Heliyon*, 4 (9). doi :10.1016/j.heliyon.2018.e00815
- Salman K. A., Z. Hassan, and K. Omar (2012). Effect of Silicon Porosity on Solar Cell Efficiency, *International Journal of Electrochemical Science*, 7, 376 - 386. doi:10.1016/S1452-3981(23)13346-3
- Shiva Kumar B., K. Sudhakar (2015). Performance evaluation of 10Â MW grid connected solar photovoltaic power plant in India, *Energy Reports*, 1, 184-192. doi : 10.1016/j.egyr.2015.10.001
- Sulaiman, S. A. (2014). Influence of dirt accumulation on performance of PV panels. *Energy Procedia*, 50, pp. 50–56, doi:10.1016/j.egypro.2014.06.006
- Tremblay O, Dessaint L A and A. I. Dekkiche (2007). A Generic Battery Model for the Dynamic Simulation of Hybrid Electric Vehicles, *IEEE Vehicle Power and Propulsion Conference*, Arlington, TX, pp.284. doi: 10.1109/VPPC.2007.4544139
- Wable S, S. Ganiger (2017). Design and manufacturing of solar panels cleaning system, *International Journal for Research in Applied Science & Engineering Technology*, 5 (7), 1-7. Available at <https://ijcrt.org/papers/IJCRT2006007.pdf>
- Wirth H (2015). Recent facts about photovoltaics in Germany, International nuclear information system, v. 47 (5), 2015, 1-90. Available at <https://www.ise.fraunhofer.de/en/publications/studies/recentfacts-about-pv-in-Germany.html>
- Xiao W and W. G. Dunford (2004). A modified adaptive hill climbing MPPT method for photovoltaic power systems. In *Proceedings of 2004 IEEE 35<sup>th</sup> annual power electronics specialists conference*. 1957–1963. doi: 10.1109/PESC.2004.1355417.
- Zhang et al., (2018). Study on the Benefit of Half-Cut Cells towards Higher Cell-to-Module Power

---

**K. Omkar**

Dept. of EEE, Shri Vishnu Engineering  
College for Women (A), Bhimavaram, India  
e-mail: omkar\_koduri@svecw.edu.in  
ORCID 0000-0001-7121-8099

**SSSR Sarathbabu Duvvuri**

Dept. of EEE, Shri Vishnu Engineering  
College for Women (A), Bhimavaram, India  
e-mail: sarath.duvvuri@svecw.edu.in  
ORCID 0000-0001-9653-2519

**S. M. Padmaja**

Dept. of EEE, Shri Vishnu Engineering  
College for Women (A), Bhimavaram, India  
e-mail: padmaja\_vrr@svecw.edu.in  
ORCID 0000-0002-1125-2436

**G. Anil Kumar**

Dept. of SREE, J N T University, Kakinada,  
India  
e-mail: gorantlaanilkumar@gmail.com  
ORCID 0000-0001-8679-9260

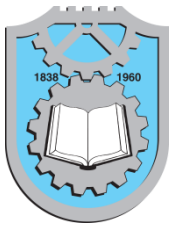
**P. L. S. Pravallika**

Dept. of EEE, Shri Vishnu Engineering  
College for Women (A), Bhimavaram, India  
India, e-mail: potulapravallika@gmail.com

**G. Durga Prasad**

Dept. of AI, Shri Vishnu Engineering  
College for Women (A), Bhimavaram, India  
e-mail: durgaprasad\_garapati@svecw.edu.in  
ORCID 0000-0002-6972-7801

---



Vol. xx, No. x (202x) x-x, doi:

# Proceedings on Engineering Sciences



www.pesjournal.net

## IDENTITY-BASED PRIVACY-PRESERVING ANONYMOUS AUTHENTICATION ACCESS CONTROL FOR SECURE CLOUD COMPUTING

N. Praneetha

S. Srinivasa Rao<sup>1</sup>

V. V. R. Maheswara Rao

P. S. Brahmanandam

I. S. Siva Rao

Keywords:

*Privacy-preserving cloud computing; Secure Data sharing; Identity-based Hierarchical Cryptographic, Access Control Policy; Secure Authentication*

### A B S T R A C T

*The storage of data with access controllability in sharing data between multiple users in a dispersed environment is now the most pressing issue in cloud computing. Cloud computing's unique feature allows its subscribers to exchange and manage their data with one another safely. However, privacy is essential for all cloud users to communicate freely and openly, as data is accessed by unwanted parties in the cloud. Cloud services have employed numerous security-related techniques for efficient and safe user data exchange. These methods provide efficient, flexible, and reliable access control rules between users when exchanging data. But, they each have advantages and disadvantages concerning key generation and data security. To address the need for adaptable, scalable, and trustworthy access control while exchanging data across a dispersed network, this research proposes a novel access control-based privacy-preserving approach. In terms of cipher text and critical policy security, this method is an extension of attribute-based encryption and the only difference is that with cloud computing, users hierarchically share data, and access control policy amongst shared users is evaluated efficiently. Our method includes sophisticated security features like the revocation of users and access rights of users for outsourced data in the cloud. It also provides scalability and dependability in producing critical structures with dynamic qualities. Experimental results demonstrate that the suggested method improves the current system in terms of cloud data sharing efficiency, scalability, and dependability.*

© 202x Published by Faculty of Engineering.



### 1. INTRODUCTION

Distributed computing is an innovative, constantly evolving science-related application that consists of interconnected data sets with shared adaptability, skill in

sharing, and web-dependent client demands. In addition, it is a promising approach to determine capacity limits and should be used everywhere. It uses robust, flexible resources in the cloud to lessen the computational

<sup>1</sup> Corresponding author: Dr. S. Srinivasa Rao  
[srinu1479cse@kluniversity.in](mailto:srinu1479cse@kluniversity.in)

expenditure incurred by data owners while sharing data via cloud clients. Distributed computing relies on cloud service providers (CSPs), who offer various cloud-based services, such as Software As A Service (SAAS), Platform As A Service (PAAS), and Infrastructure As A Service (IAAS), to their users.

Customers may use these services to monitor the effectiveness of cloud-based project management and collaboration tools. Due to the ever-changing user base and unique security concerns of the cloud, effective and valuable cloud services for users must be evaluated. CSP stores and conducts sophisticated operations to put away information for a subset of businesses that deal with cloud employees. Critical resources are present in the information that CSP processes, and as a result, CSP can cause unexpectedly large amounts of data loss. Therefore, while considering cloud security, it is essential to consider concerns about keeping private data safe.

While data privacy isn't strictly necessary, reasonably achieved access control is a highly desired feature in assistance-oriented distributed computing. Some medical services and related organizations evaluate specific components to address a variety of tasks to a group of clients rather than creating multiple copies for each group member (Ahuja and Mohanty, 2020; Rasori et al, 2022). It's often more efficient to use shared admittance privileges (SAP) to give everyone in the group access to the information they need, with or without the individual's permission. First, SAP uses and isolates information benefits for all of the group's users, and second, it avoids wasting computing resources by confirming information that isn't necessary. Standard practices for data sharing in the cloud include examining the merits of several approaches, such as assigning clients individually or in groups.

Attribute-based encryption (ABE) (Wang et al, 2011) describes secure authentication. However, this methodology employs a symmetric key-based cryptographic approach, which does not provide efficient authentication concerning key encryption and, therefore, the traditional workhorse behind access control policies in the cloud. If we expand the number of users in the cloud, the strategy taken by Zhao et al. (2017), which employs a distribution of keys, will only enable single-key communication. As a result, it will not be able to support multiple key generations in a distributed setting.

While the solution to access control is decentralized, it does not support authenticated users, it does not allow users to read and write files in the cloud, and it does not restrict access to files based on who created them (Ruj et al., 2004). Using the benefits and drawbacks of the methods mentioned, we may improve distributed computing by expanding the privacy-related features and enabling the authentication-related features related to the access control policy for data sharing among all users.

To facilitate adaptable, scalable, and trustworthy access control during data sharing in a distributed setting, this research suggests a novel access control privacy-preserving approach. The proposed method is resilient

to various relay attacks, meaning the user can replace the old file with one that includes both reading and writing. This method can also be used to revoke user access, i.e., deny access to previously authorized users before granting them access with modified permissions.

The key aims of our proposed strategy are as follows:

- a) When validating user parameters in the cloud
  - i) Only authorized users should have access to the corresponding access control data
  - ii) We verify and change the identities of any users with access to the data, whether authorized or not.
- b) We keep the design split for efficient key management so that no two users may access the data simultaneously or "co-exist" and avoid collisions.
- c) The cloud allows for numerous read/write state operations; if a user's access is revoked, that person is prevented from accessing any data.
- d) Experiments demonstrate that the suggested technique is scalable and dependable for exchanging data in the cloud, using a variety of performance indicators not previously considered.

## 2. RECENT RESEARCH STUDIES- LITERATURE SURVEY

L The researcher assessed attribute-based encryption (ABE) and gave a concise outline of the ASBE. From that point forward, the current access control methods were investigated, dependent on ABE. The possibility of ABE was first proposed by Sahai and Waters (2005) as another method for hazy character-based security. The essential issue with the arrangement is that its restricted semantics need to be impressive. A few drives have been continued in writing to settle the impressibility issue. In the ABE conspire, cipher texts are not getting to a specific client as in the customary local area key cryptography. Both cipher texts and clients' decoding significant variables may be related to the characteristics or an arrangement of highlights.

A client can unscramble a cipher text if there is coordination between the decrypted key and encrypted text. ABE strategies are arranged into key-approach trait-based security (KP-ABE) and cipher text-strategy characteristic-based security (CP-ABE) in light of how ascribes and plans are related to encrypted text and clients' unscrambling keys. In a KP-ABE plan (Li et al., 2017) a cipher text is related to many highlights, and a client's unscrambling key is associated with a single topic bush availability system. If the highlights on the cipher text satisfy the bush openness structure, then the client can unscramble the cipher text.

In a Ciphertext-Policy Attribute-Based Encryption (CP-ABE), the parts of encrypted texts and unscrambling significant elements are exchanged (Helil & Rahman, 2017); the cipher text is obtained with a bush availability plan chosen by an encrypt or, while the

comparing decoding key is planned regarding a bunch of highlights. Given that the arrangement of highlights related to an unscrambling key meets the bush openness strategy for a given cipher text, the key can decode the cipher text. Since the significant client unscrambling factors are related to many highlights, CP-ABE is adroitly closer to customary access control plans like Role-Based Access Control (RBAC) (Alturi and Ferraiolo, 2011; Roslin Dayana and Shobha Rani, 2023).

In this way, CP-ABE is more feasible to implement for performing availability command over obtained data than KP-ABE. Nonetheless, essential CP-ABE strategies combined with secure operations to back up openness control in contemporary business environmental factors (Zhao and Wan, 2017), which need colossal adaptability and proficiency in indicating rules and dealing with client highlights (Samanthula et al., 2015). In a CP-ABE plan, the significant decoding factors help client credits be organized reasonably as just one set. Clients can utilize all potential highlights in just one set given in their privileged insights to satisfy rules. To fix this issue, Samanthula et al. (2015) implemented encrypted text trait set-based Encryption (CP-ASBE or ASBE for short). ASBE is an all-inclusive CP-ABE that orchestrates client highlights concerning network operations.

ASBE can execute incredible limitations on blending ascribes to satisfy an arrangement, which gives brilliant adaptability in openness control. In the recursive list of capabilities allotted to a client, highlights from a similar set can be blended rapidly. In contrast, highlights from better places must be joined by changing over items whose activity will be clarified later. Similar security operations create the highlights for students by them. Every understudy has a variety of attributes according to the courses they have completed. The specialist needs to have an arrangement. "Understudies who took a class that fulfills and upholds such an arrangement with CP-ABE are trying since an understudy might have taken a few projects and gained various evaluations.

The encryption should ensure the understudy cannot pick union highlights from better places to go around the arrangement. As suggested by (Samanthula et al., 2015), a few potential options with plain CP-ABE are portrayed, yet they need to be more adequate. In any case, by utilizing ASBE, the issue can be fixed by allocating a few standards to the arrangement of highlights in various sets. For each course, students get different standards for the highlights. Along these lines, ASBE can execute successful cipher text plan encryption for conditions where the current ABE strategies are insufficient. Besides, ASBE's capacity to give a few qualities to a similar component permits it to adequately determine the customer denial issue, which is a difficult recommendation in CP-ABE. The denial issue can be fixed rapidly by giving different diverse experiments.

Huang et al. (2017) recommended hierachal ABE (HABE) to acquire the availability of fine-grained control in distributed storage space arrangements by

blending hierarchical identity-based Encryption (HIBE) and CP-ABE. This method also maintains transparency while granting the thinking suppliers granular flexibility overestimations. However, as managed by a comparable area master, HABE employs a disjunctive ordinary structural plan and covers all the highlights in a single conjunctive statement. Therefore, certain area aces may administer a similar quality as suggested by particular rules that are attempting to be followed. Furthermore, according to ASBE, this plan does not support certain deserving duties and is unable to sufficiently assist with drug inclusion. In distributed computing, a new and more effective method is needed to provide a dynamic access control structure amongst users.

### 3. BASIC PRELIMINARIES

This section describes the essential preliminaries, assumptions, data owner, cloud server, and data sharer. The server relates to the cloud, explores data storage with different services, and provides efficient access control policies in the user's stored data concerning credentials on authorization. The server of the cloud acts as a semi-trusted device (Chen et al., 2019). It provides efficient access control on encrypted data with authorized secret key sharing on plain text stored in the cloud. The cloud server helps to manage all the authorization privileges with their registered user credentials related to revoked data files.

The data owner is registered as a cloud user who can store data in the cloud and share secret files with other users present in the cloud concerning authorized privileges and user-related credentials. The owner of data indexes and stores all the official credentials of users, issues related to credentials with authorized details to the sharer of data, and the owner of data revokes the user's data without any notification to the sharer of data.

Sharer of data can explore only encrypted data, which provides authorization to the entire files list, which can have efficient credentials, and also shows the tender proof by cloud server, which can have efficient credentials. By using encrypted files with their mask boundary code values, which transfer data with an authorized file key, the sharer of data should identify data related to sensitive data that contain delegated credentials. Basic notations used in the proposed implementation are described in Table 1.

**Table 1.** Shows the Basic notations used in this study

Symbol	Description
$V_\mu$	Owner/user of v <sup>th</sup> user
$X_j, X, L_j$	j <sup>th</sup> attribute relations Key Distribution Center (KDC)
$l_j =  L_j , I[j, u], I_u$	Number of claimed user attributes for encrypt/decrypt
$PK[j]/SK[j], sk_{i,v}$	Public key/secret key
H, H, MSG	Hash functions with message

Based on the above parameters, the following concepts are used in the proposed implementation, i.e., basic formats of access policies, access tree structure, and ABE. Let us discuss them in detail hereunder.

### a) Basic format of access policies in cryptography

Basic access control policies are described in the following formats, which include attributes relate to Boolean functions, secret sharing linear schema and span programs relate to monotone.

An access tree structure converts Boolean functions.

For example,  
 $((x_1 \wedge x_2 \wedge x_3) \vee (x_4 \wedge x_5) \wedge (x_5 \wedge x_6)), \quad x_1, x_2, \dots, x_6$  are attributes.

Let us consider  $B : \{1, 0\}^m \rightarrow \{1, 0\}$  be the function relates to Boolean monotone for every span function, i.e.....  $(a_1, a_2, \dots, a_n) \in \{1, 0\}^m$ , the following function should satisfy all the labeled functions.

$$b(a_1, a_2, \dots, a_n) = 1 \Leftrightarrow \exists v \in \mathbb{R}^{1 \times l} : v N = [0, 1, 1, \dots, 1] \& (\forall i : a_{x(i)} = 0 \Rightarrow v_i = 0) \quad \dots (1)$$

Here  $b(a_1, a_2, \dots, a_n) = 1$  is the span function indexed with a span vector  $\{i | a_{x(i)} = 1\}$  & a span program constructed in Boolean retrieval functions.

### b) Attribute-based Encryption

Attribute-based Encryption is explored with multiplier functions. The basic scenario of ABE is described as follows:

**Initialization of system:** Identify the prime number p, generator g of the group of generative functions  $G_O \& G_T$  with the order of q, and then map the function  $e : G_0 \times G_0^i \rightarrow G_T$ , which is

associated with a hash function  $H : \{1, 0\}^* \rightarrow G_0$ . This hash function is combined with different attributes  $L_j$ , disjoint connection  $(L_i \cap L_j = \emptyset \text{ for } i \neq j)$ , then the secret key of generative function is

$$SK | j |= \{x_i, b_i, i \in L_j\} \quad \dots (2)$$

From the secret key, generate the public key from sources

$$PK[j] = \{e(g, g)^{x_i}, g^{b_i}, i \in L_j\} \quad \dots (3)$$

**Distribution of key generation:** User v receives content from the set of attributes I (v, j), then associated secret key sk for each user attribute  $i \in I[j, v]$ , then hash-based secret key generation is

$$sk_{v,i} = g^{x_i} H(v)^{b_i} \quad \dots (4)$$

$x_i, b_i \in SK[j]$  be the secure user delivery of different public keys. Decryption is also performed using the secret key.

**Data encryption with sender:** Use the encrypt function in attribute-based Encryption  $ABE.Enc(msg, \chi)$ ; the sender sends access tree structure encrypted message (cipher text(ct)) as follows:

$$CT = \langle R, \pi, ct_0 \{ct_{0,a}, ct_{1,a}, ct_{2,a}, \forall_a\} \rangle \quad \dots (5)$$

Here  $\pi(a)$  be the mapping connection  $R_a$  corresponding matrix with different attributes located and associated with the access tree of data.

**The decryption of data by receiver:** Use decryption function, i.e.  $ABE.Dec(CT, \{sk_{i,v}\})$ , CT be the encrypted text, receiver Vu explores cipher text CT with secret key sharing and then obtain output decrypted message with following conditions, i.e.

a) For each attribute

$$a \in A, dec(a) = \frac{C_{1,a} e(H(v), C_{3,a})}{e(sk_{\pi(a)}, v, C_{2,a})}$$

b)  $V_u$  evaluates  $msg = C_0 / \prod_{a \in A} dec(a)$

### 3.1 Implementation and construction of NACPPA

#### a) Implementation procedure:

This section describes the implementation of security in NACPPA with the following calculation methods:

- I. **Setup of System:** This calculation method is evaluated by the authority of a trusted user and organized by a third-party trusted user. This setup does not contain any input other than security parameters (in the form of attributes), i.e.,  $\alpha, \beta$  which are related to global public parameters, i.e., GPK (global public key)
- II. **Generation of Key:** let us assume  $(attri\{ucpk_{id,k} | k \in \square\}, \{KeyVerif_k | k \in \square\}, AMSK_{ud} \text{and } GPK)$  the key generation method for attribute authority is evaluated by AA<sub>d</sub>. It takes input as following attributes, i.e., attri, center-user-public-key (ucpk<sub>i,k</sub>), key relates to verification VK<sub>k</sub>, master key MK<sub>d</sub> relates to public global parameters i.e. GPK. It gives output as secret\_key SK<sub>ud</sub> of the data user (DU), and the pair relates to the secret key, i.e.,  $(pk_o, sk_o)$  of the data owner (DO).
- III. **Encryption of Files:** Domain authority evaluates and performs this encryption procedure. It takes input as plain text m, GPK, the secret key of DO's, public of DU's, i.e., pk<sub>u</sub>, and converted cipher text CT<sub>fog\_comm</sub>. It gives all output as cipher text CT<sub>1</sub>, CT<sub>2</sub> and stores that cipher text into the main cipher text server, i.e., cloud service provider.
- IV. **GenTrap:** input as  $(\omega, SK_{ud}, PK_o)$  Trap door generator calculation method is evaluated by the data user, i.e., DU, input for this calculation is presented with the search word  $\omega$ , secret key SK<sub>ud</sub>, and key with public PK<sub>O</sub> then it generates output as Trapdoor (tw) & key relates to re-encryption value SK<sub>ud</sub><sup>w</sup>
- V. **The Decryption of Files:** This decryption calculation method evaluates data user and domain authority. It takes input as  $(C, \Omega, RK)$ , i.e., cipher text, which consists of partial decrypted text and key retrieval RK; plain text is the output for this calculation method.

## b) Proposed NACPPA Schema

This section describes the basic algorithm implementation procedure of NACPPA, which is an extension to attribute set-based encryption to evaluate and handle the dynamic hierarchical structure of different users, as illustrated in Figure 2. Recall the procedure of domain authority and subordinate domain authorities and other data users concerning corresponding consumers and users related to data. In our proposed approach, the authority of trusted users evaluates privacy-related master key-assisted parameters present in top-level scenarios. Domain authority generates and distributes secure keys to subdomain authorities present at the next associated level. In our implemented system, each user contains a key structure generated by attributes with decrypted keys of users.

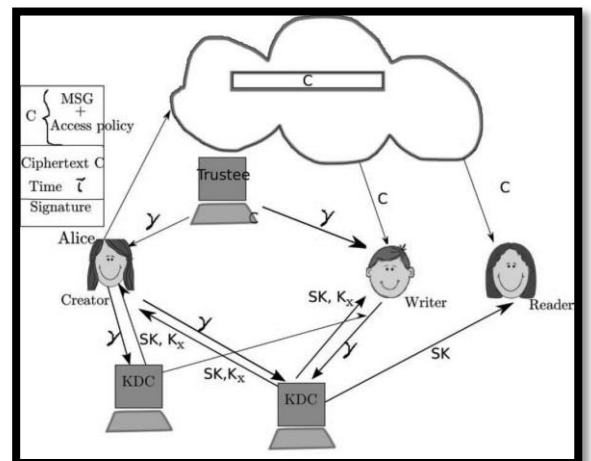


**Figure 2.** The User is represented in a hierarchical structure

We describe the basic properties of NACPPA, i.e., it consists of the following methods:

**System Setup:** The setup calculation method is executed by the authority of domain for the creation of key\_public (PK) and key\_master (MK), d is the length of key\_structure, by using bilinear map connection C be the prime order p with gen c and then evaluates random parameters  $\alpha, \beta \in Z_p, \forall i(1, 2)$ . Then, the generation of both master and public keys based on the length of key d is

$$PK = \left( C, c, h_1 = c^{\beta_1}, f_1 = c^{\frac{1}{\beta_1}}, h_2 = c^{\beta_2}, f_2 = c^{\frac{1}{\beta_2}}, e(c, c)^{\alpha} \right) \dots \dots \dots \quad (6)$$

$$MK = (\beta_1, \beta_2, c^\alpha) \dots \quad (7)$$

**Creation and grant of domain authority:** Domain authority is organized and associated with recursive attribute relations, i.e.,

$\{X_0, X_1, \dots, X_m\}$ ,  $X_i = \{x_{i,1}, x_{i,2}, \dots, x_{i,n}\}$  with  $a_{ij}$ , and related attributes. Creates key for domain authority, select identity no. of keys  $r^{\{v\}}$  for domain authority. Random selection of identity keys for each user  $a_{i,j}$ ,  $0 \leq i \leq m, 1 \leq j \leq n_i$  is utilized in the authority of the domain

$$DA(MK) = \begin{cases} A, D = c^{\frac{\alpha+r^{(u)}}{\beta_1}}, D_{i,j} = c^{r_i^{(u)}} \cdot H(a_{i,j})^{r_{i,j}^{(u)}}, \\ D'_{i,j} = c^{r_{i,j}^{(u)}} \text{ for } (0 \leq i \leq m, 1 \leq j \leq n_i), \\ E_i = c^{\frac{r^{(u)}+r_i^{(u)}}{\beta_2}} \text{ for } (1 \leq i \leq m) \end{cases} \dots \quad (8)$$

In the above generation of domain authority master key, where  $E_i$  is the form of translation, unique rule formation  $r^{(u)}$  relates to the attribute set  $A_i$  to  $r^{(u)}$  with associative translating elements  $E_i$  &  $E_i$  can be used as  $E_i / E_i$  to translator to unique key generations; these details are used decryption calculation method again.

#### User grant/ selection of novel domain authority:

In this scenario, a novel user "u" and subordinate with respect to authority of a domain and it is denoted as DA++, DA joined into the cloud system then DA verifies each user then DA generates key structure to every user and user gives grant to other relative users using authorizes which are derived from domain authority.

**User Creation (DAMK, u  $\ddot{\mathbb{N}}$ ):** This calculation method uses the master key, which is generated by the DA with the structure of the key  $\mathbb{N}$ , then evaluates the key structure for a newly generated user  $\ddot{\mathbb{N}}$ , which is the combined key set structure of  $\mathbb{N}$ . Based on unique identifier sequences present in the DA master key, evaluates the secret key for the user described in the following equation:

$$(MK_{i+1}) \\ = \begin{cases} \ddot{\mathbb{N}}, \ddot{D} = D \cdot f_i^{\ddot{r}^{(u)}}, \ddot{D}_{i,j} = D_{i,j} \cdot c^{\ddot{r}_i^{(u)}} \cdot H(a_{i,j})^{\ddot{r}_{i,j}^{(u)}}, \\ \ddot{D}'_{i,j} = D_{i,j}^1 \cdot c^{\ddot{r}_{i,j}^{(u)}} \text{ for } (a_{i,j} \in \ddot{\mathbb{N}}), \\ \ddot{E}_i = E \cdot f_2^{\ddot{r}^{(u)} + \ddot{r}_i^{(u)}} \text{ for } (\mathbb{N}_i \in \ddot{\mathbb{N}}) \end{cases} \dots \quad (9)$$

$MK_{i+1}$  is the secret key of the user structure  $\ddot{\mathbb{N}}$ , and the recipient key is directly removed from the authority of the trusted user.

**Encryption of File (PK, m,  $\tau$ ):** plain message  $m$  is to be encrypted,  $M$  be the DEK file,  $\tau$  be the tree access structure. The encryption calculation method is similar to attribute set-based Encryption but only supports polynomial equations  $q_a$  with access tree structure  $\tau$  collected from randomly selected trusted authority from root domain authority. The encryption calculation method is described as follows:

$$Cipher\_Text(CT) = \begin{cases} \tau, \tilde{G} = M \cdot e(c, c)^{\alpha \cdot s} \cdot G = h_1^s, G = h_2^s, \forall b \in B : \\ G_b = c^{q_b(0)}, G'_b = H(attr(b)^{q_b(0)}), \\ \forall a \in A : \tilde{G}_a = h_2^{q_a(0)} \end{cases} \dots \quad (10)$$

Where  $B$  defines the set of parent node with subleaf user in  $\tau$ , and  $A$  is the set of the access tree structure  $\tau$ .

**Revocation of User:** Any user who has access to owner-shared data withdrawn from the cloud system cannot access it from any location. We address this issue in our solution by using a re-encryption technique to access the shared file association where users' access is tied to the revoked format. The attributes of attribute set-based encryption are expanded by NACPPA to provide user revocation. If data owners share shared files, produce new keys for revoked users based on the domain authority security rights procedure.

**File access operations:** whenever the user sends the request to the cloud server, then the cloud server sends the encrypted request to the user, and then the user decrypts the updated data using  $Dec(CT, SK_u)$  the decryption procedure as follows:

**The decryption of Files:** This calculation method takes input as cipher text and key structure. Firstly, the decryption procedure verifies user key structure  $k$  concerning associative access tree structure  $\tau$  and cipher text content and is accessed from the data owner. Satisfy all the conditions with  $\tau$  and key structure of the user " $u$ " and then decrypt the entire content; if not satisfy the conditions, then evaluate/perform decryption\_method. The decryption method is described as follows:

$$Decr(CT, SK_u, i, t) = e(D_{i,j}, G_t) / (D'_{i,j}, G'_t) = e(c, c)^{r^{(u)}} \cdot q_t(0) \quad \dots \quad (11)$$

The decryption method for all stored encrypted content with translated polynomial interpretation  $F_z$  is described as follows:

$$F_z = e(\hat{G}_z, E_i / E'_i) \cdot F_z' = e(c, c)^{r^{(u)}} \cdot q_z(0) \quad \dots \quad (12)$$

Based on the above decryption procedure, the message to be evaluated as  $M = \hat{G} \cdot F / e(G, D)$ .

#### 4.0 Experimental Evaluation

To calculate the efficiency of the proposed approach to design an empirically secure cloud with users accessed by multiple files from different data owners in the cloud, we have implemented the NACPPA framework based on the working procedure of ABE. Using the latest version related to CloudSim, Java, and Netbeans are used to set up the newest cloud environment. Each host consists of 2.4 Hz with 4-8 GB RAM and 1TB of data storage for this implementation. Using these requirements, our proposed approach explores the following sequences:

**Setup\_NACPPA:** It generates both public and master keys, i.e., key\_public (PK) and key\_master (MK) assumptions

**NACPPA\_keyGen:** Implemented PK and MK to generate a key related to private operations with critical structures. Actual structure depth supports 1 or 2 support functions.

**NACPPA\_keyDeleg:** Based on PK and MK, which are related to the authority of the domain, this delegates some methods of DA's private keys for the newly generated user. In domain authority, the delegated key is used for the private key.

**NACPPA\_enc:** Based on access tree policy conditions, generates encrypted file using PK.

**NACPPA\_Dec:** Using private, decrypt the files

**NACPPA\_rec:** Using PK, encrypt all the files using the private key and generate re-encryption for both encrypted and decrypted files. Note that generated private is used to decrypt the file using encrypt file operations.

Experimental results of the implemented approach concerning the time taken by different operations with different methods are to be calculated. The following figures show the time taken for other instances during authentication in the client cloud with the proposed approach. To assess the effectiveness of the proposed NACPPA approach with a comparison of different authentication approaches like ASBE and CP-ABE, the following results (generated in the proposed approach) give efficient security response time, encryption for files, decryption for files, and access tree generation time for different users. The results also provide average accuracy with memory utilization for user operations like upload, requests, and download requests for efficient and secure data storage in a distributed environment. Table 1 describes total time values for processing different user instances.

**Table 1.** Total time values for different user instances

Different users	CP-ABE	KP-ABE	ASBE	NACPPA
10	5.2	3.8	4.7	2.9
30	6.3	5.9	6.3	4.4
50	7.5	6.5	5.6	4.8
70	8.4	7.3	8.2	5.7
100	9.5	8.4	7.3	6.4

As shown in Table 1 and Figure 3, compared to traditional approaches, i.e., ASBE, KP-ABE took approximately equal time to explore user instances on the cloud whenever user

instances increased, and those approaches took more time to execute the services of different users. Compared to the proposed method, it took less time than existing approaches.

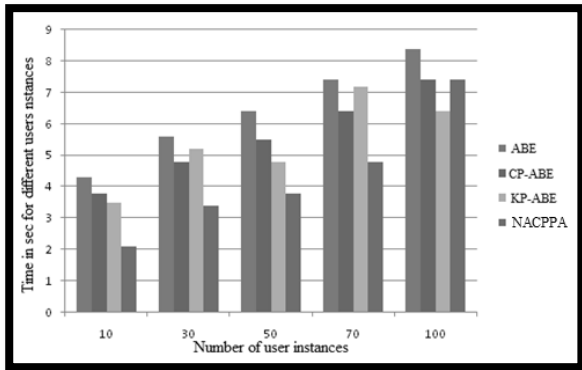


**Figure 3.** Performance evaluation for cloud setup environment to all the user operations

Encryption time for different user instance requests with the upload of original content in the secure format in the cloud with different values is described in Table 2.

**Table 3.** Encryption time values for different user instances

Different users	CP-ABE	KP-ABE	ASBE	NACPPA
100	5.3	4.7	4.6	4.5
200	6.4	5.8	6.3	3.1
300	7.4	7.7	6.3	3.3
400	8.3	7.2	8.2	4.7
500	9.6	8.4	9.4	7.6

Table 2 and Figure 4 show the encryption time evaluation values and performance evaluation of different approaches in encryption. ASBE and CP-ABE took more time to increase the user instance concerning other services. The proposed method took less time to encrypt files uploaded by different users.

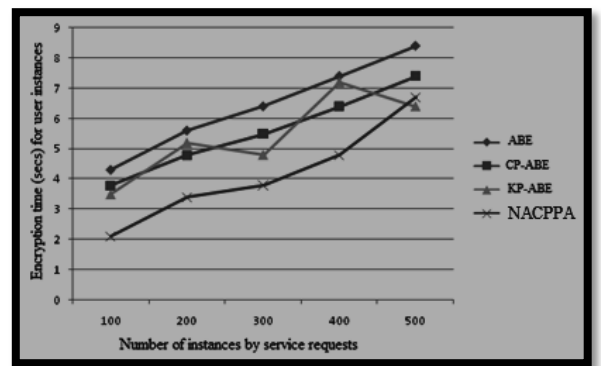


**Figure 4.** Performance evaluation of different approaches with encryption time

Different users want to download shared files from users of data owners to evaluate the decryption time values, shown in Table 3 in secure cloud storage.

**Table 3.** Description time values

No. of User Instance s	CP-ABE	KP-ABE	ASBE	NACPPA
100	4.8	5.8	5.3	4.7
200	5.3	6.7	5.9	3.7
300	4.8	8.5	6.4	3.3
400	7.4	6.9	5.7	3.9
500	6.8	7.5	7.9	6.4

Table 3 and Figure 5 show the decryption time evaluation values and performance evaluation of different approaches in decryption. Also, ASBE, KP-ABE, and CP-ABE took more time to increase the user instance concerning other services. The proposed method took less time to decrypt files uploaded by different users with different instant services.

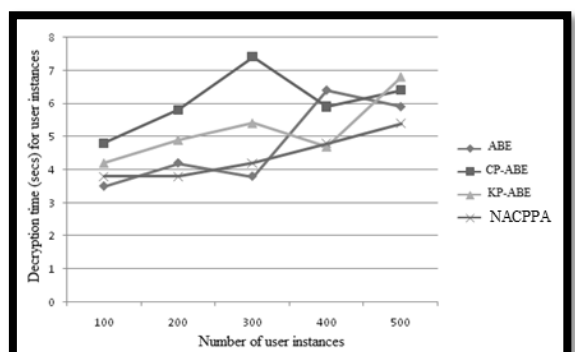


**Figure 5.** Performance evaluation of decryption time of different approaches.

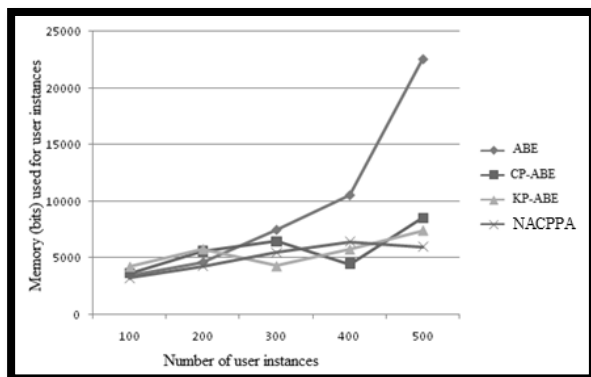
Table 4 and Figure 6 show the performance evaluation of different approaches in

memory utilization to explore user instance services.

**Table 4.** Utilization of memory values in processing user operations in secure cloud storage

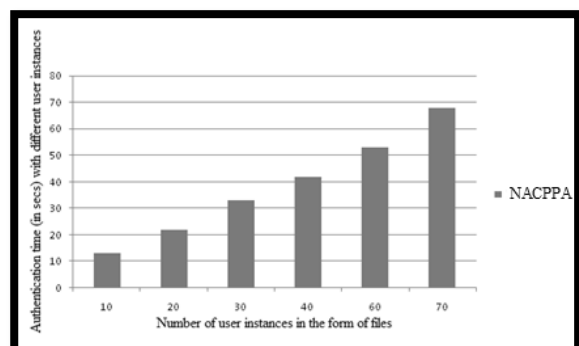
Users	CP-ABE	KP-ABE	ASBE	NACPPA
100	465 2	364 2	488 7	4760
200	532 7	432 6	522 6	5626
300	735 6	697 4	474 5	4026
400	221 32	579 6	635 4	5356
500	245 53	896 4	678 5	4324

The utilization of memory with different user operations, like storing data securely and accessing tree structures with feasible secure storage, was described in Table 4.



**Figure 6.** Performance evaluation of the proposed approach with traditional approaches in terms of memory

ASBE and KP-ABE took a lot of memory whenever increasing the user instance services. Because of less time complexity, the proposed approach runs with the lowest memory utilization in processing users' services concerning other systems.



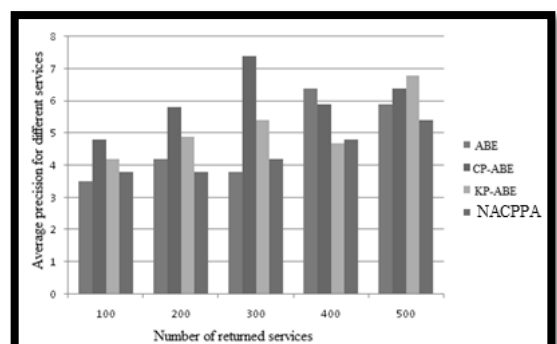
**Figure 7.** Performance evaluation of generation of access tree structure

Figure 7 shows the performance evaluation of the access tree structure concerning different users' tree construction to store data securely. Table 5 shows the average precision of accuracy values of the proposed approach with different user instance files stored in a secure format in the cloud. Based on the above results, if we increase other user instances, traditional methods give less accurate results when compared to the proposed approach derived from secure cloud storage.

**Table 5. Average accuracy values for different user instances**

Users	CP-ABE	KP-ABE	ASBE	NACPPA
100	4.5	5.9	5.1	3.6
200	5.3	6.6	5.8	4.4
300	4.8	6.3	6.3	3.5
400	7.4	6.8	5.4	4.9
500	6.9	7.2	7.6	5.4

Support different user instances in exploring data from a secure cloud, as described in Table 5.



**Figure 8.** Performance of accuracy with different user secure operations

Figure 8 shows the accuracy of different users in performing data security operations in a distributed environment. Figures 3-8 show the performance of total user instances, time for Encryption, and decryption concerning memory utilization. The proposed approach performs efficiently compared to conventional methods like ASBE, KP-ABE, and CP-ABE designed with multi-file sharing cloud environments.

#### 4. Conclusion

In this report, we carried out a novel secure authentication approach, i.e., NACPPA, to provide green, scalable, flexible user supply get admission to manage shape in cloud computing. NACPPA virtually put into effect a hierachal structure for

accessing a person's files by applying a facts delegation manner, which is present in characteristic set-based Encryption. NACPPA does not best support user protection, and it achieves the advanced idea, i.e., revocation of consumers in statistics sharing if more than one project attribute is a gift. We speak about the security performance procedure of NACPPA with specific idea-level calculation techniques. The applied experiments indicate green, comfy overall performance evaluation and evaluation of advanced safety efficiencies in cloud computing. Further extension for this is to control the corporation's keys and discuss how they may help multi-person relaxed statistics sharing depending on a cloud server in cloud computing.

#### References:

- Alturi, V., Ferraiolo, D. (2011). Role-Based Access Control. In: van Tilborg, H.C.A., Jajodia, S. (eds) Encyclopedia of Cryptography and Security. Springer, Boston, MA. doi:10.1007/978-1-4419-5906-5\_829
- Chen, Y., Wenhui Sun, Zhang, N., Zheng, Q., Lou, W., & Hou, Y. T. (2019). Secure remote monitoring framework supporting efficient fine-grained access control and data processing in IoT. In *IACR Cryptology Eprint Archive*, 86.
- Helil, N., & Rahman, K. (2017). CP-ABE Access Control Scheme for Sensitive Data Set Constraint with Hidden Access Policy and Constraint Policy. *Security and Communication Networks*, 2017, 2713595. doi:10.1155/2017/2713595
- Huang, Q., Yang, Y., & Wang, L. (2017). Secure data access control with ciphertext update and computation outsourcing in fog computing for Internet of Things. In *IEEE Access*, 5, 12941–12950. doi:10.1109/ACCESS.2017.2727054
- Li J, Lin X, Zhang Y, Han J. (2017). KSF-OABE. Outsourced attribute-based encryption with keyword search function for cloud storage. *IEEE Transactions on Services Computing* 10: 715–725
- Liu, Q., Wang, G., & Wu, J. (2014). Time-based proxy re-encryption scheme for secure data sharing in a cloud environment. *Information Sciences*, 258, 355–370. doi:10.1016/j.ins.2012.09.034
- Rasori, M., Perazzo, P., Dini, G., & Yu, S. (2022). Indirect Revocable KP-ABE with Revocation Undoing Resistance. *IEEE Transactions on Services Computing*, 15(05), 2854–2868. doi:10.1109/TSC.2021.3071859
- K. Roslin Dayana & P. Shobha Rani (2023). Trust aware cryptographic role based access control scheme for secure cloud data storage. *Automatika*, 64:4, 1072-1079, doi: 10.1080/00051144.2023.2243144
- Ruj, S., M. Stojmenovic and A. Nayak (2014). Decentralized Access Control with Anonymous Authentication of Data Stored in Clouds. *IEEE Transactions on Parallel and Distributed Systems*, 25 (2), pp. 384-394. doi: 10.1109/TPDS.2013.38.
- Sahai, A., and B. Waters. Fuzzy Identity Based Encryption. In Advances in Cryptology – Eurocrypt, volume 3494 of LNCS, pages 457–473. Springer, 2005
- Samanthula, B. K., Elmehdwi, Y., Howser, G., and Madria, S. (2015). A secure data sharing and query processing framework via a federation of cloud computing. In *Information Systems*, 48, 196–212. doi:10.1016/j.is.2013.08.004
- Wang, G., Liu, Q., Wu, J., & Guo, M. (2011). Hierarchical attribute-based encryption and scalable user revocation for sharing data in cloud servers. *Computers & Security*, 30(5), 320–331. doi:10.1016/j.cose.2011.05.006

Xu, S., Yang, G., Mu, Y., & Deng, R. H. (2018). Secure fine-grained access control and data sharing for dynamic groups in the cloud. In IEEE Transactions on Information Forensics and Security, 13(8), 2101–2113. doi:10.1109/TIFS.2018.2810065

Zhao, Z., & Wan, J. (2017). Verifiable outsourced ciphertext-policy attribute-based encryption for mobile cloud computing. *KSII Transactions on Internet and Information Systems*, 11, 3254–3272. doi: 10.3837/tiis.2017.06.024.

---

**N. Praneetha**  
KLEF University,  
Vaddeswaram- 522 302,  
India  
nyshpranee@gmail.com  
0000-0002-7027-9516

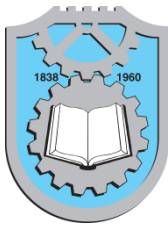
**S. Srinivasa Rao**  
KLEF University,  
Vaddeswaram-522 302,  
India  
srinu1479cse@kluniversity.in  
ORCID: 0000-0002-6183-7088

**Maheswara Rao V V R**  
Shri Vishnu Engineering  
College for Women,  
Bhimavaram, India  
mahesh\_vvr@yahoo.com  
ORCID : 0000-0002-0503-7211

---

**I S Siva Rao**  
GITAM Deemed to be University  
Visakhapatnam,  
India  
isro75@gmail.com  
ORCID: 0000-0001-9181-7507

**P. S. Brahmanandam**  
Shri Vishnu Engineering College for  
Women,  
Bhimavaram- 534202,  
India  
dranandpotula@svecw.edu.in  
ORCID: 0000-0001-9777-3496



## REVOLUTIONIZING FEATURE ENGINEERING FOR ROBUST ENSEMBLE MACHINE LEARNING BY HYBRIDIZING MRMR INSIGHT AND CHI2 INDEPENDENCE

Silpa N<sup>1</sup>

Sangram Keshari Swain

Maheswara Rao V V R

Keywords:

*Feature Engineering, Minimum Redundancy Maximum Relevance, Chi square, Ensemble Machine Learning, Incremental feature selection.*

### A B S T R A C T

*In the realm of data science, dealing with real-world datasets often presents a formidable challenge, primarily due to the sheer volume of features that significantly lack relevance or may be redundant. Effective feature engineering is vital in constructing robust ensemble ML models, where the choice of input features influences overall performance. Towards this, the present research presents a novel framework to feature engineering by hybridizing the MRMR insights and Chi2 independence techniques. MRMR emphasizes feature relevance and non-redundancy, while Chi2 quantifies the independence of features from the target variable. The hybrid framework adheres to the incremental feature engineering approach, with the goal of improving predictive accuracy, model robustness, and adaptability. Through extensive experimentation on employed water quality dataset, the framework illustrates the superiority of hybrid model over using MRMR and Chi2 independently. The results of the proposed HFE-EML exhibit substantial improvements, reaching approximately 99.10% in ensemble machine learning models' performance, reduced overfitting, and enhanced generalization.*



© 202x Published by Faculty of Engineering

### 1. INTRODUCTION AND RELATED WORK

The widespread use of real-world datasets from many areas has become commonplace in the present era of data-driven applications. The use of these datasets frequently presents a variety of obstacles, encompassing issues related to the quality and amount of data, as well as concerns regarding computing efficiency and the effectiveness of models (Cui et al., 2020; Kurada et al., 2023). Within a multifaceted context, the significance of

proficient feature engineering becomes evident as a crucial element in achieving the aims of predictive modelling (Uddin et al., 2018; Silpa et al., 2023). The function of feature engineering might be compared to that of a proficient sculptor, who carefully molds and refines the unprocessed data in order to create the metaphorical masterpiece of ML models (Kumar and Pratap, 2023). The absence of this crucial stage can greatly impede the prediction capabilities of ML models (Wang et al., 2022; Rao et al., 2023).

<sup>1</sup> Corresponding author: Silpa N  
Email: nrusimhadri.silpa@gmail.com

The process of feature engineering encompasses many activities that are crucial for enhancing the performance of ML models. These activities include the selection of pertinent features, the creation of novel characteristics, and the transformation of existing ones (Ramla, 2019). The major objective of this approach is to decrease the dimensionality of the data, remove any extraneous information, and improve the ability of the dataset to distinguish between different classes. The accuracy of predictive models are influenced by a meticulously designed collection of characteristics, forming the foundation for their construction. (Hu, 2019).

Within this undertaking, the notion of Minimum Redundancy Maximum Relevance (MRMR) emerges as a prominent focus (VVR et al., 2023). The MRMR methodology, which is a feature selection method, places emphasis on the significance of feature relevance and the reduction of feature redundancy. This is achieved by the process of determining the most pertinent qualities that have a strong correlation with the target variable, while simultaneously minimizing any duplication or overlap among the chosen attributes [Hu et al., 2020; Ren et al., 2022; Moussa et al., 2022].

In addition, the Chi-Square (Chi2) independence methodology serves as an alternate method for feature selection. The Chi2 test is a valuable tool for measuring the degree of statistical independence between characteristics and the target variable. This methodology assesses the level of correlation between categorical variables, identifying which characteristics exhibit a significant level of independence from the dependent variable. The traits that have been found using the Chi2 demonstrate high predictive capabilities, and their inclusion in the model helps to mitigate problems related to collinearity (Silpa et al., 2023). Nevertheless, it is important to acknowledge that both the MRMR and Chi2 feature selection strategies include distinct limitations. The MRMR algorithm has the potential to choose features that are non-redundant but not necessarily independent, which might result in overfitting (Jo et al., 2019; Panigrahi et al., 2023). On the other hand, the Chi2 statistical test may have difficulties when confronted with continuous data and is not capable of adequately addressing the issue of feature redundancy (Rustam et al., 2020; Fang et al., 2023). By acknowledging the merits and limitations of different methodologies, a fresh and pioneering solution arises - the hybrid approach. The proposed methodology combines the MRMR and Chi2 methodologies, effectively overcoming the inherent limitations of both methods and establishing a comprehensive approach to feature selection (Samat et al., 2021; Subhash et al., 2022).

The integration of MRMR and Chi2 in the context of feature selection signifies a significant shift in the prevailing paradigm. This novel approach provides a

holistic solution that effectively identifies features that are not only useful for the prediction at hand but also possess statistical independence. The integration of many strategies addresses the limitations of each individual methodology and also holds the potential to significantly transform feature selection in the context of robust ensemble machine learning models (Wei et al., 2020; Lu et al., 2017; Kamala and Thangaiah, 2019).

In order to have a comprehensive understanding of the practical implications of this hybrid approach, it is crucial to acknowledge that ensemble ML models are the primary benefactors of this methodology. Ensemble models, which belong to a category of ML approaches, leverage the combined capabilities of numerous algorithms in order to improve prediction performance (Soumya et al., 2023; Silpa et al., 2022; Rao et al., 2022). Ensemble models offer a more precise and dependable predicted conclusion by combining the capabilities of many algorithms. The integration of feature selection and ensemble learning plays a crucial role in enhancing the resilience and flexibility of ML models in practical scenarios (Subbarao, et al., 2023).

The main objective of the present study is to introduce a novel approach that amalgamates MRMR and Chi2 for feature engineering, demonstrating its effectiveness through extensive experimentation. The results highlight the superiority of the hybridized approach over the independent use of MRMR and Chi2, showcasing substantial enhancements in model performance, reduced overfitting, and improved generalization. This work underscores the practical significance of adopting the hybrid approach for feature selection within the realm of machine learning, paving the way for more robust and adaptable ensemble models.

This article follows to a systematic pattern in order to give a thorough examination of the proposed framework. The introductory and related work section concurrently laid the groundwork for the study, offering contextual background and highlighting key literature review points that contribute to the comprehensive foundation of the research. The subsequent section explores processes of data collection and preparation in Section 2.1. Sections 2.2 and 2.3 concentrate on the use of feature engineering. These methodologies involve the utilization of MRMR, Chi2 and hybrid approach to enhance the process of feature selection. In Section 2.5, an incremental technique is shown. The design of an ensemble ML models are elaborated upon in Section 2.6, providing a comprehensive technique for the development of a robust model. Section 2.7 underscores the significance of progressively picking the top-K characteristics. The empirical study on the hybrid approach conducted in Section 3 offers substantiating evidence for the effectiveness of the framework. In conclusion, Section 4 provides a comprehensive summary of the obtained findings and presents relevant avenues for further research.

## 2. PROPOSED HYBRID FEATURE ENGINEERING FOR ENSEMBLE MACHINE LEARNING MODELS

The field of feature engineering in ensemble ML models witnesses a paradigm shift with the advent of a novel methodology that combines the strengths of MRMR and Chi2 independence feature selection techniques. The current study presents Hybrid Feature Engineering for Ensemble Machine Learning (HFE-EML) framework, the detailed architecture is shown in Figure 1. This hybridization offers a comprehensive solution for selecting features that are both highly relevant to the prediction task and statistically independent. Bridging the gap between relevance and independence addresses a critical challenge in feature engineering, ultimately leading to more robust and efficient ensemble models. In addition, by employing an incremental feature selection strategy, the HFE-EML ensures that ensemble ML models benefit from the most informative variables at each stage of the selection process.

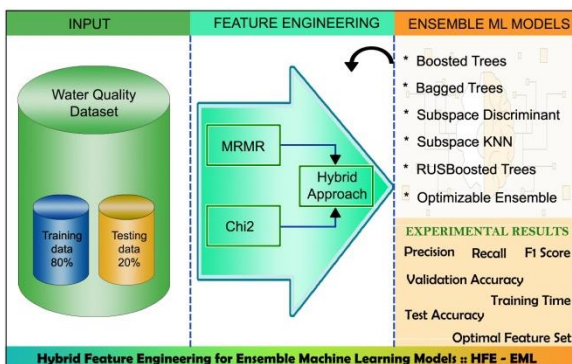


**Figure 1.** Architecture of proposed HFE - EML

The proposed HFE-EML follows a systematic approach, initially concentrates on the standard procedures for data collection and pre-processing. Later move the investigation on the hybrid approach of feature engineering by the insights of MRMR and independence of Chi2. Conduct a comprehensive analysis of hybridization's impact on ensemble machine learning model performance.

### 2.1 Data Collection and Preparation

Data collection plays a crucial role in the HFE-EML methodology. Selecting high-quality datasets is essential to assess the robustness of feature engineering and the effectiveness of ensemble ML models. The framework sources datasets from the open UCI repository, focusing on careful curation to include a wide range of characteristics and complexities. This diversity is fundamental in testing the feature engineering process and evaluating ensemble model robustness, key aspects of HFE-EML. The data collection process establishes a strong foundation for research in feature engineering and ensemble models within the HFE-EML framework.

Data preparation is an integral phase within the proposed HFE-EML methodology, where the collected dataset is thoroughly processed to ensure their readiness for feature engineering and subsequent ensemble ML model building. The initial phase of this process involves performing data cleaning procedures to address the presence of missing values and outliers. Additionally, categorical variables are encoded to ensure compatibility with machine learning algorithms. The issue of scaling and normalization of characteristics is also discussed, which improves the ability to compare various properties. The process of data preparation is crucial for establishing the foundation for future feature engineering approaches. This phase plays a significant role in enhancing the strength and dependability of ensemble ML models.

### 2.2 Feature Engineering with MRMR Insight

Feature engineering plays a pivotal and transformational role in the field of machine learning and data analysis. The process encompasses the amalgamation of artistic and scientific principles in order to carefully choose, modify, and generate significant features from unprocessed data. This procedure possesses the potential to significantly influence the efficacy of a ML model. Carefully designed features have the power to reveal concealed patterns, boost the accuracy of predictions, mitigate overfitting issues, and raise the comprehensibility of ML models. Feature engineering serves as a crucial intermediary process that establishes a connection between unprocessed data and the valuable insights and predictive capabilities offered by sophisticated ML models. One notable feature engineering strategy is the MRMR approach, which is recognised for its robustness and ability to provide valuable insights in the field of feature engineering.

The MRMR method, which is grounded in information theory, quantifies the association between characteristics and the target variable by taking into account both the significance and the overlap of features. This methodology offers a thorough perspective on the significance of features, guaranteeing that the chosen characteristics not only enhance predicted accuracy but also minimise the presence of redundant information. The primary objective of MRMR is to ascertain the most informative traits while simultaneously eliminating redundant ones.

To harness the insights provided by MRMR in feature engineering, the proposed HFE-EML framework meticulously calculates MRMR scores for each feature. These scores are computed based on their relevance to the target variable and their potential redundancy with other features. These MRMR scores play a pivotal role in guiding Algorithm 1, facilitating the selection of the most informative and non-redundant features essential for effective model training.

Algorithm 1 within the HFE-EML framework commences with the initialization of an empty set designated for storing ranked features, known as RFS. It relies on the concept of Feature Relevance (FR) to establish connections between individual features and the target class variable (Cy). The feature relevance metric is adeptly computed using entropy, ensuring the capture of critical information.

---

**Algorithm 1: Ranking Top Features with MRMR Insights in the HFE-EML Framework**

**Input:** Fx: The feature matrix (nd x nf), where nd is the number of data samples and nf is the number of features, Cy: The Class variable

**Output:** MRMR - Ranked features

1. Start with a null Ranked Feature Set RFS to store the ranked features.
  2. Determine the Feature Relevance (FR) between each feature and the target class variable Cy.
  3.  $FR(f, Cy) = H(f) + H(Cy) - H(f, Cy)$ , where H() demotes entropy.
  4. For each feature f in Fx:
    - a. Calculate  $FR(f, Cy)$ .
  5. Arrange the features in a descending order according to their FR values
  6. Initialize a variable i ( $i = 0$ ) to keep track of the number of selected features.
  7. While  $i < k$  ( $k$  is the desired number of selected features):
    - a. For each feature f in Fx (descending order of FR):
      - i. If f is not in RFS:
        - a. Determine the conditional FR (CFR) between f and each feature already in RFS.
        - b.  $CFR(f, RFS) = FR(f, Cy) - (1/|RFS|) * \sum FR(f, r)$ , where r is each feature in RFS.
        - c. Select the feature with the highest CFR(f, RFS) and add it to RFS.
        - d. Increment i by 1.
  8. Return the ranked features set RFS.
- 

The proposed HFE-EML framework is meticulously designed, making significant use of MRMR insights within Algorithm 1 to address challenges and streamline the feature selection process for ensemble models. By capitalizing on the power of MRMR, this framework adeptly combines feature relevance, conditional relevance, and entropy to identify and prioritize the most informative features critical for model construction. Notably, the HFE-EML framework is not confined to a specific type of ensemble model; it is highly adaptable and can be seamlessly integrated with a wide spectrum of ensemble techniques, ensuring its applicability across diverse domains and applications.

### 2.3 Feature Engineering with Chi2 Independence

While "Feature Engineering with MRMR Insight" sheds light on features with high relevance and low redundancy, Feature Engineering with Chi2 Independence delves into an alternative approach by harnessing the power of Chi2 independence. The Chi2 independence test evaluates the degree of statistical independence between two categorical variables. This statistical test assesses the presence of a relationship between two category variables by comparing observed frequencies with predicted ones. For numerical attributes, the Chi2 test can be modified by discretizing the data into categories or bins, effectively treating them as categorical variables. This allows the Chi2 to assess the relationship between the target variable and the bins of the continuous variable.

The proposed framework utilizes Algorithm2 that harnesses Chi2 independence, a pivotal step in optimizing feature selection within feature engineering. By calculating the Chi2 statistic for each feature, Algorithm2 meticulously assesses the level of statistical independence between individual features and the target variable, often representing a categorical class label. As it prioritizes features with higher Chi2 values, this algorithm ensures that only the most independent and informative features are selected for effective predictive modelling within the HFE-EML framework.

---

**Algorithm 2: Ranking Top Features with Chi2 Independence in the HFE-EML Framework**

**Input:** Fx: The feature matrix (nd x nf), where nd is the number of data samples and nf is the number of features, Cy: The Class variable

**Output:** Chi2 - Ranked features

1. Start with a null ranked feature set RFS to store the ranked features.
  2. For each feature f in Fx:
    - a. Generate a contingency table among feature f and the target variable Cy.
      - i. The table should have rows representing the unique values of feature fx and columns representing the unique class labels in Cy.
      - ii. Each cell (i, j) in the contingency table represents count of samples that have feature value i and belong to class j.
    - b. Calculate the Chi2 statistic value for feature f:
      - i.  $\text{Chi2}(f) = \sum [(O_{ij} - E_{ij})^2 / E_{ij}]$ , where  $(O_{ij})$  is the observed count in cell (i, j), and  $(E_{ij})$  is the expected count.
      - ii. The expected count  $(E_{ij})$  can be calculated as  $(\text{row total} * \text{column total}) / \text{grand total}$ .
    - c. Calculate the degrees of freedom (df) for the Chi2 test, which is  $(\text{number of unique feature values} - 1) * (\text{no. of unique class labels} - 1)$ .
-

- 
- d. Calculate the p-value for the Chi2 statistic value using the Chi-squared distribution with df degrees of freedom.
  - 3. Arrange the features in a descending order according to their Chi2 values (higher values indicate stronger independence).
  - 4. Set a significance level (alpha) to determine feature selection.
  - 5. While the p-value of the feature with the highest Chi2 value is less than alpha:
    - a. Add the feature with the highest Chi2 value to the set RFS.
    - b. Recalculate the p-values for the remaining features.
  - 6. Return the ranked features set RFS
- 

Following Algorithm2, which ranks features with Chi2 independence in the HFE-EML Framework, the selected features are essential for enhancing predictive model performance. The chi2-driven features are instrumental in constructing accurate and efficient machine learning models, ensuring a streamlined and optimized feature engineering process within the HFE-EML framework.

## 2.4 Feature Engineering with Hybrid Approach

The hybrid method aims to revolutionize the feature engineering process by combining insights from MRMR with the power of Chi2 to optimize feature selection for ensemble models. The core principles are:

- **Comprehensive Feature Assessment:** The hybrid approach integrates the strengths of MRMR to emphasize feature relevance and Chi2 independence to focus on feature independence. This dual consideration provides a comprehensive assessment of feature importance.
- **Optimized Feature Selection:** This approach ensures that the selected features not only contribute significantly to predictive accuracy but also minimize redundancy. This duality contributes to more effective feature selection.
- **Improved Model Robustness:** The hybrid approach offers the promise of enhancing model generalization and robustness by combining the unique benefits of MRMR and Chi2 independence. Features selected using this approach are more likely to perform well on new, unseen data.
- **Scalability and Adaptability:** Just as with MRMR and Chi2, this hybrid approach is adaptable to a wide range of ensemble techniques and is suitable for both small and large datasets.

Algorithm3 represents a dynamic and adaptable feature selection methodology embedded in the proposed HFE-EML framework. This innovative algorithm harmonizes the robust qualities of MRMR and Chi2 independence while introducing an incremental feature selection process. It is designed to continuously enhance feature selection as the ensemble model's performance evolves.

---

### Algorithm 3: Hybrid MRMR and Chi2 Feature Selection with Adaptive Incremental Approach

**Input:** Fx: The feature matrix ( $n \times m$ ), where n is the number of data samples, and m is the number of features, Cy: The Class variable, Ensemble Models, Evaluation Metrics

**Output:** HFE-EML Ranked features.

---

- 1. Initialize an empty set RFS to store the ranked features.
- 2. Apply the MRMR procedure (using Algorithm 1) to select the initial set of features, denoted as MRMR\_FSet.
- 3. Apply the Chi2 procedure (using Algorithm 2) to select the initial set of features, denoted as Chi2\_FSet.
- 4. Initialize J ( $J = 0$ ) to keep track of the number of selected features.
- 5. Initialize K ( $K = a$  small value) to control the incremental feature selection process.
- 6. While the ensemble model's performance continues to improve:
  - a. For each feature f in Fx:
    - i. If f is not in RFS:
      - a. Calculate the conditional Chi2 (CChi2) between feature f and each feature in Chi2\_FSet.
      - b.  $CChi2(f, Chi2\_FSet) = Chi2(f, y) - (1/|Chi2\_FSet|) * \sum Chi2(f, s)$ , where s is each feature in Chi2\_FSet.
      - c. Calculate the conditional MRMR (CMRMR) between feature f and each feature in MRMR\_FSet.
      - d.  $CMRMR(f, MRMR\_FSet) = MRMR(f, y) - (1/|MRMR\_FSet|) * \sum MRMR(f, s)$ , where s is each feature in MRMR\_FSet.
    - b. Select the feature with the highest CChi2(f, Chi2\_FSet) or CMRMR(f, MRMR\_FSet), whichever yields a higher value, and add it to S.
    - c. Remove the selected feature from both MRMR\_FSet and Chi2\_FSet.
    - d. Increment J by 1.
    - e. If J is greater than or equal to K:
  - 7. Train the ensemble model using the features in RFS.
  - 8. Evaluate the ensemble models' performance using the specified Evaluation\_Metric.
  - 9. If the performance improves, increase K by a small value.
  - 10. If the performance does not improve, stop the incremental feature selection process.
  - 11. Return the selected features RFS.

---

The integration of Minimum Redundancy Maximum Relevance (MRMR) and Chi-squared (Chi2) independence in Algorithm 3 represents a ground breaking approach to optimizing feature selection. This

algorithm not only seamlessly combines these two methods but also introduces an incremental process that continuously monitors and enhances the performance of ensemble machine learning models. By doing so, Algorithm 3 ensures that only the most informative and independent features are incorporated into the final selection, promising a more accurate and robust ensemble model. This adaptability is particularly valuable in real-world scenarios, where model performance can evolve over time. Algorithm 3's dynamic and responsive feature selection process aligns with the evolving nature of both the data and the models themselves. In essence, this algorithm stands poised to make significant contributions to the development of ensemble machine learning models that excel in adaptability and performance.

## 2.5 Select the Top-K Features in Incremental Approach

In the quest for optimizing feature selection within the HFE-EML framework, one essential component emerges that is incremental feature engineering to select the Top-K Features. The incremental approach integrates seamlessly with HFE-EML, providing a dynamic and adaptive solution to ensure that only the most informative features are chosen for the ensemble model. The approach begins with an initial feature set and continually assesses their relevance to the evolving ensemble model's performance. The key is to identify the top-K features, where K is determined by a predefined threshold and the model's performance. Features are continuously evaluated, and those that no longer significantly contribute are removed. This iterative approach ensures the ensemble model operates with the most pertinent attributes, enhancing its performance and adaptability. By combining elements of MRMR and Chi2 methodologies, this process strikes a balance between informativeness and independence for an optimal feature set.

## 2.6 Ensemble ML Models Construction

In the quest, the construction of ensemble machine learning models stands as a cornerstone in the predictive modeling landscape. Within the proposed HFE-EML framework, a diverse array of ensemble models is harnessed to bring about superior predictive performance. These models include:

- **Boosted Trees:** Using the power of boosting techniques, boosted trees combine the predictions of multiple decision trees to improve the accuracy of the model. Their adaptability and ability to concentrate on difficult data points make them invaluable members of the ensemble.
- **Bagged Trees:** Bagged trees employ an aggregation technique to combine the outcomes of several decision trees, each of which is trained on a randomly selected portion of the available data. The presence of variety within a dataset serves to

mitigate the problem of overfitting.

- **Subspace Discriminant:** Subspace discriminant models identify and capitalize on discriminative subspaces within the data. By concentrating on specific feature combinations, these models can extract complex patterns that might be overlooked by traditional methods.
- **Subspace KNN:** The technique of subspace K-nearest neighbours (KNN) involves the utilisation of the KNN algorithm across several feature subspaces. This facilitates a more detailed examination and can be especially advantageous when dealing with high-dimensional data.
- **RUSBoosted Trees:** RUSBoosted Trees combine the boosting methodology with random under sampling (RUS) approaches in order to effectively address the issue of unbalanced datasets.
- **Optimizable Ensemble:** The key component of the HFE-EML methodology is the optimizable ensemble model. The method facilitates the flexible choice and refinement of ensemble models, accommodating the unique attributes of the dataset and the specific demands of the task at hand.

The HFE-EML framework offers a wide range of ensemble models that cater to various data sources and prediction goals. By combining several approaches, these models provide the potential to achieve higher predicted accuracy, enhance model robustness, and exhibit flexibility in a wide range of data circumstances.

## 2.7 Select the Top-K Features in Incremental Approach

To ensure that the ensemble models operate at their optimal potential, a rigorous evaluation process is undertaken. This evaluation includes the application of the hybrid approach to feature engineering, optimizing the feature selection process by incorporating insights from both MRMR and Chi2 methodologies. Through fine-tuning the feature set for each ensemble model, the framework identifies the most informative and independent attributes, thereby enhancing the overall predictive power of the models.

The final choice of the ensemble model is influenced by the specific characteristics of the dataset and the unique requirements of the problem at hand. The model that excels in capturing and utilizing the intrinsic data patterns is selected as the best fit for the proposed HFE-EML framework. This ensemble model stands out as the ultimate predictive tool, embodying the framework's primary goal of developing highly accurate and robust predictive models tailored to the challenges and intricacies of the dataset.

## 3. EXPERIMENTAL RESULTS

This section undertakes a comprehensive assessment of the proposed method's validity through a series of

experiments. A dataset sourced from UCI serve as the foundation for this analysis. All experiments are conducted using MATLAB R2023b on a Windows 10 PC equipped with an Intel Core i7 and 16 GB RAM, ensuring a robust computing environment for reliable results. The experiments delve into the efficacy of three distinct feature engineering approaches: MRMR, Chi2, and the proposed hybrid approach, each aiming to enhance the feature selection process. Additionally, six ensemble models—Boosted Trees, Bagged Trees, Subspace Discriminant, Subspace KNN, RUSBoosted Trees, and the Optimizable Ensemble are implemented and evaluated. The results of experiments provide valuable insights into the performance of the proposed method, as presented in the subsequent sections.

In the presented results, the metric labels are defined as follows: "P" corresponds to Precision, "R" represents Recall, "F1" designates the F1 Score, and "VA" signifies Validation Accuracy. These metrics are fundamental in assessing the performance and effectiveness of all ML models.

The experimental results shown in Table 1, shed light on the significance of feature engineering in enhancing an ensemble boosted trees ML model. When the number of features (K) is set to 10, all the feature selection techniques, including MRMR, Chi2, and the proposed HFE-EML, demonstrate relatively similar levels of accuracy, reaching approximately 93.2% to 93.4%. However, it's essential to note that the sequential feature selection lags slightly behind in performance, with a value of 91.6%. The proposed HFE-EML method not only achieves higher accuracy in validation and also demonstrates superior precision, recall, and F1 scores when compared to other techniques. This highlights its robustness in effectively handling a larger number of features, a characteristic shared with boosted trees.

**Table 1.** Results of Feature Engineering on Ensemble Boosted Trees ML Model

Feature Engineering	P	R	F1	VA
<b>No. of Features K=10</b>				
Sequential Features	97.67	94.66	96.14	91.60
Using MRMR	98.46	94.18	96.27	93.20
Using Chi2	98.00	93.01	95.44	<b>93.41</b>
Proposed HFE-EML	98.35	94.33	96.30	93.39
<b>No. of Features K=14</b>				
Sequential Features	97.81	94.16	95.95	93.00
Using MRMR	98.52	96.74	97.62	94.30
Using Chi2	98.52	96.74	97.62	94.30
Proposed HFE-EML	99.01	96.36	97.67	<b>94.81</b>
<b>No. of Features K=16</b>				
Sequential Features	99.29	96.24	97.74	94.60
Using MRMR	97.43	97.43	97.43	94.30
Using Chi2	97.49	97.50	97.50	95.20
Proposed HFE-EML	97.63	97.64	97.64	<b>96.90</b>

Feature engineering was applied to 20% of the test data, and the resulting accuracy scores achieved by boosted trees for various K values are illustrated in Figure 2. The proposed approach consistently outperforms both MRMR and Chi2 in generating favourable results.

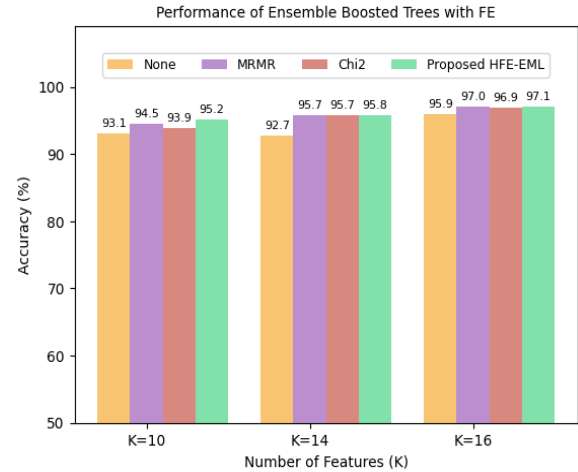


**Figure 2.** Performance of Ensemble Boosted Trees

The results presented in Table 2 highlight the impact of feature engineering on an ensemble bagged trees ML model. In the context of bagged trees, the proposed HFE-EML method consistently demonstrates its effectiveness by achieving high F1-scores and validation accuracy. The only exception is when k=14, where MRMR outperforms HFE-EML. This deviation could be attributed to the intricate interplay between the dataset's characteristics and the specific feature selection requirements at that particular K value, which may favor MRMR's approach.

**Table 2.** Results of Feature Engineering on Ensemble Bagged Trees ML Model

Feature Engineering	P	R	F1	VA
<b>No. of Features K=10</b>				
Sequential Features	97.1	94.63	95.85	92
Using MRMR	98.45	94.89	96.64	93.4
Using Chi2	98.09	94.94	96.49	93.2
Proposed HFE-EML	98.23	96.2	97.2	<b>93.9</b>
<b>No. of Features K=14</b>				
Sequential Features	97.67	93.70	95.65	92.20
Using MRMR	98.66	96.21	97.42	<b>95.01</b>
Using Chi2	98.31	96.33	97.31	94.60
Proposed HFE-EML	98.23	96.46	97.34	94.7
<b>No. of Features K=16</b>				
Sequential Features	96.29	96.29	96.29	94.80
Using MRMR	97.56	97.56	97.56	94.50
Using Chi2	97.63	97.64	97.64	95.80
Proposed HFE-EML	97.77	97.77	97.77	<b>95.90</b>

Figure 3 displays the outcomes of feature engineering on bagged trees with various K values when evaluated on test data. It reveals a marginal improvement in the performance of the proposed approach compared to other methods.

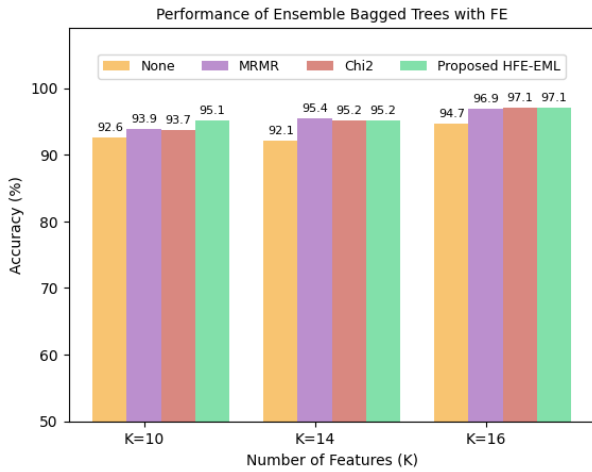


**Figure 3.** Performance of Ensemble Bagged Trees

In the analysis, the ensemble subspace discriminant demonstrated lower performance compared to boosted trees and bagged trees, even after applying feature engineering techniques. However, a notable exception emerged at k=16, as indicated in Table 3. In this case, the proposed HFE-EML method achieved a remarkable accuracy of 91.12, outperforming the other models.

**Table 3.** Results of Feature Engineering on Ensemble Subspace Discriminant ML Model

Feature Engineering	P	R	F1	VA
<b>No. of Features K=10</b>				
Sequential Features	96.33	88.80	92.41	87.50
Using MRMR	98.87	89.69	94.05	<b>89.30</b>
Using Chi2	99.22	89.43	94.07	89.00
Proposed HFE-EML	98.87	89.69	94.05	89.20
<b>No. of Features K=14</b>				
Sequential Features	99.15	90.06	94.39	89.00
Using MRMR	98.94	89.69	94.09	89.40
Using Chi2	99.22	89.84	94.30	89.20
Proposed HFE-EML	99.01	89.99	94.28	<b>89.41</b>
<b>No. of Features K=16</b>				
Sequential Features	89.78	89.78	89.78	88.90
Using MRMR	89.60	89.60	89.60	89.30
Using Chi2	90.16	90.17	90.17	89.00
Proposed HFE-EML	90.64	90.65	90.65	<b>91.12</b>

The experimental findings were further corroborated by the test data results, including those for the Ensemble Subspace Discriminant model, as presented in Figure 4. These results show a consistent pattern that reinforces the effectiveness of the HFE-EML method in achieving superior accuracy.

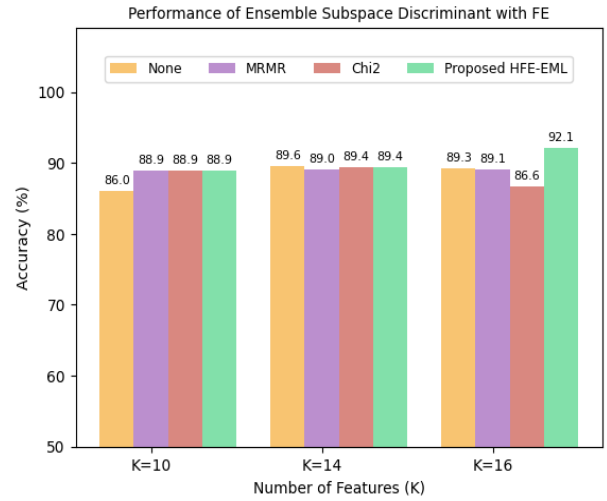


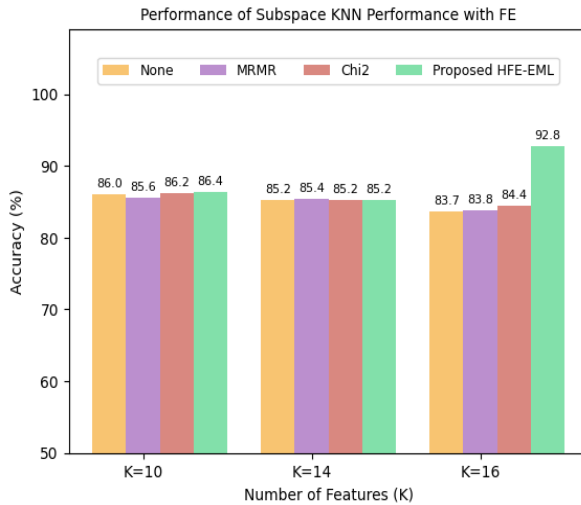
**Figure 4.** Performance of Ensemble Subspace Discriminant

The results from Table 4 highlight variations in the performance of the ensemble subspace KNN model across different feature engineering methodologies and K values. However, a remarkable improvement is observed when considering a higher number of features, particularly at K=16, where the proposed hybrid model demonstrates noticeable performance.

**Table 4.** Results of Feature Engineering on Ensemble Subspace KNN ML Model

Feature Engineering	P	R	F1	VA
<b>No. of Features K=10</b>				
Sequential Features	96.33	88.80	82.41	87.50
Using MRMR	95.90	88.76	92.19	<b>87.70</b>
Using Chi2	96.33	88.98	92.51	87.30
Proposed HFE-EML	96.61	88.95	92.62	86.80
<b>No. of Features K=14</b>				
Sequential Features	94.78	89.18	91.89	<b>86.90</b>
Using MRMR	95.55	88.78	92.04	86.00
Using Chi2	94.78	89.18	91.89	85.88
Proposed HFE-EML	94.63	89.27	91.88	85.60
<b>No. of Features K=16</b>				
Sequential Features	88.69	88.69	88.69	87
Using MRMR	89.01	89.01	89.01	88
Using Chi2	88.97	88.97	88.97	86.3
Proposed HFE-EML	90.71	90.71	90.71	<b>92.56</b>

Similar to the ensemble subspace discriminant model's performance, the ensemble subspace KNN exhibits lower test accuracy levels in comparison to boosted and bagged trees on the selected dataset. However, as the number of features increases, the proposed methodology demonstrates outperformance, as depicted in Figure 5.

**Figure 5.** Performance of Subspace KNN Performance

As indicated by the data showcased in Table 5, RUSBoosted Trees demonstrate superior performance compared to other ensemble machine learning techniques investigated thus far. This noteworthy result underscores the effectiveness of RUSBoosted Trees in the context of the study's evaluation and contributes valuable insights to the research findings.

**Table 5.** Results of Feature Engineering on Ensemble RUSBoosted Trees ML Model

Feature Engineering	P	R	F1	VA
<b>No. of Features K=10</b>				
Sequential Features	91.95	96.44	94.14	89.8
Using MRMR	86.79	98.01	92.06	87.70
Using Chi2	89.34	97.83	93.39	89.80
Proposed HFE-EML	94.14	98.45	96.25	<b>92.30</b>
<b>No. of Features K=14</b>				
Sequential Features	91.11	97.51	94.20	88.40
Using MRMR	92.66	98.87	95.66	93.60
Using Chi2	94.71	97.74	96.02	93.40
Proposed HFE-EML	89.27	99.06	93.91	<b>93.50</b>
<b>No. of Features K=16</b>				
Sequential Features	97.42	97.42	97.42	92.01
Using MRMR	99.11	99.11	99.11	93.60
Using Chi2	94.71	97.74	96.02	93.40
Proposed HFE-EML	89.27	99.06	93.91	<b>93.79</b>

This model stands out for its commendable accuracy, showcasing robust performance even without feature engineering. Figure 6 visually confirms the model's strong performance, demonstrating its effectiveness not only in training but also in maintaining accuracy when applied to testing data, emphasizing its reliability across different datasets.

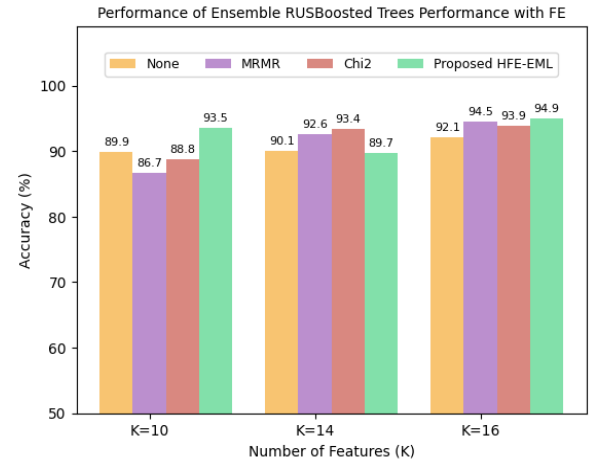
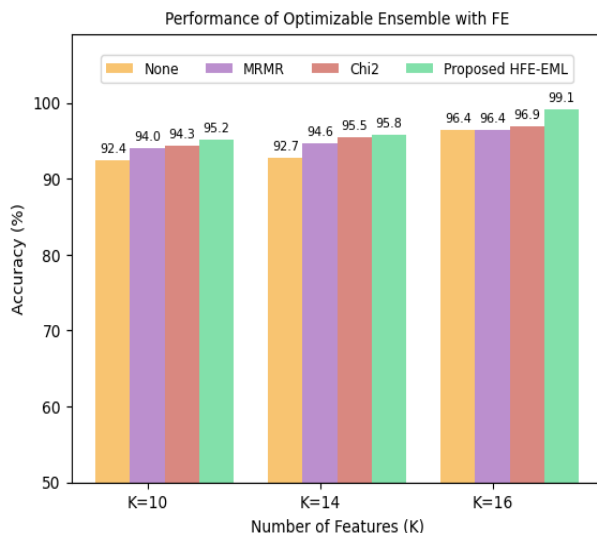
**Figure 6.** Performance of Ensemble RUSBoosted Trees

Table 6 presents intriguing insights into the impact of various feature engineering methods on an Optimizable Ensemble ML Model across varying feature dimensions (K).

**Table 6.** Results of Feature Engineering on Optimizable Ensemble ML Model

Feature Engineering	P	R	F1	VA
<b>No. of Features K=10</b>				
Sequential Features	97.10	94.44	95.75	92.30
Using MRMR	98.38	95.02	96.67	93.50
Using Chi2	98.73	95.04	96.85	93.60
Proposed HFE-EML	98.35	95.37	96.84	<b>94.30</b>
<b>No. of Features K=14</b>				
Sequential Features	97.74	94.28	95.98	93.50
Using MRMR	97.03	96.83	96.93	95.50
Using Chi2	98.59	96.41	97.49	95.50
Proposed HFE-EML	99.29	97.20	98.24	<b>95.80</b>
<b>No. of Features K=16</b>				
Sequential Features	97.42	97.42	97.42	93.9
Using MRMR	97.42	97.42	97.42	93.9
Using Chi2	97.49	97.50	97.50	96.0
Proposed HFE-EML	99.15	99.16	99.16	<b>98.96</b>

The "Proposed HFE-EML" method consistently excels, achieving impressive results even with a larger feature set of 16, and notably, it performs better than all employed ensemble ML models. Moreover, on test data also it outperforms, as illustrated in Figure 7, confirming its robustness and generalizability. High accuracy suggests robust generalization to unseen data, particularly noteworthy for the "Proposed HFE-EML" method. These results underscore the Optimizable Ensemble ML Model's capacity for enhancement through feature engineering, implying that, with careful optimization and feature selection, it is possible to build highly accurate and robust predictive models.



**Figure 7.** Performance of Optimizable Ensemble

The experimental results unequivocally establish the superiority of the hybrid approach, Proposed HFE-EML, surpassing various ensemble methods in precision, recall, F1-score, and accuracy. This exceptional performance persists consistently through the incremental feature engineering stages applied to the utilized water quality dataset, affirming the effectiveness and robustness of the proposed model.

#### 4. CONCLUSION AND FUTURE WORK

This research has addressed the significant challenge of handling extensive real-world datasets in the field of data science. The abundance of input features, many of which lack relevance or may be redundant, poses a considerable hurdle to the effectiveness of ensemble ML models. While feature engineering aims to eliminate irrelevant and redundant features, selecting an optimal subset remains a challenging problem.

This study has introduced a novel framework for feature engineering by combining the MRMR and Chi2 independence feature selection techniques. MRMR focuses on feature relevance and non-redundancy, while Chi2 quantifies feature independence from the target variable. The hybridization of MRMR and Chi2 offers a comprehensive solution that selects features both informative to the prediction task and statistically independent. This hybrid framework follows an incremental feature engineering approach and aims to enhance ensemble ML models, improving predictive accuracy, model robustness, and adaptability. The experimental results clearly demonstrate that, with the proposed hybrid approach, an accuracy of 99.10% can be achieved in predicting water quality. Additional investigation can delve into the dynamic adaptation of feature selection techniques in the context of changing data streams.

#### References:

- Cui, X., Li, Y., Fan, J., Wang, T., & Zheng, Y. (2020). A hybrid improved dragonfly algorithm for feature selection. *IEEE Access*, 8, 155619-155629. doi: 10.1109/ACCESS.2020.3012838
- Fang, Y., Wei, S., Zhao, Y., Zhang, L., & Chen, L.-L. (2023). Radar-Specific Emitter Identification With Only Envelope Power Based on Multidimensional Complex Noncentral Chi-Square Classifier. *IEEE Sensors Journal*, 23(17), 20223-20235. doi : 10.1109/JSEN.2023.3298352.
- Hu, K., Wang, J., Liu, Y., & Chen, D. (2019). Automatic feature engineering from very high-dimensional event logs using deep neural networks. In *Proceedings of the 1st International Workshop on Deep Learning Practice for High-Dimensional Sparse Data* (pp. 1-9). Association for Computing Machinery. doi: 10.1145/3326937.3341262
- Hu, Q., Si, X. et al. (2020). Machinery fault diagnosis scheme using redefined dimensionless indicators and mRMR feature selection. *IEEE Access*, 8, 40313-40326. doi: 10.1109/ACCESS.2020.2976832.
- Jo, I., Lee, S., & Oh, S. (2019). Improved measures of redundancy and relevance for mRMR feature selection. *Computers*, 8(2), 42. doi: 10.3390/computers8020042
- Kamala, R., & Thangaiah, R. J. (2019). An improved hybrid feature selection method for huge dimensional datasets. *IAES International Journal of Artificial Intelligence*, 8(1), 77.
- Kumar, P., & Pratap, B. (2023). Feature engineering for predicting compressive strength of high-strength concrete with machine learning models. *Asian Journal of Civil Engineering*, 1-14.
- Kurada, R. R., Kanadam, K. Pavan, Ramu, Y., Silpa, N., Rao, V. V. R. M., & Pattem, S. (2023). Story Telling with Basic and Advanced Data Visualizations of Blockchain Technologies. In *Int. Conf. on Augmented Intelligence and Sustainable Systems (ICAIS)* (pp. 1254-1259). doi:10.1109/ICAIS58487.2023.10250661.
- Lu, H., Chen, J., Yan, K., Jin, Q., Xue, Y., & Gao, Z. (2017). A hybrid feature selection algorithm for gene expression data classification. *Neurocomputing*, 256, 56-62. doi: <https://doi.org/10.1016/j.neucom.2016.07.080>.
- Moussa, M. M., Alzaabi, Y., & Khandoker, A. H. (2022). Explainable Computer-Aided Detection of Obstructive Sleep Apnea and Depression. *IEEE Access*, 10, 110916-110933. doi: 10.1109/ACCESS.2022.3215632.
- Panigrahi, A., et al. (2023). En-MinWhale: An Ensemble Approach Based on MRMR and Whale Optimization for Cancer Diagnosis. *IEEE Access*, 11, 113526-113542. <https://doi.org/10.1109/ACCESS.2023.3318261>.

- Ramla, M. (2019). Influence of Feature Selection Methods on Cardiotocography Data: A Quantitative Investigation. Int. Journal of Engineering and Advanced Technology (IJEAT), 8(4S2). doi: 10.35940/ijeat.D1006.0484S219
- Rao, V. V. R. Maheswara, et al. (2023). An Optimal Machine Learning Model Based On Selective Reinforced Markov Decision To Predict Web Browsing Patterns. Journal of Theoretical and Applied Information Technology, 101(2), 859-873.
- Rao, V. V. R. Maheswara, Silpa, N., Gadiraju, Mahesh, Shankar, Reddy Shiva. (2022). An Enhanced Machine Learning Classification System to Investigate the Status of Micronutrients in Rural Women. Lecture Notes in Networks and Systems, 341, doi: 10.1007/978-981-16-7118-0\_4.
- Ren, Z., Ren, G., & Wu, D. (2022). Deep Learning Based Feature Selection Algorithm for Small Targets Based on mRMR. Micromachines, 13(10), 1765. doi: <https://doi.org/10.3390/mi13101765>
- Rustam, F., Mehmood, A., Ahmad, M., Ullah, S., Khan, D. M., & Choi, G. S. (2020). Classification of Shopify App User Reviews Using Novel Multi Text Features. IEEE Access, 8, 30234. doi: 10.1109/ACCESS.2020.2972632.
- Samat, A.,et al. (2021). GPU-Accelerated CatBoost-Forest for Hyperspectral Image Classification Via Parallelized mRMR Ensemble Subspace Feature Selection. IEEE Journal of Selected Topics in Applied Earth Observations and Remote Sensing, 14, 3200-3214. <https://doi.org/10.1109/JSTARS.2021.3063507>.
- Silpa, N., R. V. V. R. M., Subbarao, M. V., Pradeep, M., Grandhi, C. R., & Karunasri, A. (2023). A Robust Team Building Recommendation System by Leveraging Personality Traits Through MBTI and Deep Learning Frameworks. In EditorInitials. EditorLastName (Ed.), 2023 International Conference on IoT, Communication and Automation Technology (ICICAT) (pp. 1-6). doi:10.1109/ICICAT57735.2023.10263718.
- Silpa, N., Rao, V. M., et al. (2023, May). An Enriched Employee Retention Analysis System with a Combination Strategy of Feature Selection and Machine Learning Techniques. In 2023 7th Int. Conf.on Intelligent Computing and Control Systems (ICICCS) (pp. 142-149). IEEE. doi: 10.1109/ICICCS56967.2023.10142473
- Silpa, N., & Rao, V. M. (2022). Machine learning-based optimal segmentation system for web data using Genetic approach. Journal of Theoretical and Applied Information Technology, 100(11), 3552-3561.
- Soumya A. K., Ritu Shree, & Anu Sharma. (2023). Impact loading analysis of particulate polymer composites with an efficient hybrid machine learning approach. Proceedings on Engineering Sciences, 5(S1), 97-102.
- Subbarao, M. V., Rani, U. L. S., Sindhu, J. T. S., Kumar, G. P., Ravuri, V., & Silpa, N. (2023). A Comprehensive Study of Machine Learning Algorithms for Date Fruit Genotype Classification. In 2023 Int. Con. on Applied Intelligence and Sustainable Computing (ICAISC) (pp. 1-7). IEEE. doi: 10.1109/ICAISC58445.2023.10199785.
- Subhash, A., Kalyani, S., Al-Badarneh, Y. H., & Alouini, M.-S. (2022). On the Asymptotic Performance Analysis of the k-th Best Link Selection Over Non-Identical Non-Central Chi-Square Fading Channels. IEEE Transactions on Communications, 70(11), 7191-7206. <https://doi.org/10.1109/TCOMM.2022.3213276>.
- Uddin, M. F., Lee, J., Rizvi, S., & Hamada, S. (2018). Proposing Enhanced Feature Engineering and a Selection Model for Machine Learning Processes. Applied Sciences, 8(4), 646. doi: <https://doi.org/10.3390/app8040646>
- VVR, M. R., N. S., Gadiraju, M., Reddy, S. S., Bonthu, S., & Kurada, R. R. (2023). A Plausible RNN-LSTM based Profession Recommendation System by Predicting Human Personality Types on Social Media Forums. Int. Con. on Computing Methodologies and Communication (ICCMC) (pp. 850-855). doi:10.1109/ICCMC56507.2023.10083557.
- Wang, C., Baratchi, M., Bäck, T., Hoos, H. H., Limmer, S., & Olhofer, M. (2022). Towards time-series feature engineering in automated machine learning for multi-step-ahead forecasting. Engineering Proceedings, 18(1), 17.
- Wei, G., Zhao, J., Feng, Y., He, A., & Yu, J. (2020). A novel hybrid feature selection method based on dynamic feature importance. Applied Soft Computing, 93, 106337. doi: 10.1016/j.asoc.2020.106337

---

**Silpa N**

Centurion University of Technology  
and Management,  
Bhubaneswar,  
India  
nrusimhadri.silpa@gmail.com  
ORCID : 0000-0003-3411-0358

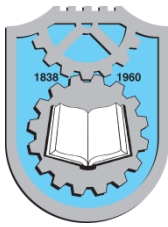
**Sangram Keshari Swain**

Centurion University of Technology  
and Management,  
Bhubaneswar,  
India  
sangram@cutm.ac.in  
ORCID : 0000-0002-6900-2851

**Maheswara Rao V V R**

Shri Vishnu Engineering College for  
Women,  
Bhimavarm,  
India  
mahesh\_vvr@yahoo.com  
ORCID : 0000-0002-0503-7211

---



## New Chung-Li Meteor Radar in Taiwan – Preliminary Results

Ching-Lun Su  
Po-Hsun Chiu  
Ruey-Ming Kuong  
Hsyang-Chan Chen<sup>1</sup>  
Yen-Hsyang Chu  
A. Narendra Babu  
P. S. Brahmanandam

Keywords:

Meteor radar; Underdense Meteor Trail; Middle Atmosphere Neutral Wind Velocity; Interferometry.

### ABSTRACT

A new 39.9 MHz meteor radar was implemented in 2022 in Jhongli area, Taiwan, which is operated by National Central University in Taiwan and referred to as Chung-Li meteor radar. This radar is a bistatic radar with transmitter and receiver systems located at Bade City and Xinwu District, respectively, with a horizontal separation of about 22.3 km between them. The antenna array of the receiving system is composed of 5 cross-Yagi antenna elements for receiving circularly polarized radar returns from the meteor trails which is arranged in a cross shape with separations of 1.5□ or 2.5□ between different antenna pairs. In this article, detailed characteristics of the new Chung-Li VHF meteor radar will be introduced and the preliminary results of the meteor winds in height range from 80-110 km, which are estimated from the Doppler velocities of the echoes from under dense meteor trails, are presented. We find that the phases of observed meteor winds are in good agreement with those of Horizontal Wind Model (HWM). However, there are discrepancies in horizontal wind velocities between Chung-Li meteor radar observations and HWM model predictions. Plausible causes of the discrepancy are discussed.



© 202x Published by Faculty of Engineering

### 1. INTRODUCTION

Middle atmosphere that situates in height range from 50 to 100 km is a critical zone connecting lower and upper atmospheres. Scientists have long been aware that many quasi-periodic oscillations in temperature and density of thermosphere and wave-like variations in ionospheric electron density are results from the gravity waves associated with disturbances in lower atmosphere propagate upward through middle atmosphere and eventually into upper atmosphere to produce the

perturbation phenomena therein (Hines, 1959; Kelley, 1989; Fritts, 2003; Yu et al., 2017).

In light of its importance in the investigation of lower and upper atmospheric coupling, middle atmosphere has been observed and monitored globally not only in temporal, but also in spatial domains using different means, including in-situ measurement made with payloads on board sounding rockets (e.g., Chu et al., 2007), remote sensing using satellite payloads (e.g. Yee et al., 1999), optical all-sky imagery (Swenson and

<sup>1</sup> Corresponding author: Prof. Y H Chu & Dr. P S Brahmanandam  
e-mail: [yhchu@ss.jupiter.ss.ncu.edu.tw](mailto:yhchu@ss.jupiter.ss.ncu.edu.tw); [dranandpotula@svecw.edu.in](mailto:dranandpotula@svecw.edu.in)

Mende, 1994), coherent scatter radar (e.g., Murayama et al., 1999), GPS-based Satellite Radio Occultation techniques (Potula et al., 2011; Brahmanandam et al., 2012; Uma et al., 2016) and meteor radar (e.g., Su et al., 2014).

Meteor radar experiments conducted by a number of groups around the world have shown that there are discrepancies in the horizontal wind velocities between radar measurements and HWM model predictions (Hibbins et al., 2011; Day et al. 2012; Xiao et al., 2013; Su et al., 2014). In this article, an attempt is made to compare horizontal wind measured by newly implemented Chung-Li meteor radar in Taiwan to compare with those predicted by horizontal wind model (HWM) over Taiwan area. The characteristics of the Chung-Li meteor radar will be introduced in Section 2, in which interferometric technique that is used to compute angular position of the radar echoes from under dense meteor trains and the method of estimating horizontal wind velocity are also described. Comparison in the horizontal winds between meteor wind measurements and HWM model predictions are made in Section 3. Discussion and conclusion are drawn in Section 4.

## 2. SYSTEM DESCRIPTION

The Chung-Li meteor radar operating at 39.9 MHz is a pulsed-type bistatic radar with transmitter and receiver systems located at Bade City and Xinwu District, respectively, with a horizontal separation of about 22.3 km between them. Inter-pulse period is 1.6 ms and pulse width is 70  $\mu$ s, in which 7-bit Barker code is implemented for the observation of the radar echoes from under dense meteor trail. The radar probing range is from 70 to 218.5 km with a range resolution of 1.5 km. The transmitting antenna is a single cross-Yagi antenna, and the receiving antenna is composed of 5 cross-Yagi antenna elements to receive circularly polarized radar returns from the meteor trails. The receiving antenna array is arranged in a cross shape with separations of  $1.5\lambda$  or  $2.5\lambda$  between different antenna pairs.

With the configuration of this receiving antenna array, angular locations of the meteor trails can be calculated from the phase differences of the echoes between different pairs of the receiving antenna elements in accordance with specific interferometric equations exclusively for the Chung-Li meteor radar. The use of zenith and azimuth angles combined with the Doppler velocities of the detected meteor trails, the horizontal wind velocity deduced from the Doppler velocity of the under dense meteor trail echoes can be estimated. Details on the interferometric technique and radar signal analysis and processing, especially the procedure of radar system phase calibration based on the echoes from ionospheric field-aligned irregularities (FAIs) of

sporadic E (Es) layer combined with international geomagnetic reference field (IGRF) model, refer to Su et al. (2014).

## 3. OBSERVATIONAL RESULTS

Upper panel of Figure 1 shows a typical time series of the intensity of the radar echoes from under dense meteor trail, which is in an exponential decay over time with duration of about 0.5 s and a peak intensity of 84.22 dB. Middle panel depicts time series of the echo phase over time. From the slope of the echo phase, we can obtain corresponding Doppler velocity of 25.2 m/s. Lower panel presents a typical example of range-time-intensity distribution of under dense meteor trail echoes (bottom panel) detected by the Chung-Li meteor radar on March 11, 2023, at 00:36:12 LT, in which parallel echo patterns with stronger intensity located at range of 118 km and the relatively weak echoes distributed symmetrically above and below the central echos are clearly seen. Obviously, this horizontally stratified echo pattern is the result of the decoding process of the echoes with 7-bit Barker code.

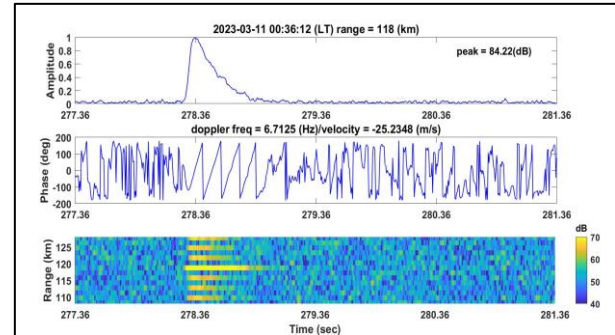


**Figure 1.** Typical example of time sequence of under dense meteor trail echoes with 7-bit Barker code.

Figure 2 shows angular and height distributions of the meteor trail echoes detected by the Chung-Li meteor radar on March 11, 2023, in which azimuth angle is measured with respect to due north and positive (negative) for eastward (westward) directions. As shown, there is a tendency for the occurrence of the meteor trails to peak in northeast direction with zenith angles of about  $40^\circ$ - $65^\circ$ . The height range that the meteor trail echoes occur is mainly from 70 to 110 km.

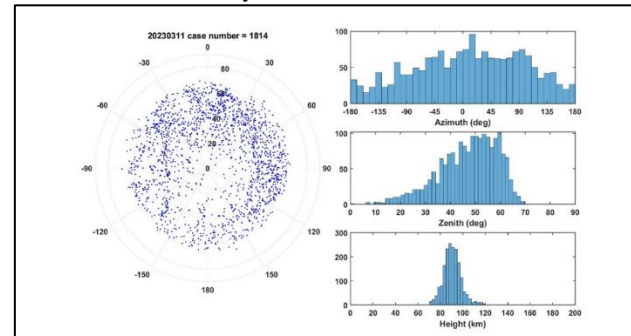


**Figure 2.** Angular and height distributions of the meteor trail echoes detected by the Chung-Li meteor radar on March 11, 2023.

Once angular locations and Doppler velocities of the meteor trail echoes are both obtained, the horizontal wind velocity in a specific height range and dwell time can be estimated in accordance with following matrix relation (Su et al., 2014)

$$\begin{bmatrix} \vec{V}_{r1} \\ \vec{V}_{r2} \\ \vdots \\ \vec{V}_{rN} \end{bmatrix} = \begin{bmatrix} \cos \phi_{M1} \sin \theta_{M1} & \sin \phi_{M1} \sin \theta_{M1} \\ \cos \phi_{M2} \sin \theta_{M2} & \sin \phi_{M2} \sin \theta_{M2} \\ \vdots \\ \cos \phi_{MN} \sin \theta_{MN} & \sin \phi_{MN} \sin \theta_{MN} \end{bmatrix} \begin{bmatrix} |\vec{V}| \cos \phi_v \\ |\vec{V}| \sin \phi_v \end{bmatrix} \quad (1)$$

Or

$$\mathbf{A} = \mathbf{B} \cdot \mathbf{C} \quad (2)$$

where  $\phi_{Mi}$  and  $\theta_{Mi}$  are, respectively, azimuth and zenith angles of  $i$ th meteor trail echo,  $|\vec{V}|$  denotes wind speed and  $\phi_v$  is wind direction,  $\mathbf{A}$  is column matrix of Doppler velocity  $\vec{V}_{ri}$ ,  $\mathbf{B}$  is position matrix and  $\mathbf{C}$  is column matrix of horizontal wind velocity components. As a result, we have

$$\mathbf{C} = \begin{bmatrix} |\vec{V}| \cos \phi_v \\ |\vec{V}| \sin \phi_v \end{bmatrix} = \begin{bmatrix} |\vec{V}| \cos \phi_v \\ |\vec{V}| \sin \phi_v \end{bmatrix} \quad (3)$$

where  $C_1$  and  $C_2$  are, respectively, meridional and zonal components of horizontal wind velocity. Figure 3 compares meridional (left panel) and zonal (right panel) wind velocity components observed by the meteor radar with those predicted by HWM model for the data on March 11, 2023. As indicated in right panel of Figure 3, the radar-observed zonal wind velocity bears good correlation with those of HWM model without phase discrepancy. Nevertheless, the former tends to be about 15-20% smaller than the latter at large. For the meridional wind velocity, the correlation between meteor radar observation and HWM model prediction is a little bit smaller than that for zonal wind. In addition, their mean bias error (MBE) and root mean square error (RMSE) are also larger than those of the zonal wind velocity.

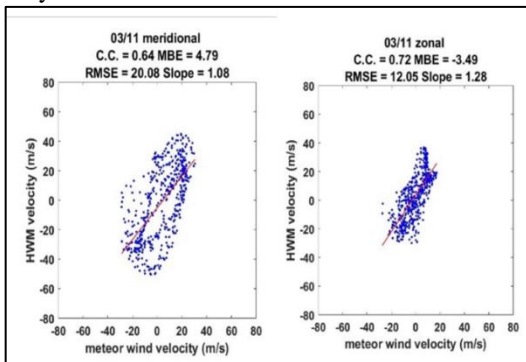


**Figure 3.** Scatter diagrams of radar-observed meridional (left panel) and zonal (right panel) wind velocity components observed by the meteor radar

versus model-predicted wind components for the data on March 11, 2023.

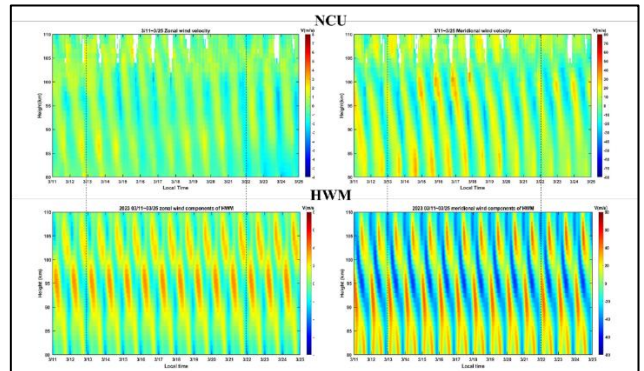


**Figure 4.** Comparisons of radar-observed meridional (right panels) and zonal (left panel) wind velocity components (upper panels) to those of HWM model predictions (lower panels) for March 11-25, 2023.

Figure 4 presents comparisons of time sequences of radar-observed meridional (right panels) and zonal (left panel) wind velocity components (upper panels) to those of HWM model predictions (lower panels) for the period of March 11-25, 2023. As shown, irrespective of its occurrence of very weak semidiurnal component below 90 km, zonal neutral wind component throughout height range from 90 to 110 km over Taiwan is primarily dominated by solar diurnal tides. It is obvious that the phases of the radar-observed solar diurnal tides are coherent with those of the HWM model predictions. However, detailed examination shows that there is around 90° phase shift in the meridional wind components between meteor radar observations and HWM model predictions in the height range between 80-105 km. Moreover, semidiurnal tides are present and dominate neutral wind oscillations below 90 km.

#### 4. DISCUSSION AND SUMMARY

As shown in Figure 2, a small number of the meteor trail echoes occurred in the height range above 110 km. It is very unlikely that the meter-scale under dense meteor trails can be survived in a time scale about 0.1-1 sec in upper region of ionospheric Es layer owing to large molecular diffusion coefficient and small ion-neutral collisional frequency (Kelley, 1989). Therefore, these echoes may be possibly resulted from the ionospheric Es FAIs through Bragg scattering (Chu et al. 2011). It is important to ascertain the sources of these unusual meteor trail echoes for the need of an operational system that is designed to persistently provides continuous horizontal wind velocity in middle atmosphere.

In addition to the anomalous meteor trail echoes, from Figures 3 and 4, the meteor radar-measured horizontal wind velocities are in general smaller than those predicted by HWM model. Su et al. (2014) has

compared meteor radar wind with HWM model wind using the data collected by 52 MHz Chung-Li meteor radar system during the Leonid meteor shower period of November 11-25, 2012. They found that radar-measured horizontal wind velocities are in general larger than those of HWM model predictions, in which a significant discrepancy in the two above 100 km can be as large as up to a factor of 5. Obviously, present results are not consistent with those obtained by Su et al. (2014). This feature suggests that HWM-predicted horizontal wind velocity in middle atmosphere may not be accurate enough to be representative of the true horizontal wind velocity over Taiwan area. Therefore, further and more analysis are required to better ascertain the validity of the HWM model.

In summary, the newly implemented Chung-Li meteor radar has shown that it is a workable radar system to detect the echoes from under dense meteor trails for the

remote sensing of horizontal wind velocity in middle atmosphere over Taiwan area. A comparison of the radar-measured horizontal wind velocity with those predicted by HWM model shows that the wind product of this radar system are reasonable and reliable, suggesting the algorithms of radar signal analysis and processing implemented in the radar system are logically correct and valid.

**Acknowledgement:** This work was partially supported by the National Science Council of Taiwan, R.O.C., under grants MOST 110-2111-M-008-011. We would like to express our deep appreciation to Central Weather Administration in Taiwan for their kind help in constructing and implementing the Chung-Li meteor radar system..

## References:

- Brahmanandam, P. S., G. Uma, J. Y. Liu, Y. H. Chu, N. S. M. P. Latha Devi, and Y. Kakinami (2012). Global S4 index variations observed using FORMOSAT-3/COSMIC GPS RO technique during a solar minimum year, *J. Geophys. Res.*, 117, A09322, doi:10.1029/2012JA017966.
- Chu, Y. H., C. L. Su, M. F. Larsen, and C. K. Chao (2007). First measurements of neutral wind and turbulence in the mesosphere and lower thermosphere over Taiwan with a chemical release experiment, *J. Geophys. Res.*, 112, A02301, doi:10.1029/2005JA011560.
- Chu, Y.-H., P. S. Brahmanandam, Wang, C.-Y., Su, C.-L., & Kuong, R.-M. (2011). Coordinated sporadic E layer observations made with Chung-Li 30MHz radar, ionosonde and FORMOSAT-3/COSMIC satellites. *Journal of Atmospheric and Solar-Terrestrial Physics*, 73(9), 883–894. doi:10.1016/j.jastp.2010.10.004
- Day, K. A., M. J. Taylor, and N. J. Mitchell (2012). Mean winds, temperatures and the 16- and 5-day planetary waves in the mesosphere and lower thermosphere over Bear Lake Observatory (42°N, 111° W), *Atmos. Chem. Phys.*, 12, 1571–1585, 2012.
- Fritts, D. C. and M. J. Alexander (2003). Gravity wave dynamics and effects in the middle atmosphere, *Rev. Geophys.*, 41, 1003, doi: 10.1029/2001RG000106.
- Hibbins, R. E., M. P. Freeman, S. E. Milan, and J. M. Ruohoniemi (2011). Winds and tides in the mid-latitude Southern Hemisphere upper mesosphere recorded with the Falkland Islands SuperDARN radar, *Ann. Geophys.*, 29, 1985–1996, 2011.
- Hines, C. O. (1959). An interpretation of certain ionospheric motions in terms of atmospheric waves, *J. Geophys. Res.*, 64, 2210–2211, doi:10.1029/JZ064i012p02210, 1959.
- Kelley, M. C., The Earth's Ionosphere, Academic Press, San Diego, Calif., 1989.
- Murayama, Y., K. Igarashi, I. Nishimuta, R. Yamazaki, K. I. Oyama, T. Tsuda, T. Nakamura, S. Fukao, H. U. Widdel, and K. Schlegel (1999). Cooperative wind observation in the upper mesosphere and lower thermosphere with foil chaff technique, the MU radar, and Yamagawa MF radar, *Earth Planets Space*, 51, 719–729.
- Potula, B. S., Y.-H. Chu, G. Uma, H.-P. Hsia, and K.-H. Wu (2011). A global comparative study on the ionospheric measurements between COSMIC radio occultation technique and IRI model, *J. Geophys. Res.*, 116, A02310, doi:10.1029/2010JA015814.
- Su, C. L., H. C. Chen, Y. H. Chu, M. Z. Chung, R. M. Kuong, T. H. Lin, K. J. Tzeng, C. Y. Wang, K. H. Wu, and K. F.

Yang (2014), Meteor radar wind over Chung-Li (24.9°N, 121°E), Taiwan, for the period 10–25 November 2012 which includes Leonid meteor shower: Comparison with empirical model and satellite measurements. *Radio Sci.*, 49, doi:10.1002/2013RS005273.

Swenson, G. R., and S. B. Mende (1994). OH emission and gravity waves (including a breaking wave) in all-sky imagery from Bear Lake, UT, *Geophys. Res. Lett.*, 21, 2239 – 2242.

Uma, G., Brahmanandam, P. S., & Chu, Y. H. (2016). A long-term study on the deletion criterion of questionable electron density profiles caused by ionospheric irregularities – COSMIC radio occultation technique. *Advances in Space Research*, 57(12), 2452–2463. doi:10.1016/j.asr.2016.03.034

Xiao, C., H. Xiong, A. K. Smith, X. Qingchen, and X. Chen (2013). Short-term variability and summer-2009 averages of the mean wind and tides in the mesosphere and lower thermosphere over Langfang, China (39.4°N, 116.7°E), *J. Atmos. Sol. Terr. Phys.*, 92, 65–77.

Yee, J-H., Cameron, G. E., and D. Y. Kusnierzewicz (1999). Overview of TIMED, *SPIE*, 3756, 244–254.

Yu, Y., W. Wang, and M. P. Hickey (2017). Ionospheric signatures of gravity waves produced by the 2004 Sumatra and 2011 Tohoku tsunamis: A modeling study, *J. Geophys. Res. (Space Physics)*, 122, 1146–1162, doi:10.1002/2016JA023116.

---

**Ching-Lun Su**

Institute of Space Science  
Natl. Central University  
Jhong-Li, Taiwan  
clsu@ss.jupiter.ss.ncu.edu.tw

**Po-Hsun Chiu**

Institute of Space Science  
Natl. Central University  
Jhong-Li, Taiwan  
allanfu963369@gmail.com

**Ruey-Ming Kuong**

Institute of Space Science  
Natl. Central University  
Jhong-Li, Taiwan  
mkuong@wpl.ss.jupiter.ss.ncu.edu.tw

**Hsyang-Chan Chen**

Institute of Space Science  
Natl. Central University  
Jhong-Li, Taiwan  
JohnChen@wpl.ss.jupiter.ss.ncu.edu.tw

**Yen-Hsyang Chu**

Institute of Space Science  
Natl. Central University  
Jhong-Li, Taiwan  
e-mail: yhchu@ss.jupiter.ss.ncu.edu.tw  
ORCID 0000-0002-9451-7988

**A. Narendra Babu**

Department of Electronics and Communication  
Engineering,  
LBR College of Engineering  
Mylavaram- 521230  
India  
narendraalur@gmail.com  
ORCID 0000-0002-3185-1997

**P. S. Brahmanandam**

Shri Vishnu Engineering College for Women (A)  
Bhimavaram- 534202  
India  
dranandpotula@svecw.edu.in  
ORCID: 0000-0001-9777-3496

---